공학박사학위논문

Routing Method for Two-dimensional Dispersion Coefficients in Open Channel and Its Application for Remotely Sensed Tracer Tests

개수로에서 2차원 분산계수 추적법 및 원격관측 추적자 실험에의 적용

2020년 2월

서울대학교 대학원

건설환경공학부

백 동 해

Routing Method for Two-dimensional Dispersion Coefficients in Open Channel and Its Application for Remotely Sensed Tracer Tests

개수로에서 2차원 분산계수 추적법 및
원격관측 추적자 실험에의 적용

지도교수 서 일 원
이 논문을 공학박사 학위논문으로 제출함

2019년 10월

서울대학교 대학원
건설환경공학부
백 동 해

백동해의 박사학위논문을 인준함

2019년 12월

위 원 장 황진환 (인)

부 위 원 장 서일원 (인)

위 원 박용성 (인)

위 원 백경오 (인)

위 원 송창근 (인)

Abstract of dissertation

Routing Method for Two-dimensional Dispersion Coefficients in Open Channel and Its Application for Remotely Sensed Tracer Tests

By

Donghae Baek

Doctor of Philosophy in Civil and Environmental Engineering

Seoul National University

Professor Il Won Seo, Advisor

The depth-averaged two-dimensional (2D) advection-dispersion equation (ADE) has been widely used to analyze the mixing phenomenon of the various dissolved and suspended matters in river systems. In depth-averaged 2D ADE, dispersion coefficients are essential parameters to explain the spreading of pollutant clouds, caused by complexities of flow structures and river environments. The dispersion

coefficients in 2D ADE can be calculated by the routing based-observation methods using the tracer test data. The 2D stream-tube routing procedure (2D STRP) has been the only method to calculate both longitudinal and transverse dispersion coefficients of 2D ADE simultaneously for the transient concentration conditions. In this study, the limitations of 2D STRP were quantitatively analyzed using the hypothetically generated data. Besides, the new routing-based observation method (2D STRP-*i*) and the remote sensing-based experimental framework for tracer tests were developed to overcome the limitations of existing determination methods for dispersion coefficients.

The performance of existing 2D STRP was evaluated in terms of the variation of Peclet number, and the spatially varied velocity distributions. The results of the evaluations showed that the existing 2D STRP well provided the temporal distribution of tracer concentration in the high Peclet number, but it could not reproduce the reliable results when the tracer clouds reached wall boundaries and the Peclet number decreased. The new routing-based observation method (2D STRP-*i*) was developed to improve the drawback of the existing method. The 2D STRP-*i* derived from the 2D ADE in the orthogonal curvilinear coordinate system, assuming the steady-state flow condition. 2D STRP-*i* could adequately reproduce the reliable temporal distribution even if the effect of wall boundaries was significant.

A remote sensing based-experimental framework for tracer tests was developed to acquire the spatio-temporal concentration distribution of tracer clouds in open channel flows. Tracer tests using Rhodamine WT were conducted in the large-scaled

experimental channels to collect the RGB images using a commercial digital camera mounted on a UAV and the concentration of Rhodamine WT using in-situ fluorometric probes. The empirical relationship between the image data and the Rhodamine WT concentration data was estimated using an artificial neural network (ANN) model. The acquired spatio-temporal concentration distributions by the proposed method gave general as well as detailed views of the tracer cloud moving dynamically in open channel flows that cannot be easily observed using conventional in-situ measurements.

The 2D STRP-*i* was applied to the remotely measured tracer data to calculate the dispersion coefficients. The *Latin Hypercube Simulation* was adopted to determine the optimum values of dispersion coefficients. The results of simulations showed that the RMSE distributions were non-convex with many local minima. In addition, the optimal dispersion coefficients were differently found according to the evaluation functions. In this study, the multiple evaluation indices were selected to determine the dispersion coefficients more robustly. The results showed that the longitudinal dispersion coefficients were similarly determined by both 2D STRP and STRP-*i*, while the existing 2D STRP generally underestimated the values of transverse dispersion coefficients compared to the results of 2D STRP-*i*.

Keywords: depth-averaged pollutant transport modeling, shear dispersion, routing procedure, remote sensing technique, spatio-temporal measurements, artificial neural network, 2D tracer test

Student number: 2015-30277

Table of contents

List of figures

List of tables

List of symbols

Latin Uppercase

A	mean cross-sectional area
B_C	bulk dispersion coefficient
C	depth-averaged concentration
$\hat{C}$	predicted concentration
C_p	peck concentration
D_{ij}	dispersion coefficient in tensor form
D_L	longitudinal dispersion coefficient
D_T	transverse dispersion coefficient
DN	digital number of image data
H_j	hidden node in neural network
H_n	number of hidden nodes in neural network
K	longitudinal dispersion coefficient in one-dimensional transport model
L_{CV}	distance of complete vertical mixing
L_b	radiance reflected from riverbed
L_c	back-scattered radiance from waterbody
L_n	characteristic length of Peclet number
L_p	the path radiance through the atmosphere
L_u	total radiance reaching detector

Pe	Peclet number
P_m	degree of mixing
Q	flow discharge
Q_m	maximum flow discharge
S_L	longitudinal stream-tube dispersion coefficient
S_T	transverse stream-tube dispersion coefficient
TV	total variation
U	depth-averaged velocity component in *x*-direction
V	depth-averaged velocity component in *y*-direction
W_{jk}	weight factor in neural network
X	measuring location in *x*-direction

Latin Lowercase

b_k	bias factor in neural network
c	Reynolds-averaged concentration
c'	vertical deviation of concentration
h	local water depth
m_s	metric coefficient in longitudinal direction
m_n	metric coefficient in transverse direction
q_c	cumulative discharge
$\mathbf{n}$	normal vector

r gradient ratio between upstream and downstream surface of control volume

$\bar{t}$ time to centroidal mass arrival time

u Reynolds-averaged velocity component in x-direction

u' vertical deviation of velocity component in x-direction

v Reynolds-averaged velocity component in y-direction

v' vertical deviation of velocity component in y-direction

w Reynolds-averaged velocity component in z-direction

x x-direction in cartesian coordinate

y y-direction in cartesian coordinate

y' normalized transverse distance from left bank

z z-direction in cartesian coordinate

Greek Uppercase

Δs longitudinal distance increment

Δn transverse distance increment

Γ gamma function

Ψ normalized shape factor

Greek Lowercase

δ_j activation function in neural network

ε_x turbulent diffusion coefficient in x-direction

ε_y turbulent diffusion coefficient in *y*-direction

ε_z turbulent diffusion coefficient in *z*-direction

η dimensionless cumulative discharge

λ wavelength of light

τ dummy time variable

ω normalized dummy variable

ξ dummy longitudinal distance variable

ψ dummy transverse distance variable

1. Introduction

1.1 Background and necessities of study

When pollutants are introduced to river systems in which the channel width is typically larger than the water depth, the depth-averaged two-dimensional (2D) advection-dispersion equation (ADE) has been widely used to analyze the contaminant mixing after completion of the vertical mixing (Fischer et al., 1979). In depth-averaged 2D ADE, dispersion coefficients are essential parameters to represent the spreading of pollutant clouds caused by vertical variations of velocities and other processes such as turbulent diffusions and mixing due to channel irregularities. Thus, dispersion coefficients in 2D ADE involve a variety of properties characterized by the hydraulic, geomorphological, as well as ecological factors.

The determination method for 2D dispersion coefficients can be classified into the observation method and the estimation method, as shown in Fig. 1.1. In the estimation method, the dispersion coefficients were indirectly estimated by theoretical formula and empirically constructed regression equations without concentration data. The empirical approaches require enough dataset of measured data to associate the various statistical characteristics of hydraulic information to the observed dispersion coefficients in various conditions of streams. The accuracy of such empirical approaches could be dominantly affected by the qualities of the dataset used to fit the regression curves. Thus, in order to construct the robust empirical relationship between

the dispersion coefficients and stream characteristics, sufficient numbers of accurate 2D dispersion coefficients should be provided from the various conditions of streams.

The dispersion coefficients have generally been obtained by the observation methods using the concentration data measured by the tracer tests. The tracer test is the experimental procedures to measure the concentration distributions of the tracers, which are detectable chemical materials such as fluorescent dyes, radioisotopes as well as electroconductivity of solute material (Godfrey and Frederick, 1970; Nordin et al., 1974; Kilpatrick et al., 1989; Seo et al., 2006; Seo et al., 2016; Jung et al., 2019). Among the observation methods in Fig. 1.1, the moment-based methods such as the simple moment method (Sayre and Chang, 1968) and the stream-tube moment method (Beltaos, 1980) only provide the transverse dispersion coefficient using the tracer concentration data in the conditions where the tracers (pollutants) were continuously injected. The moment-based method cannot provide the longitudinal dispersion coefficients in 2D ADE when tracers are instantaneously injected. To overcome this drawback of the moment-based method, Baek et al. (2010) proposed the 2D stream-tube routing procedure to facilitate to observe both longitudinal and transverse dispersion coefficients simultaneously in the transient concentration conditions.

Fischer (1968) first adopted the concept of routing for concentration distributions to develop the one-dimensional routing procedure (1D RP), which calculates the longitudinal dispersion coefficients in 1D ADE. The 1D RP inherently required the concentration distribution in the longitudinal space, but the acquisition of spatial concentration distributions with high resolution is technically limited in the

conventional tracer tests. Thus, Fischer (1968) introduced the frozen cloud approximation (FCA) to estimate the spatial distribution from the temporal distribution measured at the fixed measuring sections. The FCA assumed that the shape of the dispersing cloud changes only slightly during the time taken to pass the observation point (Fischer et al., 1979), and the centroid of pollutant clouds moves with the mean flow velocity in the stream (Singh and Beck, 2003). This assumption could be acceptable in cases where the Péclet number, which is defined as the ratio of advective transport rate to dispersion transport rate, was sufficiently high.

The FCA has played an essential role in the routing procedure-based calculation methods. Despite that, the validity of FCA has not been evaluated sufficiently. Only a few studies mentioned that FCA could introduce errors in the estimation of the dispersion coefficients (Singh and Beck, 2003). The 2D STRP also requires the FCA in order to estimate the depth-averaged 2D spatial concentration distribution from the temporal concentration data. For calculation of 2D dispersion coefficients using 2D STRP, the time-series data of continuous transverse concentration profiles at both upstream and downstream sections are required. However, the acquisition of spatially continuous concentration profiles is typically challenging in the experimental framework of conventional tracer tests. In conventional tracer tests, the tracer concentration is usually obtained as time-series data from sensor probes installed at limited fixed points in river cross-sections. Therefore, it is very challenging to observe the spatially continuous distributions of tracer clouds over the cross-sections of streams, using conventional techniques based on the *in-situ* measurements. Due to this technical limitation, the most previous studies that used 2D STRP for calculation of 2D

dispersion coefficients interpolated and extrapolated using the kriging algorithm to obtain the transverse concentration profiles from the concentration data which were measured at the several numbers of measuring points.

To overcome the limitations mentioned above, suitable experimental techniques, which can observe the spatial distribution with the high resolution, are needed for observing the river mixing in details. Fischer (1966) attempted to acquire the spatial distribution of tracer clouds in natural streams from aerial photography using a film camera mounted on a manned aircraft. The spatial concentration distributions were qualitatively estimated by human color recognition. This approach, however, was used only as supplementary data to understand the longitudinal mixing behavior in natural streams. In recent years, the multi- or hyperspectral images, obtained by satellite and aircraft, have often been employed to observe the spatial distribution of various water quality constituents such as chlorophyll-a, suspended sediment, and colored dissolved organic matter in large lakes and coastal areas over the past three decades (Ritchie et al., 1990; Harrington et al.,1992; Schiebe et al., 1992; Chacon-Torres et al., 1992; Pattiaratchi et al.,1994; Brando and Dekker, 2003; Cannizzaro and Carder, 2006; Matthews, 2011; Olmanson et al., 2013). Although satellite-based remote sensing has been successfully applied to observe water quality constituents in large-scale water environments, they have not been found suitable for observing pollutant mixing in small rivers and streams due to their insufficient spatial and temporal resolution (Olmanson et al., 2013; Palmer et al., 2015); The resolutions of most spectral images acquired by satellite platforms including Landsat-8 Operational Land Imager (OLI)/Thermal Infrared Sensor (TIRS), Sentinel-2 and Terra Moderate Resolution

Imaging Spectroradiometer (MODIS) are the order of 10 meters, and their temporal resolutions specified by the revisit interval of satellites are several days (Gholizadeh et al., 2016; Transon et al., 2018). To observe the dispersion processes of tracer materials in open channels where the scale of width is on the order of several meters, the higher spatial and temporal resolution of aerial images is required. In more recent years, unmanned aerial vehicles (UAVs) have been considered as an alternative to satellite constellations for river measurements (Flynn and Chapra, 2014; Tamminga et al., 2015; Detert and Weitbrecht, 2015; Wigmore and Mark, 2017; Woodget et al., 2017). UAVs can carry out river surveys with high resolutions, both spatially and temporally. Moreover, the use of UAVs facilitates to acquire high-resolution aerial images during tracer experiments regardless of experimental sites and times.

As aforementioned, 2D STRP is the only method that can provide both longitudinal and transverse dispersion coefficients among the existing observation methods. Recently, some studies reported that 2D STRP yielded over- and underestimated dispersion coefficients compared to theoretical values (Seo et al., 2016; Choi, 2017; Shin et al., 2019). In this study, the performance of 2D STRP was evaluated to investigate its applicability in the natural stream. Then, a new routing procedure-based calculation method (2D STRP-*i*) was developed to determine dispersion coefficients more accurately in open channels. Furthermore, the remote sensing-based experimental framework for tracer tests, which can observe the concentration distributions of tracer in both spatially and temporally, was developed to support the analysis of pollutant transport in open channels.

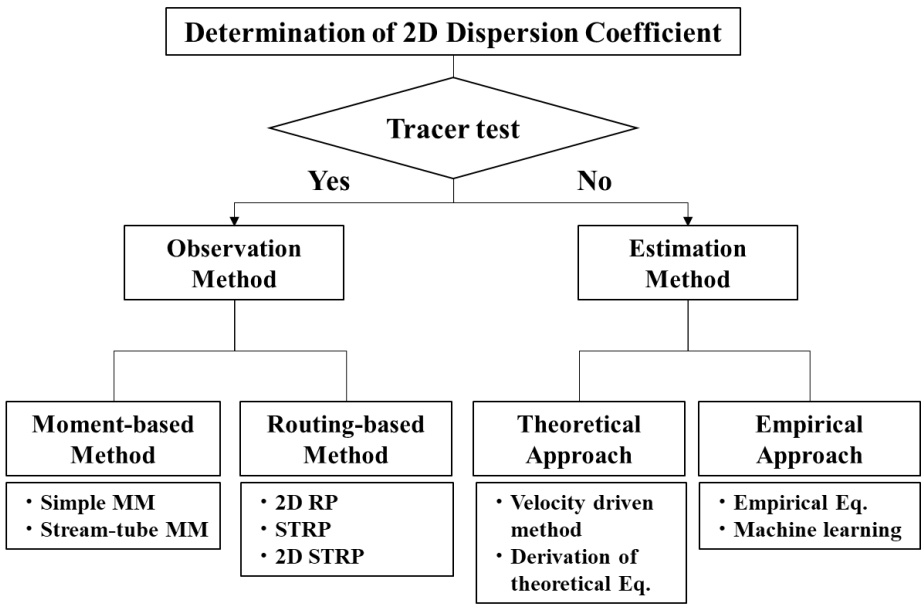

Figure 1.1 Determination methods for 2D dispersion coefficients (revised from Baek and Seo, 2016)

1.2 Objectives and methodology

The primary goal of the present study is to develop a new routing-based method to calculate the dispersion coefficients accurately in the open channel flows, using the concentration data obtained from tracer tests. The detailed objectives of this study are as followings:

(1) Analysis of the limitations of 2D stream-tube routing procedures (2D STRP)

(2) Development of a new calculation method for two-dimensional dispersion coefficients

(3) Development of a remote sensing based-experimental frameworks for tracer tests

For the first objective, the numerical model for simulation of the depth-averaged 2D pollutant transport was implemented based on the Finite Volume Method (FVM). Using the implemented numerical models and well-known analytical solution, the synthetic spatio-temporal distributions of pollutant clouds were generated in order to evaluate the 2D STRP, which is the only method to calculate both longitudinal and transverse dispersion coefficients simultaneously in the condition of transient mixing behavior. The evaluations were performed on the various Péclet number and velocity distributions.

In the second objective, the 2D STRP was improved to overcome the existing limitations, considering the spatially varied advection and the wall boundary effect.

The two-dimensional dispersion coefficients were calculated by the newly-developed method (2D STRP-*i*) on the synthetic data, as well as the field test data described in the following third objective.

In the third objective, an experimental framework for remote sensing-based tracer tests was developed to acquire the spatio-temporal concentration distribution in open channel flows to complement the limitations of the conventional tracer tests. Tracer tests using fluorescent dye were performed in large-scale experimental channels to acquire both aerial images using a commercial digital camera mounted on a drone and *in-situ* measured concentrations by fluorometers. By the machine learning-assisted techniques, the aerial RGB image data were converted to spatio-temporal concentration in the whole experimental sections, including areas where concentration data were not collected. The outline of this research is summarized in Fig. 1.2.

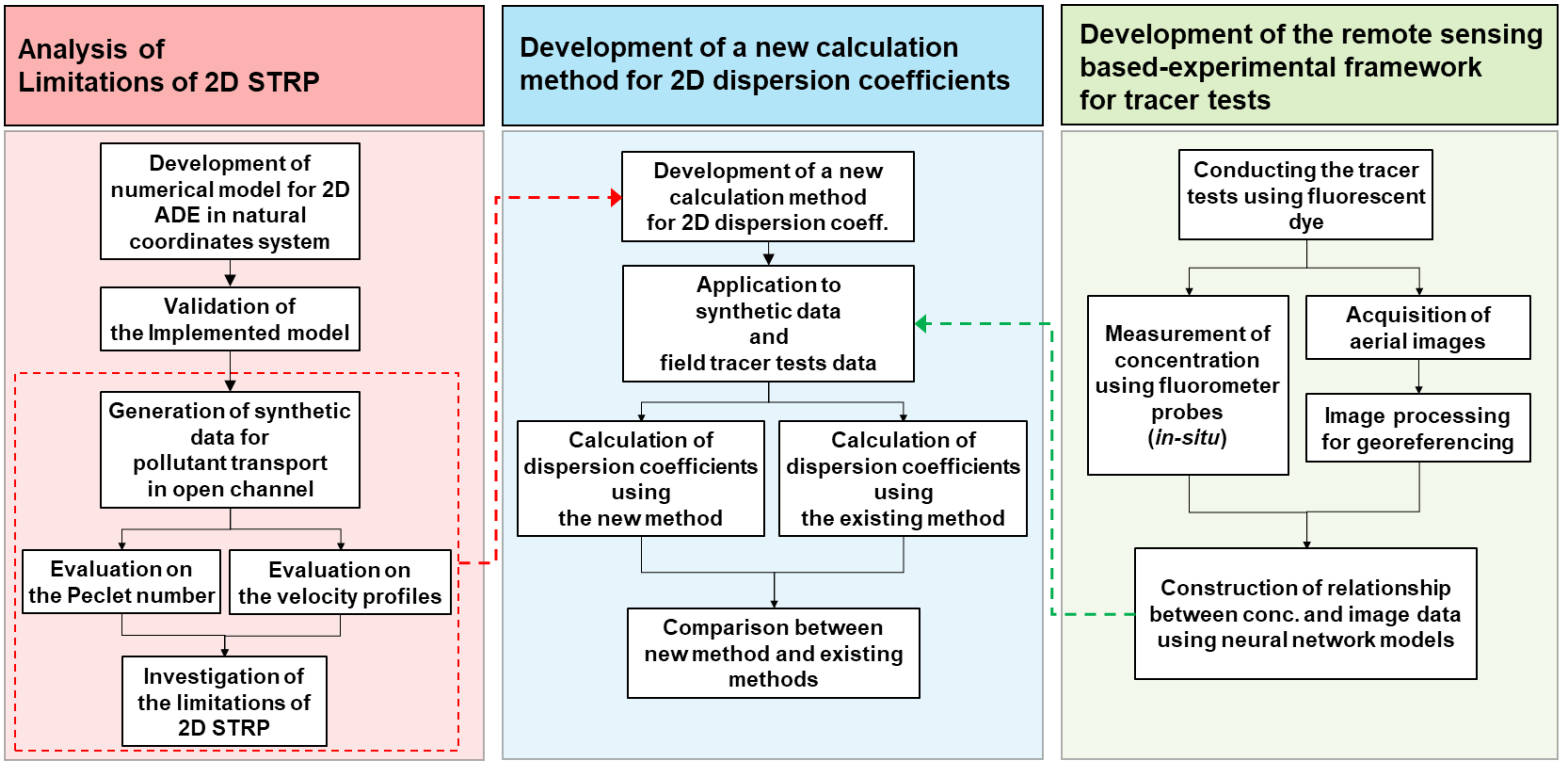

Figure 1.2 Summary of the research objective

2. Theoretical backgrounds

2.1. Pollutant transport model in the natural river

2.1.1 Necessity of 2D pollutant transport models

When Pollutant matter is instantaneously released into the open channel flows, the pollutant mixing behavior can be classified into the three stages depending on the major factors which cause the spreading of pollutant clouds, as illustrated in Fig.2.1. In order to predict the pollutant mixing in open channels effectively and also efficiently, the proper modeling approaches should be chosen considering the characteristics of mixing behaviors. The flow of rivers is generally the turbulent flow with high Reynolds number, so the mass of pollutants, which is instantaneously released, is three-dimensionally spread by turbulent diffusion in the near-field. The modeling of pollutant transport for this stage requires the three-dimensional analysis, so the understanding of the turbulent motions of fluid particles is necessary. This initial stage is relatively short, but the computational effort is much larger compared to other stages. The geomorphological characteristics of the natural river are the large aspect ratio, which is the ratio of the channel width to water depth. Thus, the pollutant mixing in the vertical direction is rapidly complete, and then the pollutant mixing can be considered as the depth-averaged two-dimensional behaviors. The vertical turbulent diffusion coefficients must be known to estimate the longitudinal distance from the release point to the section for achieving the completion of vertical mixing.

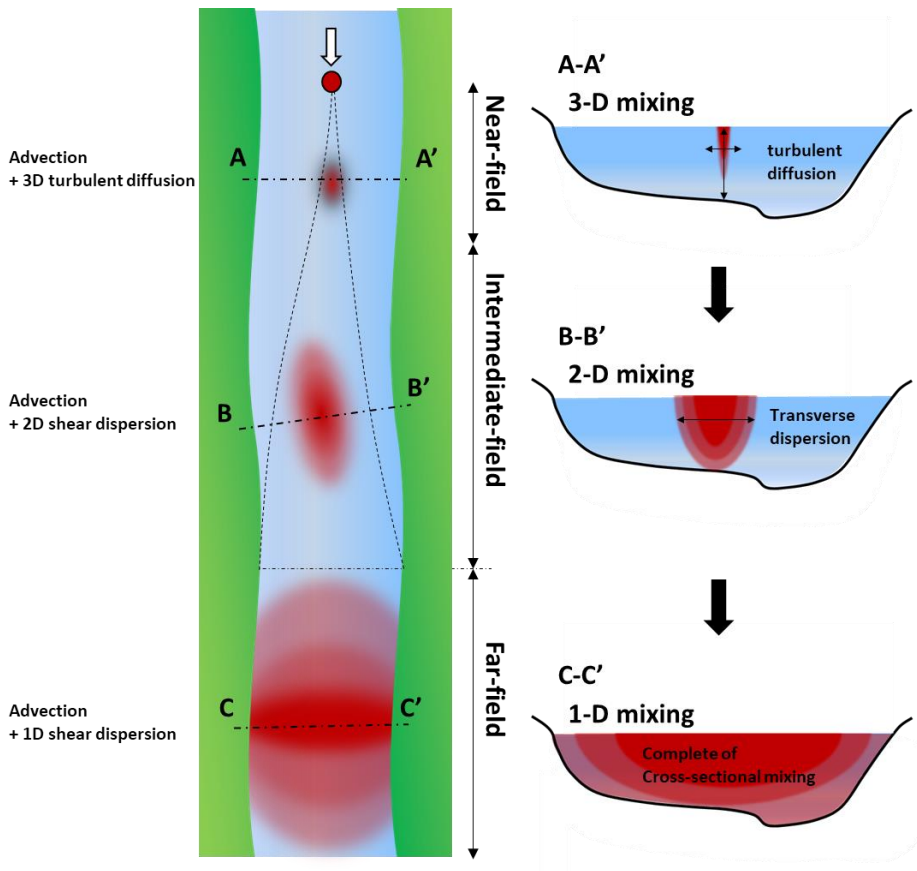

Figure 2.1 Conceptual diagram of the mixing stages in the open channels

When it can be assumed that the vertical velocity profile is the logarithmic profiles, and the turbulent Schmidt number is the unity, the depth-averaged vertical turbulent diffusion coefficient could be derived as follows.

$$\overline{\varepsilon}_z = \frac{1}{h}\int_0^h \kappa h u^* \frac{z}{h}\left(1-\frac{z}{h}\right)dz = \frac{\kappa}{6} h u^* \tag{2.1}$$

where z is the vertical coordinates; h is the water depth; u^* is the shear velocity; κ is the von Karman constant. When the pollutants are released from the water surface, the complete distance of the near-field has been approximately assumed as Eq. (2.2), based on the analytical solution (Fischer et al., 1979; Rutherford, 1994).

$$L_{CV} = 0.536\frac{UH^2}{\varepsilon_z} \tag{2.2}$$

where U is the cross-sectional mean velocity; H is the cross-sectional mean water depth. The value of 0.536 is achieved when 98% of pollutant concentration is mixed from the water surface to the channel bed.

After the vertical mixing is completed, the concentration distribution of pollutant clouds could be assumed as depth-averaged fields in the intermediate field. For

modeling for this stage, the depth-averaged flow fields and concentration fields are required. As compared to the three-dimensional model, both the depth-averaged hydrodynamics and pollutant transport models are more efficient in terms of computational costs. The two-dimensional dispersion coefficients in depth-averaged transport models are 100 times larger than the turbulent diffusion coefficients (Park, 2017), so the turbulent diffusion coefficients sometimes neglected or included in the dispersion coefficients. The derivation of two-dimensional transport models and modeling of dispersion coefficients will be considered in the next sections.

The water channels of rivers were confined by riverbanks. Thus, the pollutant clouds eventually reach the sidewall, and the pollutant mixing is gradually completed over the cross-section of river channels. The distance to the completion of the intermediate field could be calculated if the transverse dispersion coefficient is known.

$$L_{CT} = 0.134\frac{UW^2}{D_T} \tag{2.3}$$

The empirical values for transverse dispersion coefficients have been suggested as $0.15HU^*$(Fischer et al., 1979). This stage is much longer than the interval of the near-field. Using the Eq. (2.2) and Eq. (2.3), the ratio of L_{CT} to L_{CV} can be represented by following.

$$\frac{L_{CT}}{L_{CV}} = 0.11\left(\frac{W}{H}\right)^2 \tag{2.4}$$

As shown in Eq. (2.4), the ratio of L_{CT} to L_{CV} increased with increasing the aspect ratio of channel cross-sections. As mentioned above, the natural rivers generally have a large aspect ratio over 10. Notably, the channelized rivers across the urban area and the industrial complexes, such as the Han River and Nakdong River in South Korea, has a significant aspect ratio. For instance, the aspect ratio of the Han River is approximately 40, so L_{CT} is 160 times larger than L_{CV} (MOLTI, 2008). Moreover, L_{CT} is approximately calculated as 120 km, using Eq. (2.3). This distance is corresponding to a quarter of the total length. Thus, the depth-averaged pollutant transport model is needed to predict the pollutant transport for the open channels of which the aspect ratio is large.

2.1.2 2D ADE in the cartesian coordinate system

The advection-diffusion equation has been a general mathematical model to simulate the mass transport in many physical problems. The transport phenomena in open channel flow such as riverine, coastal, and lacustrine environments are generally affected by the turbulent flow with high Reynolds numbers. Its three-dimensional mathematical expressions in the cartesian coordinate system can be written as:

$$\frac{\partial c}{\partial t}+\frac{\partial (uc)}{\partial x}+\frac{\partial (vc)}{\partial y}+\frac{\partial (wc)}{\partial z}=\frac{\partial}{\partial x}\left(\varepsilon_x \frac{\partial c}{\partial x}\right)+\frac{\partial}{\partial y}\left(\varepsilon_y \frac{\partial c}{\partial y}\right)+\frac{\partial}{\partial z}\left(\varepsilon_z \frac{\partial c}{\partial z}\right) \quad (2.5)$$

where u, v and w are Reynolds-averaged velocities; ε_x, ε_y and ε_z are turbulent diffusion coefficients in x, y, and z-direction of Cartesian coordinate; c is the solute concentration of mass transported in the fluid medium.

For practical engineering problems, the depth-averaged two-dimensional models can be used to reduce the computational efforts and expenses, instead of three-dimensional models. In the river system, of which channel width is typically larger than the water depth, the mass of solute matters of interest well mixed vertically before it gets fully mixed transversely. Thus, the depth-averaged values of pollutant concentration could be efficient to represent the mixing behaviors in the natural

rivers. The two-dimensional depth-averaged advection-dispersion equation (2D ADE) can be derived by integrating Eq. (2.5) from the bed $z = b(x, y)$ to the surface $z = a(x, y)$ using Leibnitz's rule (Rutherford, 1994).

$$\begin{aligned}
&\int_b^a \frac{\partial c}{\partial t} dz + \frac{\partial}{\partial x}\int_b^a (uc)\, dz + \frac{\partial}{\partial y}\int_b^a (vc)\, dz \\
&= \frac{\partial}{\partial x}\int_b^a \varepsilon_x \frac{\partial c}{\partial x} dz + \frac{\partial}{\partial y}\int_b^a \varepsilon_y \frac{\partial c}{\partial y} dz + \left[c\left(u\frac{\partial a}{\partial x} + v\frac{\partial a}{\partial y} - w \right) \right]_a \\
&- \left[c\left(u\frac{\partial b}{\partial x} + v\frac{\partial b}{\partial y} - w \right) \right]_b - \left(\varepsilon_x \frac{\partial c}{\partial x}\frac{\partial a}{\partial x} + \varepsilon_y \frac{\partial c}{\partial y}\frac{\partial a}{\partial y} - \varepsilon_z \frac{\partial c}{\partial z} \right)_a \\
&+ \left(\varepsilon_x \frac{\partial c}{\partial x}\frac{\partial b}{\partial x} + \varepsilon_y \frac{\partial c}{\partial y}\frac{\partial b}{\partial y} - \varepsilon_z \frac{\partial c}{\partial z} \right)_b
\end{aligned} \tag{2.6}$$

With the assumption that the mass fluxes that are normal to the boundaries are zero at both the surface and the bed, the following equation can be obtained.

$$\begin{aligned}
&\frac{\partial (hC)}{\partial t} + \frac{\partial (hCU)}{\partial x} + \frac{\partial (hCV)}{\partial y} \\
&= \frac{\partial}{\partial x}\left[-\int_0^h u'c'dz + h\varepsilon_x \frac{\partial C}{\partial x} \right] + \frac{\partial}{\partial y}\left[-\int_0^h v'c'dz + h\varepsilon_y \frac{\partial C}{\partial y} \right]
\end{aligned} \tag{2.7}$$

where C is depth-averaged concentration; h is local depth of flow; U and V are depth-averaged velocity along x and y directions, respectively; u' and v' denote vertical

deviations of point velocity from depth-averaged velocity U and V, respectively; and c' is deviation of local concentration from depth-averaged concentration C. The integral terms of the product of velocity and concentration deviations in Eq. (2.7) are expressed in the form of a dispersion term by Taylor's assumption; Fischer (1979) proposed a theoretical model of 2D shear dispersion in tensor forms that are applied to skewed shear flows in two directions. These terms are modeled using the concentration gradients based on the Fickian-type approach.

$$\int_0^h \left(u'c'\right)dz = -h\left(D_{xx}\frac{\partial C}{\partial x} + D_{xy}\frac{\partial C}{\partial y}\right) \tag{2.8a}$$

$$\int_0^h \left(v'c'\right)dz = -h\left(D_{yx}\frac{\partial C}{\partial x} + D_{yy}\frac{\partial C}{\partial y}\right) \tag{2.8b}$$

where D_{xx}, D_{xy}, D_{yx} and D_{yy} are components of the dispersion coefficients in tensor form. Substituting both Eq. (2.8a) and Eq. (2.8b) to Eq. (2.7), the final form of 2D ADE in the Cartesian coordinate system is derived as follows.

$$\begin{aligned}&\frac{\partial\left(hC\right)}{\partial t} + \frac{\partial\left(uUC\right)}{\partial x} + \frac{\partial\left(hVC\right)}{\partial y}\\ &= \frac{\partial}{\partial x}\left[h\left(D_{xx}+\varepsilon_x\right)\frac{\partial C}{\partial x} + hD_{xy}\frac{\partial C}{\partial x}\right] + \frac{\partial}{\partial y}\left[hD_{yx}\frac{\partial C}{\partial y} + h\left(D_{yy}+\varepsilon_y\right)\frac{\partial C}{\partial y}\right]\end{aligned} \tag{2.9}$$

The first term in Eq. (2.9) describes the time rate of change of mass. The second and third terms on the left-hand side are the advection terms. The terms in the right-hand side express the dispersion terms, and these terms represent the spreading of mass due to the turbulent diffusion and shear dispersion. The advection-dispersion process in the depth-averaged field is schematically expressed in Fig. 2.2.

As described above, The dispersion coefficients in Eq. (2.9) appear due to the vertical deviation of advective fluxes in the depth-integration process. Fischer (1979) derived the mathematical expression for dispersion tensors in skewed shear flow. In the three-dimensional transport equation, as expressed in Eq. (2.5), the Reynolds averaged vertical velocity components are negligible because the magnitude of vertical velocities is much smaller than the horizontal velocity components. Converting the Eq. (2.5) into the Lagrangian coordinate system and applying the order of magnitude analysis, the deviation of concentration from the depth-averaged value is found as:

$$c'(z) = \int_0^z \frac{1}{\varepsilon_z} \int_0^z \left(u' \frac{\partial C}{\partial x} + v' \frac{\partial C}{\partial y} \right) dz dz \tag{2.10}$$

By substituting the Eq. (2.10) into Eq. (2.8), the dispersion coefficients in tensor forms can be expressed as Eq. (2.11).

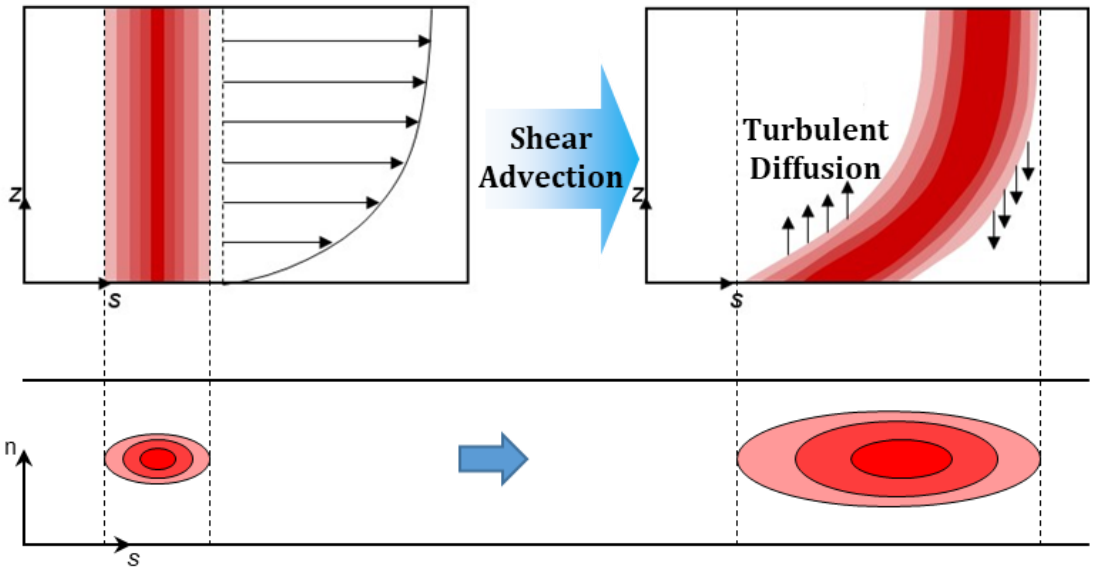

Figure 2.2 Conceptual diagram of the mass transport in shear flow (adapted from Park, 2017)

$$D_{xx} = -\frac{1}{h}\int_0^h u' \int_0^z \frac{1}{\varepsilon_z} \int_0^z u' dz dz dz \tag{2.11a}$$

$$D_{xy} = -\frac{1}{h}\int_0^h u' \int_0^z \frac{1}{\varepsilon_z} \int_0^z v' dz dz dz \tag{2.11b}$$

$$D_{yx} = -\frac{1}{h}\int_0^h v' \int_0^z \frac{1}{\varepsilon_z} \int_0^z u' dz dz dz \tag{2.11c}$$

$$D_{yy} = -\frac{1}{h}\int_0^h v' \int_0^z \frac{1}{\varepsilon_z} \int_0^z v' dz dz dz \tag{2.11d}$$

The dispersion coefficients induced by velocity deviation in the shear flow can be theoretically calculated using Eq. (2.11). Although the Eq. (2.11) can provide physically derived dispersion coefficients, this calculation requires the detailed three-dimensional velocity components, as well as vertical turbulent diffusivity from the laboratory or the field tests.

In the straight channel where the main flow direction is aligned with the *x*-axis, the dispersion coefficients, D_{xy} and D_{yx} in the Eq. (2.9) can be removed, and the equation can be simplified with replacing D_{xx} and D_{yy} to D_L and D_T, respectively, as shown in follows.

$$\frac{\partial(hC)}{\partial t} + \frac{\partial(uUC)}{\partial x} + \frac{\partial(hVC)}{\partial y} = \frac{\partial}{\partial x}\left(hD_L \frac{\partial C}{\partial x}\right) + \frac{\partial}{\partial y}\left(hD_T \frac{\partial C}{\partial y}\right) \tag{2.12}$$

where D_L is the longitudinal dispersion coefficient; D_T is the transverse dispersion coefficient.

2.1.3 2D ADE in the natural coordinate system

In the natural rivers with channel meanders and irregular boundaries, the main flow direction continuously varies so longitudinal and transverse directions with respect to the flow direction do not always coincide with the x, y-axis of the Cartesian coordinate system. In this case, the dispersion coefficients have to be considered as the tensor form in Eq. (2.9). These make the analysis of mixing behavior complicated in the natural rivers. Instead of adopting the Cartesian coordinate system, the orthogonal curvilinear coordinate system, in which the principal axes are aligned with the main flow direction and its perpendicular direction, is more suitable to analyze the mixing process in natural streams. Chang (1971) and Fukuoka and Sayre (1977) derived the continuity equation and the mass transport equation in the orthogonal curvilinear coordinate system.

$$m_s m_n \frac{\partial h}{\partial t} + \frac{\partial}{\partial s}\left(m_n hU\right) + \frac{\partial}{\partial n}\left(m_s hV\right) = 0 \tag{2.13}$$

$$\begin{aligned} & m_s m_n \frac{\partial}{\partial t}\left(hC\right) + \frac{\partial}{\partial s}\left(m_s hUC\right) + \frac{\partial}{\partial n}\left(m_n hVC\right) \\ & = \frac{\partial}{\partial s}\left(\frac{m_n}{m_s} hD_L \frac{\partial C}{\partial s}\right) + \frac{\partial}{\partial n}\left(\frac{m_s}{m_n} hD_T \frac{\partial C}{\partial n}\right) \end{aligned} \tag{2.14}$$

where s and n are the longitudinal and transverse curvilinear distance; m_s and m_n are metric coefficients. The system is composed of three mutually orthogonal sets of

coordinate surfaces, which are called longitudinal, transverse, horizontal coordinate surfaces, as shown in Fig. 2.3.

The metric coefficients m_s and m_n are the scale factors to correct the differences between distances along the primary axis and those measured along the respective axes (Yotsukura, 1977) illustrated in Fig. 2.3. m_s and m_n are defined as follows.

$$m_s = \frac{\Delta L_s}{\Delta s} \tag{2.15a}$$

$$m_n = \frac{\Delta L_n}{\Delta n} \tag{2.15b}$$

where ΔL_s and ΔL_n are the distance for a given increment in both longitudinal and transverse axis, respectively. When the longitudinal distances increase with Δs in the longitudinal axis, the corresponding distances can differ transversely due to the channel curvatures. The transverse distances are similarly varied by the velocity distribution. Thus, the metric coefficients are the function of *s* and *n*. and these are determined by hydraulic conditions, mainly, depth-averaged velocity vectors. Holly (1985) reported that the metric coefficients were typically ranged from 0.8 to 1.2. If the channel is the straight channel, the metric coefficients are equal to 1. In this case, the Eq. (2.14) becomes identical to Eq. (2.5) expressed in the Cartesian coordinates.

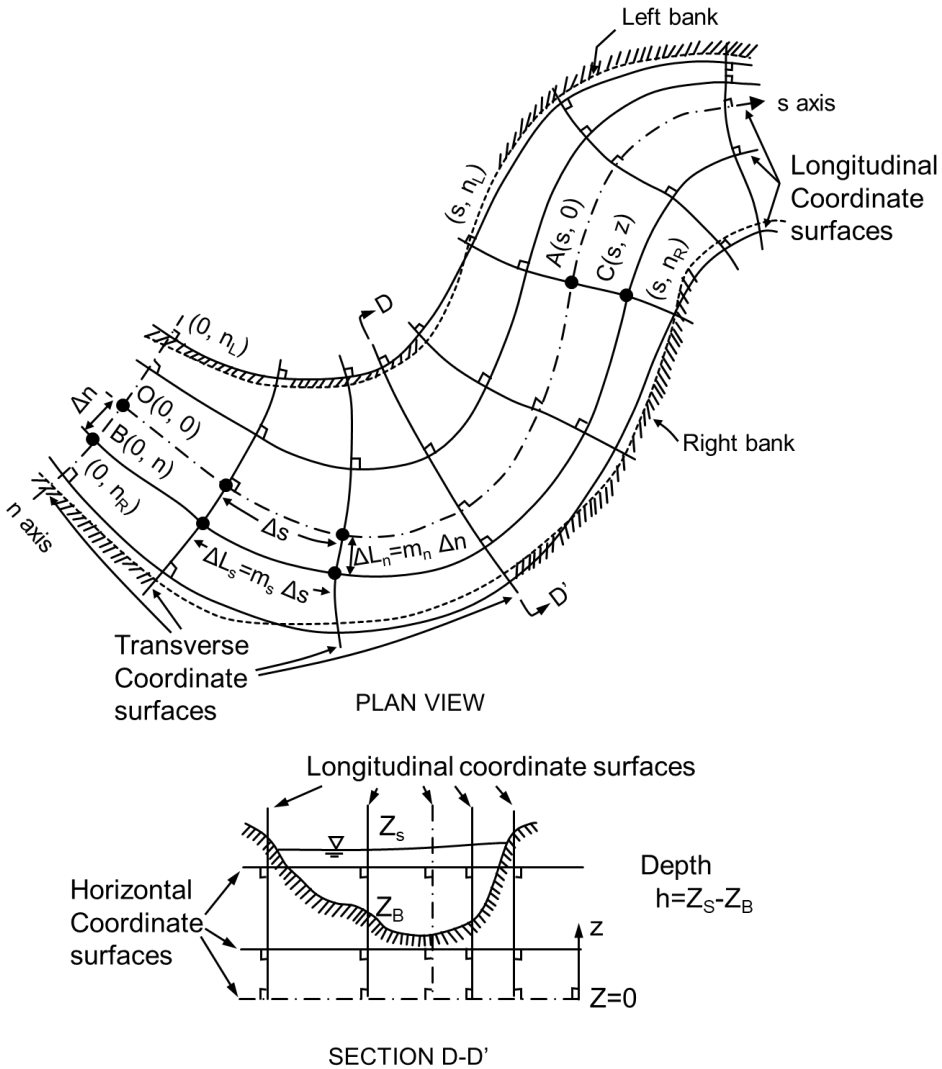

Figure 2.3 Orthogonal curvilinear coordinate system for natural channels (revised from Yotsukura, 1977)

The merit of the 2D ADE in the orthogonal curvilinear coordinate system is that the dispersion process can be expressed by the longitudinal and transverse direction, instead of the tensor forms. And the irregular shape of the domain can be transformed into the rectangular domain. This point is beneficial to implement the numerical models. In both numerical discretization and derivation of the analytical solution, the wall boundary condition is usually treated as the zero-flux normal to the impermeable boundaries. In meandering channel or width-varied channel, the normal direction to boundaries involves the derivative in both x and y-direction in the Cartesian coordinates. The use of Eq. (2.15) makes the implementation of numerical models for 2D ADE easier.

2.2 Determination of the dispersion coefficient from tracer test data

2.2.1 Experimental methods for conventional tracer tests

The tracer tests have been conducted to analyze the mixing behaviors in the natural stream. In this experimental test, the detectable chemical materials are artificially injected into the flow, and the temporal concentration profiles are measured in the several cross-sections. In many previous studies, the tracer materials such as the fluorescent dye, salt solutions, radioisotopes, and sulfur hexafluoride have been generally chosen due to its high detectability. Since the 1960s, the Rhodamine WT, which is a kind of fluorescent dye, has been widely used as a tracer for mixing study in rivers and groundwaters because it is mostly conservative and easily detectable with low background concentration (Mukherjee et al., 2005; Rowinski et al., 2007; Sun et al., 2001). It has also been known that the Rhodamine WT is relatively safe regarding the impact on the aquatic environment compared to the other chemical tracers. The influence of fluorescent dyes on small aquatic organisms in rivers was well documented by Rowinski and Chzanowski (2001).

The concentration of Rhodamine WT can be measured using its optical characteristics. When Rhodamine WT is irradiated with light of a particular wavelength (approximately 540 nm), it emits light of a longer wavelength (approximately 590 nm). It has been well known that the fluorescence intensity of Rhodamine WT is proportional to its concentration in the ranges below 200 ppb approximately. Using these characteristics, the most commercial fluorometers to

measure the concentration of Rhodamine WT use a light-emitting diode (LED) as the source of the irradiating light that has a peak wavelength of approximately 540 nm, and receive the emitted light intensities that has a peak wavelength of approximately 590 nm by the photodiodes through the optical filters.

The experimental procedures of 2D tracer tests using Rhodamine WT are categorized as follows: (1) installation of taglines and probe sensors for concentration measurements at the measurement sections; (2) measurement of hydraulic data; (3) injection of tracer material as summarized in Fig. 2.1. In step (1), the first cross-section must be installed in the downstream where the complete vertical mixing is achieved to observe the 2D mixing behaviors. The distance from the injection point to the first measuring section can be estimated using the Eq. (2.16) (Fischer et al., 1979).

$$L_{CV} = 0.3\frac{UH^2}{\varepsilon_V} \tag{2.16}$$

where L_{CV} is a distance of complete vertical mixing; U is the cross-sectional averaged velocity; H is the mean water depth; ε_V is the vertical turbulent mixing coefficient. At the measuring sections, the available number of fluorometer probes are laterally installed in uniform intervals, so that lateral variation of concentration can be measured. In step (2), the hydraulic data such as velocity

distributions, discharge of flow and water depth are measured using the Acoustic Doppler Current Profiler (ADCP), or Acoustic Doppler Velocimetry (ADV) at each measuring section. In Step (3), the injection volume of tracer should be determined considering the measurable ranges of fluorometers used. The tracer is typically injected into the center of the stream section, Kilpatrick (1970) suggested the dosage formula shown in Eq. (2.17).

$$V_s = 2.0 \times 10^{-3} \left(\frac{Q_m L}{U} \right)^{0.93} C_p \qquad (2.17)$$

where V_s is the volume of stock Rhodamine WT 20% dye in liters; Q_m is the maximum stream discharge at the downstream site; L is the distance to the downstream measuring section; C_p is the peak concentration at the downstream measuring section.

2.2.2 The routing procedure for 1D mixing models.

Fischer (1968) first developed the routing procedure for the 1D mixing model (1D RP), which can predict the concentration-time curves at the downstream section, using the concentration-time curves measured at upstream in order to calculate the dispersion coefficients from data of tracer tests. The concept of routing procedure has been used initially to predict flood waves in a hydraulic field (Baek and Seo, 2010).

In terms of the cross-sectionally averaged concentration fields, Fischer (1968) derived the analytical solution to 1D ADE for arbitrarily distributed concentration at the initial time (t_1), as expressed in Eq. (2.18).

$$C(x,t_2)=\int_{-\infty}^{\infty}\frac{C(\xi,t_1)}{A\sqrt{4K(t_2-t_1)}}\exp\left[-\frac{\{x-\xi-U(t_2-t_1))\}^2}{4K(t_2-t_1)}\right]d\xi \qquad (2.18)$$

where $C(x,t_2)$ is the concentration distribution when $t=t_2$; $C(\xi,t_1)$ is the value of concentration measured at the specific location $(x=\xi)$ when $t=t_1$; U is the mean velocity of the centroidal mass of pollutant clouds; A is the mean cross-sectional area; K is the longitudinal dispersion coefficient. The Eq. (2.18) describes the superposition of concentration distribution by prediction of mass transport on the individual mass slug composing the pollutant clouds at the time t_1, illustrated in Fig. 2.4.

In conventional tracer tests, tracer concentrations are usually obtained as the time-series data from sensor probes installed at limited fixed points in river cross-sections. It is very challenging to observe the spatial distributions of tracer clouds over the experimental reaches under the use of the *in-situ* measurements. Because of this limitation, The spatial concentration distributions at both t_1 and t_2 in Eq. (2.18) were estimated by the *frozen cloud approximation*, in which no dispersion takes place while the cloud passes the measuring probes (Fischer et al., 1979). By this assumption, the temporal concentration profiles at the locations of the upstream measuring section, X_1 and downstream measuring section, X_2 can be transformed to spatial distributions at the time to centroidal mass arrival, $\overline{t_1}$ and $\overline{t_2}$, as illustrated in Fig. 2.5. From the temporal concentration data obtained at X_2, the spatial concentration distribution at the time $\overline{t_2}$ can be estimated by Eq. (2.19).

$$C(X_2,t)=C\left(x,\overline{t_2}\right) \tag{2.19}$$

in which,

$$x=X_2+U\left(\overline{t_2}-t\right) \tag{2.20}$$

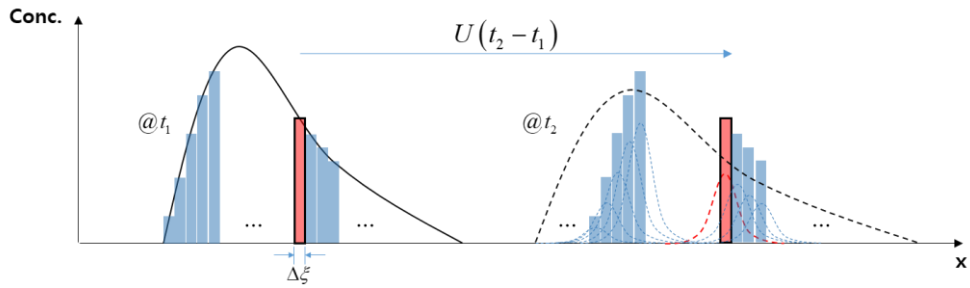

Figure 2.4 Schematic representation of 1D spatial routing procedure (revised from Fischer, 1979)

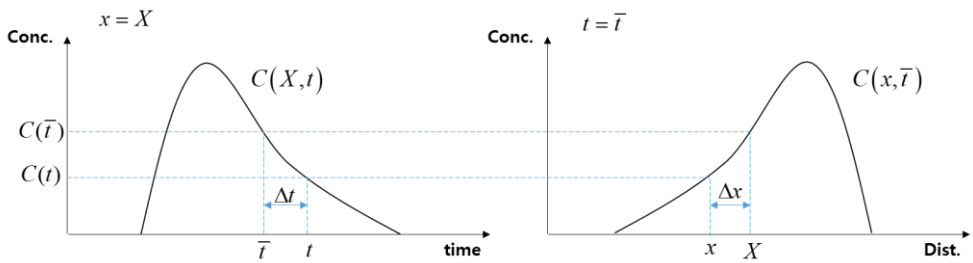

Figure 2.5 Schematic representation of the frozen cloud approximation (revised from Rutherford, 1994)

where X_2 is the location of measuring probe in the longitudinal direction; t is the time taken after injection; $\overline{t_2}$ is the mean time of passage past a probe located at the longitudinal station X_2. The mean velocity of the centroidal mass of pollutant clouds can be obtained as follows.

$$U = \frac{X_2 - X_1}{\overline{t_2} - \overline{t_1}} \tag{2.21}$$

Similarly to Eq. (2.20), the concentration, $C\left(\xi, \overline{t_1}\right)$, at an arbitrary location, ξ, can correspond with the concentration value at an arbitrary time τ of temporal profile observed at measuring location, X_1.

$$\xi = X_1 + U\left(\overline{t_1} - \tau\right) \tag{2.22}$$

$$d\xi = U d\tau \tag{2.23}$$

By substituting the equations from Eq. (2.19) to Eq. (2.23) into Eq. (2.18), the equation for the routing procedure can be finally expressed in the temporal domain.

$$C(X_2,t)=\int_{-\infty}^{\infty}\frac{C(X_1,\tau)\cdot U}{A\sqrt{4K(\bar{t}_2-\bar{t}_1)}}\exp\left[-\frac{\{U(\bar{t}_2-\bar{t}_1-t-\tau)\}^2}{4K(\bar{t}_2-\bar{t}_1)}\right]d\tau \qquad (2.24)$$

For satisfying the FCA in the transformation of temporal distribution to spatial distribution, the shape of the pollutant cloud has not to change during the time taken to pass the observation point. However, it cannot be physically achieved in the open channel flows because most conditions of river flow are shear flow induced by the bottom friction as well as irregularities of channels. Fischer (1966) stated that the conversion from temporal concentration profile to spatial distribution is only an approximate procedure. Besides, Singh and Beck (2003) mentioned that the frozen cloud approximation introduced errors in the estimate of the dispersion coefficients. Despite that, the quantitative analysis of the errors introduced by the frozen cloud approximation has not been investigated in the previous studies. Moreover, most of the calculation methods to estimate the dispersion coefficients were based on this assumption. Thus, in order to calculate the dispersion coefficients accurately, the limitations of frozen cloud approximation in open channel flows should be rigorously analyzed.

2.2.3 Routing procedure for 2D dispersion coefficients

Methods for calculation of the dispersion coefficients in the 2D ADE have been proposed by several studies (Seo et al.,2006; Baek et al., 2006; Baek and Seo, 2010). When concentration data, which is obtained by tracer tests, are available, the dispersion coefficients can be calculated by using both moment methods and routing methods. In case of the moment methods, even though the moment-based methods were suggested by many researchers including Sayre and Chang (1968), Holley et al. (1972), Krishnappan and Lau (1977), and Beltaos (1980), these models mainly focused on the transverse dispersion coefficients, D_T , in the steady-state concentration conditions.

To overcome these disadvantages, the routing procedure-based method for 2D dispersion coefficients have been developed, listed in Table. 2.1. First, the 2D routing procedure (2D RP) was developed by Baek et al. (2006) for the calculation of both D_L and D_T of 2D ADE for transient conditions. The equation of the 2D RP can be derived from the analytical solution of the two-dimensional diffusion, extending the 1D RP suggested by Fischer (1968). In the derivation procedure for 2D RP, the 2D spatial routing equation was first derived, as shown in Eq. (2.25)

$$C(x,y,t_2)=\int_0^W\int_{-\infty}^{\infty}\frac{C(\xi,\psi,t_1)}{4\pi(t_2-t_1)\sqrt{D_L D_T}}\cdot \exp\left(-\frac{(x-\xi)^2}{4D_L(t_2-t_1)}\right)\exp\left(-\frac{(y-\psi)^2}{4D_T(t_2-t_1)}\right)d\xi d\psi \tag{2.25}$$

where $C(\xi,\psi,t_1)$ is the observed concentration as a function of longitudinal distance and transverse distance at the time t_1 ; $C(x,y,t_2)$ is predicted concentration as a function of longitudinal distance and transverse distance at a time t_2; ξ is dummy longitudinal distance variable of integration; and ψ is dummy transverse distance variable of integration. In order to apply Eq. (2.25) for calculation of dispersion coefficients, the spatial tracer distributions at a certain time have to be obtained. Because acquiring the spatial concentration distribution is usually limited in conventional tracer tests, Baek et al. (2006) converted the Eq. (2.25) into the routing equation for the temporal concentration profiles under the frozen cloud approximation as follows.

$$C(x_2,y,t)=\int_0^W\int_{-\infty}^{\infty}\frac{C(x_1,\psi,\tau)U}{4\pi(\bar{t_2}-\bar{t_1})\sqrt{D_L D_T}}\cdot \exp\left(-\frac{U^2(\bar{t_2}-\bar{t_1}-t+\tau)^2}{4D_L(\bar{t_2}-\bar{t_1})}\right)\exp\left(-\frac{(y-\psi)^2}{4D_T(\bar{t_2}-\bar{t_1})}\right)d\tau d\psi \tag{2.26}$$

where $C(x_1,\psi,\tau)$ is the observed concentration as a function of time and transverse distance at an upstream site, and $C(x_2,y,t)$ is predicted concentration as a function of time and transverse distance at a downstream site, and τ is dummy time variable of integration. Through the Eq. (2.26), the concentration profile at a downstream can be calculated, and then by matching between the calculated concentration and the observed concentration, the dispersion coefficients can be evaluated iteratively. When the dispersion coefficients with the lowest error are found, the values are regarded as the observed dispersion coefficients. The routing procedure is one of the inverse methods which calculates the model parameters inversely by matching solutions to the measured data. 2D RP does not consider the non-uniformities of the channel width and channel meandering. In order to improve the applicability of the routing procedure to natural streams, Seo et al. (2006) developed a routing procedure, called as the stream-tube routing procedure (STRP), combined with the stream-tube concept.

$$S(x_2,\eta)=\int_0^1 \frac{S(x_1,\omega)}{\sqrt{4\pi B_C(x_2-x_1)}}\cdot\exp\left(-\frac{-(\eta-\omega)^2}{4B_C(x_2-x_1)}\right)d\omega \qquad (2.27)$$

where $S(x_2,\eta)$ is the predicted dosage profile as a function of the normalized cumulative discharge at x_2; η is the normalized cumulative discharge; $S(x_1,\omega)$ is the measured dosage profile as a function of the normalized cumulative discharge

at x_1; ω is the normalized dummy variable of integration; B_C is the bulk dispersion coefficient given by

$$B_C = \frac{\Psi H^2 U}{Q^2} D_T \tag{2.28}$$

where Ψ is the normalized shape factor defined by Beltaos (1980); H is the mean depth; Q is the total discharge. Although STRP can account for the irregularities of a stream channel, it is disadvantaged by an inability to obtain the longitudinal dispersion coefficient, D_L, due to the conversion of concentration into a dosage.

Baek and Seo (2010) developed the two-dimensional stream-tube routing procedure (2D STRP) to improve the limitations of STRP further. Likewise, the derivation of 1D RP and 2D RP, the spatial routing equation in stream-tube coordinates, was preferentially derived as Eq. (2.29).

$$C(x,\eta,t_2) = \int_0^1 \int_{-\infty}^{\infty} \frac{C(\xi,\omega,t_1)}{4\pi(t_2-t_1)\sqrt{D_L S_T}} \cdot \exp\left(-\frac{(x-\xi)^2}{4D_L(t_2-t_1)}\right) \cdot \exp\left(-\frac{(\eta-\omega)^2}{4S_T(t_2-t_1)}\right) d\xi d\omega \tag{2.29}$$

where S_T is the stream-tube dispersion coefficients. The transverse dispersion coefficient, D_T, can be calculated from S_T following Beltaos (1980).

$$S_T = UB_C \tag{2.30}$$

Due to the difficulty of acquisition of spatial concentration distribution in the conventional tracer tests, Eq. (2.29) was transformed into the temporal routing equation under the FCA.

$$C(x_2,\eta,t) = \int_0^1 \int_{-\infty}^{\infty} \frac{C(x_1,\omega,\tau)U}{4\pi(t_2 - t_1)\sqrt{D_L S_T}} \cdot \exp\left(-\frac{U^2\left(\overline{t_2} - \overline{t_1} - t + \tau\right)^2}{4D_L\left(\overline{t_2} - \overline{t_1}\right)} \right) \cdot \exp\left(-\frac{(\eta - \omega)^2}{4S_T\left(\overline{t_2} - \overline{t_1}\right)} \right) d\tau d\omega \tag{2.31}$$

The merit of using this method is that both D_L and D_T can be obtained simultaneously from data of tracer tests. Moreover, by adopting the stream-tube concept, irregularities of the channel can be reflected, and the pattern of the stream-wise variation of the dispersion coefficient can be revealed because they are calculated at each section along the river.

Table 2.1 shows the observation methods based on the concept of a routing procedure. 2D STRP is the most advanced version of the routing procedure developed through several improvements of applicability to the natural stream. 2D STRP has often been applied to calculate 2D dispersion coefficients in a natural stream, as well as the experimental channels in laboratories (Seo et al., 2016; Baek and Seo, 2016; Choi, 2017; Shin, 2018). Although The 2D STRP has been the only way to calculate the longitudinal and transverse dispersion coefficients simultaneously for transient pollutant clouds, some studies have reported limitations of 2D STRP. Choi (2017) showed that 2D STRP could provide inaccurate dispersion coefficients after the tracer cloud reaches sidewall boundaries. To adjust the dispersion coefficients, which were calculated after the wall reflection, He suggested the quadratic polynomial function for the correction coefficients. Moreover, Shin (2018) reported that the applications of 2D STRP to the tracer test data in meandering channels resulted in the overestimated values of the dispersion coefficients both longitudinally and transversely compared to theoretically derived values. Thus, the more detailed evaluation of the performance of 2D STRP is required to improve its limitations.

Table 2.1 Summary of routing procedures for dispersion coefficients

	1D RP	2D RP	STRP	2D STRP
Equation	Eq. (2.24)	Eq. (2.26)	Eq. (2.27)	Eq. (2.31)
Dimensions	1D	2D	2D	2D
Consider longitudinal dispersion	○	○	×	○
Consider transverse dispersion	×	○	○	○
Consider river irregularities	×	×	○	○

2.3 Remote sensing techniques for water environments

In remote sensing of the hydrological environments, the spectral signals of light intensities have been analyzed to retrieve meaningful information such as water depth, water qualities, and the type of bed materials from image data. Light intensities are recorded as pixel intensities on images according to the amount of photons reaching the sensors of optical devices. The primary source of photons reaching sensors is usually solar radiation in the natural environments, and photons reaching the optic sensors are conceptually accounted for through four primary sources, as expressed in Fig. 2.6 and Eq. (2.32) (Legleiter et al., 2004; Bukata et al., 2018):

$$L_u(\lambda) = L_b(\lambda) + L_c(\lambda) + L_s(\lambda) + L_p(\lambda) \tag{2.32}$$

where $L_u(\lambda)$ is the total radiance reaching the sensor, $L_b(\lambda)$ is the radiance reflected from the river bed, $L_c(\lambda)$ is the back-scattered radiance from the water bodies, $L_s(\lambda)$ is the radiance reflected from the interface between the atmosphere and the water, $L_p(\lambda)$ is the path radiance through the atmosphere, and λ denotes the wavelength of the light.

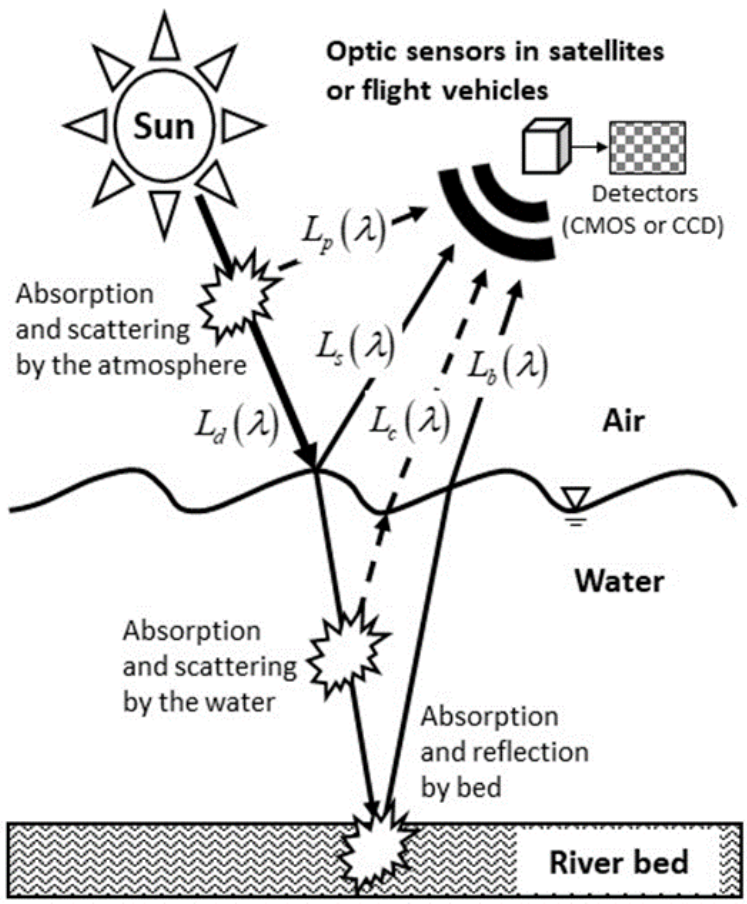

Figure 2.6 The path covered by light from the sun through the water body to the remote sensing sensor (adapted from Laanen, 2007)

The second term in Eq. (2.32), L_c, is the principal component which is related to water quality parameters (WQPs) like the concentration of the dissolved matter, suspended sediments, and chlorophyll-a, and is a direct consequence of the inherent optical properties (IOPs) such as absorption and back-scattering (Legleiter and Fonstad, 2012; Bukata et al.,2018). The IOPs represent the optical characteristics of water bodies which are dominated by the concentration of dissolved and suspended matters in the water medium. If the relationship between the IOPs and concentrations of specific matters are known, the WQPs of interest can be retrieved from remotely sensed L_c. In optically deep water such as in oceanic and lacustrine environments, L_c can be directly observed from spectral images with atmospheric and surface reflection correction algorithm because the effect of L_b is negligible. However, in optically shallow water such as in coastal and riverine environments, the extraction of L_c from L_u is challenging due to the optical complexities caused by the strong signal of L_b. In some studies, L_c has been successfully extracted from a remotely sensed signal using inversion techniques (Lee et al., 1999; Louchard et al., 2003; Mobley et al., 2005), but these techniques are mainly designed for multi- and hyperspectral image data (Cannizzaro and Carder, 2006).

In both multi- and hyper-spectral images, the continuous spectral signals of radiance, ranged from 350 to 2500 nm approximately, are recorded as digital numbers in each spectral band. The difference between multi- and hyperspectral

images is the number of bands to record the radiance with respect to the wavelength. The hyperspectral sensors in the most satellite platforms include more than 100 bands with narrow spectral bandwidth, but the multi-spectral sensors record the radiance in a fairly limited number (approximately ten bands) of discrete spectral bands (Transon et al., 2018). Although the water quality parameters (WQPs) in open channel flows can be detected by remote sensing techniques using hyper- or multi-spectral images, the acquisition of these images in both spatially and temporally high resolution is not widely available and is usually expensive (Winterbottom and Gilvear, 1997; Gholizadeh et al., 2016). In the river and open channel flows, to investigate the mixing of pollutants transported by fast-moving water, the concentration distributions in spatially and temporally high resolution are required to obtain the rate of change of concentration with respect to space and time.

The use of an RGB-based digital camera mounted on a UAV can acquire spatially and temporally high-resolution video images at a low cost. In the RGB-based digital camera, the visible light reaching optic sensors such as complementary metal-oxide semiconductors (CMOS) or charge-coupled device (CCD) recorded in three spectral bands called as R-, G- and B-band. Typical digital cameras record the light intensity as the digital number (*DN*) which are the integer numbers ranging between 0 to 255. The basal and maximum values of *DN* are relative, depending on the exposure setting of the camera. Some studies have carried out mapping of bathymetry in the natural river using RGB images applying the regression and semi-empirical approaches rather than using the physical-based approach (Winterbottom and Gilvear, 1997;

Jordan and Fonstad, 2005; Fonstad and Marcus, 2005; Carbonneau et al., 2006; Flener et al., 2012). However, the use of the RGB image for observing WQP in riverine environments has yet to be sufficiently studied.

3. Implementation of a numerical tool for 2D ADE

3.1 Outline of the numerical tool

The numerical model was implemented in order to evaluate the frozen cloud approximation in various hydraulic conditions. The governing equations are 2D ADE in the natural coordinate systems, as expressed in the Eq. (2.13) and Eq. (2.14). The governing equations are discretized using the Finite Volume Method (FVM) to ensure mass conservation. FVM is based on the gauss's divergence theorem, so the integral form of governing equations is used for discretization. The solution domain is subdivided into a finite number of small control volumes (Ferziger and Peric, 2002). The numerical solution can be obtained as the cell-averaged values of control volume at the centroid of control volumes.

In the numerical calculation for pollutant transport, the velocity components in the natural coordinate system are required as the known values for advection terms. The velocity information could be obtained by the hydrodynamics models as well as the measured data in the field tests. When the computational grid for *s*-axis in the natural coordinate system is parallel to flow direction, the velocity components, *V,* in advection terms are negligible by the continuity equation described in Eq. (2.13). So, the advection fluxes can be considered as the uni-directional flux. The numerical model which was implemented in this study, however, incorporated both *U* and *V* in advection terms for general purposes.

3.2 Discretization of governing equation

As described in previous chapters, the governing equation of 2D ADE with source term (λ) in the natural coordinate system can be written as:

$$\begin{aligned} & m_s m_n \frac{\partial}{\partial t}(hC) + \frac{\partial}{\partial s}(m_n hUC) + \frac{\partial}{\partial n}(m_s hVC) \\ & = \frac{\partial}{\partial s}\left(\frac{m_n}{m_s} hD_L \frac{\partial C}{\partial s}\right) + \frac{\partial}{\partial n}\left(\frac{m_s}{m_n} hD_T \frac{\partial C}{\partial n}\right) + \lambda \end{aligned} \tag{3.1}$$

In order to discretize the governing equation described as a partial differential equation, Eq. (3.1) is integrated over the finite control volume.

$$\begin{aligned} & \frac{\partial}{\partial t}\int_{CV} m_s m_n (hC)\,dV + \int_{CV} \frac{\partial}{\partial s}(m_n hUC)\,dV + \int_{CV} \frac{\partial}{\partial n}(m_s hVC)\,dV \\ & = \int_{CV} \frac{\partial}{\partial s}\left(\frac{m_n}{m_s} hD_L \frac{\partial C}{\partial x}\right)dV + \int_{CV} \frac{\partial}{\partial n}\left(\frac{m_s}{m_n} hD_T \frac{\partial C}{\partial n}\right)dV + \int_{CV} \lambda\,dV \end{aligned} \tag{3.2}$$

where $\int_{CV}(\cdot)\,dV$ is the volume integral operator. Applying the Gauss's divergence theorem to the convection terms and dispersion terms in Eq (3.2), the volume integral over the control volumes is replaced with the surface integral over the boundary

surface of the control volume.

$$\begin{aligned}&\int_{CV} m_s m_n \frac{\partial}{\partial t}(hC)dV + \int_S (m_n hUC)\cdot \mathbf{n}dS + \int_S (m_s hVC)\cdot \mathbf{n}dS \\ &= \int_S \left(\frac{m_n}{m_s} hD_L \frac{\partial C}{\partial x}\right)\cdot \mathbf{n}dS + \int_S \left(\frac{m_s}{m_n} hD_T \frac{\partial C}{\partial n}\right)\cdot \mathbf{n}dS + \bar{\lambda}\Delta V_{CV}\end{aligned} \tag{3.3}$$

where $\int_S (\cdot)dS$ is the surface integral operator; $\mathbf{n}$ is the vector normal to surface element around the control volume; $\bar{\lambda}$ is the averaged value of the source within the control volume. The physical meaning of Eq. (3.3) is that the sum of the flux components through the surface of the control volume is identical to the net rate of the total amount of solute mass in the control volume (Versteeg and Malalasekera, 2007).

Integration of convection and dispersion terms in Eq. (3.3) over the finite calculation gird gives:

$$
\begin{aligned}
& T_I \\
& + \left[\left(m_n hUC \right)_e \Delta n - \left(m_n hUC \right)_w \Delta n \right] \\
& + \left[\left(m_s hVC \right)_n \Delta s - \left(m_s hVC \right)_s \Delta s \right] \\
& = \left[\left(\frac{m_n}{m_s} hD_L \frac{\partial c}{\partial x} \right)_e \Delta n - \left(\frac{m_n}{m_s} hD_L \frac{\partial c}{\partial x} \right)_w \Delta n \right] \\
& + \left[\left(\frac{m_s}{m_n} hD_T \frac{\partial c}{\partial n} \right)_n \Delta s - \left(\frac{m_s}{m_n} hD_T \frac{\partial c}{\partial n} \right)_s \Delta s \right] \\
& + \bar{\lambda} \Delta V_{CV}
\end{aligned}
\tag{3.4}
$$

where T_I is the volume integration for time derivative term in Eq. (3.4); *e*, *w*, *n*, and *s* denote the surfaces of control volume for calculation node *P*. The node *P* denotes the computational node to be solved. The surfaces are positioned mid-points between adjacent nodes. The calculation grid around the calculation node *P* is described in Fig. 3.1.

The solution resolved by FVM assigned at each nodal point, which is generally located at the center of control volumes. The mass fluxes (convective and dispersive fluxes) and gradient values of properties at surfaces are required in order to calculate properties in nodal points. When the dispersion coefficients and essential hydraulic data such as velocity and water depth fields are available, the required values at surfaces can be calculated using the interpolation schemes derived by Taylor expansion.

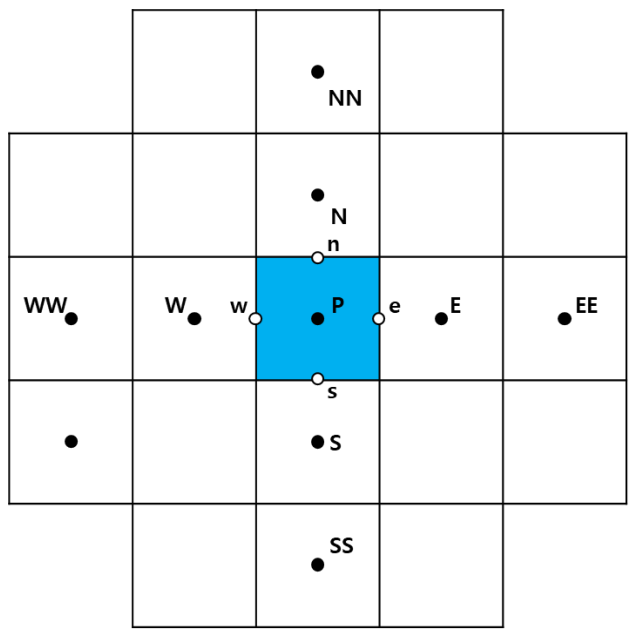

Figure 3.1 The notations of control volumes around calculation node P

3.2.1 Interpolation schemes for advection term

The order of convective flux is typically more significant than that of dispersive flux in the natural river. When the flow condition is steady-state, the longitudinal coordinate surfaces in the natural coordinate system follow streamline (Yotsukura, 1976; Rutherford, 1994). In this case, the convective fluxes are dominated by the longitudinal velocity components (U). The properties at a certain point are mainly influenced by longitudinal convective fluxes of the upstream side. Thus, it is very important to consider the directionality of convective flux and the magnitude of the Péclet number.

As explained above, the Péclet number in the natural stream is typically high, so mass transport is dominated by convection effect. In such a case, upwind differencing schemes, which is the upstream-weighted scheme, can effectively discretize the transport equations.

(1) First-order upwind scheme

First-order upwind scheme (UDS) is the simplest approximation to interpolate the surface values. If the convective flux is positive in a certain control volume, the properties at the surfaces surrounding node P are approximated as:

$$\phi_e = \phi_P \tag{3.5a}$$

$$\phi_w = \phi_W \tag{3.5b}$$

$$\phi_n = \phi_P \tag{3.5c}$$

$$\phi_s = \phi_S \tag{3.5d}$$

where ϕ indicates any property transported, such as concentration in this study. This scheme never yields oscillatory solutions, but it achieves this by being numerically diffusive with the first-order accuracy in terms of Taylor series expansion. Thus, this scheme requires an extremely fine computational grid (Lien and Leschziner, 1994).

(2) Quadratic upstream interpolation for convective kinetics (QUICK)

Quadratic upstream interpolation for convective kinetics (Leonard, 1979), also called QUICK, employs the values at three nodal points neighboring the node *P* to evaluate the surface values. The surface values of the control volume are interpolated using the parabola, rather than straight lines. The parabola is constructed using the two nodal points at upstream and one nodal point a downstream. If the convective flux is positive as for UDS, the QUICK gives:

$$\phi_e = \frac{6}{8}\phi_P + \frac{3}{8}\phi_E + \frac{1}{8}\phi_W \tag{3.6a}$$

$$\phi_w = \frac{6}{8}\phi_W + \frac{3}{8}\phi_P + \frac{1}{8}\phi_{WW} \tag{3.6b}$$

$$\phi_n = \frac{6}{8}\phi_P + \frac{3}{8}\phi_N + \frac{1}{8}\phi_S \tag{3.6c}$$

$$\phi_s = \frac{6}{8}\phi_S + \frac{3}{8}\phi_P + \frac{1}{8}\phi_{SS} \tag{3.6d}$$

The QUICK scheme has a third-order truncation error in terms of the Taylor series. However, the overall approximation is second-order accuracy when midpoint-rule is used to approximate the surface integral in FVM. This scheme provides higher accuracy of the numerical solution so that the use of QUICK for convection term significantly reduces numerical diffusion compared to UDS, given the same size of the computational grid. Nevertheless, the QUICK scheme can yield unphysically oscillatory solutions when the gradient of the concentration is significant, which could lead to negative concentration.

(3) Total Variance Diminishing scheme (TVD)

The upstream-weighted schemes, of which the accuracy is higher than second order, inherently suffer from the unboundedness problem when subject to the steep gradients or discontinuity in the solution. The higher-order upwind schemes can be generalized by the flux-limiter function, as shown in Eq. (3.7).

$$\phi_e = \phi_P + \frac{1}{2}\psi(r)(\phi_E - \phi_P) \tag{3.7a}$$

$$\phi_w = \phi_W + \frac{1}{2}\psi(r)(\phi_P - \phi_W) \tag{3.7b}$$

$$\phi_n = \phi_P + \frac{1}{2}\psi(r)(\phi_N - \phi_P) \tag{3.7c}$$

$$\phi_s = \phi_S + \frac{1}{2}\psi(r)(\phi_P - \phi_S) \tag{3.7d}$$

where ψ is the flux-limiter function; r is the gradient ratio between surfaces of upstream and downstream, and also called a smoothness parameter. For example, the value of the gradient ratio, r , at the surface *e* is defined as:

$$r_e = \frac{\phi_P - \phi_W}{\phi_E - \phi_P} \tag{3.8}$$

The convectional discretization schemes can be generalized by Eq. (3.7) with the appropriate flux-limiter function. Eq. (3.7) becomes identical to the first-order upwind scheme, the central differencing scheme, and the second-order upwind scheme when the flux-limiter function is set to 0, 1, and 2, respectively.

Harten (1983) proposed the concept of Total variation diminishing (TVD) in order to measure the oscillatory character of the solution (Zhang et al., 2015). The total

variation (TV) is defined as:

$$TV\left(\phi^t\right)=\sum_i\left(\phi_{i+1}{}^t-\phi_i^t\right) \tag{3.9}$$

Harten (1983) stated that monotonicity of numerical solution must be preserved to avoid the spurious oscillation, and monotonicity preserving can be achieved if the following conditions are maintained over the time or iteration step.

1) No new local extrema are created within the spatial solution domain.

2) The value of a local minimum is nondecreasing, and the value of a local maximum is nonincreasing.

Harten (1983) also showed that the above conditions were satisfied when total variation (TV) was nonincreasing over time.

$$TV\left(\phi^{t+1}\right)\le TV\left(\phi^t\right) \tag{3.10}$$

The discretization schemes, of which numerical solutions are satisfied with Eq. (3.10), are called the TVD scheme. Sweby (1984) found the constraint conditions of flux-limiter, which provide the second-order accuracy with unconditionally bounded solution based on the concept of TVD.

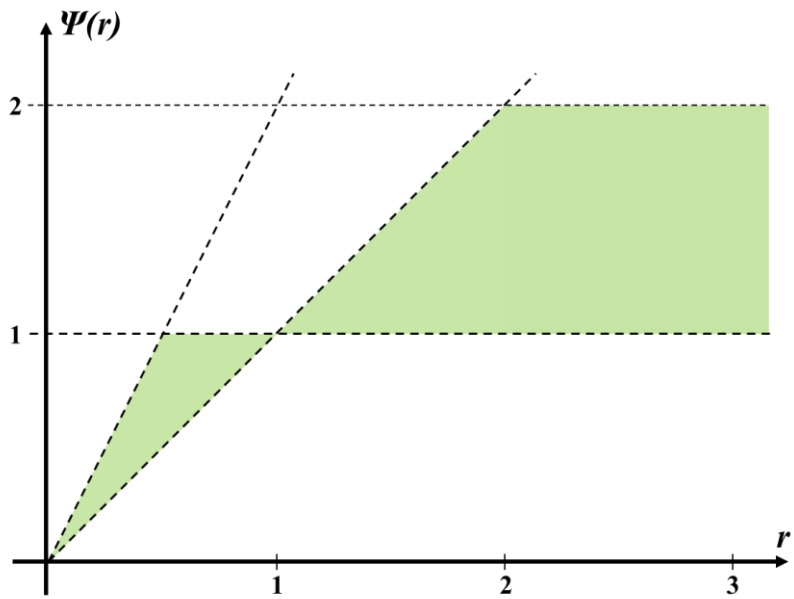

Figure 3.2 Sweby diagram, flux-limiter region for second-order TVD schemes (adapted from Sweby, 1984)

$$\psi(r) = \min(2r, 2), \qquad r > 0 \tag{3.11}$$

Fig.3.2 shows the Sewby diagram (or TVD diagram), which represents Eq. (3.11). The shaded region indicates the region of flux-limiter function which provides the second-order scheme with oscillation-free. This diagram implies that the interpolation schemes, of which the flux-limiter function is linear, cannot achieve unconditional oscillation-free. Thus, the flux-limiter functions have to be the nonlinear function to exist in the TVD region in Fig. 3.2.

Based on Sweby's diagram, a variety of second-order TVD schemes have been suggested. Some selected TVD schemes, which are widely employed for numerical modeling of convection-dominated transport, are summarized in Table 3.1 and Fig. 3.3. In this study, the flux-limiter functions in Table 3.1 are implemented to approximate the surface values in Eq. (3.4)

Table 3.1 Summary of the second-order TVD schemes

Scheme name	Limiter function $\psi(r)$	Source
Van Leer	$\frac{r+\lvert r\rvert}{1+r}$	Van Leer (1974)
Van Albada	$\frac{r+r^2}{1+r^2}$	Van Albada et al. (1982)
SUPERBEE	$\max\left[0,\min(2r,1),\min(r,2)\right]$	Roe (1985)
Sweby ($\beta=1.5$)	$\max\left[0,\min(\beta r,1),\min(r,\beta)\right]$	Sweby (1984)
UMIST	$\max\left[0,\min(2r,(1+3r)/4,(3+r)/4,2)\right]$	Lien and Leschziner (1993)

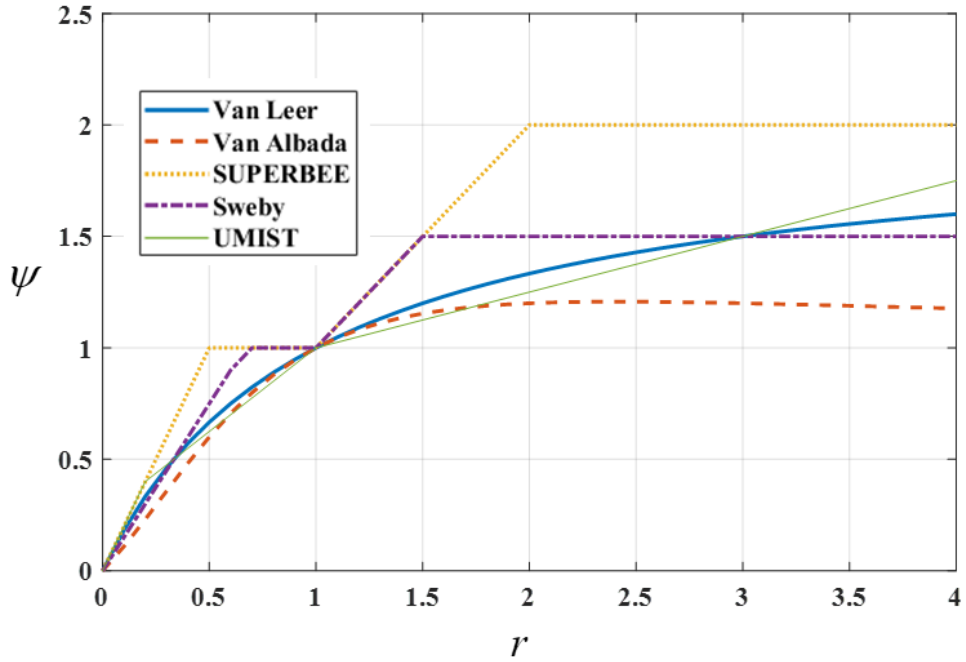

Figure 3.3 The second-order Flux-limiter functions on TVD diagram

3.2.2 Interpolation schemes for dispersion term

The first and second terms in the left-hand side of Eq. (3.4) represent the dispersive flux passing through the surfaces of the control volume. These terms involve the spatial gradient of concentration at the surface of the control volume. It is common practice to discretize the dispersion terms using the central differencing scheme (CDS) (Ferziger and Peric, 2002). By applying the CDS, the gradient values at the surface are obtained by the linear approximation with the values at neighbor nodes. The truncation error of CDS is second-order in terms of Taylor series. The gradient values of Eq. (3.4) can be approximated as:

$$\left(\frac{\partial C}{\partial s}\right)_e = \frac{C_E - C_P}{s_E - s_P} = \frac{C_E - C_P}{\Delta s} \tag{3.12a}$$

$$\left(\frac{\partial C}{\partial s}\right)_w = \frac{C_P - C_W}{s_P - s_W} = \frac{C_P - C_W}{\Delta s} \tag{3.12b}$$

$$\left(\frac{\partial C}{\partial n}\right)_n = \frac{C_N - C_P}{n_N - n_P} = \frac{C_N - C_P}{\Delta n} \tag{3.12c}$$

$$\left(\frac{\partial C}{\partial n}\right)_s = \frac{C_P - C_S}{n_P - n_S} = \frac{C_P - C_S}{\Delta n} \tag{3.12d}$$

Substituting Eq. (3.12) into Eq. (3.4) yields:

$$
\begin{aligned}
&T_I \\
&+\left[\left(m_n hUC\right)_e \Delta n-\left(m_n hUC\right)_w \Delta n\right] \\
&+\left[\left(m_s hVC\right)_n \Delta s-\left(m_s hVC\right)_s \Delta s\right] \\
&=\left[\left(\frac{m_n}{m_s} hD_L\right)_e\left(\frac{C_E-C_P}{\Delta s}\right)\Delta n-\left(\frac{m_n}{m_s} hD_L\right)_w\left(\frac{C_P-C_W}{\Delta s}\right)\Delta n\right] \\
&+\left[\left(\frac{m_s}{m_n} hD_T\right)_n\left(\frac{C_N-C_P}{\Delta n}\right)\Delta s-\left(\frac{m_s}{m_n} hD_T\right)_s\left(\frac{C_P-C_S}{\Delta n}\right)\Delta s\right] \\
&+\bar{\lambda}\Delta V_{CV}
\end{aligned}
\tag{3.13}
$$

Eq. (3.13) can be rearranged by introducing the new parameters.

$$
\begin{aligned}
&T_I \\
&+\left[\left(F_L\right)_e C_e-\left(F_L\right)_w C_w\right]\Delta n \\
&+\left[\left(F_T\right)_n C_n-\left(F_T\right)_s C_s\right]\Delta s \\
&=\left[\left(E_L\right)_e\left(C_E-C_P\right)-\left(E_L\right)_w\left(C_P-C_W\right)\right]\Delta n \\
&+\left[\left(E_T\right)_n\left(C_N-C_P\right)-\left(E_T\right)_s\left(C_P-C_S\right)\right]\Delta s \\
&+\bar{\lambda}\Delta V_{CV}
\end{aligned}
\tag{3.14}
$$

where,

$$F_L = m_n hU \tag{3.15a}$$

$$F_T = m_s hV \tag{3.15b}$$

$$E_L = \frac{m_n}{m_s}\frac{hD_L}{\Delta s} \tag{3.15c}$$

$$E_T = \frac{m_s}{m_n}\frac{hD_T}{\Delta n} \tag{3.15d}$$

The physical meaning of F_L and F_T are the flow discharge passing through control volume, and both E_L and E_T are dispersion conductance at each surface of the control volume.

3.2.3 Discretization for the time derivative

In order to discretize the time derivative term by the concept of FVM, the discretized equation, Eq. (3.4), need to be integrated over the finite time step.

$$
\begin{aligned}
&\int_t^{t+\Delta t} T_I dt = \\
&-\int_t^{t+\Delta t}\left[\left(F_L\right)_e C_e - \left(F_L\right)_w C_w\right]\Delta n dt \\
&-\int_t^{t+\Delta t}\left[\left(F_T\right)_n C_n - \left(F_T\right)_s C_s\right]\Delta s dt \\
&+\int_t^{t+\Delta t}\left[\left(E_L\right)_e \left(C_E - C_P\right) - \left(E_L\right)_w \left(C_P - C_W\right)\right]\Delta n dt \\
&+\int_t^{t+\Delta t}\left[\left(E_T\right)_n \left(C_N - C_P\right) - \left(E_T\right)_s \left(C_P - C_S\right)\right]\Delta s dt \\
&+\int_t^{t+\Delta t} \bar{\lambda}\Delta V_{CV} dt
\end{aligned}
\tag{3.16}
$$

The temporal integration of the left-hand side term is expressed as:

$$
\int_t^{t+\Delta t} T_I dt = \int_t^{t+\Delta t}\int_{CV} m_s m_n \frac{\partial}{\partial t}\left(hC\right)_p dV dt \tag{3.17}
$$

By applying the Forward Euler scheme (FE) to the time derivative in Eq. (3.17), it yields:

$$
\begin{aligned}
\int_t^{t+\Delta t} T_I dt &= \int_t^{t+\Delta t} \int_{CV} m_s m_n \frac{\partial}{\partial t}(hC)_p \, dV dt \\
&= \int_{CV} \int_t^{t+\Delta t} \left[m_s m_n \frac{(hC)_p^{\,t+\Delta t} - (hC)_p^{\,t}}{\Delta t} dt \right] dV \\
&= \left(\overline{m_s m_n}\right)_P \left[(hC)_p^{\,t+\Delta t} - (hC)_p^{\,t} \right] \Delta V
\end{aligned}
\tag{3.18}
$$

where the superscript t indicates a current time step and $t+\Delta t$ is the timestep after Δt from the current timestep. FE scheme is an explicit time marching method. This method predicts the variables at the forward time level using the variables in the current time level. Thus, the solutions can be explicitly calculated at each node (Ferziger and Peric, 2002). The solutions by FE have the first-order accuracy in terms of the Taylor series.

The temporal integration for the terms in the right-hand side gives:

$$
\begin{aligned}
&\left[(F_L)_e C_e^{\,t} - (F_L)_w C_w^{\,t} \right] \Delta n \Delta t \\
&+ \left[(F_T)_n C_n^{\,t} - (F_T)_s C_s^{\,t} \right] \Delta s \Delta t \\
&= \left[(E_L)_e \left(C_E^{\,t} - C_P^{\,t} \right) - (E_L)_w \left(C_P^{\,t} - C_W^{\,t} \right) \right] \Delta n \Delta t \\
&+ \left[(E_T)_n \left(C_N^{\,t} - C_P^{\,t} \right) - (E_T)_s \left(C_P^{\,t} - C_S^{\,t} \right) \right] \Delta s \Delta t \\
&+ \bar{\lambda} \Delta V_{CV} \Delta t
\end{aligned}
\tag{3.19}
$$

By Combining Eq. (3.18) and Eq. (3.19), and rearranging the discretized equations, the final form of the discretized equation can be obtained as follows

$$
\begin{aligned}
C_p^{\,t+\Delta t} &= C_p^{\,t} + \\
&\frac{\Delta t}{h_P \Delta V \left(\overline{m_s m_n}\right)_P} \cdot \Big\{ -\left[\left(F_L\right)_e C_e^{\,t} - \left(F_L\right)_w C_w^{\,t} \right] \Delta n - \left[\left(F_T\right)_n C_n^{\,t} - \left(F_T\right)_s C_s^{\,t} \right] \Delta s \\
&\qquad + \left[\left(E_L\right)_e \left(C_E^{\,t} - C_P^{\,t}\right) - \left(E_L\right)_w \left(C_P^{\,t} - C_W^{\,t}\right) \right] \Delta n \\
&\qquad + \left[\left(E_T\right)_n \left(C_N^{\,t} - C_P^{\,t}\right) - \left(E_T\right)_s \left(C_P^{\,t} - C_S^{\,t}\right) \right] \Delta s \\
&\qquad + \bar{\lambda} \Delta V \Big\}
\end{aligned}
\tag{3.20}
$$

In Eq. (3.20), the discharge at surface of control volume (F_L and F_T), dispersion conductance (E_L and E_T), and water depth (h_p) must be known values to calculate the numerical solution for the depth-averaged concentration. As aforementioned, this study assumes the flow condition is steady-states, so the above variables are invariant with respect to time but spatially varied.

3.2.4 Conditions for numerical stability

The explicit-type temporal discretization does not provide an unconditionally stable solution. For numerical stability, sufficient conditions have to be guaranteed to prevent the solution grows unphysically. One can use the von Neumann stability analysis to find the numerical condition that provides stable solutions.

By rearranging the discretized equation with respect to the nodal points, Eq. (3.20) can be written as:

$$C_p^{\,t+\Delta t} = \alpha_P C_P^{\,t} + \alpha_E C_E^{\,t} + \alpha_W C_W^{\,t} + \alpha_N C_N^{\,t} + \alpha_S C_S^{\,t} \tag{3.21}$$

where,

$$\alpha_E = -\frac{1}{m_s}\psi\frac{U\Delta t}{2\Delta s} + \frac{1}{m_s m_s}\frac{D_L \Delta t}{(\Delta s)^2} \tag{3.22a}$$

$$\alpha_W = \left[1 - \frac{\psi}{2}\right]\frac{1}{m_s}\frac{U\Delta t}{\Delta s} + \frac{1}{(m_s)^2}\frac{D_L \Delta t}{(\Delta s)^2} \tag{3.22b}$$

$$\alpha_V = \alpha_N = \alpha_S = \frac{1}{(m_n)^2}\frac{D_T \Delta t}{(\Delta n)^2} \tag{3.22c}$$

$$\alpha_p = 1 - \left(\frac{1}{m_s}\frac{U}{\Delta s}\Delta t - \frac{1}{m_s}\frac{U}{\Delta s}\psi\Delta t + \frac{2}{m_s \Delta s m_s}\frac{D_L}{\Delta s}\Delta t + \frac{2}{m_n \Delta n m_n}\frac{D_T}{\Delta n}\Delta t \right)$$
$$= 1 - \left(\alpha_E + \alpha_W + 2\alpha_V\right)$$

(3.22d)

In von Neumann stability analysis, the boundary condition is assumed as a periodic boundary condition. The exact solution is assumed as:

$$C_{(I,J)}{}^{t} = \sigma^t e^{ik_1 s} e^{ik_2 n} \tag{3.23}$$

where σ is the amplification factor; i is $\sqrt{-1}$; k_1 and k_2 are the arbitrary wavenumber. Substitution of Eq. (3.23) into Eq. (3.21) yields followings

$$\begin{aligned} \sigma^{t+1} e^{ik_1 s} e^{ik_2 n} &= \alpha_P \sigma^t e^{ik_1 s} e^{ik_2 n} \\ &+ \alpha_E \sigma^t e^{ik_1 (s+\Delta s)} e^{ik_2 n} + \alpha_W \sigma^t e^{ik_1 (s-\Delta s)} e^{ik_2 n} \\ &+ \alpha_N \sigma^t e^{ik_1 s} e^{ik_2 (n+\Delta n)} + \alpha_S \sigma^t e^{ik_1 s} e^{ik_2 (n-\Delta n)} \end{aligned} \tag{3.24}$$

Dividing both the left and right-hand side of Eq. (3.24) by the right-side of Eq. (3.23) yields:

$$\begin{aligned}\sigma = \alpha_P &+ \left(\alpha_E + \alpha_W\right)\cos\left(k_1\Delta x\right) \\ &+ 2\alpha_V \cos\left(k_2\Delta y\right) \\ &+ \left(\alpha_E - \alpha_W\right) i \sin\left(k_1\Delta x\right)\end{aligned} \tag{3.25}$$

For the bounded numerical solution, the absolute value of the amplification factor, $|\sigma|$, must be less than 1. The most restrictive case could appear when both $k_1\Delta x$ and $k_2\Delta x$ are π. Rearranging Eq. (3.25) with $k_1\Delta s = k_2\Delta n = \pi$ leads:

$$\left[1-\psi\right]\frac{1}{m_s}\frac{U\Delta t}{\Delta s} + \frac{1}{\left(m_s\right)^2}\frac{2D_L\Delta t}{\left(\Delta s\right)^2} + \frac{1}{\left(m_n\right)^2}\frac{2D_T\Delta t}{\left(\Delta n\right)^2} \le 1 \tag{3.26}$$

In Eq. (3.26), $U\Delta t/\Delta s$ in the first term is the Courant number, and both $D_L\Delta t/\left(\Delta s\right)^2$ and $D_T\Delta t/\left(\Delta n\right)^2$ are the ratio Courant number to the numerical Péclet number, also called the Fourier number in heat transfer. When the simulation condition is pure convection, the stability condition is governed by the CFL number. However, when both advection and dispersion effect simultaneously affect the mixing process, the stability condition has to be controlled, considering both the CFL number and Fourier number. By rearranging Eq. (3.26), the stability condition for

time step can be derived as:

$$\Delta t \le \frac{1}{\left[\left[1-\psi\right]\frac{1}{m_s}\frac{U}{\Delta s}+\frac{1}{\left(m_s\right)^2}\frac{2D_L}{\left(\Delta s\right)^2}+\frac{1}{\left(m_n\right)^2}\frac{2D_T}{\left(\Delta n\right)^2}\right]} \tag{3.27}$$

It is assumed that the information of velocity and dispersion coefficient is known, so the calculation time step for bounded solutions depends on the calculation grid size. The maximum time step could be obtained when ψ is 2.

3.2.5 Boundary conditions

The boundary surfaces on the computation grid require special treatments. The properties on the surfaces around control volumes have to be interpolated by the numerical scheme, as shown in the previous chapters, but the nodes adjacent to the boundary of the computation domain do not have the neighbor nodes in a certain direction. The boundary conditions in this study are treated as follows. The notation for surface and neighbor nodes is referred to Fig. 3.1, and the location of the boundary is depicted in Fig. 3.3.

(1) Inlet boundary

The west face of the first node in s-direction is the inlet boundary. The values of the inlet boundary can be assigned by the specific values (Dirichlet boundary condition).

$$C_w = C_{inlet} \tag{3.28}$$

The specific values of concentration could be obtained by concentration measurement in tracer tests.

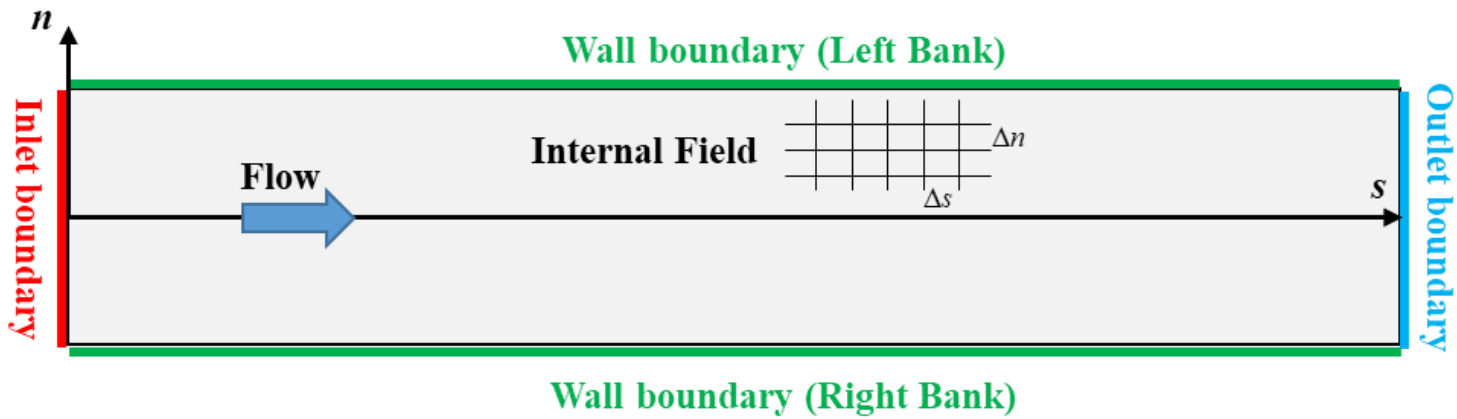

Figure 3.4 The schematic diagram for the computation domain

The values at the surface for internal nodes are approximated using upwind-weight schemes (especially TVD schemes). The approximation for the property of the east surface (*e*) requires the west-neighbor node (*W*) to calculate the smoothness factor. However, the west-neighbor node (*W*) is nonexistent for the inlet boundary, so the values at the west-neighbor node (*W*) are specified as C_{inlet} in manners of the first of the upwind scheme.

This treatment influence on the approximation of the gradient values for dispersion term, shown in Eq. (3.12b), by replacing the west-neighbor node (*W*) with C_{inlet}. The gradient values at the inlet boundary are defined as:

$$\left(\frac{\partial C}{\partial x}\right)_w = \frac{C_P - C_{inlet}}{x_P - x_w} = \frac{C_P - C_{inlet}}{\Delta x / 2} \tag{3.29}$$

Besides, E_L shown in Eq. (3.15c) is re-specified though Eq. (3.29) for the inlet boundary as follows.

$$\left(E_T\right)_{inlet} = \frac{m_n}{m_s}\frac{2hD_L}{\Delta s} \tag{3.30}$$

(2) Outlet boundary

In order to treat the properties at the east surface of the nodes adjacent to the outlet boundary, the Neumann boundary condition, which imposes the specified values on the derivative of properties at the surface, is applied. Due to the absence of the east-neighbor node (*E*) of the nodes, the derivative at the surface is defined by replacing the east-neighbor node (*E*) with the property at outlet boundary, C_{outlet}, likewise Eq. (3.28). By approximating the derivatives of properties at the outlet boundary with the zero-gradient, the property at the boundary is assigned as the property at node *P,* as shown in Eq. (3.31).

$$\left(\frac{\partial C}{\partial s}\right)_{outlet} = \frac{\left(C_{outlet} - C_P\right)}{\Delta x / 2} = 0 \tag{3.31a}$$

$$C_{outlet} = C_P \tag{3.31b}$$

Therefore, the accuracy at the boundary becomes the first-order accuracy in terms of the Taylor series.

(3) Wall boundary

The wall boundaries are the bank of the channel in the river. These boundaries are assumed as the impermeable wall in the calculations. Thus, both advective and

dispersive fluxes are imposed as zero. The transverse velocities are previously neglected by the concept of stream-tube. The dispersive fluxes across the wall boundaries are set to zero.

$$\left(\frac{\partial C}{\partial n}\right)_{\mathrm{n}=L} = \frac{2\left(C_L - C_P\right)}{\Delta x} = 0 \qquad (3.32a)$$

$$\left(\frac{\partial C}{\partial n}\right)_{n=R} = \frac{2\left(C_P - C_R\right)}{\Delta x} = 0 \qquad (3.32b)$$

3.2.6 Initial conditions

The initial condition of the numerical model developed in this study can be classified into the instantaneous and continuous injection of the pollutant mass for the general purpose of pollutant transport modeling. For the case of the instantaneous injection, the location of the injection point at the initial time has to be specified. The ambient concentration was set to zero if the initial concentration distribution is not given. As aforementioned, the numerical solutions were specified in the centroid of each control volume. Thus, the initial values were also specified as the averaged values in the control volume, so the injected must be input considering the size of the control volume at the injection point. Although the developed numerical models adopted the TVD schemes to minimize the effect of the high gradient of concentration values in the computational domain, the suddenly injected mass at the initial time caused the numerical errors in the solution domain because of discontinuity of concentration values in the surrounding injection point. In order to relax the discontinuity of concentration, the mass to be injected was distributed as a quadrangular pyramid-shaped-distribution centered at the injection point.

For the continuous injection, the treatments of mass injection depend on the location of the injection point. If the injection point coincides with the boundary of the domain, the boundary condition at the specific surface of the boundary can be considered as the Dirichlet condition to give the specific concentration values. If the injection of mass is required in the internal field, the injected mass is specified in the source term, shown in Eq. (3.20).

3.3 Evaluation of numerical model

The implemented numerical model was validated comparing with the analytical solution for the depth-averaged 2D ADE shown in Eq. (3.33)

$$C(s,n,t)=\frac{M}{4\pi t\sqrt{D_L D_T}}\exp\left(-\frac{(s-Ut)^2}{4D_L t}\right)\sum_{m=-\infty}^{m=\infty}\exp\left[-\frac{\left(n+(2m-1)\frac{W}{2}\right)^2}{4D_T t}\right] \quad (3.33)$$

where M is the mass introduced. As shown in Fig. 3.5, the results of the analytical solution over time are inserted into the inlet boundary. Then, the numerical solutions at the outlet boundary were compared to the analytical solution at the corresponding location.

In order to calculate both numerical and analytical solutions, the non-dimensional variables were introduced as follows (Rutherford, 1994).

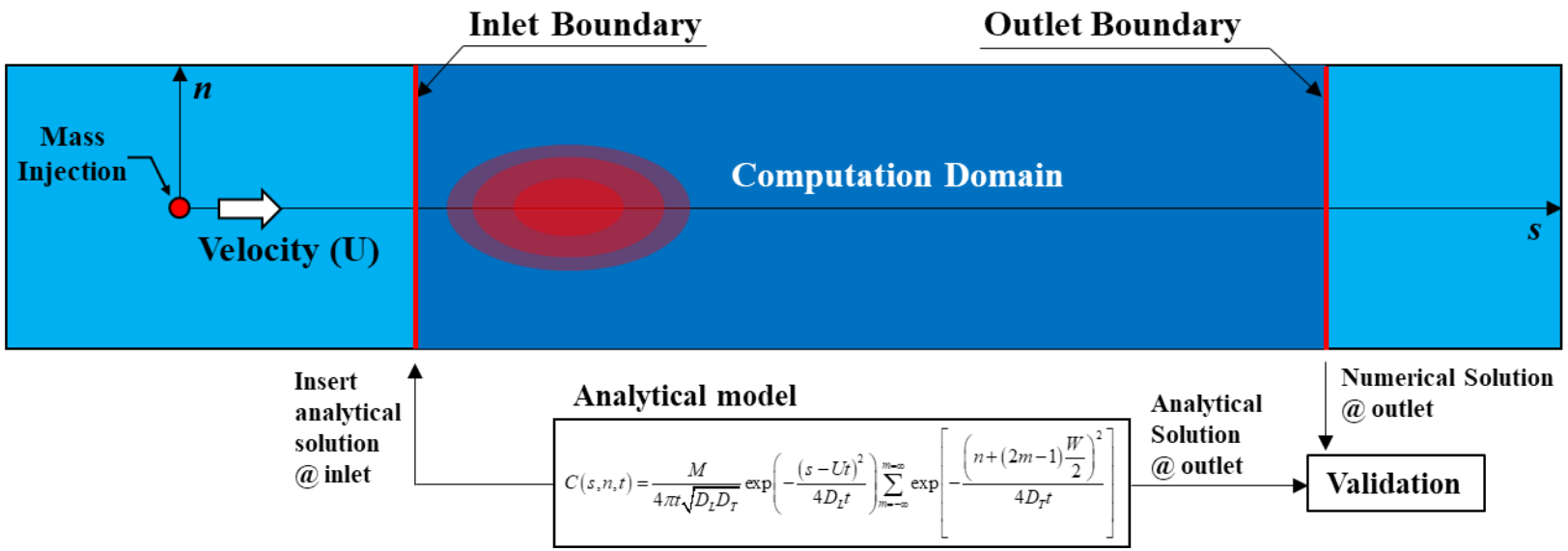

Figure 3.5 The Procedure of validation of the numerical model

$$s^* = \frac{s}{L_n} = \frac{sD_T}{U(W/2)^2} \tag{3.34a}$$

$$n^* = \frac{n}{W} \tag{3.34b}$$

$$t^* = \frac{t}{t_n} = \frac{D_T t}{(W/2)^2} \tag{3.34c}$$

$$C^* = \frac{s}{C_m} = \frac{sQ}{m} \tag{3.34d}$$

where s^* is the nondimensional longitudinal distance; n^* is the nondimensional transverse distance; t^* is the nondimensional time; C^* is the nondimensional concentration; C_m is the fully mixed concentration; L_n and t_n are the longitudinal distance and time when the transverse mixing is completed. The nondimensional variables are based on the length scale of transverse mixing. When the mass is injected at the center of width, the degree of mixing reaches asymptotically to 1 at $s^* = 1$. Conventionally the transversely complete mixing is considered when the values of p_m reaches to 0.98.

Table 3.2 configuration of the numerical computations for evaluation of TVDs

The number of cells	501×201 (s$\times$ n)	
Grid size	Δs^*	0.00072
	Δn^*	0.00498
Time step	Δt^*	8.8e-5
Location of boundary	Inlet	0.04
	Outlet	0.4
Mass injection (kg)	1	
Water depth (m)	1	
Péclet number	1,250 – 3,750	

For model validation, the inlet boundary for numerical calculation was located at $s^* = 0.04$, and the outlet boundary is set to $s^* = 0.4$. The Péclet number for simulation condition is governed by the longitudinal dispersion coefficient which is independent for non-dimensional variables. The numerical model was validated in three different Péclet numbers, of which the characteristic of length was defined as the L_n.

(1) Selection of TVD scheme

As shown in the previous chapter, some TVD schemes were implemented in the numerical model. In order to select appropriate limiter function, all types of limiter functions in Table 3.1 were evaluated as compared to Eq. (3.33). Fig. 3.6 shows the concentration-time curves at the centerline of the outlet boundary. The computational results represented in Fig. 3.6 shows the upwind scheme (UD) is quite diffused in all conditions due to the first-order truncation error. The TVD schemes remarkably improved the numerical solutions in all conditions, compared to UD. Fig. 3.7 represents the root mean square error (RMSE) of each TVD scheme. For *Pe*=1,250, all TVD schemes provide similar levels of RMSE, but the slightly different performances of schemes were found with increasing Péclet number. The numerical error, especially for peak concentration, increased with increasing Péclet number for all cases. Among the TVD schemes which were evaluated in this study, UMIST provided the lowest RMSE against to the exact solution. The RMSE of UMIST was

approximately 4-5 times lower than that of UD. Van Leer and Van Albada show slightly larger RMSE than UMIST. However, the differences in RMSE resulted in each scheme were not critical. SUPERBEE, which even provided the worst performance, showed three times lower RMSE than that of UD.

(2) The measure of computation time

For the selection of the proper numerical scheme, the computation time is also an essential factor in the purpose of engineering. The CPU time was measured to evaluate the efficiency of TVD schemes. The averaged CPU times were measured during the computations for 200 time-step. The CPU time for each scheme was normalized by the CPU time of UD. Fig. 3.8 represents the normalized CPU time for each scheme. The UMIST required at least 2.8 times more CPU time compared to UD. Moreover, the CPU time of UMIST steeply increased with the increment of the number of cells. On the other hand, both Van Leer and Van Albada required only 1.2 times more CPU time than UD. The increment of the number of cells did not cause a significant increment of the CPU time. Thus, Van Albada was finally chosen for the flux-limiter function in the application for this study.

a) *Pe* = 1,250

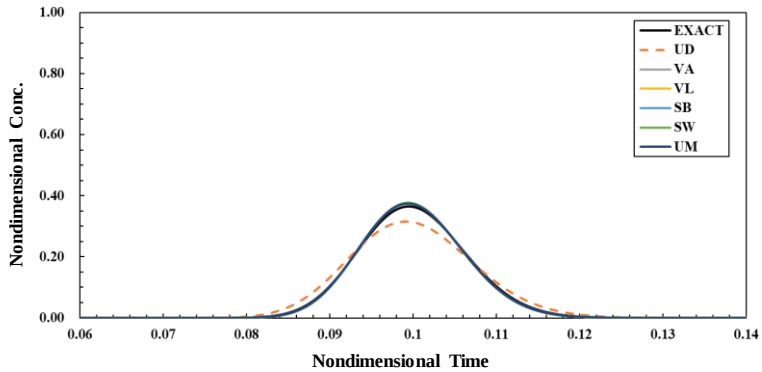

b) *Pe* = 2,500

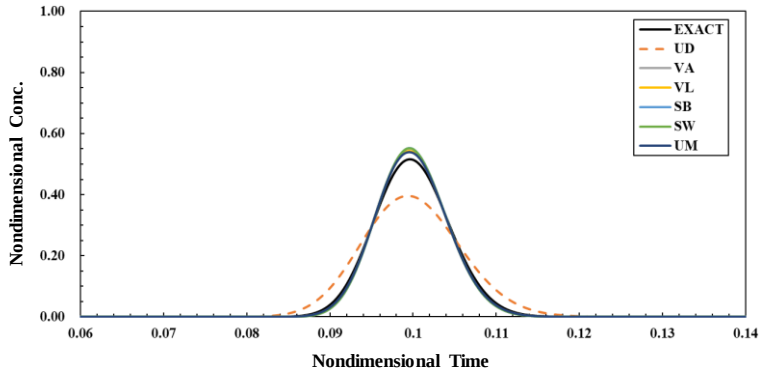

c) *Pe* = 3,750

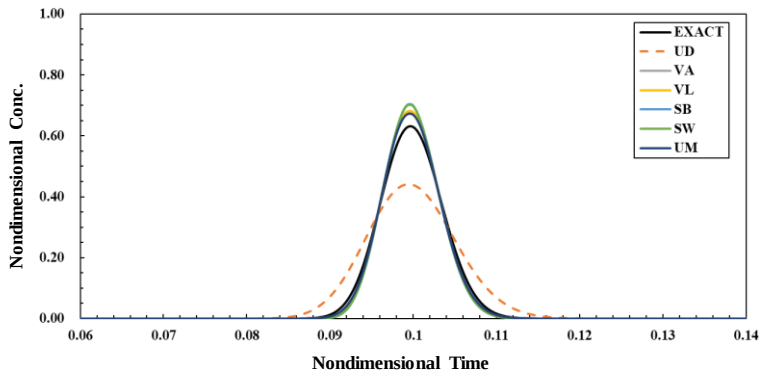

Figure 3.6 The Comparison of TVD schemes for different Péclet numbers (UD: upwind scheme; VA: Van Albada; VL: Van Leer; SB: SUPERBEE; SW: Sweby; UM: UMIST)

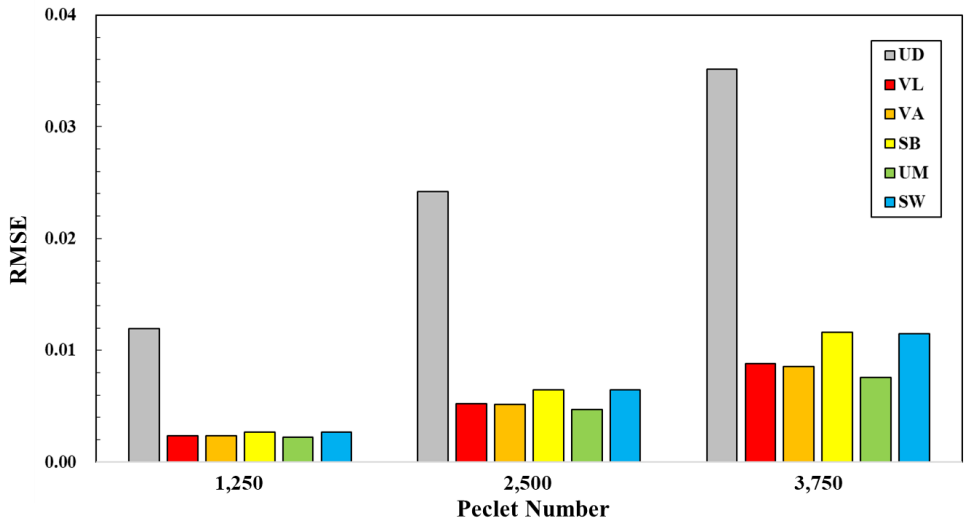

Figure 3.7 Root mean square error of TVD schemes

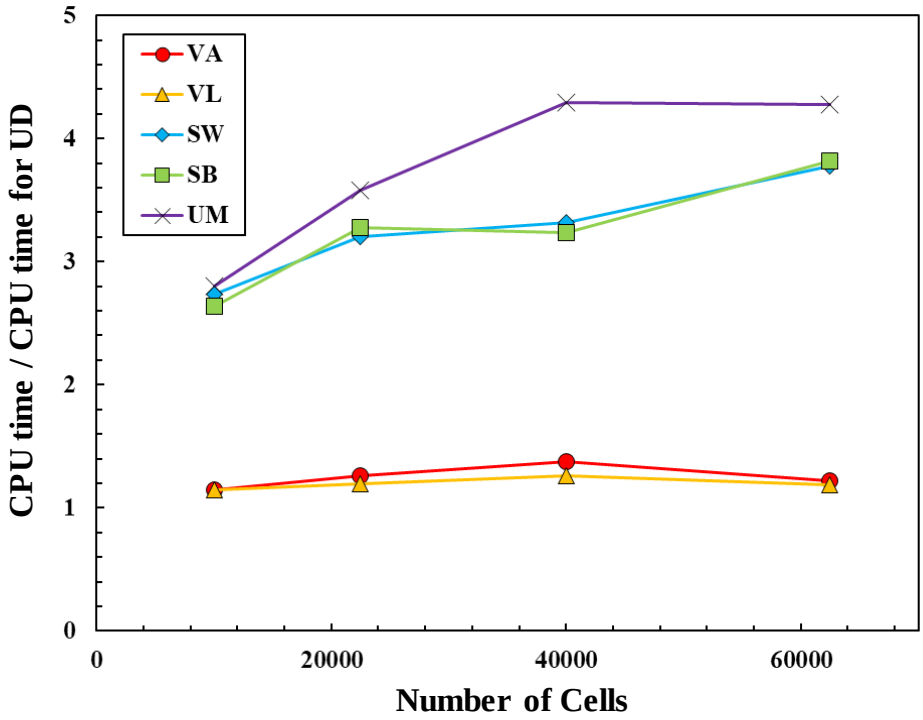

Figure 3.8 Normalized CPU time for TVD schemes

(3) Grid convergence test

The spatial discretization schemes for both advection and dispersion terms are accurate up to the second-order. In order to verify the order of truncation error for the implemented numerical model, the grid convergence tests were performed on the different sizes of computational grids. The Péclet number was equal to the value of 2,500 for all cases. In this test, the range of the number of cells was from 101 by 101 to 351 by 351, as shown in Table 3.3. The location of boundaries was the same as Table. 3.1. The computation timestep was controlled by 80 % of the maximum time step by Eq. (3.27) to ensure numerical stability. The equivalent grid size, shown in Eq. (3.35), was used to investigate the numerical error according to the order of grid sizes.

$$\Delta G = \sqrt{\left(\Delta s^*\right)^2 + \left(\Delta n^*\right)^2} \tag{3.35}$$

The numerical error was evaluated by the mean absolute error (MAE) shown as follows.

$$MAE = \frac{\sum \left| C_{ex} - C_{cal} \right|}{N} \tag{3.36}$$

where C_{ex} is the exact solutions; C_{cal} is the numerical solutions; N is the number of grids.

Fig. 3.9 shows the results of grid convergence tests. Fig. 3.9 a) represents that the numerical errors dramatically decrease as grid size is reduced. The numerical errors are high in the initial range of time from 0.01 to 0.02. The numerical solution in the region of high concentration gradient would not be adequately approximated as the grid size grows. This erroneous region was asymptotically relaxed with a reduction of grid size. Fig. 3.9 b) represents the relationship between maximum MAE and grid size. When the grid size is reduced, the magnitude of numerical error decreased by the squared grid size approximately. This tendency implies that the implemented model has second-order accuracy in space.

Fig. 3.10 represents the concentration-time curve at several transverse distances of outlet boundary for the case G301. And Fig. 3.11 shows the transverse distribution of the solution at a certain time. The results of the implemented model well agreed with the exact solution showing the determination coefficient over 0.9. Thus, the numerical error for peak concentration, shown in Fig. 3.6, can be resolved by sufficiently fine computational grid sizes. The grid convergence tests must be performed repeatably in order to find the proper grid size when the simulation conditions change.

Table 3.3 configuration of the numerical computations for grid tests

Case	Number of cells	Equivalent grid size	Timestep	MAPE
G101	101×101	0.0090	0.000808	0.0098
G151	151×151	0.0060	0.000819	0.0043
G201	201×201	0.0045	0.000828	0.0023
G251	251×251	0.0036	0.000829	0.0016
G301	301×301	0.0030	0.000831	0.0011

a) Mean absolute error over time

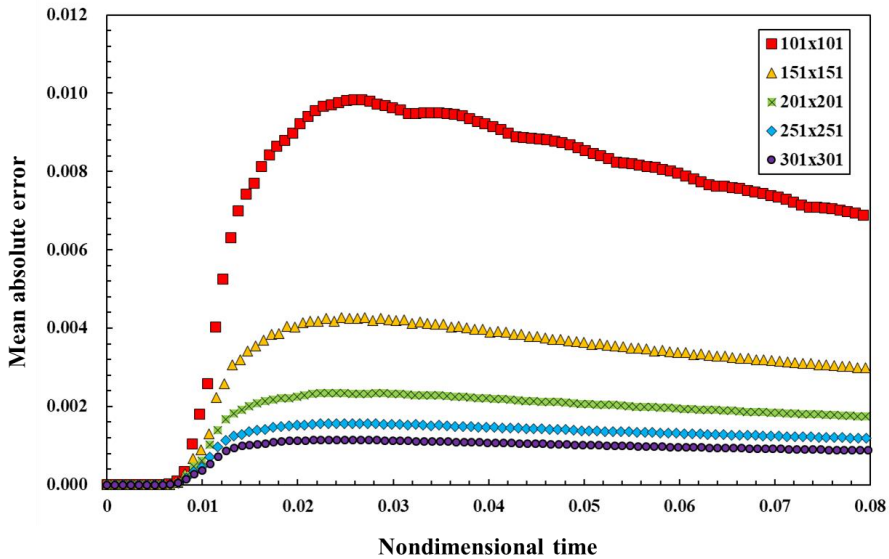

b) Relationship between Mean absolute error and grid size

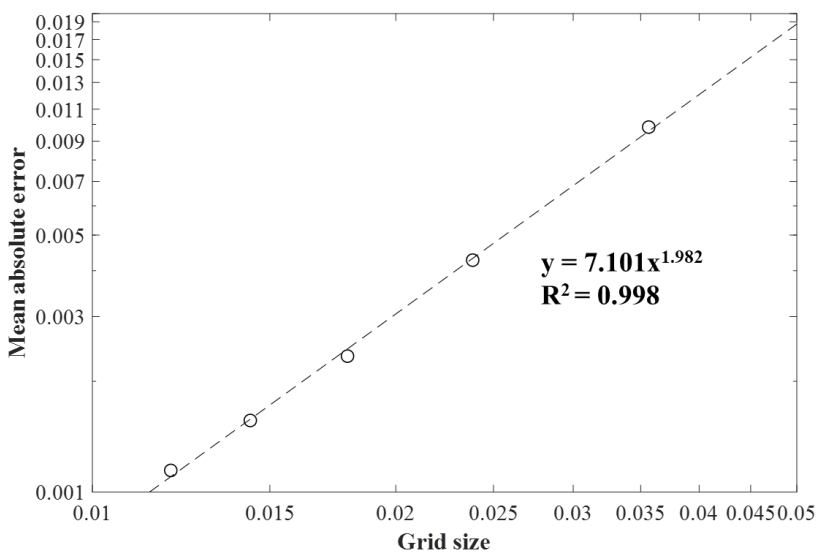

Figure 3.9 Evaluation of numerical error with different size of the grid

a) n*=0.5

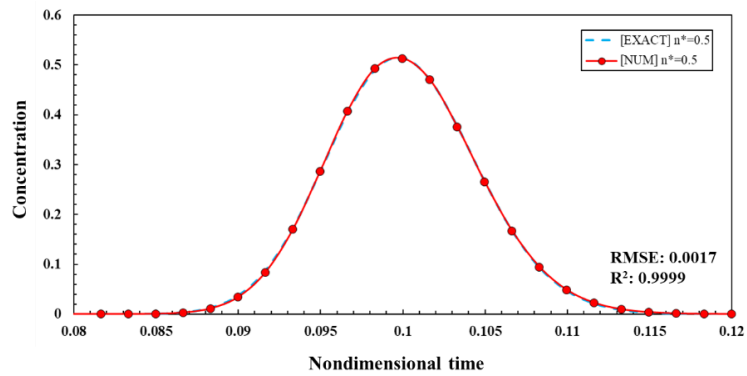

b) n*=0.67

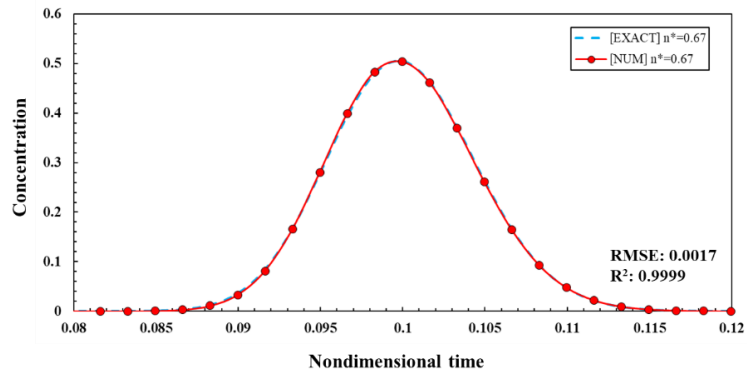

c) n*=0.83

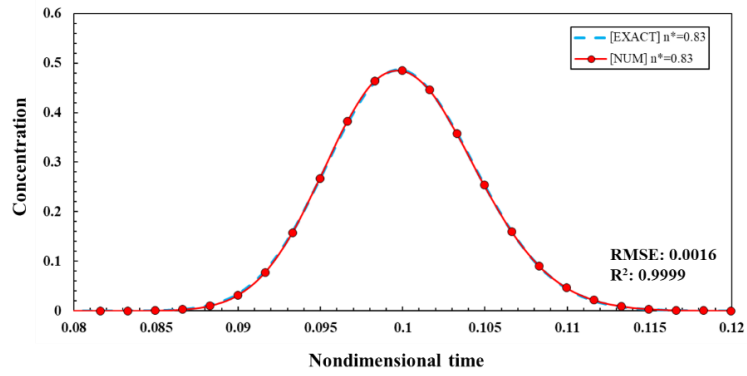

Figure 3.10 Concentration-time curves at outlet boundary

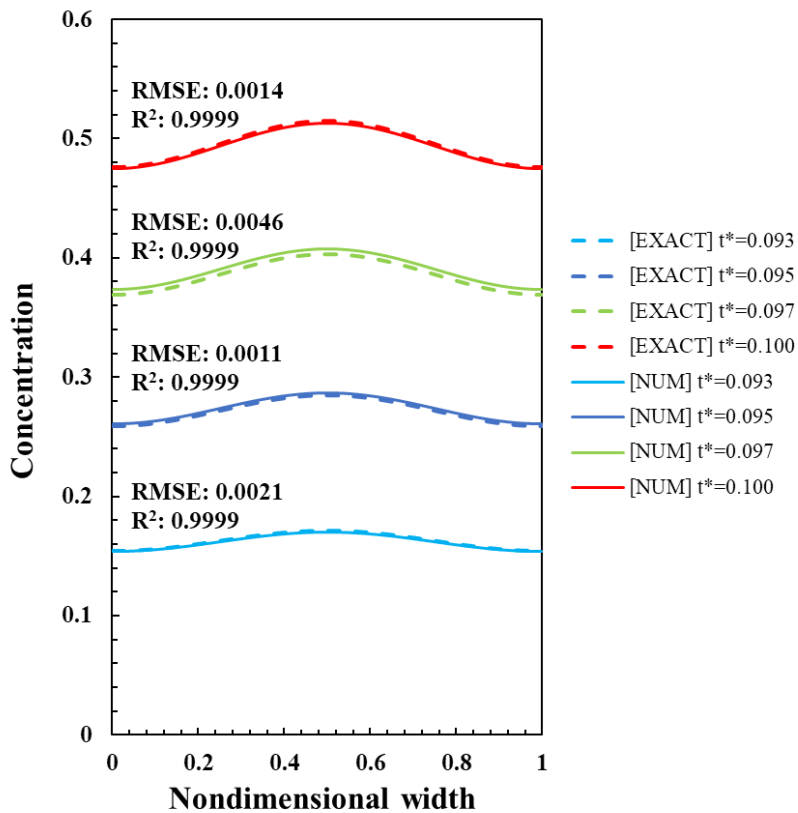

Figure 3.11 Transverse distribution of concentration at the outlet boundary

4. Evaluation of 2D stream-tube routing procedure

4.1 Overview of the evaluation procedure for 2D STRP

The 2D STRP is the analytical solution of the simplified 2D ADE for the arbitrary distribution of the initial concentration. In this study, the limitations of 2D STRP were hypothesized as follows.

(1) The spatial distribution of concentration is estimated by the FCA, so the results of 2D STRP could be affected by the Peclet number.

(2) The results of 2D STRP cannot consider the effect of wall boundaries because it was derived in the conditions where the channel is infinitely wide.

(3) the velocity of tracer clouds traveled by flows for each stream-tube can be estimated by the mean time of passage at upstream and downstream sections.

In order to test the above hypotheses, the results of 2D STRP was evaluated in two kinds of test conditions. In Test. 1, the evaluation was performed in the condition of uniform flow to investigate the effects of Peclet number and wall boundary, and the velocity of tracer clouds traveled by flows was evaluated in the condition of the spatially varied flows in the Test. 2. The concentration data used for the evaluation of 2D STRP were generated by the analytic solutions and numerical solutions. The evaluation cases used in this study were summarized in Table. 4.1.

In the cases for test 1, the mixing characteristics for each case were dependent on the Peclet number defined as follows.

$$Pe = \frac{UL_n}{D_L} \tag{4.1}$$

where U is the mean velocity; L_n is the longitudinal distance when the concentration was mixed completely in a transverse direction. The results simulated by the analytical solution were converted to nondimensional variables, as shown in Eq. (3.34). If Peclet numbers of evaluation cases are identical for any arbitrary velocity magnitudes, dispersion coefficients, and channel width, the concentration distribution can be expressed identically in nondimensional space and time. The range of *Peclet* numbers for evaluations was from 900 to 9,000 in the condition of uniform flow.

In test 2 for evaluation of velocity of traveled tracer clouds, the transversely varied velocity profiles were generated by Eq. (4.2), which was proposed by Seo and Baek (2004).

$$\frac{u}{U} = \frac{\Gamma(\alpha+\beta)}{\Gamma(\alpha)\Gamma(\beta)}(y')^{\alpha-1}(1-y')^{\beta-1} \tag{4.2}$$

where u is the depth-averaged velocity magnitude; y' is the transverse distance from left bank normalized by channel width; α and β are the shape parameters;

Γ is the gamma function which is defined as:

$$\Gamma(\alpha) = \int_0^{\infty} (y')^{\alpha-1} e^{-y'} dy' \tag{4.3}$$

The Eq. (4.2) is identical to the probability distribution of beta distribution. When α and β are equal, the velocity distribution can be symmetrical. In the evaluation cases, the values of α and β ranged from 1 to 2, and the velocity distributions on the parameters are shown in Fig. 4.1.

For each case, ten measuring sections were set as uniform intervals ($\Delta s^* = 0.01$), as expressed in Fig. 4.2. The concentration data recorded in time were employed as input values in 2D STRP. In 2D STRP, the temporal concentration distribution is calculated at the downstream section inserting the temporal distribution at the upstream section. Then, the concentration-time distributions calculated by 2D STRP were compared to the concentration-time distribution measured at downstream sections. Both D_L and D_T for 2D STRP were set to be identical to the values which were used to generate the synthetic data.

Table 4.1 Simulation conditions for evaluation of 2D STRP

Case	Mean velocity U (m/s)	Water depth H (m)	Channel width W (m)	Dispersion coefficients		Parameters for velocity distribution (Beta function)		Peclet number	Remark
				D_L (m^2/s)	D_T (m^2/s)	α	β		
P900-B10	0.5	1	12	1	0.01	1	1	900	Test 1
P1125-B10				0.8				1,125	
P1500-B10				0.6				1,500	
P2250-B10				0.4				2,250	
P4500-B10				0.2				4,500	
P9000-B10				0.1				9,000	
P9000-B12				0.1	0.01	1.2	1.2	9,000	Test 2
P9000-B14									
P9000-B16						1.6	1.6		
P9000-B18									
P9000-B20						2.0	2.0		

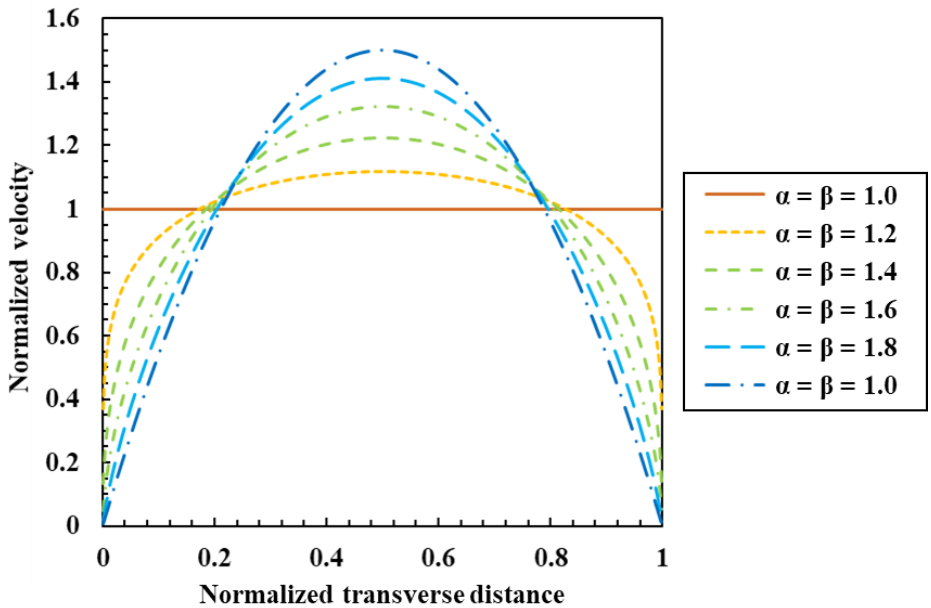

Figure 4.1 Velocity distributions generated by the beta distribution

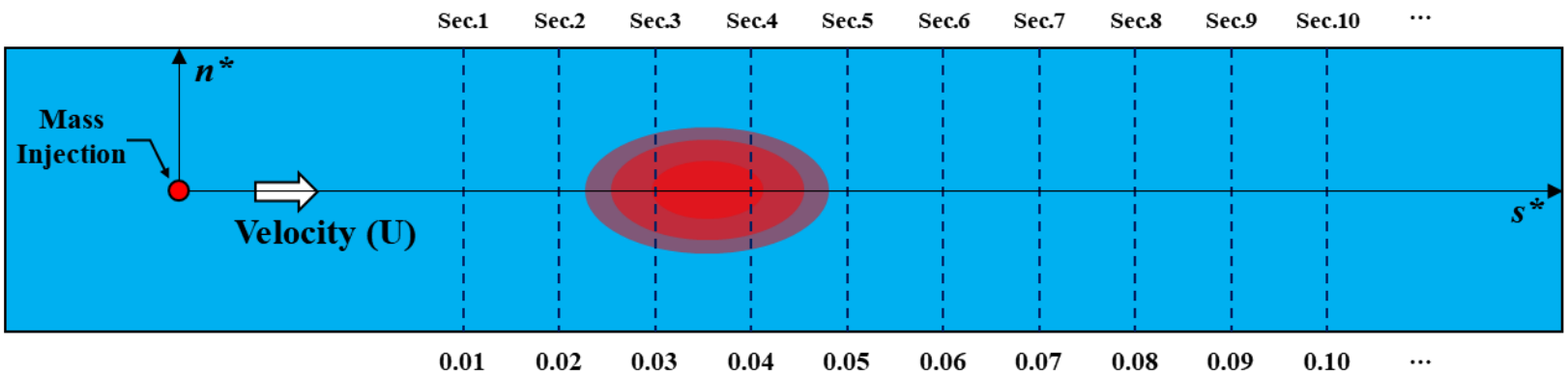

Figure 4.2 Locations of the concentration measuring sections for evaluations of 2D STRP

4.2 Evaluation of 2D STRP in the condition of uniform flow

The performance of 2D STRP in the condition of uniform flow, in which the shape parameters of Eq. (4.2) are equal to 1 and are evaluated on the six cases depending on the Peclet numbers defined as Eq. (4.1). The Peclet numbers were controlled by changing of longitudinal dispersion coefficients (D_L). Fig. 4.3 shows the input data expressed as the C-t-q distributions and the predicted results by 2D STRP at each section for the case of P1125-B10. The figure shows the temporal distributions at each section are positively skewed, and the tracer clouds spread both longitudinally and transversely. The results of the 2D STRP shown in Fig. 4.3 agreed well with the true distributions, but the discrepant tendencies appeared when the tracer clouds reached either side of wall boundaries. The discrepancy between predicted and true distributions was evaluated by the normalized sum of squared residuals (NSSR) shown as following.

$$NSSR = \frac{\sum_{i=1}^{n}\left(C_i - \hat{C}_i\right)^2}{C_p} \tag{4.4}$$

where C_i is the concentration in the true distribution generated by analytical solutions; $\hat{C}_i$ is the predicted concentration by 2D STRP; C_p is the peak concentration for the true distribution at each section.

a) Input C-t-q distribution (Routing from s*=0.04 to s*=0.05)

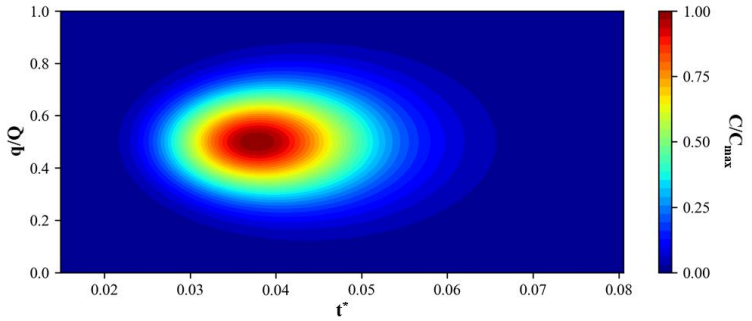

b) Predicted C-t-q distribution (Routing from s*=0.04 to s*=0.05)

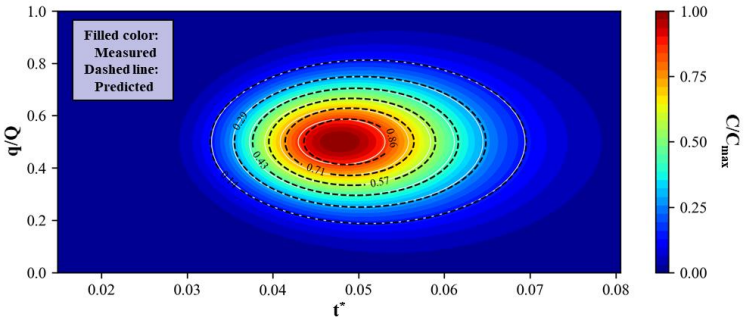

c) Input C-t-q distribution (Routing from s*=0.06 to s*=0.07)

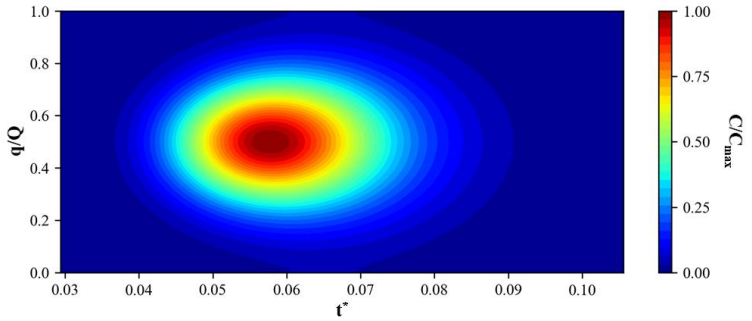

d) Predicted C-t-q distribution (Routing from s*=0.06 to s*=0.07)

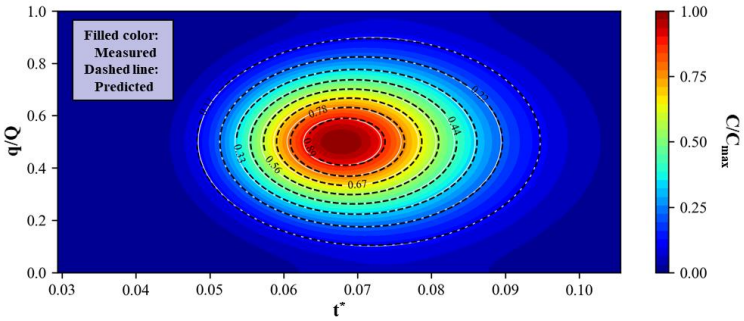

e) Input C-t-q distribution (Routing from s*=0.08 to s*=0.09)

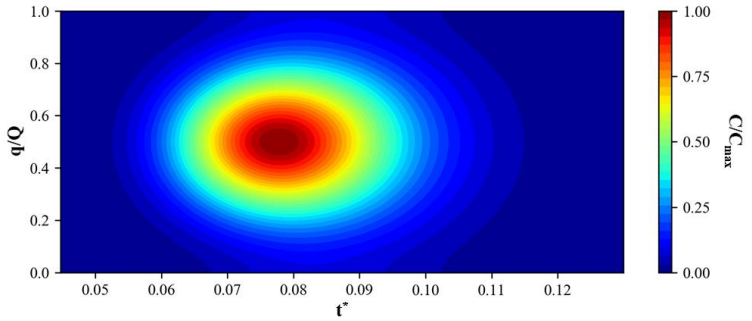

f) Predicted C-t-q distribution (Routing from s*=0.08 to s*=0.09)

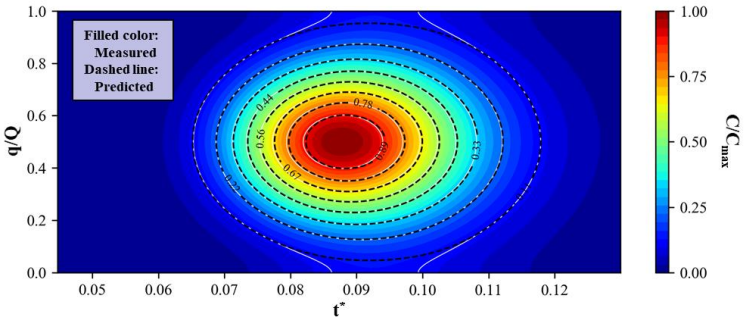

g) Input C-t-q distribution (Routing from s*=0.10 to s*=0.11)

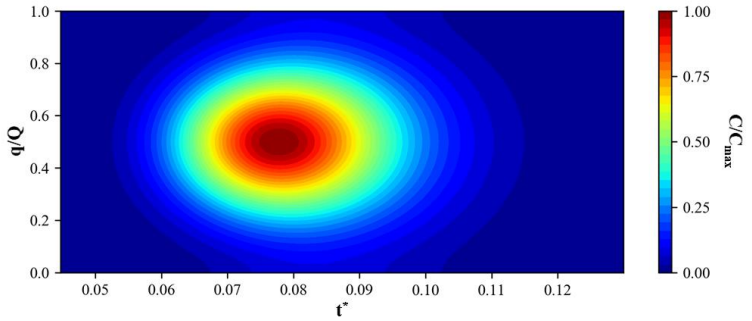

h) Predicted C-t-q distribution (Routing from s*=0.10 to s*=0.11)

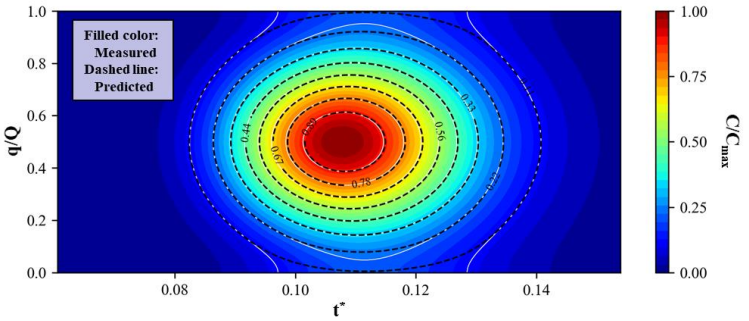

Figure 4.3 Predicted concentration distribution by 2D STRP for P1125-B10

In order to identify whether the concentration distribution reaches sidewall boundaries, The P_w, which is the ratio between minimum and maximum values of the cumulative concentration over time, was introduced shown in Eq. (4.5).

$$p_w = \frac{\int_0^\infty C_w dt}{\max\left(\int_0^\infty C dt\right)} \tag{4.5}$$

where C_w is the concentration at either side of the wall boundaries. The P_w is similar to the degree of mixing defined by (Rutherford, 1994). The P_w was initially 0 after the injection of mass. The value of P_w gradually approached to 1 over time. The value of unity for P_w means that the pollutant concentration is fully mixed in the spanwise direction so that the two-dimensional mixing is completed. In the simulation results for the evaluation cases, the values of P_w exceeded 0.1 after the maximum concentration of pollutant clouds passed through s^*=0.08 approximately.

Fig. 4.4 shows the evaluated NRSS with P_w for each case. The overall trend showed that the NRSS initially tended to decrease with increasing the nondimensional longitudinal distance (s^*) before the pollutant clouds reached sidewall (P_{wr}<0.01). Then, NSSR was steeply increased with increasing the values of P_w. In the intervals for the values of P_w less than 0.01, The discrepancy of the results by 2D STRP tended to decrease as the Peclet number increased. It was inferred that the accuracy of 2D

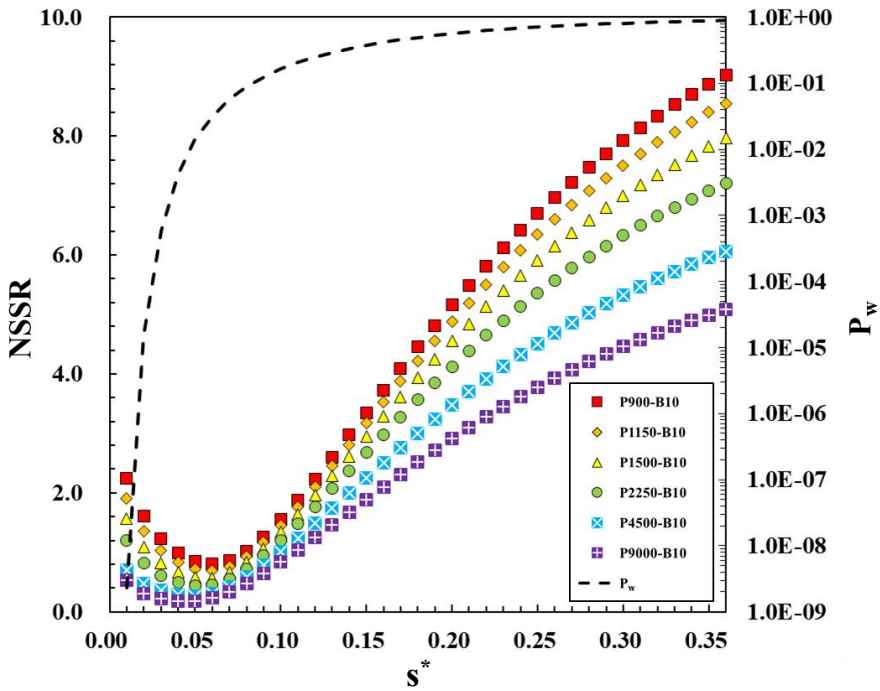

Figure 4.4 The Normalized sum of squared residuals of concentration distribution calculated by 2D STRP in the uniform flow

STRP could be affected by the Peclet number and the effect of wall boundaries. To investigate the effect of the Peclet number on the concentration distribution, the characteristics of spatial distribution estimated by FCA were analyzed. The 2D STRP (Eq. (2.19)) was derived from Eq. (2.17) introducing the frozen cloud approximation. The spatial distributions, which are calculated by the analytical solution of 2D ADE, are the gaussian distributions. Thus, the centroid of the spatial distribution of pollutant clouds must be identical to the location of maximum concentration because spatial distributions are always symmetrical. Fig. 4.5 shows the spatial concentration distribution, which is converted from the temporal distribution by FCA. The markers (x) indicate the centroid of pollutant clouds. The spatial distribution converted by FCA showed skewed distributions. The centroid of pollutant clouds was not identical to the location of the maximum concentration because the pollutant clouds were dispersed while the pollutant clouds passed through the measuring sections.

Table 4.2 shows the statistical comparisons between estimated and true spatial distributions at the mean time of passage. The longitudinal skewness of the true distribution was the value of 0 regardless of the location of sections and the Peclet numbers, while the negative skewness was calculated for all estimated distributions. As shown in Fig. 4.6, the values of skewness tended to approach the value of 0 with an increase in the Peclet number. In the case of the variance of spatial distribution, both longitudinal and transverse variance slightly differed compared to that of the spatial distributions, shown less than 5%. The locations of the centroid of spatial distributions tended to close to the location of the maximum concentration with an

a) Pe = 900

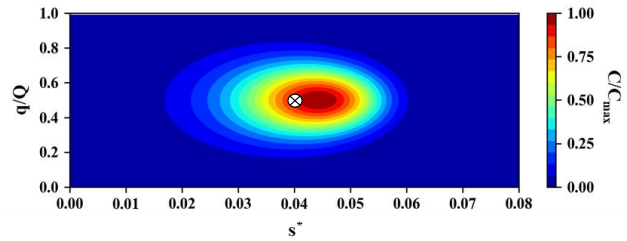

b) Pe = 1,125

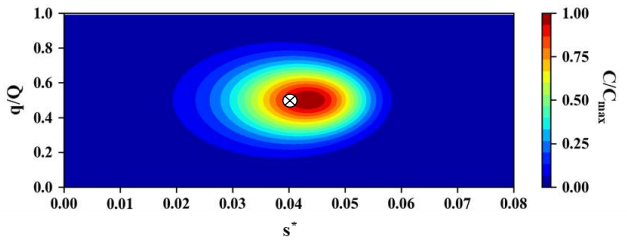

c) Pe = 1,500

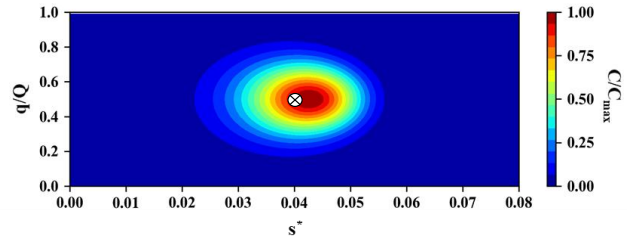

d) Pe = 2,500

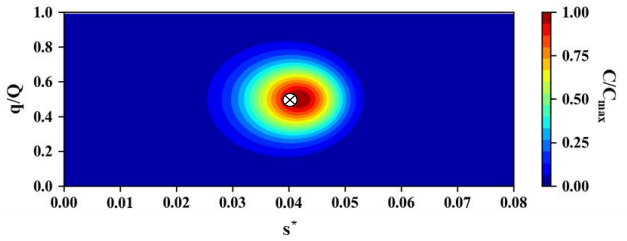

e) Pe = 4,500

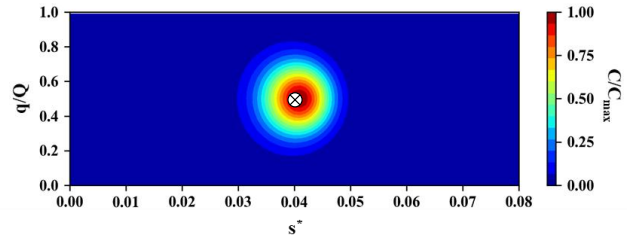

f) Pe = 9,000

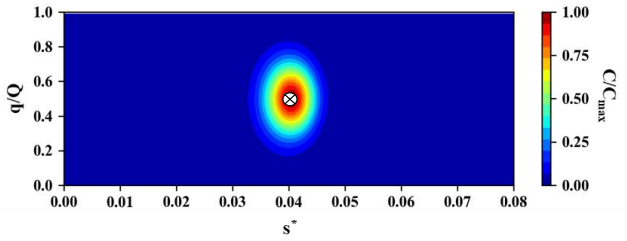

Figure 4.5 Spatial concentration distribution obtained by FCA from temporal data measured at Sec. 2

Table 4.2 The statistical characteristics of the spatial distribution estimated by FCA

Pe	s*	X_s	t_C	S_C		S_{max}		σ_s^2		σ_n^2		γ_1		MAE
				FCA	TRUE	FCA	TRUE	FCA	TRUE	FCA	TRUE	FCA	TRUE	
900	0.02	36	80.00	36.66	40.03	43.88	40.50	147.05	158.81	1.57	1.60	-0.57	0.00	0.29
	0.04	72	152.01	72.10	76.00	79.88	76.50	312.84	303.98	3.03	3.04	-0.61	0.00	0.21
	0.06	108	224.02	108.01	112.01	115.88	112.50	463.11	448.05	4.41	4.44	-0.56	0.00	0.17
	0.08	144	296.04	144.00	148.02	151.88	148.50	608.34	592.08	5.68	5.72	-0.49	0.00	0.15
	0.10	180	368.05	180.00	184.02	187.88	184.50	752.53	736.09	6.79	6.83	-0.44	0.00	0.14
	0.12	216	440.05	216.00	220.03	223.88	220.50	896.53	880.10	7.73	7.78	-0.41	0.00	0.12
	0.14	252	512.05	252.00	256.03	259.88	256.50	1040.50	1024.10	8.52	8.57	-0.38	0.00	0.11
	0.16	288	584.05	288.00	292.03	295.88	292.50	1184.46	1168.10	9.17	9.23	-0.35	0.00	0.10
	0.18	324	656.05	324.00	328.02	331.88	328.50	1328.43	1312.09	9.72	9.77	-0.33	0.00	0.09
	0.20	360	728.04	360.00	364.02	367.88	364.50	1472.40	1456.09	10.16	10.21	-0.31	0.00	0.08
1,125	0.02	36	78.40	36.33	39.21	42.75	39.21	121.94	125.12	1.55	1.57	-0.60	0.00	0.27
	0.04	72	150.41	72.03	75.20	78.75	75.20	248.99	240.65	3.00	3.01	-0.59	0.00	0.18
	0.06	108	222.42	108.00	111.21	114.75	111.21	366.14	355.87	4.39	4.41	-0.51	0.00	0.15
	0.08	144	294.43	144.00	147.22	150.75	147.22	481.57	471.09	5.66	5.69	-0.44	0.00	0.13
	0.10	180	366.44	180.00	183.22	186.75	183.22	596.79	586.30	6.77	6.81	-0.40	0.00	0.12
	0.12	216	438.44	216.00	219.22	222.75	219.22	711.97	701.51	7.72	7.76	-0.36	0.00	0.11
	0.14	252	510.44	252.00	255.22	258.75	255.22	827.15	816.71	8.51	8.56	-0.34	0.00	0.10
	0.16	288	582.44	288.00	291.22	294.75	291.22	942.33	931.90	9.17	9.21	-0.31	0.00	0.09
	0.18	324	654.44	324.00	327.22	330.75	327.22	1057.51	1047.10	9.72	9.75	-0.30	0.00	0.08
	0.20	360	726.43	360.00	363.22	366.75	363.22	1172.69	1162.29	10.16	10.20	-0.28	0.00	0.07
1,500	0.02	36	76.80	36.11	38.40	40.50	38.40	93.69	92.12	1.53	1.54	-0.62	0.00	0.23
	0.04	72	148.80	72.00	74.40	76.50	74.40	184.23	178.57	2.97	2.98	-0.53	0.00	0.16
	0.06	108	220.81	108.00	110.41	112.50	110.41	270.93	264.98	4.36	4.38	-0.44	0.00	0.13
	0.08	144	292.82	144.00	146.41	148.50	146.41	357.37	351.39	5.64	5.66	-0.38	0.00	0.11
	0.10	180	364.83	180.00	182.41	184.50	182.41	443.77	437.79	6.76	6.79	-0.34	0.00	0.10
	0.12	216	436.83	216.00	218.42	220.50	218.42	530.16	524.20	7.71	7.74	-0.31	0.00	0.09
	0.14	252	508.83	252.00	254.42	256.50	254.42	616.55	610.60	8.51	8.54	-0.29	0.00	0.09
	0.16	288	580.83	288.00	290.42	292.50	290.42	702.93	697.00	9.17	9.20	-0.27	0.00	0.08
	0.18	324	652.83	324.00	326.41	328.50	326.41	789.32	783.39	9.71	9.74	-0.26	0.00	0.07
	0.20	360	724.83	360.00	362.41	364.50	362.41	875.71	869.79	10.16	10.19	-0.24	0.00	0.06

Table 4.2 The statistical characteristics of the spatial distribution estimated by FCA (cont.)

Pe	s*	X_s	t_c	S_C		S_{max}		σ_s^2		σ_n^2		γ_1		MAE
				FCA	TRUE	FCA	TRUE	FCA	TRUE	FCA	TRUE	FCA	TRUE	
2,250	0.02	36	75.20	36.01	37.60	39.38	37.60	62.53	60.16	1.50	1.50	-0.59	0.00	0.17
	0.04	72	147.20	72.00	73.60	75.38	73.60	120.64	117.76	2.94	2.94	-0.44	0.00	0.13
	0.06	108	219.21	108.00	109.60	111.38	109.60	178.26	175.37	4.34	4.35	-0.36	0.00	0.11
	0.08	144	291.22	144.00	145.61	147.38	145.61	235.87	232.97	5.62	5.64	-0.31	0.00	0.10
	0.10	180	363.22	180.00	181.61	183.38	181.61	293.47	290.58	6.75	6.77	-0.28	0.00	0.08
	0.12	216	435.22	216.00	217.61	219.38	217.61	351.07	348.18	7.70	7.72	-0.26	0.00	0.08
	0.14	252	507.22	252.00	253.61	255.38	253.61	408.66	405.78	8.50	8.52	-0.24	0.00	0.07
	0.16	288	579.22	288.00	289.61	291.38	289.61	466.26	463.38	9.17	9.19	-0.22	0.00	0.06
	0.18	324	651.22	324.00	325.61	327.38	325.61	523.85	520.98	9.71	9.73	-0.21	0.00	0.05
	0.20	360	723.22	360.00	361.61	363.38	361.61	581.45	578.57	10.16	10.18	-0.20	0.00	0.05
4,500	0.02	36	73.60	36.00	36.80	37.13	36.80	30.34	29.44	1.47	1.47	-0.44	0.00	0.12
	0.04	72	145.60	72.00	72.80	73.13	72.80	59.14	58.24	2.91	2.91	-0.31	0.00	0.09
	0.06	108	217.60	108.00	108.80	109.13	108.80	87.95	87.04	4.31	4.32	-0.26	0.00	0.07
	0.08	144	289.61	144.00	144.80	145.13	144.80	116.75	115.84	5.60	5.61	-0.22	0.00	0.06
	0.10	180	361.61	180.00	180.81	181.13	180.81	145.55	144.64	6.73	6.74	-0.20	0.00	0.06
	0.12	216	433.61	216.00	216.81	217.13	216.81	174.35	173.44	7.69	7.70	-0.18	0.00	0.05
	0.14	252	505.61	252.00	252.81	253.13	252.81	203.15	202.24	8.50	8.51	-0.17	0.00	0.05
	0.16	288	577.61	288.00	288.81	289.13	288.81	231.94	231.04	9.16	9.17	-0.16	0.00	0.04
	0.18	324	649.61	324.00	324.81	325.13	324.81	260.74	259.84	9.71	9.72	-0.15	0.00	0.04
	0.20	360	721.61	360.00	360.80	361.13	360.80	289.54	288.64	10.16	10.17	-0.14	0.00	0.03
9,000	0.02	36	72.80	36.00	36.40	37.13	36.40	15.01	14.56	1.46	1.46	-0.30	0.00	0.08
	0.04	72	144.80	72.00	72.40	73.13	72.40	29.41	28.96	2.90	2.90	-0.22	0.00	0.06
	0.06	108	216.80	108.00	108.40	109.13	108.40	43.81	43.36	4.30	4.30	-0.18	0.00	0.05
	0.08	144	288.80	144.00	144.40	145.13	144.40	58.21	57.76	5.59	5.60	-0.16	0.00	0.04
	0.10	180	360.80	180.00	180.40	181.13	180.40	72.61	72.16	6.73	6.73	-0.14	0.00	0.04
	0.12	216	432.80	216.00	216.40	217.13	216.40	87.01	86.56	7.69	7.69	-0.13	0.00	0.04
	0.14	252	504.80	252.00	252.40	253.13	252.40	101.41	100.96	8.49	8.50	-0.12	0.00	0.04
	0.16	288	576.80	288.00	288.40	289.13	288.40	115.81	115.36	9.16	9.17	-0.11	0.00	0.03
	0.18	324	648.80	324.00	324.40	325.13	324.40	130.21	129.76	9.71	9.72	-0.10	0.00	0.03
	0.20	360	720.80	360.00	360.40	361.13	360.40	144.61	144.16	10.16	10.17	-0.10	0.00	0.03

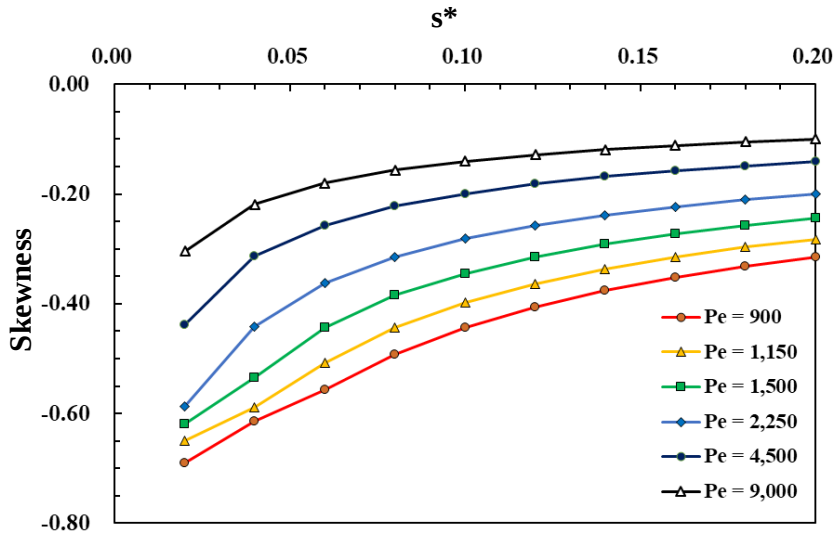

Figure 4.6 Longitudinal skewness of the spatial distribution by FCA

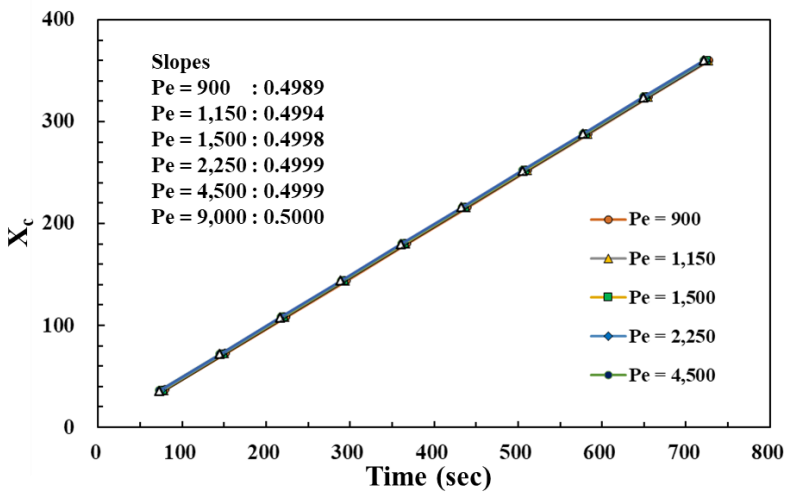

Figure 4.7 The centroid of the spatial distribution by FCA over time

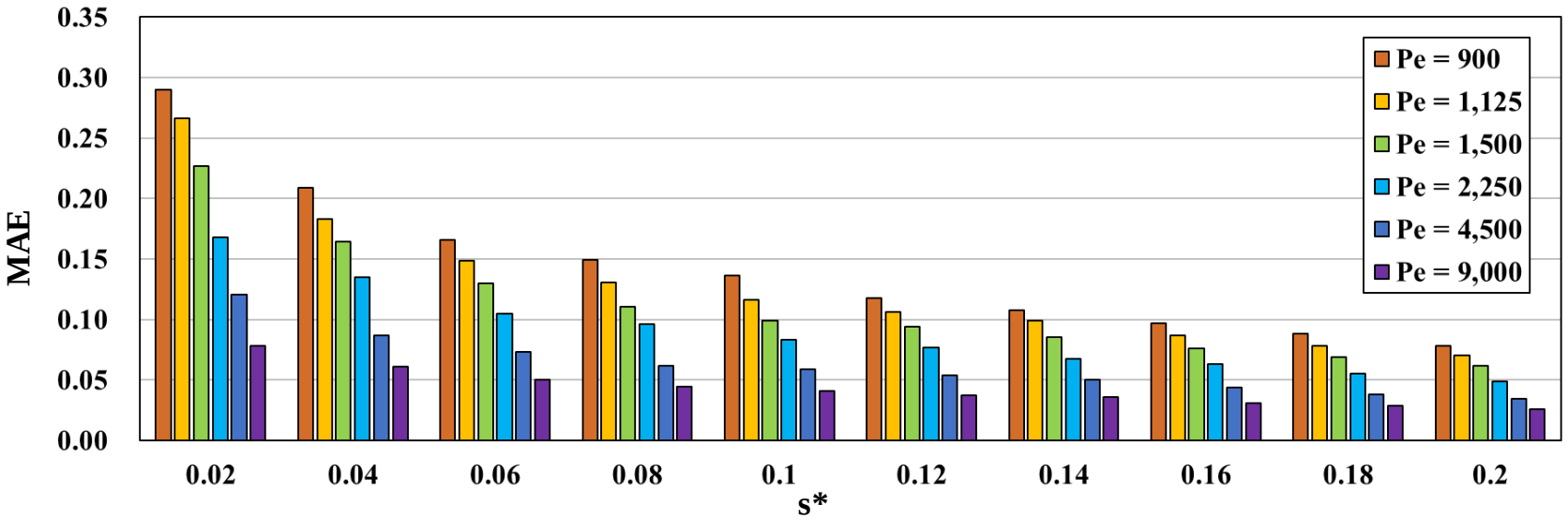

Figure 4.8 Mean absolute error of the spatial distribution estimated by FCA

increase in the Peclet number. However, the change rates of the centroid over time were calculated as the values close to the magnitude of mean velocity regardless of the Peclet numbers. The overall error was evaluated by the mean absolute error (MAE) shown in Fig. 4.8. Although the FCA helps to estimate the spatial distribution of pollutant clouds from the temporal distribution, this assumption may be applicable for the Peclet number over 2,250 approximately to estimate the spatial distribution with the value of MAE less than 20 % for overall sections. For 2,250 of Peclet number, the NRSS were evaluated less than 0.45 before the pollutant clouds reached wall boundaries.

For the effect of the wall reflection, the 2D STRP could not reproduce the accurate concentration distributions because 2D STRP, which is expressed by Eq. (2.17) and Eq. (2.19), was derived in the domain where the channel width is infinitely wide. To investigate the effect of wall reflection, the Case P9000-B10, in which the Peclet number was the highest among the cases in this study, was used so that the evaluations were performed in the condition where the effect of FCA is minimized as far as possible. Fig. 4.9 shows the transverse profiles for cumulative concentration for synthetic concentration fields and the predicted results by 2D STRP. For cumulative profiles in synthetic data, the gradient of the cumulative concentration at wall boundaries was zero, and the values of cumulative concentration increased along the dimensionless longitudinal distance. however, the results of 2D STRP showed the steep gradient of cumulative concentration curves, and the increment of cumulative concentration at the wall boundaries less than that of synthetic data which

a) Cumulative concentration for synthetic data (P9000-B10)

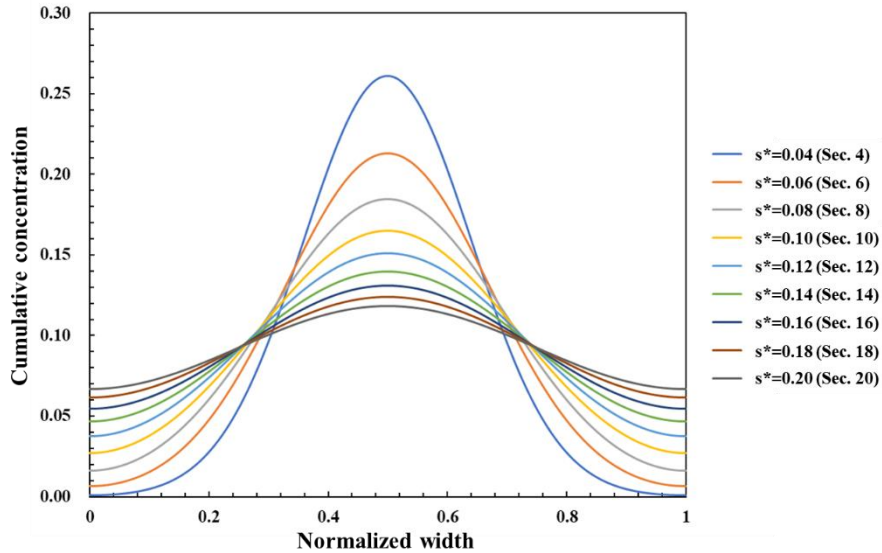

b) Cumulative concentration predicted by 2D STRP (P9000-B10)

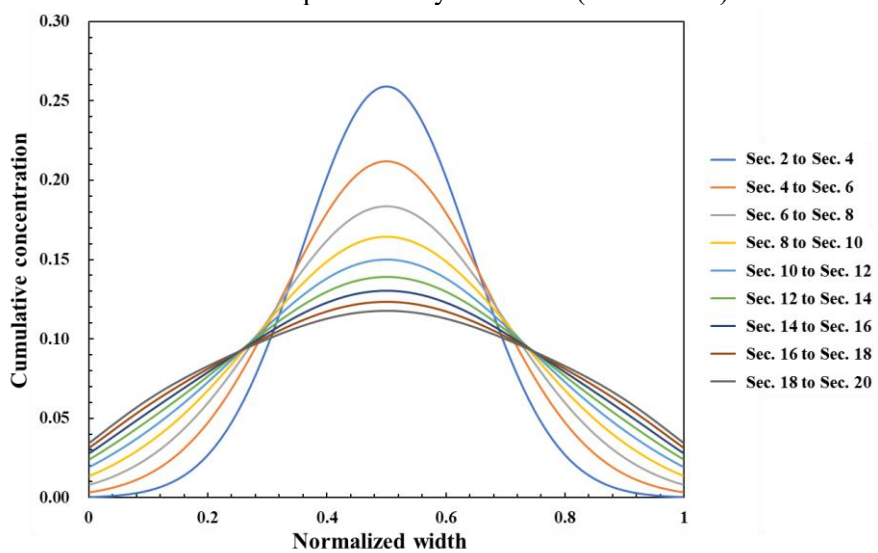

Figure 4.9 Cumulative concentration at each section (P9000-B10)

were generated by the analytical solution with consideration of the wall effect. In addition, the mass was not conserved in the results of 2D STRP because the pollutant mass was continuously leaked by the transversely dispersive fluxes. Fig. 4.10 shows the absolute errors of the cumulative concentration curves predicted by 2D STRP. The absolute error was normalized by the peak concentration at each section. The absolute error of cumulative concentration curves by 2D STRP increased, especially near the wall boundaries. Fig. 4.11 shows that the normalized absolute error at the wall boundary for the interval where the P_w exceeded 0.01 linearly increased with respect to the values of P_w. Even if the true dispersion coefficients were known, the 2D STRP could not predict the accurate concentration distributions due to the absence of the consideration of wall boundaries. In other words, when the optimization techniques applied to find the optimal dispersion coefficients, the optimal values of both D_L and D_T could be found as the values affected by the inaccurate results of 2D STRP in the conditions where the effect of wall reflection is significant.

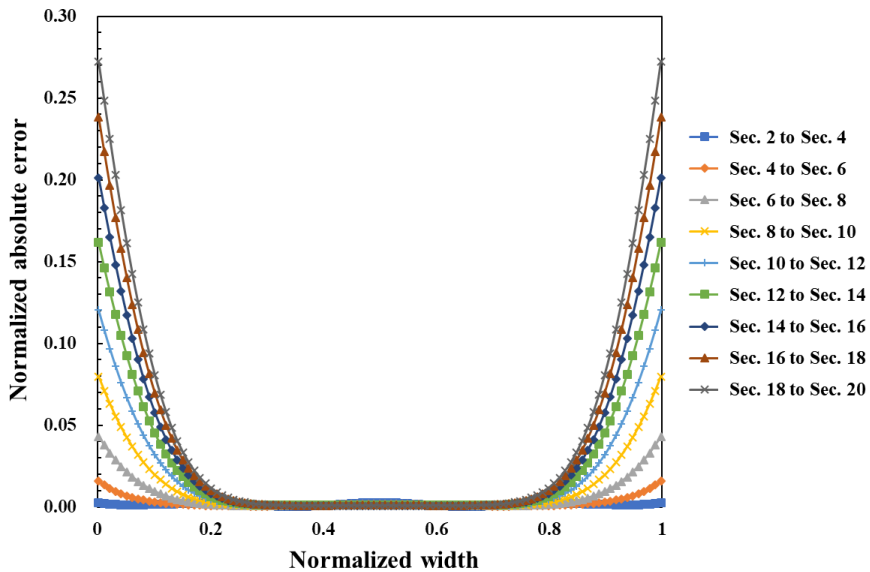

Figure 4.10 Normalized absolute error of cumulative concentration by 2D STRP (P9000-B10)

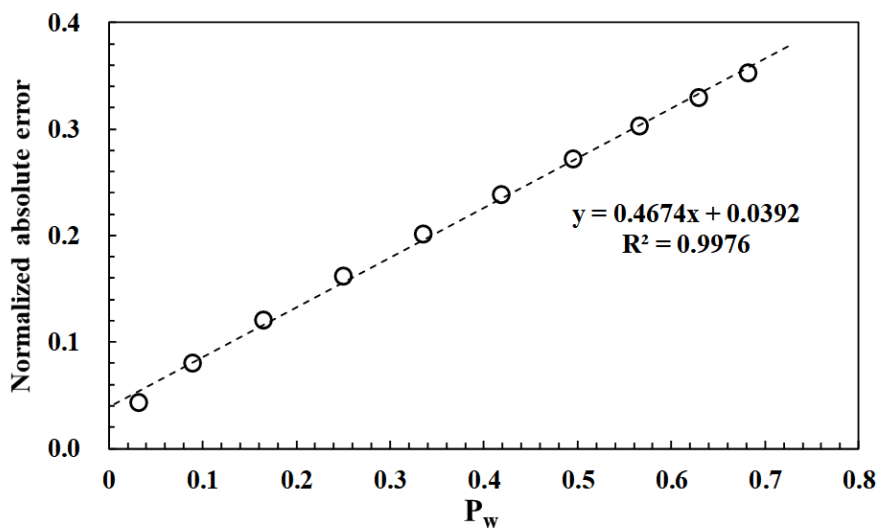

Figure 4.11 Relationship between the P_w and the normalized absolute error of cumulative concentration by 2D STRP at the wall boundary (P9000-B10)

4.3 Evaluation of 2D STRP in the condition of spatially varied flows

In this test, the results of 2D STRP were evaluated in the condition of the spatially varied flows. To minimize the discrepancy error induced by the FCA, the Peclet number was chosen as the value of 9,000, which is the highest values among the evaluation cases in this study. To generate the synthetic concentration data, the numerical model, which was described in Chapter 3, was used. The computational domain was chosen as the size of 501×501, based on the grid convergence tests. The spatially varied velocity profiles were generated shown in Fig. 4.1 using Eq. (4.2).

2D STRP is a semi-analytical solution for the simplified 2D ADE in stream-tube coordinates. In the derivation of 2D STRP, the hydraulic parameters in the dispersion terms are replaced by the reach-averaged values. By this treatment, the transverse dispersion coefficients are incorporated into the bulk dispersion coefficients (B_C), as shown in Eq. (2.28).

$$B_C = \frac{\Psi H^2 U}{Q^2} D_T \tag{2.28}$$

where U and H is the cross-sectional averaged velocity and water depth; Ψ is the dimensionless shape factor calculated as Eq. (4.6).

$$\Psi = \frac{1}{W}\int_{n=0}^{W}\left(\frac{h}{H}\right)^2\left(\frac{u}{U}\right)dn \tag{4.6}$$

where u and h are the depth-averaged velocity and local water depth; U and H are the cross-sectional averaged velocity and water depth, respectively.

Fig. 4.12 shows the tracer velocities (U_{tc}), which were calculated by the arrival time to the centroid of mass at each measuring section. For all cases, the tracer cloud, which was injected at the centerline, was initially advected by the maximum velocity and then is gradually approached to the cross-sectional mean velocity of flow (U_f). The mean velocity of the tracer cloud was varied over time, so the bulk dispersion coefficients (B_C) were calculated using the mean values for each section.

The longitudinal velocities for each stream-tube are required in 2D STRP in order to advect the mass of tracer clouds measured at the upstream section to the downstream direction. In the condition of the spatially varied flow, the rate of advection for each stream-tube could be transversely varied. In 2D STRP, the velocity of the traveled tracer cloud for each steam-tube is estimated by following.

$$U_{st} = \frac{X_{dw} - X_{up}}{\bar{t}_{dw} - \bar{t}_{up}} \tag{4.7}$$

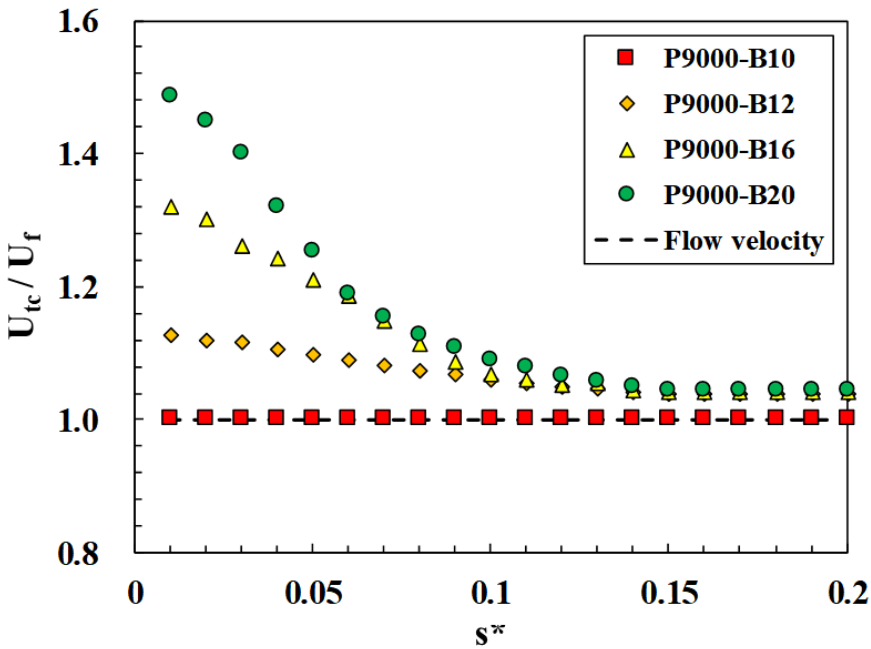

Figure 4.12 Comparison between the cross-sectional averaged flow velocity and tracer velocity

where X_{up} and X_{dw} are the longitudinal distance at upstream and downstream section; $\overline{t}_{up}$ and $\overline{t}_{dw}$ are the mean time of passage in the upstream and downstream section. The mean time of passage for both sections is statistically identical to the first moment of temporal distribution. Note that the mean time of passage was individually calculated on each steam-tube. in order to investigate whether 2D STRP well predicts the concentration distribution in the condition of the spatially varied flows, the results of 2D STRP, which use the cross-sectional mean velocity, were also applied for the comparison.

Fig. 4.13 shows the temporal distribution of the predicted results by 2D STRP. In this figure, the results of 2D STRP using the spatially different velocities for each stream-tube are represented as the black dashed lines, and the black dashed lines for results by using the cross-sectional mean velocity of flow for white dashed lines. These figures represent the concentration distribution bifurcated near to the side banks. The V-shaped tails were more elongated as transported more to downstream sections. This tendency strengthened with an increase in the ratio of the maximum velocity to the mean velocity, that is, the deviation of velocity profiles for each case. In the case of the results by 2D STRP using the constant longitudinal velocity, the V-shaped tails were not strengthened due to the absence of the effect of horizontal shear flow. Moreover, the arrival time to peak value was delayed, while the values near the boundaries were early reached to the downstream sections.

Fig. 4.14 shows that the results, which used the longitudinal velocities individually determined for each stream-tube, well agreed with the temporal

a) Input C-t-q distribution (Routing from s*=0.04 to s*=0.05)

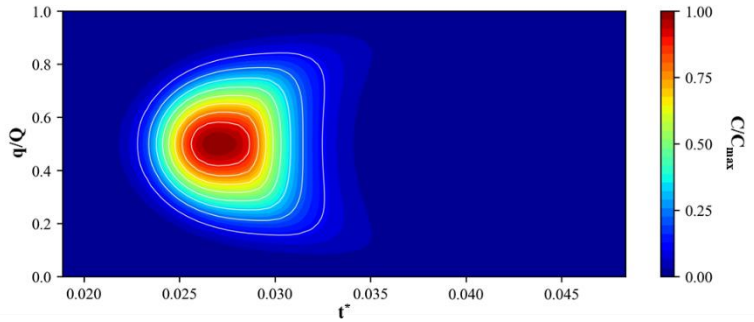

b) Predicted C-t-q distribution (Routing from s*=0.04 to s*=0.05)

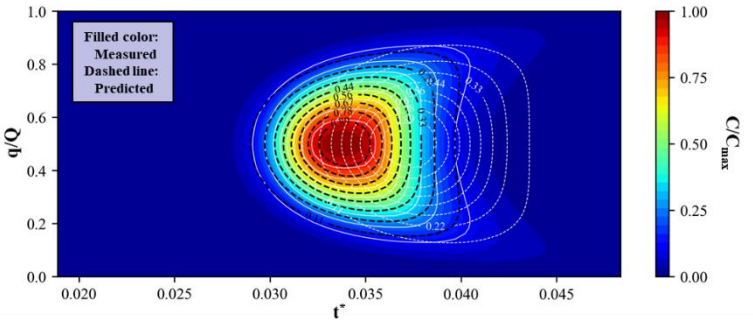

c) Input C-t-q distribution (Routing from s*=0.06 to s*=0.07)

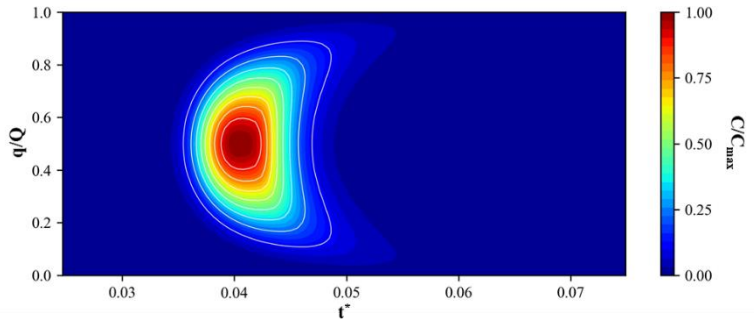

d) Predicted C-t-q distribution (Routing from s*=0.06 to s*=0.07)

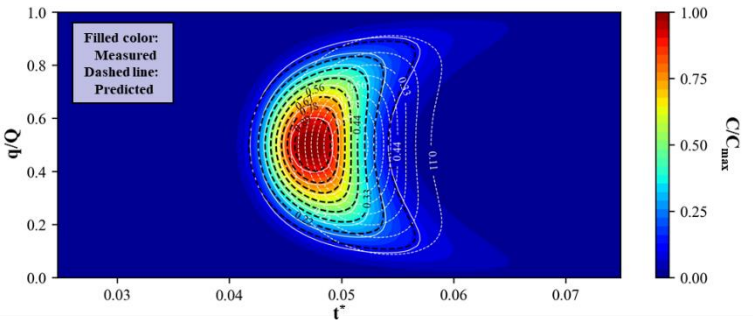

e) Input C-t-q distribution (Routing from s*=0.08 to s*=0.09)

f) Predicted C-t-q distribution (Routing from s*=0.08 to s*=0.09)

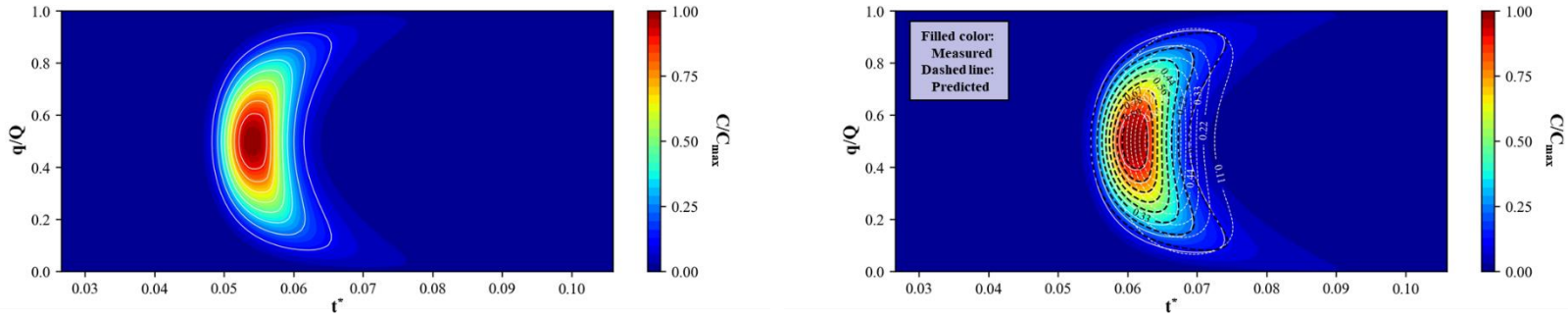

g) Input C-t-q distribution (Routing from s*=0.10 to s*=0.11)

h) Predicted C-t-q distribution (Routing from s*=0.10 to s*=0.11)

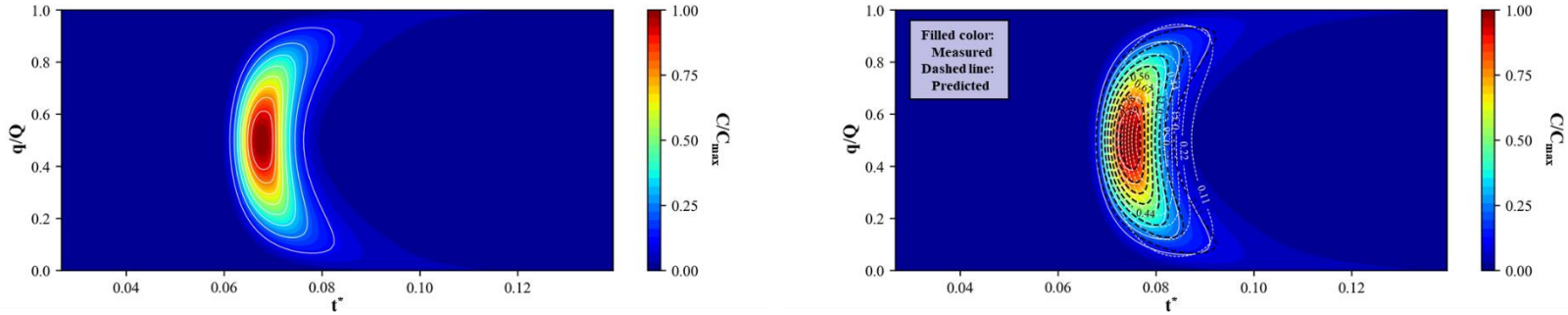

Figure 4.13 Predicted concentration distribution by 2D STRP for P9000-B20

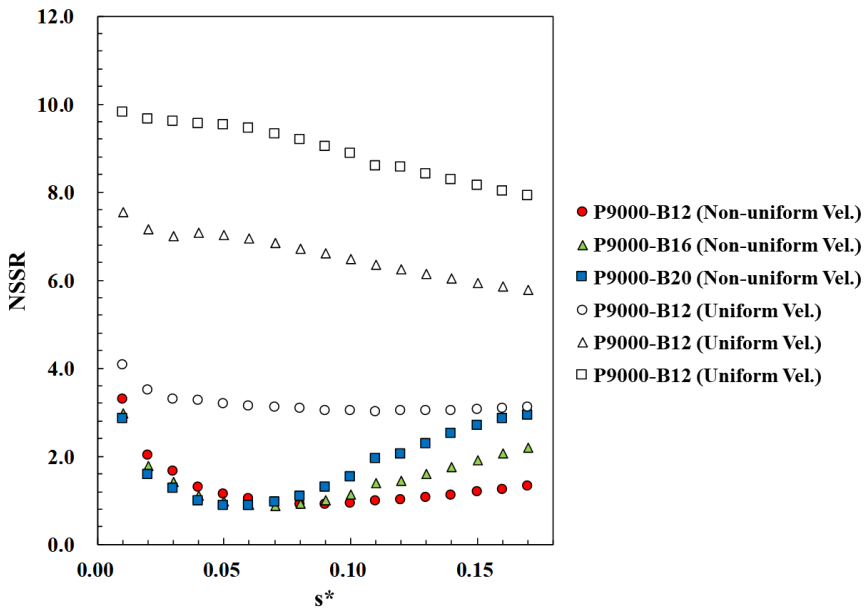

Figure 4.14 The Normalized sum of squared residuals of concentration distribution calculated by 2D STRP in spatially varied flows

distribution in downstream sections, but the values of NSSR increased after the tracer clouds reached the wall boundaries. However, the results by using the uniform velocity show significant differences in all cases.

As a result of this test, the 2D STRP well predict the concentration distributions even in the spatially varied flows, but the effect of the wall was also found, as shown in the condition of uniform flows. the results of evaluations of 2D STRP in both the uniform flow and the spatially varied flows can be summarized as:

1) The results of 2D STRP were affected by the Peclet number due to FCA. FCA can estimate the spatial distribution with the value of MAE less than 20% when the Peclet number is higher than 2,250 in the uniform flow.

2) The 2D STRP cannot predict accurate concentration distribution if the pollutant clouds reach the river embankments. The 2D STRP does not consider the wall boundary conditions.

3) The 2D STRP can reproduce the skewed concentration distribution induced by the horizontal shear flows as considering individual advection for each stream-tube.

In this study, the 2D STRP was evaluated in the ideal conditions, which is generated by the analytical solution and numerical model. The results showed that the 2D STRP could be applied in the sufficiently high values of Peclet number, approximately 2,250. The pollutant mixing is generally dominated by river flows, so

the Peclet number is sufficient for the application of frozen cloud assumptions high in the usual river environments. However, the limitations of 2D STRP related to the wall reflection can be problematic for the calculation of the accurate dispersion coefficients.

5. Development of the improved 2D STRP

5.1 Development of the improved 2D STRP

In order to overcome the limitations of existing 2D STRP, the improved stream-tube routing procedure (2D STRP-*i*) was developed in this study. The derivation of 2D STRP-*i* started from the continuity equation and the mass transport equation in the orthogonal curvilinear coordinate system (Yotsukura and Sayre, 1976; Shen, 1978). By assuming that the flow condition is steady-state, the Eq. (2.13) and Eq. (2.14) can be reduced as follows.

$$\frac{\partial}{\partial s}\left(m_n h U\right)+\frac{\partial}{\partial n}\left(m_s h V\right)=0 \tag{5.1}$$

$$\begin{aligned} &m_s m_n h\frac{\partial C}{\partial t}+m_n h U\frac{\partial C}{\partial s}+m_s h V\frac{\partial C}{\partial n} \\ &=\frac{\partial}{\partial s}\left(\frac{m_n}{m_s}hD_L\frac{\partial C}{\partial s}\right)+\frac{\partial}{\partial n}\left(\frac{m_s}{m_n}hD_T\frac{\partial C}{\partial n}\right) \end{aligned} \tag{5.2}$$

The orthogonal curvilinear coordinates system expressed in Fig. 2.3, was transformed into the stream-tube coordinates system by introducing the cumulative discharge shown as following.

$$q_c = \int_{n_L}^{n} m_n h U_s dn \tag{5.3}$$

where n_L is the location of the left bank in the transverse direction.

The integration of Eq. (5.1) with respect to the lateral direction (*n*-direction) from the left bank (n_L) and substituting this into Eq. (5.3) yields followings.

$$m_s h V = -\frac{\partial}{\partial s}\int_{n_L}^{n} \left(m_n h U\right) dn = -\frac{\partial q}{\partial s} \tag{5.4}$$

Then, substituting Eq. (5.4) into the Eq. (5.2), and rearranging Eq. (5.2) with chain rules yields followings (Shen, 1978; Harden and Shen, 1979).

$$\frac{\partial C}{\partial t} + \frac{U}{m_s}\frac{\partial C}{\partial s} = \frac{1}{m_s m_n h}\frac{\partial}{\partial s}\left(\frac{m_n}{m_s} h D_L \frac{\partial C}{\partial s}\right) + \frac{U}{m_s}\frac{\partial}{\partial q}\left(m_s h^2 U D_T \frac{\partial C}{\partial q}\right) \tag{5.5}$$

Although the quantity in the dispersion terms varies with the lateral direction, previous studies (Yotsukura and Cobb, 1972; Sayre, 1979; Lau and Krishnappan, 1981; Holly, 1985; Baek and Seo, 2010) mentioned that the solution of Eq. (5.5) is

insensitive to such variation, so this quantity assumed as the averaged values. Thus, Eq. (5.5) can be reduced as:

$$\frac{\partial C}{\partial t} + U_{ST}\frac{\partial C}{\partial s} = S_L\left(\frac{\partial^2 C}{\partial s^2}\right) + S_T\frac{\partial^2 C}{\partial q^2} \tag{5.6}$$

where,

$$U_{ST} = \frac{U_s}{m_s} \tag{5.7}$$

$$S_L = \frac{1}{Q}\int_0^Q \frac{D_L}{m_s^{\,2}}dq = \left(\overline{\frac{D_L}{m_s^{\,2}}}\right) \tag{5.8}$$

$$S_T = \frac{U}{m_s}\cdot\frac{1}{Q}\int_0^Q m_s h^2 U D_T dq = \overline{U}^2\,\overline{h}^2\,\overline{D_T} \tag{5.9}$$

The Eq. (5.6) represents the 2D ADE in the steam-tube coordinates. The U_{ST} indicates the scaled longitudinal velocity for each stream-tube, and both S_L and S_T are the factor of dispersion longitudinally and transversely. The overbar means the cross-sectional averaged values. The averaged dispersion coefficients can be inversely computed as:

$$\overline{D_L} = S_L \overline{m_s^2} \tag{5.10}$$

$$\overline{D_T} = \frac{S_T}{\overline{U^2}\,\overline{h^2}} \tag{5.11}$$

The mathematical form of Eq. (5.6) is identical to that of 2D ADE in the cartesian coordinates for the straight channel. Thus, Eq. (5.6) can be solved analytically using the well-known analytical solution expressed as follows.

$$C(s,q,t) = \frac{M/h}{4\pi t\sqrt{S_L S_T}} \exp\left(-\frac{(s - s_0 - U_{ST}t)^2}{4S_L t}\right) \cdot \sum_{m=-\infty}^{\infty}\left[\exp\left(-\frac{(q - 2mQ - q_0)^2}{4S_T t}\right) + \exp\left(-\frac{(q - 2mQ + q_0)^2}{4S_T t}\right)\right] \tag{5.12}$$

where s_0 and q_0 are injection points in s- and q-coordinates. The transverse dispersion term is expressed as the summation of solutions for the imagery sources, which is released outside the boundaries to accommodate the zero-gradient concentration condition at the side bank. The Eq. (5.12) can predict the concentration distribution, $C(s, q)$, at a specific time when the pollutant mass, M, is instantaneously released at a specific point (s, q).

When the pollutant mass is given as the arbitrary distribution, $f(s, q)$, at the initial time ($t = t_1$) as illustrated in Fig. 4.19, the initial mass distribution can be approximated as a series of separated individual slug (Baek and Seo, 2010). The solution to the given arbitrary mass distribution can be obtained by the superposition of solutions that are independently predicted for individual mass release using the Eq. (5.12) as long as Eq. (5.6) is linear (Fischer et al., 1979; Rutherford, 1994). The solution to the individual mass located at a specific point (ξ, ω) can be written as follows:

$$C(s,q,t_2) = \frac{C(\xi,\omega,t_1)\Delta\xi\Delta\omega}{4\pi t\sqrt{S_L S_T}} \exp\left(-\frac{\left(s-\xi-U_{ST}(t_2-t_1)\right)^2}{4S_L(t_2-t_1)}\right) \cdot \sum_{m=-\infty}^{\infty}\left[\exp\left(-\frac{(q-2mQ-\omega)^2}{4S_T(t_2-t_1)}\right)+\exp\left(-\frac{(q-2mQ+\omega)^2}{4S_T(t_2-t_1)}\right)\right] \tag{5.13}$$

where the concentration at a point (ξ, ω) can be calculated as:

$$C(\xi,\omega) = \frac{f(\xi,\omega)}{h\Delta\xi\Delta\omega} \tag{5.14}$$

The solution superposed over the whole independently predicted distribution for the

individual slug could be written as:

$$C(s,q,t_2)=\sum_{\omega}\sum_{\xi}\frac{C(\xi,\omega,t_1)\Delta\xi\Delta\omega}{4\pi t\sqrt{S_L S_T}}\exp\left(-\frac{\left(s-\xi-U_{ST}(t_2-t_1)\right)^2}{4S_L t}\right)\cdot \sum_{m=-\infty}^{m=\infty}\left[\exp\left(-\frac{(q-2mQ-\omega)^2}{4S_T(t_2-t_1)}\right)+\exp\left(-\frac{(q-2mQ+\omega)^2}{4S_T(t_2-t_1)}\right)\right] \tag{5.15}$$

If both $\Delta\xi$ and $\Delta\omega$ are infinitely small, the Eq. (5.15) can also be expressed as:

$$C(s,q,t_2)=\int_{\omega=0}^{Q}\int_{\xi=-\infty}^{\infty}\frac{C(\xi,\omega,t_1)}{4\pi t\sqrt{S_L S_T}}\exp\left(-\frac{\left(s-\xi-U_{ST}(t_2-t_1)\right)^2}{4S_L t}\right)\cdot \sum_{m=-\infty}^{\infty}\left[\exp\left(-\frac{(q-2mQ-\omega)^2}{4S_T(t_2-t_1)}\right)+\exp\left(-\frac{(q-2mQ+\omega)^2}{4S_T(t_2-t_1)}\right)\right]d\xi d\omega \tag{5.16}$$

The Eq. (5.16) can predict the spatial concentration distribution at a time t_2 using the initial mass distribution at the time t_1. However, measuring the spatial concentration distribution for the whole range of the study domain is usually limited. Therefore, the FCA is required in order to estimate the spatial distribution from

temporal distribution at the fixed measuring locations, as in the derivation of 1D RP and 2D STRP. The spatial concentration distribution for both dependent and independent variables and the spatial coordinates can be transformed into the temporal distribution and temporal coordinates using equations from Eq. (5.17) to Eq. (5.20).

$$C\left(s,q,t_2\right)=C\left(X_2,q,t\right) \tag{5.17}$$

$$C\left(\xi,\omega,t_1\right)=C\left(X_1,\omega,\tau\right) \tag{5.18}$$

$$s=X_2+U_{ST}\left(\overline{t_2}-t\right) \tag{5.19}$$

$$\xi=X_1+U_{ST}\left(\overline{t_1}-\tau\right) \tag{5.20}$$

Applying the FCA into Eq. (5.16), the 2D STRP-*i* can be finally derived as follows.

$$C\left(X_2,q,t\right)=\int_{\omega=0}^{Q}\int_{\tau=-\infty}^{\infty}\frac{C\left(X_1,\omega,\tau\right)U_{ST}}{4\pi\left(\overline{t_2}-\overline{t_1}\right)\sqrt{S_L S_T}}\exp\left(\frac{\left[X_2-X_1-U_{ST}\left(t-\tau\right)\right]^2}{4D_L\left(\overline{t_2}-\overline{t_1}\right)}\right)$$
$$\cdot\sum_{m=-\infty}^{\infty}\left[\exp\left(\frac{-\left(q-2mQ-\omega\right)^2}{4S_T\left(\overline{t_2}-\overline{t_1}\right)}\right)+\exp\left(\frac{-\left(q-2mQ+\omega\right)^2}{4S_T\left(\overline{t_2}-\overline{t_1}\right)}\right)\right]d\tau d\omega$$

(5.21)

Both the existing 2D STRP and 2D-STRP-*i* are derived by applying the stream-tube concept. However, the derivation of the existing 2D STRP does not consider the metric coefficients (m_s and m_n). The governing equation of the existing 2D STRP is identical to the 2D ADE in the orthogonal curvilinear coordinate system with $m_s = m_n = 1$. Thus, the channel irregularity may not be appropriately reflected in the predictions. Besides, the analytical solution used in 2D STRP is derived in transversely unbounded channels, so the wall reflection of pollutant clouds cannot be considered.

The improved version of STRP in this study considered the metric coefficients. The consideration of metric coefficients can consider the horizontal channel irregularities, as well as the meandering channel. The analytical solution used in 2D STRP-*i* can predict the impinging of pollutant clouds to wall boundary using the method of image. And the advective transport was considered as the mean velocity of each stream-tube, as illustrated in Fig.5.1. Thus, the advection was considered as transversely varied effects.

a) Conceptual diagram for 2D STRP (existing)

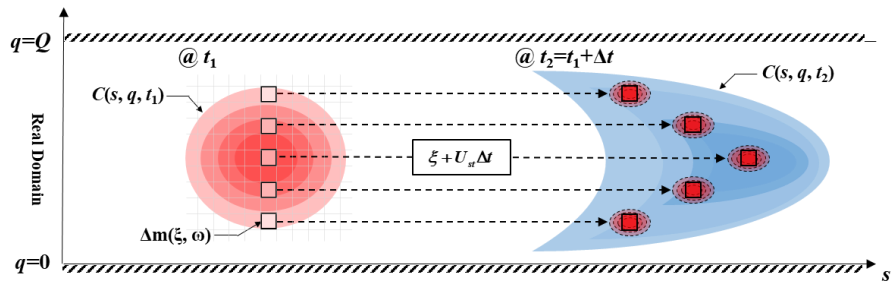

b) Conceptual diagram for 2D STRP-*i* (improved)

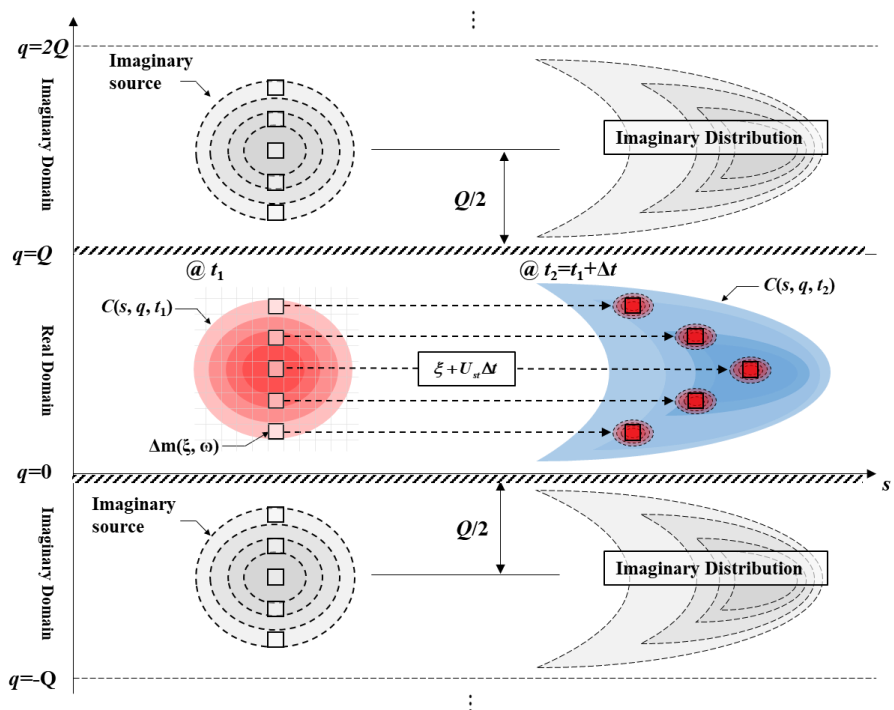

Figure 5.1 Conceptual diagrams for comparison between 2D STRP and 2D STRP-*i*

5.2 Evaluation of the improved 2D STRP

The performance of the 2D STRP-*i* was tested to verify its improvement according to the wall reflection. The evaluation cases were identical to the cases for evaluation of the 2D STRP were to compare both results. Fig. 5.2 shows the NSSR of the concentration distribution predicted by 2D STRP-*i* developed in this study. The values of NSSR for all cases gradually decreased but increased as Peclet number incensed. 2D STRP-*i* also applied the concept of FCA, so the results can be affected by Peclet number. As compared with Fig. 4.4, the results of existing 2D STRP were inaccurately predicted as the values of P_w increased. However, 2D STRP-*i* well predicted the concentration distribution even in the sections where the values of P_w approached the unity, which indicates the complete of transverse mixing. The improvement of 2D STRP on the wall reflection was well represented in Fig. 5.3. Fig. 5.3 shows the comparison of NSSR of the existing 2D STRP and 2D STRP-*i*. The results of 2D STRP-*i* were very close to the results of the existing 2D STRP on the value of P_w less than 0.01. That is, both results were approximately same before the tracer clouds reached wall boundaries. However, when the values of P_w exceeded 0.01, The 2D STRP-*i* reduced the values of NSSR by 10 % approximately. It means that 2D STRP-*i*, which can consider the effect of wall reflection, could provide more accurate solutions compared to the existing 2D STRP in the condition where the value of P_w is larger than 0.01.

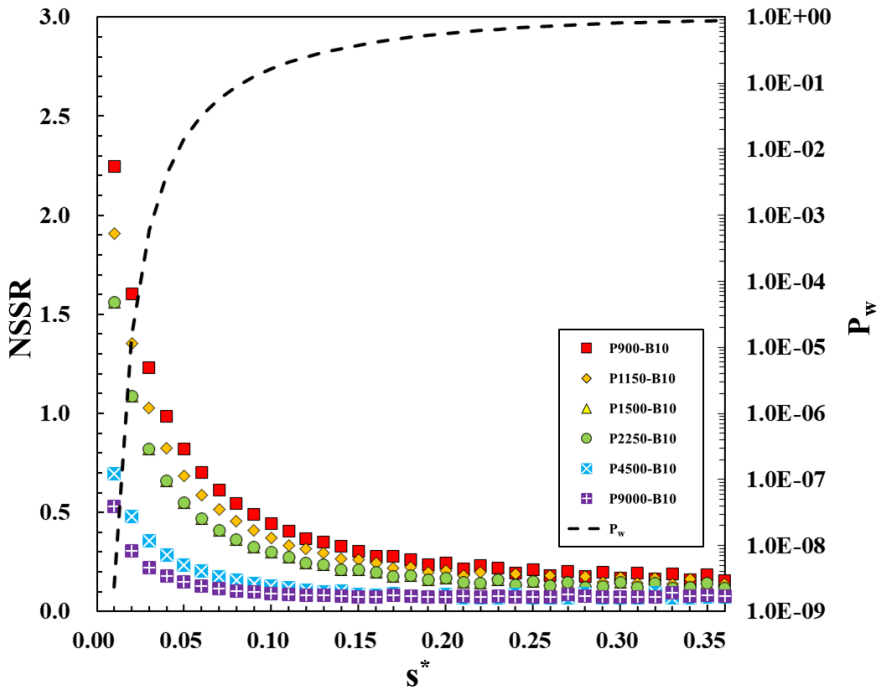

Figure 5.2 The normalized sum of squared residuals of concentration distribution calculated by 2D STRP-*i* in the uniform flow

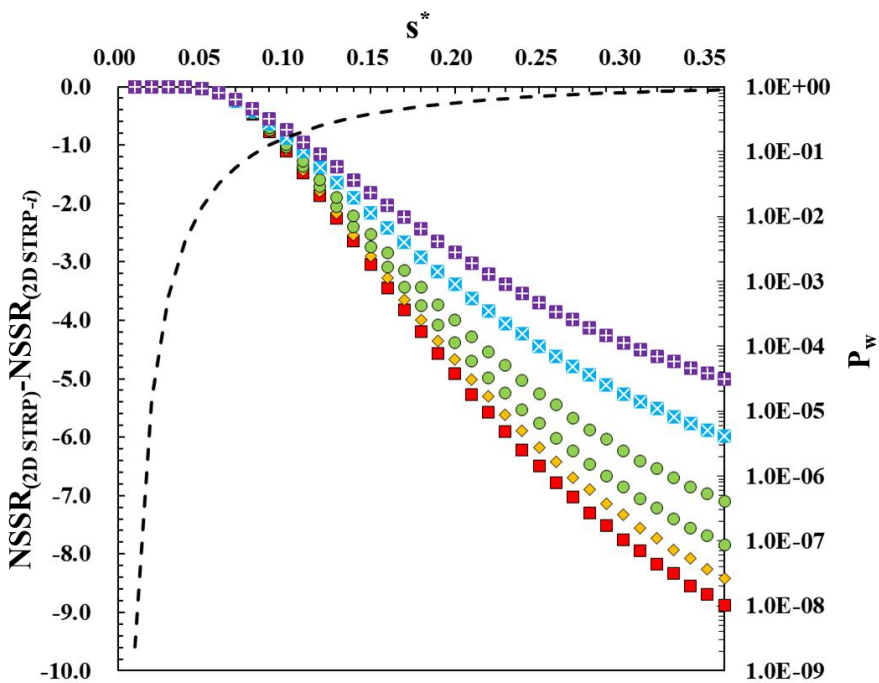

Figure 5.3 Comparison between the results of 2D STRP and 2D STRP-*i*

6. Development of remote sensing-based tracer tests

6.1 Outline of the experimental procedure

The conventional experimental methods for tracer tests, which are the *in-situ* based methods described in chapter 2.2.1, have been generally performed to obtain the temporal concentration data to analyze the pollutant mixing behaviors. When the dispersion coefficients are calculated based on the routing procedure using the tracer test data, the continuous transverse concentration profiles at each time are required. However, the conventional tracer tests provide the concentration data at limited fixed points over the cross-sections. Due to this limitation, previous studies (Baek et al., 2006; Baek and Seo, 2010; Seo et al., 2016; Shin et al., 2019) have interpolated the discrete concentration-time curves measured at each point to obtain the continuous concentration profiles. Also, the extrapolation is needed to estimate the values of concentration near the side walls. This remedy could cause the artificial dispersion to the concentration curves if the gradients of concentration curves are not proper in the interpolated curves.

In order to overcome the limitations of the conventional tracer tests, the remote sensing-based experimental techniques, which can observe the spatio-temporal concentration distributions, were developed using the RGB digital camera mounted on the UAV (also called a *drone*). The potential utilities of RGB images for the spatial measurement of the fluorescent dye were investigated. The experimental procedures proposed in this study are classified into four steps: 1) the tracer tests based on the

in-situ measurements, 2) the aerial image acquisitions using UAV, 3) the pre-processing for assigning coordinate system and 4) the conversion of RGB images to concentration by the ANN model. The experimental procedures in step 1) is identical to the conventional in-situ measurement-based tracer tests described in Chapter 2.2.1. The acquisitions of both the *in-situ* measured concentration and RGB images in step 1) and step 2) are simultaneously performed during the tracer tests. The acquired images in step 2), then, are preprocessed to assign the coordinate system based on projective transformation in step 3). The conversion of RGB images to concentrations is finally performed using the ANN model to obtain the spatio-temporal tracer concentrations in step 4). The experimental procedures are depicted as the flow chart in Fig. 6.1.

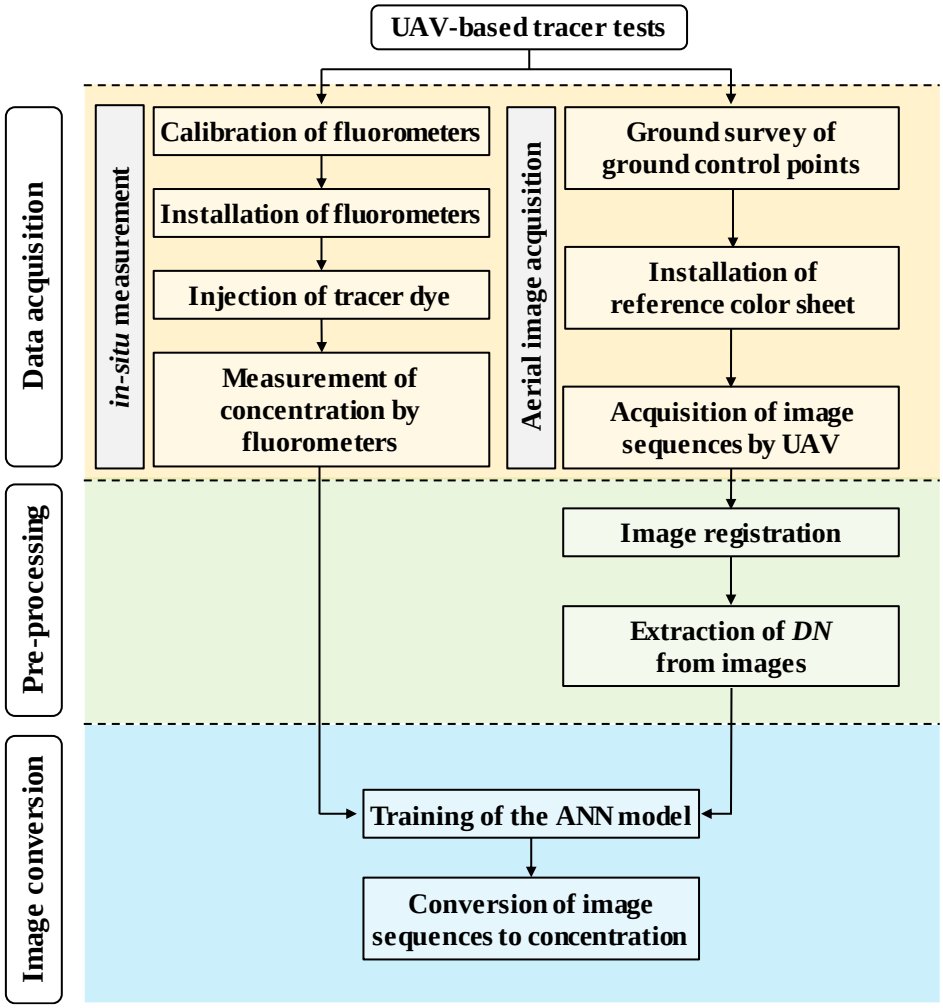

Figure 6.1 The flow chart for UAV-based tracer tests

6.2 Acquisition of aerial imagery

A commercial RGB-based digital camera mounted on a UAV used to obtain aerial images during tracer tests. The aerial images obtained in the video format. The video images are recorded in 24 or 30 frames per second (fps) with 4K pixel resolution. As depicted in Fig. 6.2, the UAV is remotely controlled, maintaining its altitude from the ground to acquire image data on the study area. The camera settings for exposure and white balance have to be manually set up, referring to the reference color to prevent the pixel values from automatically changing depending on ambient light intensity. To obtain the reference color, polytetrafluoroethylene (PTFE) sheets were installed in close proximity to the experimental channels. This PTFE sheet has been generally used to measure the reference values for solar radiance in the field because it offers nearly Lambertian reflection with high reflectance values of 95% over a broad spectral range from 350 to 2500 nm (Peddle et al., 2001). The Lambertian reflection means that the light intensity reflected from the surface is isotropic. These characteristics of the PTFE sheet are helpful to observe identical reference colors at any angle of view of the camera mounted on UAV. All *DN* values in the images are normalized by the *DN* values of the PTFE sheet.

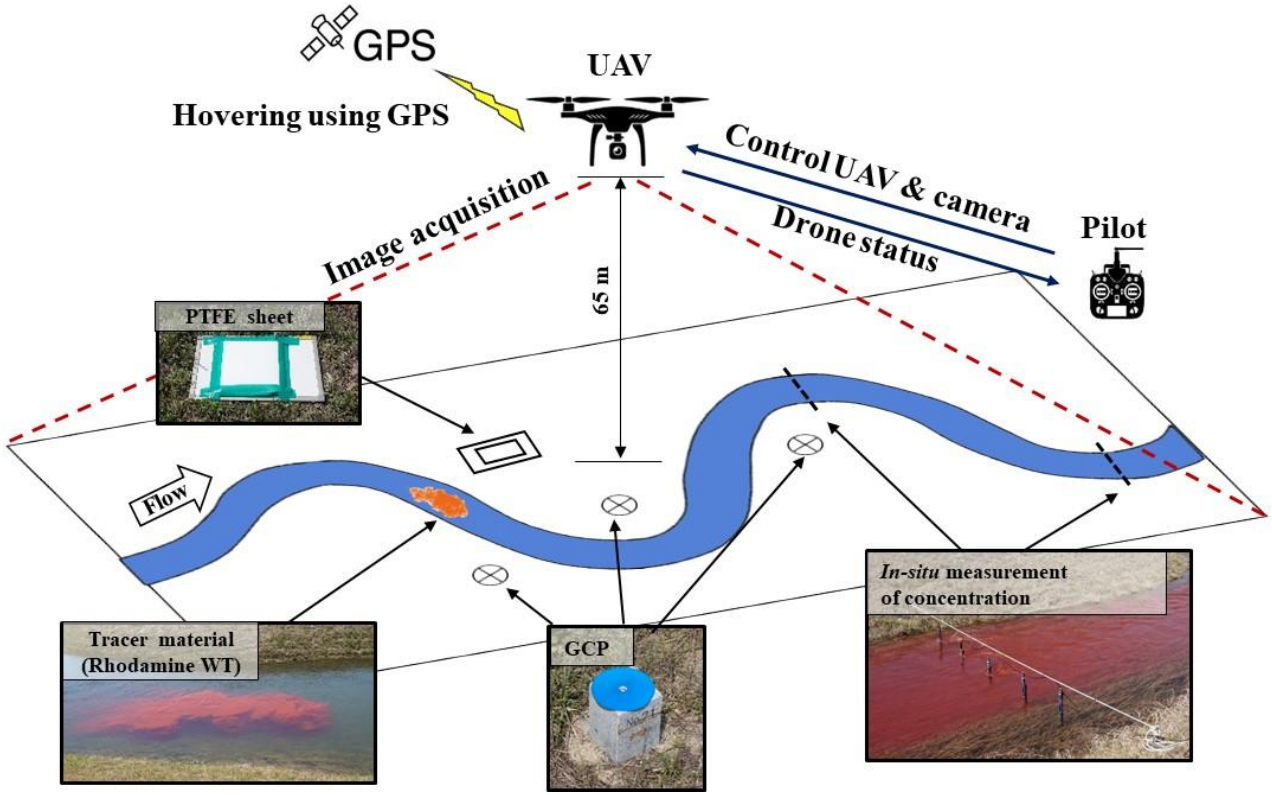

Figure 6.2 Schematics of image acquisition by UAV with a digital camera

6.3 Preprocessing of aerial imagery

In the image sequence, the image coordinates corresponding to the position of the experimental channel could be randomly displaced within the field-of-view (FOV) over time due to the mechanical vibration and the horizontal position error of UAV. Thus, the ground control points (GCP) should be installed near the channels, and their locations should be surveyed using RTK-GPS to convert the unstably changing image coordinates of the experimental channel to the fixed world coordinates in the UTM coordinate system. The procedures for conversion of image coordinates to UTM coordinate involves two steps: (1) tracking the image coordinates of GCPs, and (2) the conversion of the image coordinate to UTM coordinates for all pixels. In step (1), the image coordinates of GCPs that changed over time are tracked using the normalized cross-correlation method (NCC) described as:

$$NCC(i,j)=\frac{\sum_{X,Y}\left[I(X,Y)-\bar{I}_{i,j}\right]\left[I_{tmp}(X-i,Y-j)-\bar{I}_{tmp}\right]}{\sqrt{\sum_{X,Y}\left[I(X,Y)-\bar{I}_{i,j}\right]^2\sum_{X,Y}\left[I_{tmp}(X-i,Y-j)-\bar{I}_{tmp}\right]^2}} \tag{6.1}$$

where I is the full image; $\bar{I}_{i,j}$ is the mean of I in the region under the template image; I_{tmp} is the template image; $\bar{I}_{tmp}$ is the mean of I_{tmp}; X and Y are the image coordinates in the full image; i and j are the image coordinates in the template image.

The template images (15 by 15-pixel windows centered on each GCP) are extracted from an image of the first frame. The image coordinates of all GCPs in all frames are then automatically found by selecting the image coordinates that showed the peak cross-correlation between the template images and the full image at each time. In step (2), using the pairs of coordinates for the GCPs, the image coordinates for all pixels can be converted to the UTM coordinates system by the projective transformation following Fujita et al. (1998).

$$x = \frac{p_1 X + p_2 Y + p_3}{p_4 X + p_5 Y + 1} \tag{6.2a}$$

$$y = \frac{p_6 X + p_7 Y + p_8}{p_4 X + p_5 Y + 1} \tag{6.2b}$$

where x and y are the world coordinates in the UTM system; and p_i is the transformation coefficient. The transformation coefficients can be obtained by solving the matrix system using the known four pairs of coordinates (Fujita et al., 1998). In this step, the spatial resolution of the converted images can be reduced for computational efforts.

6.4 ANN model of retrieving concentration from image data

In several studies, Eq. (2.32) has been physically extended based on the radiative transfer model to extract the WQP, bathymetry, and type of substrates from spectral image data (Philpot, 1987; Estep, 1994; Mobley et al., 1994; Maritorena, 1994; Lee et al., 1998). However, in most previous studies, the empirical calibration approaches with *in-situ* measurements have generally been employed based on the regression analysis because it was challenging to estimate the parameters in the physical-based model due to optical complexity of the shallow waters (Ritchie et al., 1975; Rimmer et al., 1987; Lathrop and Lillesand, 1991; Harrington et al., 1992; Lathrop, 1992; Dierberg and Carriker, 1994; Fraser, 1998; Aguirre-Gomez, 2000). The relationship between images and the WQP of interest have been found by simple linear, multivariate linear, or nonlinear regression analysis (Liu, 2003). In the case of the nonlinear regression for retrieving the WQPs from images, the form of the regression equation should be known as prior knowledge. Recently, instead of nonlinear regression approaches, ANN techniques have been widely applied by many researchers to establish the empirical relationship between remotely sensed data and WQPs (Keiner and Yan, 1998; Zhang et al., 2002; Chen et al., 2015; Nazeer et al., 2017). These studies reported that the ANN models were more accurate than nonlinear regression models when the relationship between remotely sensed data and WQP was highly nonlinear.

In this study, the ANN approach will be applied to construct the empirical relationship between the *DN* values in the RGB images and the concentration of the

fluorescent dye. The trainable parameters in the model are updated with optimal values to minimize the error between the *in-situ* measured values and the predicted values. In this study, the ANN model will be implemented using *Tensorflow* r1.0, which is an open-source library developed by *Google* for implementing machine learning applications based on the C++ and Python programming language. The architecture of ANN models consisted of an input layer, a single hidden layer with the activation function, and an output layer.

In the architecture of ANN models, the number of nodes in the input layer is determined by the number of the available independent variable which can express the target values. The *DN* values of each band were used as the input values, x_i, in the input layer to construct the ANN models, which can estimate the concentration of tracers using the *DN* values of RGB images. The x_i in the input layer is transferred to the output layer, passing through the hidden layer. The number of nodes in the hidden layer is the user-defined values and should be carefully determined depending on the complexity of the function to be estimated (Keiner and Yan, 1998).

The input values are multiplied by the weight factor which is defined at the connections between the input and hidden nodes, then summed, and is added to the value of bias as follows:

$$H_j = \sum_{i=1}^{n} W_{ij} x_i + b_j \tag{6.3}$$

where W_{ij} is the weight factors at each connection; b_j is the bias at each node in the hidden layer; and j is the node in the hidden layer. The optimal values of weight factors and bias for minimizing the error between the predicted and target values are initially unknown. In this study, to initiate the training of the ANN model, the initial values for weight factors are selected by Xavier initialization (Glorot and Bengio, 2010), in which the weight factors are randomly selected from the uniform distribution with the interval of $\pm 1/\sqrt{n_x}$, where n_x is the number of nodes in the previous layer. The initial value for b_j was set to 0.

The H_j values in the hidden layer are then transferred to the output layer, passing through the activation function, δ_j. The use of activation functions allows the ANN model to express the nonlinear relationship between input values and target values. Any nonlinear functions which are continuous and differentiable can be chosen for the activation function. In this study, the hyperbolic tangent function will be adopted as the activation function following previous studies (Keiner and Yan, 1998; Zhang et al., 2002; Chen et al., 2015; Nazeer et al., 2017).

$$\delta_j = \tanh(H_j) \tag{6.4}$$

The values from the activation function in the hidden layer are multiplied by the weight factors located between the hidden layer and the output layer. In this study, the output layer consisted of a single node, and it represents the concentration value predicted by the ANN model.

$$\hat{C} = \sum_{j=1}^{n} \delta_j W_{jk} + b_k \tag{6.5}$$

where $\hat{C}$ is the predicted concentration; W_{jk} is the weight factors between the hidden layer and the output layer, where k indicates the nodes in the output layer.

The predicted concentrations in the output layer were evaluated from the cost function in Eq. (6.5). In this study, the sum of the squared error is used as the cost function.

$$E = \frac{1}{2} \sum_{m=1}^{M} \left(\hat{C}_{(m)} - C_{o(m)} \right)^2 \tag{6.6}$$

where *M* is the number of the dataset and C_0 is the *in-situ* measured concentration considered as a target value.

In this study, to minimize the cost function, all trainable parameters in the neural network are iteratively updated using the *AdaGrad* algorithm (Duchi et al., 2011) given in Eq. (6.7). In this algorithm, the learning rate, η, is adaptively modified at each iteration so that the cost function is quickly and stably converged to the minimum value.

$$W_{new} = W_{old} - \frac{\eta}{\sqrt{A}} \frac{\partial E}{\partial W_{old}} \tag{6.7a}$$

where

$$A_{new} = A_{old} + \left(\frac{\partial E}{\partial W_{old}} \right)^2 \tag{6.7b}$$

To update the trainable parameters, the gradients of the error with respect to the parameters in Eq. (6.7a) and Eq. (6.7b) need to be obtained. *Tensorflow* automatically draws the calculation graph for each operation step, then finds the gradient values at each training step using the backpropagation algorithm based on the chain rule. The detailed procedures of the backpropagation algorithm are well described by Rumelhart et al. (1986).

6.5 Application of remote sensing-based tracer test in REC channels

6.5.1 Tracer tests based on in-situ measurements in REC

Tracer tests were carried out at the River Experimental Center (REC) of the Korea Institute of Civil Engineering and Building Technology (KICT) in South Korea to collect concentration data and aerial RGB images. The experimental channel, called A3 channel, is an alternately curved channel that was constructed to model the meandering channel in the natural river system. The three channels with different sinuosities were connected, as shown in Fig. 6.3a. The channel discharge can be maintained up to 8 m^3/s by operating two pumps. The bed material mainly consisted of sand and various types of vegetation.

The hydraulic and concentration data were measured during tracer tests. For measuring the discharge, velocity profiles, and water depth, an Acoustic Doppler Current Profiler (ADCP), Sontek-RiverSureyor S5, was used in this study. The accuracy for the velocity profiles is $\pm 0.25\%$ of the measured velocity or ± 0.2 cm/s. Twenty percent of Rhodamine WT solution, a fluorescent dye, was used as a tracer material. Fluorometer probes, YSI-600OMS, was used to measure the temporal concentration of the tracer at fixed locations, as shown in Fig. 6.3b. The accuracy of the fluorometers were $\pm 5\%$ of the reading values or 1 ppb. The fluorometer probes were calibrated using the standard solutions of known concentrations in the range from 0 ppb to 200 ppb before installation.

In this study, the three cases of tracer tests were performed in three channels. The hydraulic data were measured at six cross-sections, and the fluorometers were installed at three cross-sections at each channel. In the cross-sections for the concentration measurements, the five fluorometers were transversely distributed with uniform spacing. The results of the measurements on each case are summarized in Table 6.1, and concentration distributions of five fluorometer probes at each section of Case EXP-A315 are shown in Fig. 6.4. Fig. 6.4 illustrates that the concentration distributions of the tracer cloud were transversely skewed due to the meandering effect. From these figures, one can also notice that the transverse mixing of the tracer cloud was gradually completed having the long tail, as shown in Fig. 6.4c.

a) Experimental channels

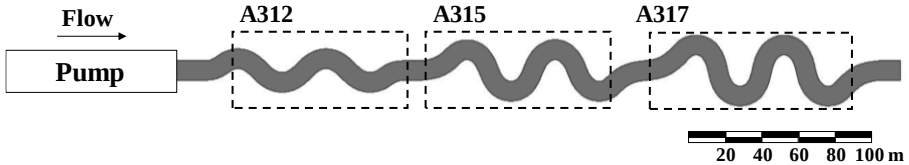

b) Details of measurement sections

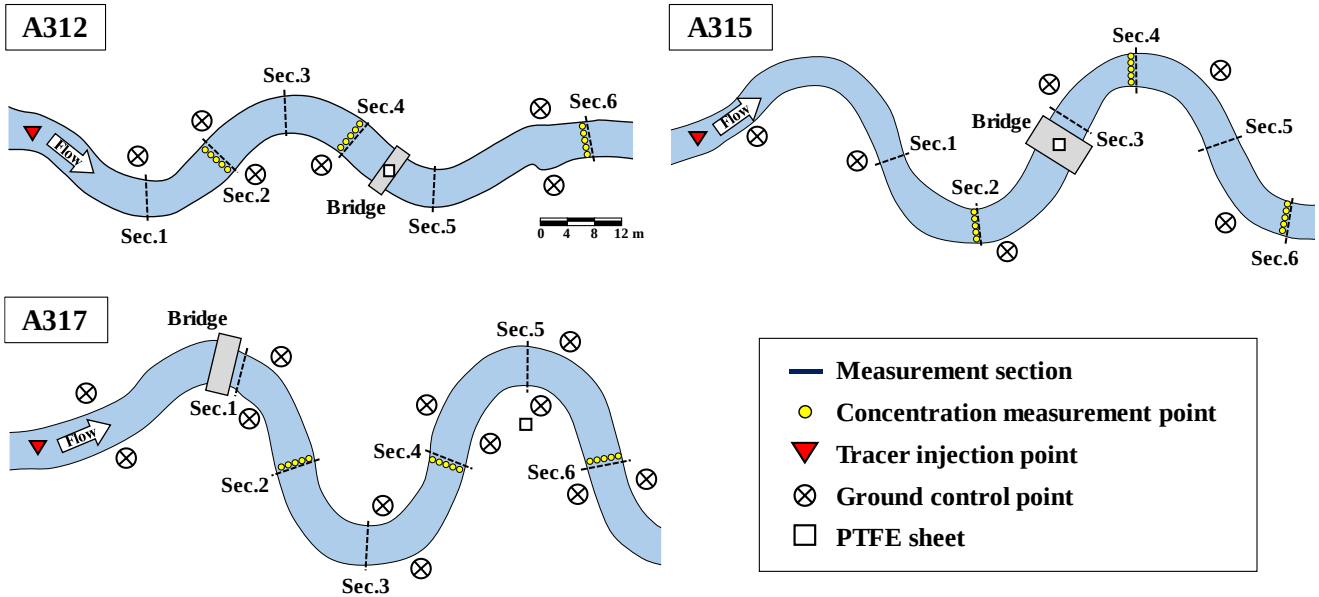

Figure 6.3 Experimental channels and measurement sections

Table 6.1 Results of hydraulic and concentration measurements

Case	Experiment Date (YY/MM/DD)	Channel sinuosity	Sections	Hydraulic data				Concentration data			
				Discharge (m^3/s)	Width (m)	Mean depth (m)	Mean velocity (m/s)	Tracer volume (ml)	Peak concentration (ppb)	Peak concentration arrival time (sec)	Time to centroid (sec)
Exp-A312	17/05/18	1.2	Sec.1	2.18	6.73	0.59	0.64	200	-	-	-
			Sec.2		6.15	0.51	0.76		115	41	48.4
			Sec.3		6.16	0.47	0.78		-	-	-
			Sec.4		6.38	0.51	0.72		72	68	84.3
			Sec.5		6.16	0.57	0.73		-	-	-
			Sec.6		5.74	0.63	0.68		44	125	150.8
			Average	-	6.22	0.55	0.72				
Exp-A315	16/04/26	1.5	Sec.1	1.06	5.46	0.48	0.60	150	-	-	-
			Sec.2		5.21	0.45	0.47		41	72	100.2
			Sec.3		4.94	0.38	0.64		-	-	-
			Sec.4		4.92	0.41	0.49		33	148	180.6
			Sec.5		4.99	0.52	0.40		-	-	-
			Sec.6		4.75	0.42	0.49		19	209	243.4
			Average	-	5.04	0.44	0.52				
Exp-A317	17/05/19	1.7	Sec.1	2.02	6.06	0.59	0.62	200	-	-	-
			Sec.2		6.34	0.59	0.63		75	70	86.2
			Sec.3		6.23	0.61	0.65		-	-	-
			Sec.4		6.34	0.65	0.61		48	132	144.3
			Sec.5		6.43	0.61	0.63		-	-	-
			Sec.6		6.32	0.62	0.65		27	203	228.8
			Average	-	6.29	0.61	0.63		-	-	-

a) Sec. 2

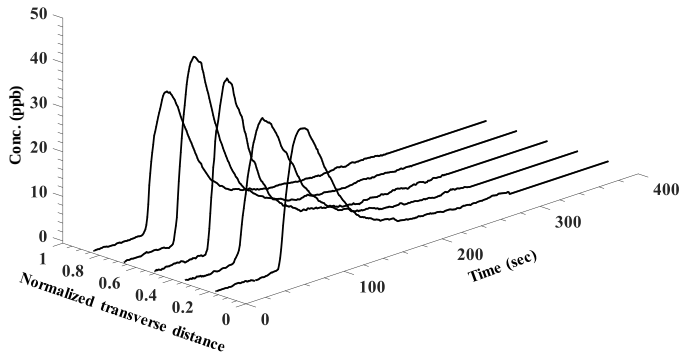

b) Sec. 4

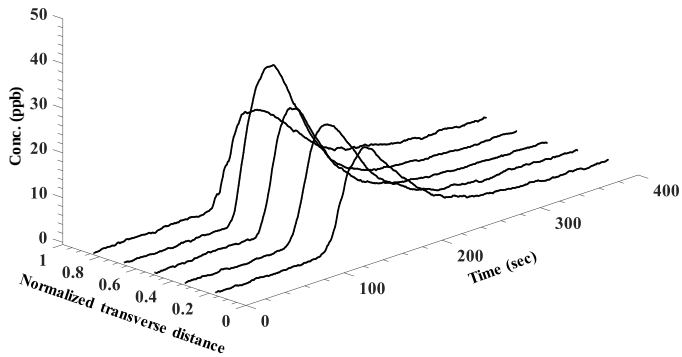

c) Sec. 6

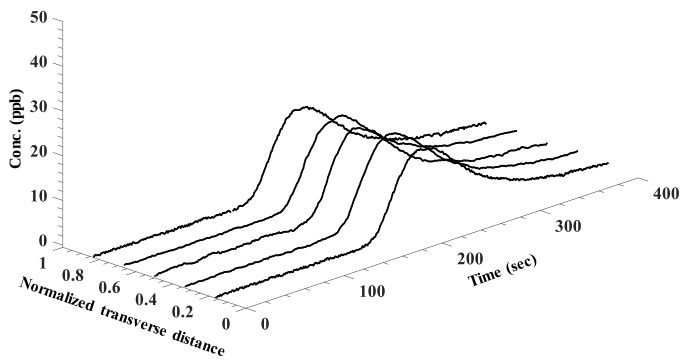

Figure 6.4 Concentration distribution at each section of EXP-A315

6.5.2 Acquisition of aerial imagery in REC

In this study, a commercial RGB-based digital camera mounted on a UAV was used to obtain aerial images during tracer tests. The aerial images were obtained in the MOV video format. The video images were recorded in 24 frames per second (fps) and 3840 × 2160 pixels in spatial resolution. The UAV was remotely controlled at 60 to 70 meters from the ground. To obtain the reference values for solar radiation, polytetrafluoroethylene (PTFE) sheets were installed close to the experimental channels. All *DN* values in the images were normalized by the *DN* values of the PTFE sheet. The acquisition of aerial digital images was summarized in Table 6.2.

For conversion of image coordinates into the UTM coordinate system, six points of the GCPs were surveyed in EXP-A312 and EXP-A315, and twelve points were surveyed in EXP-A317, as shown in Fig. 6.3b. The converted image was shown in Fig. 6.5 for EXP-A317. The mean absolute errors of the transformed coordinates of the GCPs were less than 10 cm in all cases. The processed images were averaged over 1 second, temporally, and 5 × 5 cm, spatially, to reduce the noise and computational efforts.

Table 6.2 Summary of aerial image acquisitions

Case	Image size (pixel)	ISO sensitivity	Shutter speed (sec)	Frame rate (fps)	Video duration (sec)	Number of frames	Pixel intensities on the PTFE (λ_R, λ_G, λ_B)
Exp-A312	3,840 × 2,160	100	1/2,500	24	560	13,440	111, 110, 106
Exp-A315					489	14,670	219, 213, 204
Exp-A317					987	23,688	204, 205, 213

a) Original image in image coordinate

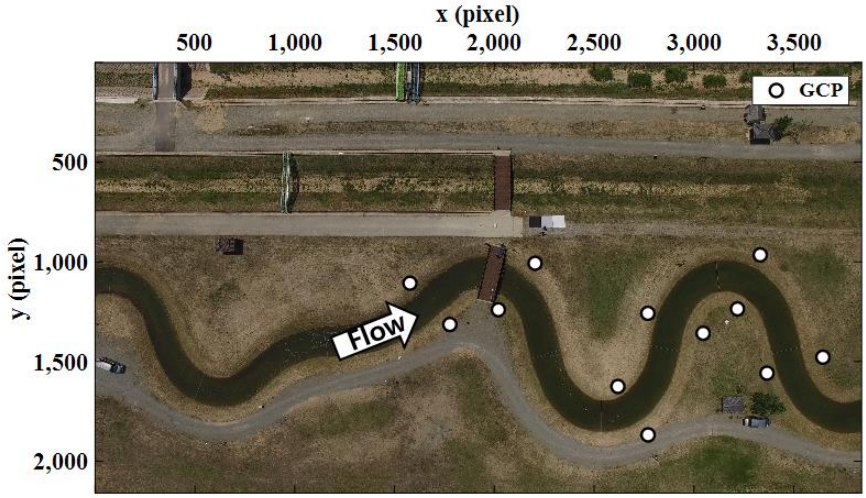

b) Converted image in UTM coordinate

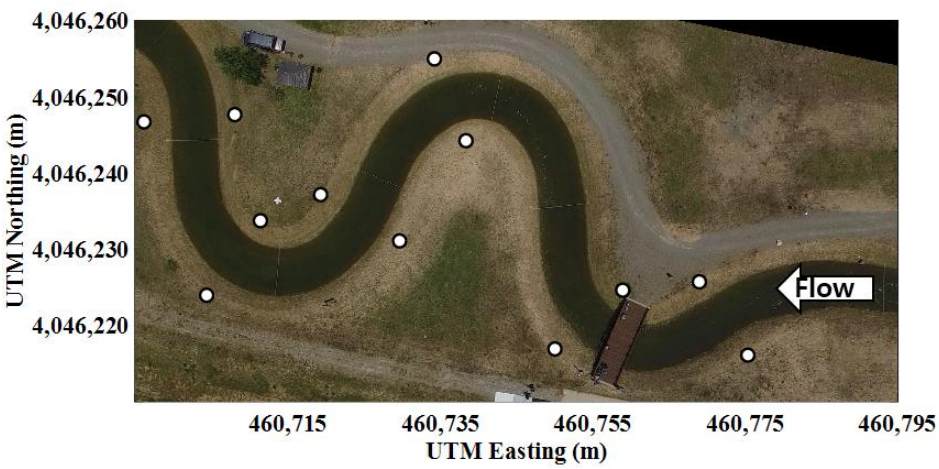

Figure 6.5 Conversion of coordinate system for EXP-A317

6.5.3 Retrieval of tracer cloud distribution from image data

6.5.3.1 Response of *DN* values to change of concentration

The *DN* values of the RGB bands were extracted over time from the pixels corresponding to the position of the fluorometer probe in *in-situ* measurements. Fig. 6.4 shows the comparison between the *DN* values in each band and the concentration of the center probes at the cross-section in EXP-A312. The *DN* values of each band tended to have a specific relation with the tracer concentration. The base of the *DN* values named DN_0 in this study and the rate of change of the *DN* values varied depending on the sensor locations.

DN_0 represented the upwelling radiance recorded in the images when the tracer material was absent in the water body. In the shallow water, the remotely sensed radiance has often been described as a function of the water depth, the IOPs, and the bottom reflectance (Lyzenga, 1981). The solar radiance transmitted through the water is exponentially attenuated based on the Lambert-Beer's law in which the decay of light is described as the function of path length, absorbance, and concentration of a medium. The amount of attenuation in the water column is determined by the water depth and the IOPs. IOPs such as absorption and scattering coefficients result from the individual contribution of the co-existing absorbing and scattering constituents (Pozdnyakov and Grassl, 2003). In this study, in the absence of tracer material, the IOPs could be assumed to be spatially homogeneous in all cases because the water in the experimental channels was supplied continuously

from the same water supply tank during the experiments. However, DN_0 values still varied spatially due to the variant water depth and type of bed materials. After introducing the tracer material, the IOPs would be changed with respect to the concentration of the tracer material. This caused the upwelling radiance, recorded as *DN* values, to be changed with respect to the concentration of the tracer material. The rate of change of *DN* was spatially heterogeneous due to the spatially variable water depth and bed material.

As shown in Fig. 6.6, the correlation analysis revealed that the *DN* values of the R-band, $DN(\lambda_R)$, were positively correlated to the concentration of Rhodamine WT, while *DN* of the G-band, $DN(\lambda_G)$, showed a negative correlation. The *DN* values of B-band, $DN(\lambda_B)$, also tended to decrease slightly with an increase in concentration but not responded to the change of concentration in some locations. These results could be related to the optical characteristics of tracer material. Rhodamine WT emits light of 582 nm wavelength when absorbing light of 558 nm wavelength (Wilson et al., 1986). Although the spectral response range on the R-, G- and B-band of the commercial digital camera used in this study was unknown, it could be inferred that the absorbance wavelength of Rhodamine WT of around 558 nm was included in the G-band, while the fluorescence wavelengths of around 582 nm were included in R-band.

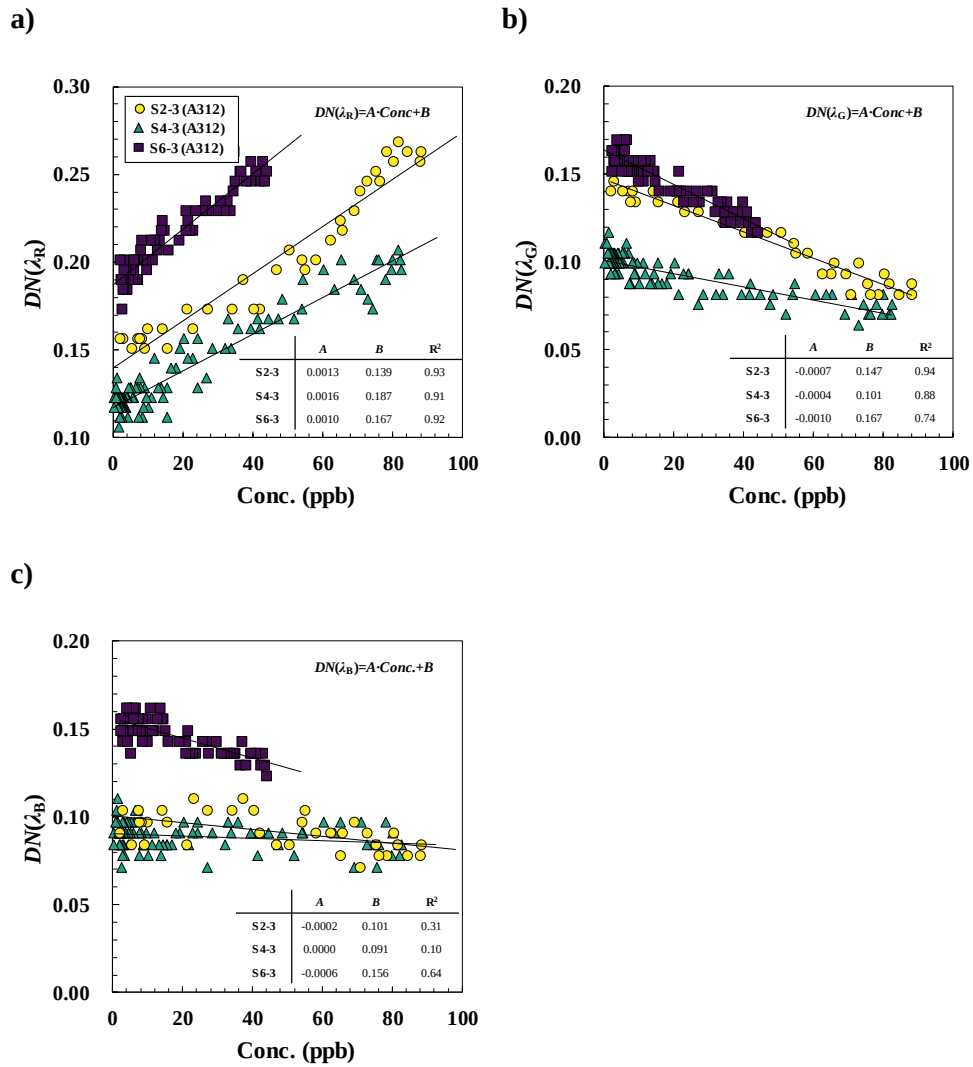

Figure 6.6 The response of DN values to the concentration of the center probe at each section (EXP-A312): a) DN values in R-band; b) DN values in G-band; c) DN values in B-band

6.5.3.2 Construction of neural network models

In this study, as aforementioned, an ANN model was used to construct the empirical relationship between the *DN* values of each band and the tracer concentration. The selection of input variables in the ANN model is difficult because prior knowledge of the relationship between the *DN* values and the tracer concentration was unknown. Therefore, the NN1 model was first constructed using the *DN* values of each band as the input variables, assuming that the *DN* values in each band were directly correlated to the tracer concentration. To compare the results of the NN1 models, a multivariate linear regression (ML) model was also constructed using the same input variables, as shown in Eq. (6.8).

$$\hat{C} = \alpha \cdot DN\left(\lambda_R\right) + \beta \cdot DN\left(\lambda_G\right) + \gamma \cdot DN\left(\lambda_B\right) \tag{6.8}$$

where $\hat{C}$ is the predicted concentration and α, β, and γ are the regression coefficients. The regression coefficients were found by minimizing the sum of the squares of the residuals between the estimated and measured concentrations. This was achieved using *scikit-learn*, which is the open-source library for data mining and data analysis in the Python language.

In addition to the NN1 model, to include the effect of spatially varied water depth and bed materials, the NN2 model was constructed using the DN_0 values in each

band as well as the DN values as the input variables. The ANN models could thus learn the heterogeneous properties according to the spatially varied DN_0. The DN_0 values were obtained by time-averaging the images for 30 seconds before the tracer material was injected to reduce the effect of the randomly fluctuating water surface. Both the ANN models and the ML model were individually trained for each experimental case, and the combinations of the input variables are shown in Table 6.3.

For training and testing the ANN models, the data sets were randomly split into the training data and the test data as 70% and 30% of the data set, respectively. The number of neurons in the hidden layer (H_n) was determined using the k-fold cross-validation, as shown in Fig. 6.7. The training data were randomly partitioned into five subsamples of equal size. Four of the subsamples were used for the training subset, and the remaining subsample was used for the validation subset. The sub-models, which were constructed with a specific H_n, were trained using the training subset and were evaluated using the mean square error (MSE) with the validation subset. The training of sub-models was performed following the procedures described in Section 5.4. The validation processes were repeated by replacing the validation subset with other subsamples so that all subsamples were used once as the validation data. The performance of H_n was assessed using the averaged MSE of the repeated validation results. From the results of the k-fold cross-validation in the range of H_n from 1 to 20, the best performances were shown when H_n was 7 for the NN1-series models and 15 for the NN2-series models, respectively.

The final models that showed the best performance were retrained using the total training data and were evaluated using the test data. To evaluate the model performance, several statistical indexes were calculated as given below:

$$R^2 = 1 - \frac{\sum_{i=1}^{n}\left(C_i - \hat{C}_i\right)^2}{\sum_{i=1}^{n}\left(C_i - \overline{C_i}\right)^2} \tag{6.9a}$$

$$\text{RMSE} = \sqrt{\frac{1}{n}\sum_{i=1}^{n}\left(C_i - \hat{C}_i\right)^2} \tag{6.9b}$$

$$\text{PBIAS} = \frac{\sum_{i=1}^{n}\left|C_i - \hat{C}_i\right|}{\sum_{i=1}^{n} C_i} \times 100 \tag{6.9c}$$

where, C_i and $\hat{C}_i$ are the observed concentration and the predicted concentration, respectively; R^2 is the coefficient of determination; PBIAS is the percentage bias.

The test results of the trained models for EXP-A312 are shown in Fig. 6.8. The results of ML-A312 showed underestimated predictions, especially in the ranges of high concentrations, while NN1-A312 produced better predictions on the high concentrations than ML-A312. However, the results of both ML-A312 and NN1-A312 were widely scattered from the 1:1 line compared to the result of NN2-A312,

which produced the most accurate prediction among the models. The results of the three models for the cases of EXP-A315 and EXP-A317 showed a similar tendency as that of the case of EXP-A312. Fig. 6.9 illustrates the performance of each model for all experimental cases. R^2 of NN2 was in the range of 0.91-0.94, whereas R^2 of ML is below 0.87 for all cases. For the NN2 models, RMSE and PBIAS were reduced by 33-62% and 9-19%, respectively, from those of ML models.

In summary, the results of model validations demonstrated that a nonlinear relationship existed between *DN* and the concentration of Rhodamine WT, especially in the high concentration range. Therefore, the results of the neural network models, which can learn the nonlinear relationship by the activation function, performed better than those of the linear regression approaches. Both the ML and NN1 models which used only the *DN* values as the input variables produced large errors in the overall ranges since these two models cannot consider the spatially different base values of *DN* and the rate of change on the concentration. The NN2 model, which included DN_0 in the input variables, gave more accurate predictions by reflecting the heterogeneous response of *DN*. This means that DN_0 in NN2 played an essential role in calibrating the spatially heterogeneous response of *DN*. Therefore, it is expected that the location of fluorometers in *in-situ* measurements should be installed considering the spatial variabilities of DN_0 in each case.

The limitations of the adoption of ANN models in this study are as follows. Because ANN models were trained based on the *in-situ* measured concentration ranged from 0 ppb to the peak concentration of the first cross-section, the accuracy

for the concentration exceeding the range of the *in-situ* measured values cannot be evaluated. Thus, the trained ANN model produced reliable spatial concentration distributions after peak concentration arrival time at the cross-sections, which were close to the injection point. Also, the ANN models could yield different performances according to the architectures of ANN models and the types of cost functions. Thus, even though the architectures of ANN models selected in this study successfully converted the RGB images to concentration values for the three cases, yet better architectures of ANN models could be constructed differently from that of this study.

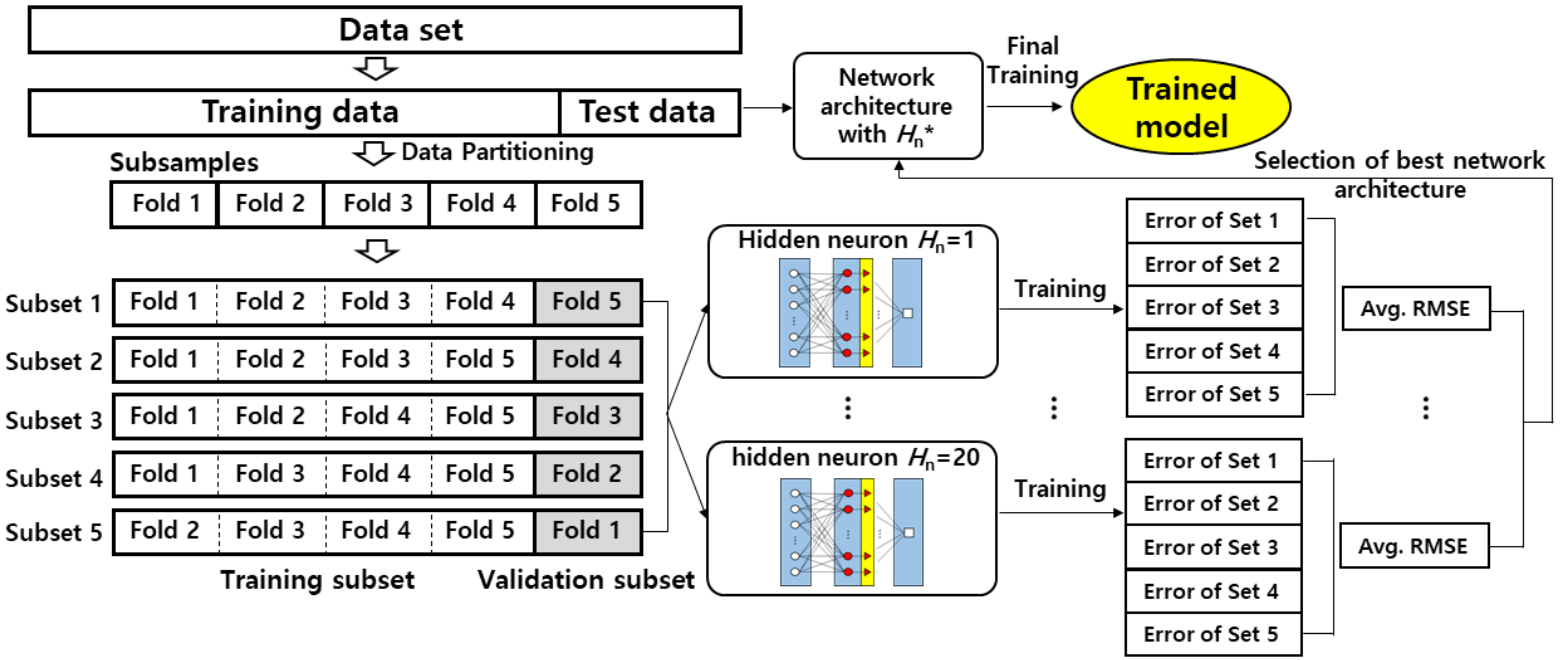

Figure 6.7 Schematic diagram of the selection of the number of neurons in hidden layer and training the neural network

Table 6.3 Summary of model implementations

Method	Model	Input variables	Number of data set (Train / Test)	Number of neurons
Multivariate linear regression	ML-A312	$DN(\lambda_R)$, $DN(\lambda_G)$, $DN(\lambda_B)$,	1,368 / 586	-
	ML-A315		2,388 /1,023	-
	ML-A317		1,731 /741	-
Artificial neural network	NN1-A312	$DN(\lambda_R)$, $DN(\lambda_G)$, $DN(\lambda_B)$	1,368 / 586	7
	NN1-A315		2,388 /1,023	7
	NN1-A317		1,731 /741	7
	NN2-A312	$DN(\lambda_R)$, $DN(\lambda_G)$, $DN(\lambda_B)$, $DN_0(\lambda_R)$, $DN_0(\lambda_G)$, $DN_0(\lambda_B)$	1,368 / 586	15
	NN2-A315		2,388 /1,023	15
	NN2-A317		1,731 /741	15

a) ML-A312

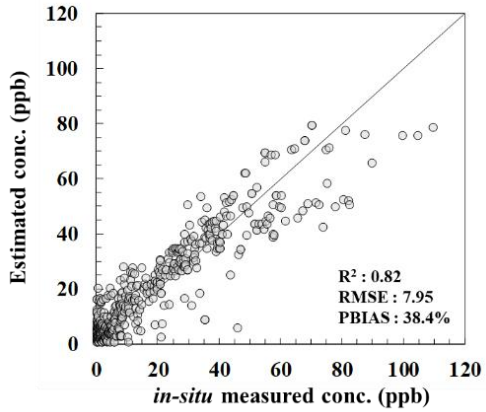

b) NN1-A312

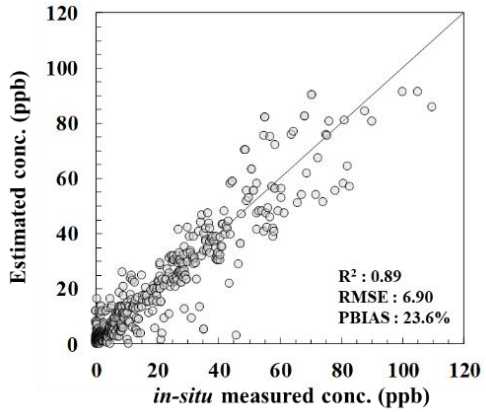

c) NN2-A312

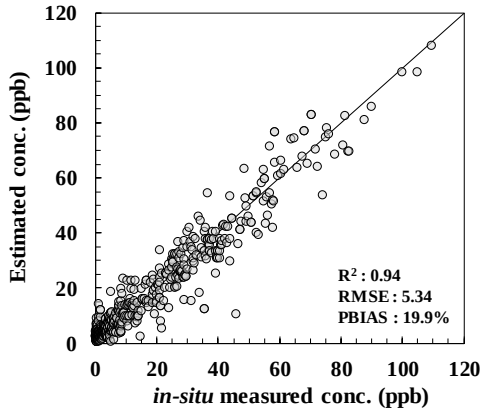

Figure 6.8 Comparison between estimated and in-situ measured concentration (EXP-A312)

a) R^2

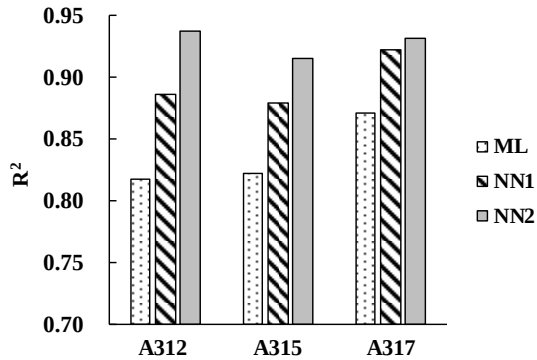

b) RMSE

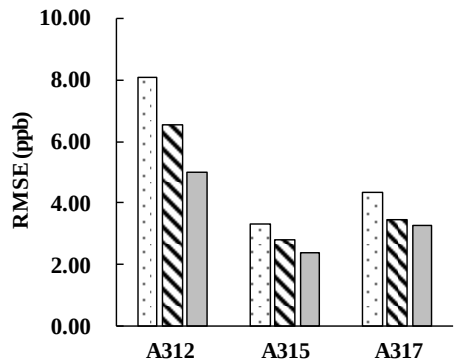

c) PBIAS

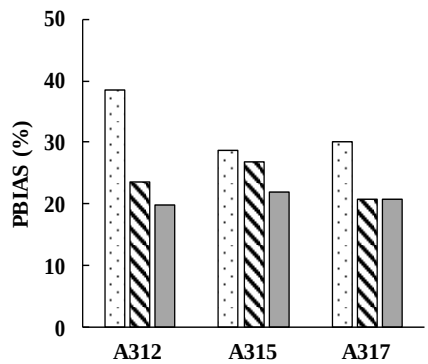

Figure 6.9 Results of the trained models on the test data set

6.5.4 Spatio-temporal distribution of tracer clouds

In this study, using the NN-2 model, the RGB images of each case were converted to the concentration fields to obtain the spatio-temporal concentration distributions of the tracer cloud in experimental channels. To remove the abnormally converted values that were caused by electrical noise in digital images and the effect of sun glint on the irregularly fluctuated water surface, the concentration fields were filtered using the adaptive median filter suggested by Hwang and Hoddad (1995). Any unwanted objects such as bridges and tag lines in the images were removed, and these unmeasured regions were then interpolated using a 2D cubic spline.

Fig. 6.10 shows the distribution of the tracer cloud with time for EXP-A317. The trajectories of the peak concentration over time are represented with dashed lines in Fig. 6.10. This figure shows that the tracer clouds were advected following the thalweg line as dispersing longitudinally and transversely over time in the meandering channels. In addition, it was observed that the tail of the dispersing cloud started to stretch at the inner bank side of Sec. 1 as the tracer cloud exited the first bend, which was also clearly captured in the original RGB image as shown in Fig. 6.10 a). When the tracer clouds passed through the second bend (Sec. 3), as shown in Fig. 6.10 b), the generation of tails on the opposite side was initiated. At this moment, the bifurcation occurred at the rear of the tracer clouds, which was deepened in the next bend (Sec. 5), similarly reported by Fischer (1966). Thus, this figure clearly demonstrates that the method proposed in this study could facilitate a comprehensive analysis in both time and space by providing the spatio-temporal

distribution of the tracer concentration at high resolutions, which is not possible with the conventional *in-situ* method of the tracer test.

a) t = 90 sec

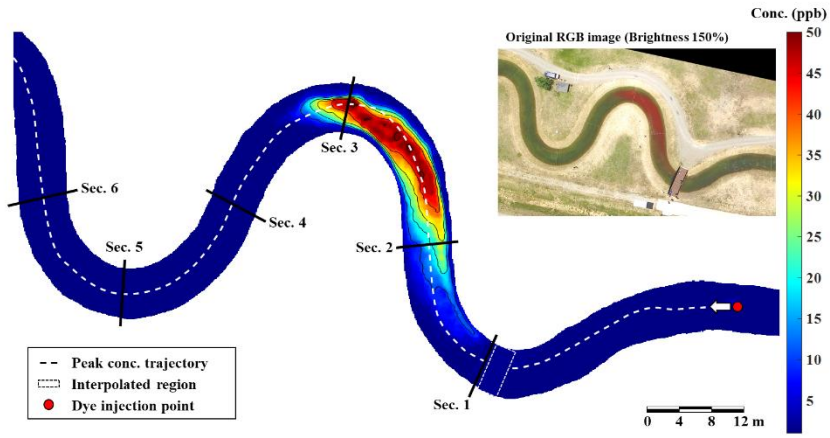

b) t = 120 sec

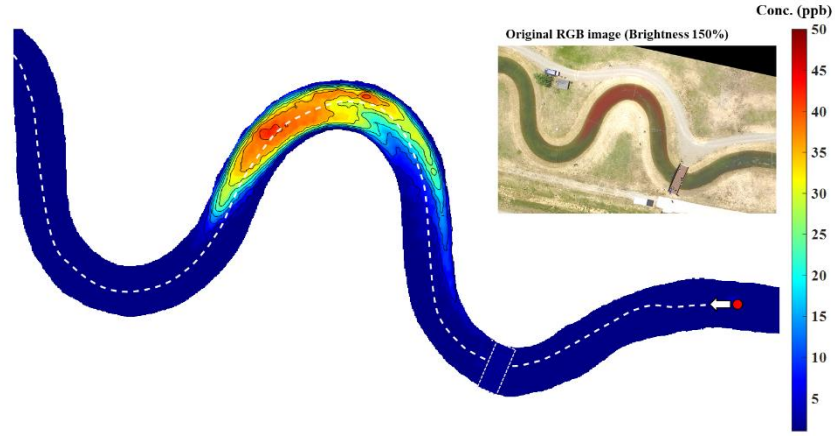

c) t = 150 sec

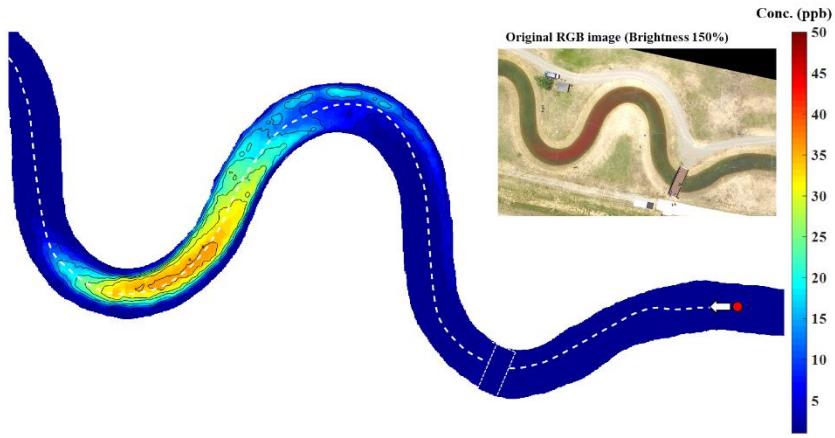

d) t = 175 sec

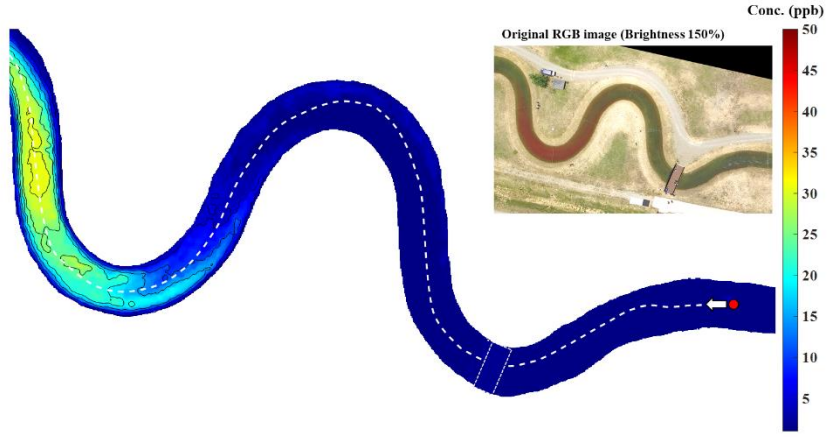

Figure 6.10 Transport of the tracer cloud for Case EXP-A317

6.5.5 Assessment of cross-applicability

The NN2-A312, NN2-A315, and NN2-A317 models were separately trained using each experimental case. To assess whether the trained models can be universally applied to the experimental conditions not previously experienced, the cross-validation of the model was conducted by applying each model to a different dataset of each experiment.

Fig. 6.11 shows the time series results of each model at the center of Sec. 2 in EXP-A315. The NN2-A315 model, which was trained using the dataset of EXP-A315, showed good agreement with the *in-situ* measured concentration. On the other hand, the results using the NN2-A312 and NN2-A317 models, in which the dataset of EXP-A315 was not used in the training phase, showed overestimated results with inaccurately simulated basal and peak concentrations. Nevertheless, all the models showed high R^2 values because the rising and falling tendencies of the breakthrough curve in the *in-situ* measurements were well reproduced by the NN2-A312 and NN2-A317 models. The assessment of cross-applicability for all cases showed the same tendency as summarized in Table 6.4.

From the evaluation of cross-applicability, each trained model showed site-specific characteristics. The trained models could not be applied universally to the image data acquired at the different experimental sites. This limitation of the empirical approach regarding the site-specific problem has been frequently reported in studies of various water environments (Dekker et al., 1996; Liu et al., 2003; Catts

et al., 1985; Fraser ,1998; Lathrop, 1992; Whitlock et al., 1982). Since the spectral response varies according to the constituents in the water body, DN_0 can be affected by the background water quality caused by dissolved or suspended matters in the water body. Moreover, DN_0 could be more strongly influenced by the radiance reflected from the bed materials in the shallower water depth, and thus the ANN models, which were trained using DN_0, could yield site-specific results. For this reason, the proposed method requires simultaneous *in-situ* measurements during the image acquisitions to train the ANN models accurately.

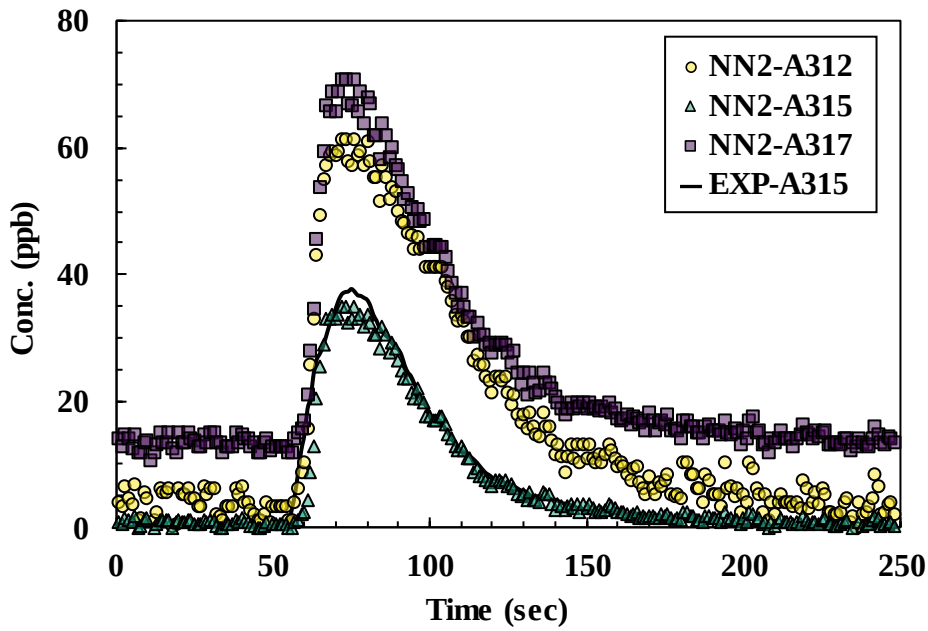

Figure 6.11 Evaluation of cross-applicability at the center of Sec.2 (EXP-A315)

Table 6.4 Evaluation of cross-applicability

Exp. case	EXP-A312			EXP-A315			EXP-A317		
Model	**NN2-A312**	**NN2-A315**	**NN2-A317**	**NN2-A312**	**NN2-A315**	**NN2-A317**	**NN2-A312**	**NN2-A315**	**NN2-A317**
R^2	0.94	0.84	0.77	0.74	0.91	0.83	0.86	0.88	0.93
RMSE (ppb)	5.280	18.66	15.12	13.86	2.419	21.13	13.84	4.789	3.430
PBIAS (%)	19.9	71.9	73.6	155	21.9	277	105	26.9	20.9

7. Application of the improved 2D STRP

7.1 Pre-processing of remotely sensed data

On the remotely measured data for tracer tests in REC channels, the dispersion coefficients were calculated using the 2D STRP-*i*, as well as the existing 2D STRP. The application procedure can be summarized in the following steps.

(1) Transforming UTM coordinates to the natural coordinates system

(2) Extracting concentration profiles at selected measuring sections.

(3) Application of the routing procedures (2D STRP and 2D STRP-*i*) to predict temporal concentration distribution in the downstream section.

(4) Determination of dispersion coefficients for the best-fitted prediction.

The remotely measured data which were assigned in the UTM coordinates system was transformed into the orthogonal curvilinear coordinates or the stream-tube coordinates in order to define the longitudinal surface of streamflow, which was described in Chapter 2. Previous studies (Yotsukura and Sayre, 1976; Lau and Krishnappan, 1981; Lane et al., 2000; Merwade et al., 2005) have defined the longitudinal axis using various characteristics of the streams such as the centerline of the channel, channel bank, half of the cumulative discharge, and the maximum

depth (thalweg line) for transforming their arbitrary coordinates systems to the orthogonal curvilinear coordinates. In this study, the longitudinal direction was determined as the trajectory of the maximum concentration, shown in Fig. 6.10 for EXP-A317 representatively, in order to reflect the actual path of pollutant clouds. Based on the trajectory of the maximum concentration, the transverse surfaces were assigned normal to the longitudinal surfaces. The longitudinal surfaces at each transverse point were obtained tracing the constant values of cumulative discharge. The cumulative discharges, Eq. (5.3), were calculated using the local velocity and depth measured by ADCP at each measuring section, as shown in Fig. 7.1. Then the cumulative discharges in the unmeasured regions between the measuring sections were linearly interpolated based on the measured profiles.

Fig. 7.2 shows the remotely measured concentration data, which were transformed in the stream-tube coordinates based on the trajectory of the maximum concentration. This figure is corresponding concentration distribution in the UTM coordinates, shown in Fig. 6.10. Fig. 7.3 shows the centroid of pollutant mass at each time. The slopes could indicate the time rate of advective distance from the injection point for each case. The values of slopes were very close to the mean velocity measured by ADCP, shown in Table. 6.1. Thus, the longitudinal and transverse surfaces in the stream-tube coordinates were well estimated to express the direction of primary flows, although the surfaces were estimated by the cumulative discharge interpolated by the limited measured data at each section. The values for metric coefficients (m_s and m_n) were determined by graphically using Eq. (2.15).

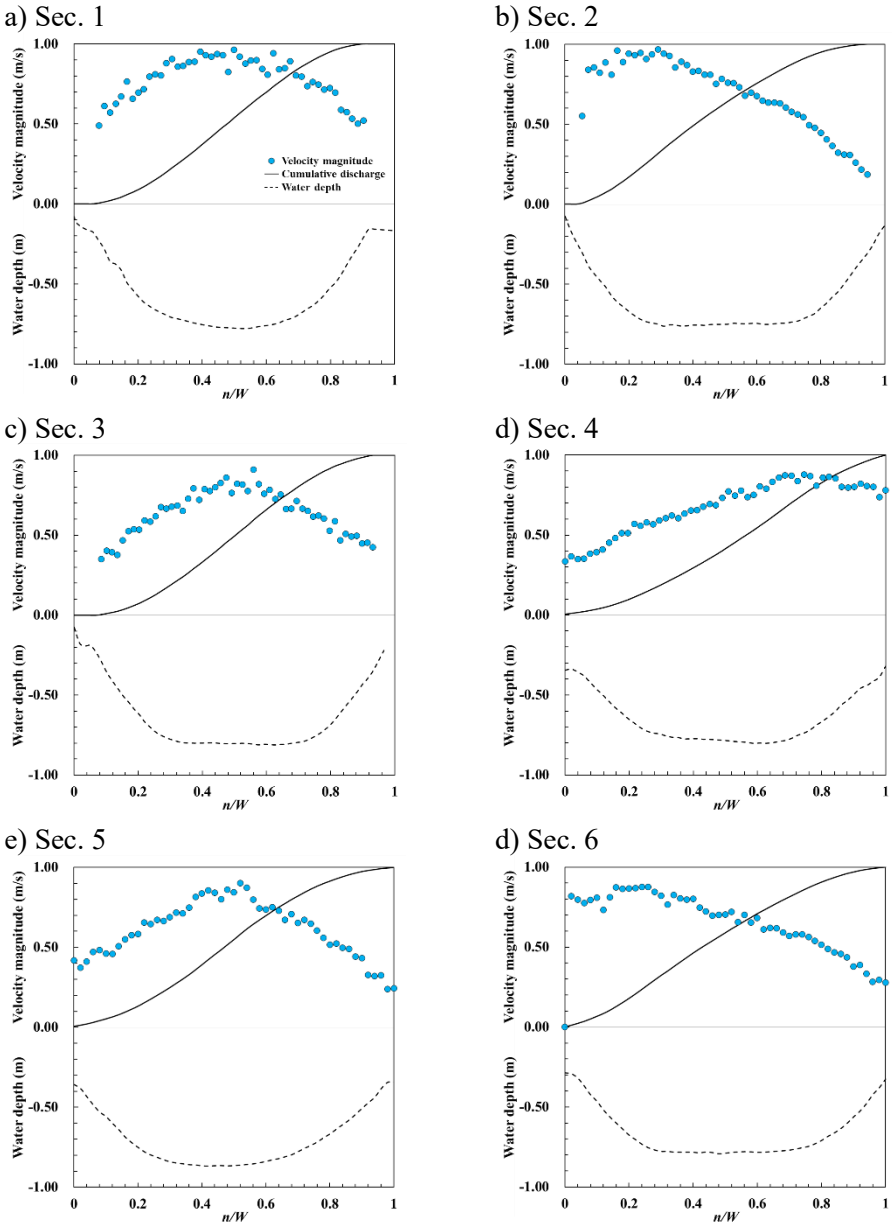

Figure 7.1 depth-averaged velocity profiles and water depth measured by ADCP (EXP-A317)

a) t = 90 sec

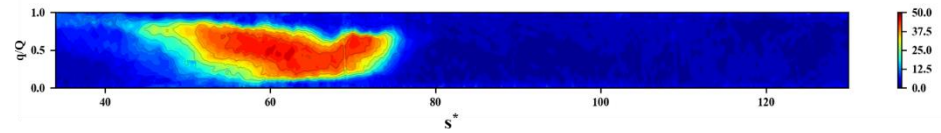

b) t = 120 sec

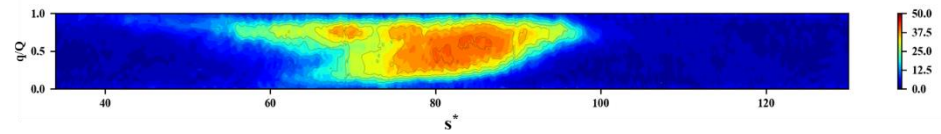

c) t = 150 sec

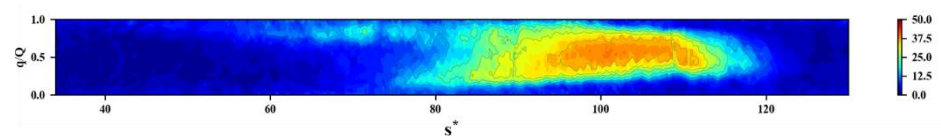

d) t = 175 sec

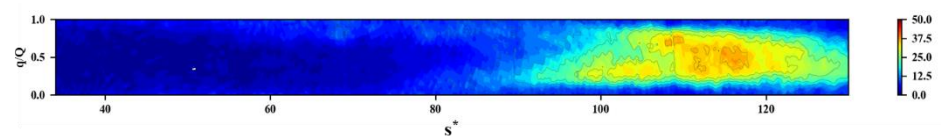

Figure 7.2 Remotely measured concentration data transformed in stream-tube coordinates (EXP-A317)

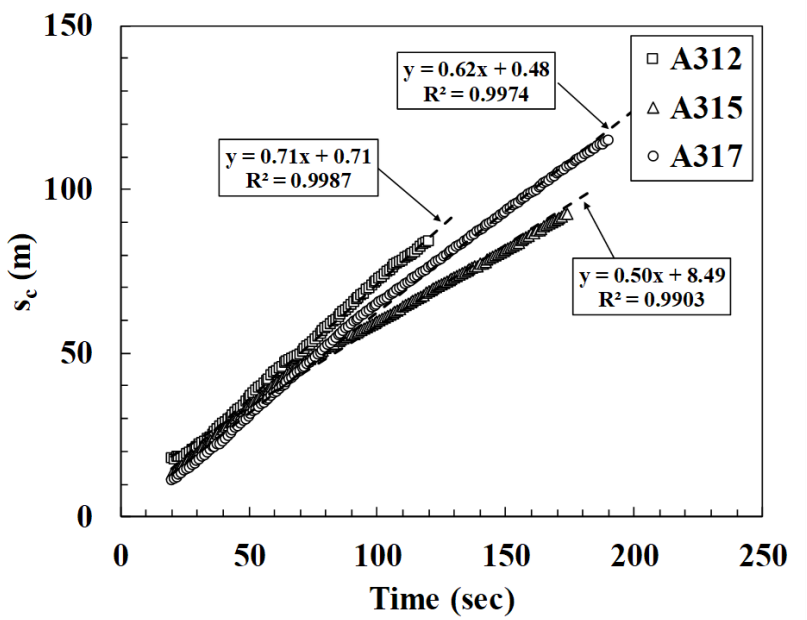

Figure 7.3 The location of the centroid of tracer clouds at each time

The value of P_W was also calculated to check the impingement of tracer clouds on the wall boundaries. Fig. 7.4 shows the values of P_W for each section. The P_W was oppositely alternated in the left and right banks. The P_W in the right bank was significant even in the first measuring section in both cases of EXP-A315 and EXP-A317. The maximum concentration approximately transported in the centerline, but the tails of tracer clouds were elongated along either side of the bank, depending on the skewed velocity distribution. Based on the evaluation of 2D STRP and 2D STRP-*i* described in Chapter. 5 and Chapter. 6, the results of 2D STRP were sensitively responded to the value of P_W. Thus, the application of the existing 2D STRP could be problematic due to the significant impingement of tracer clouds on the wall boundaries.

a) EXP-A315

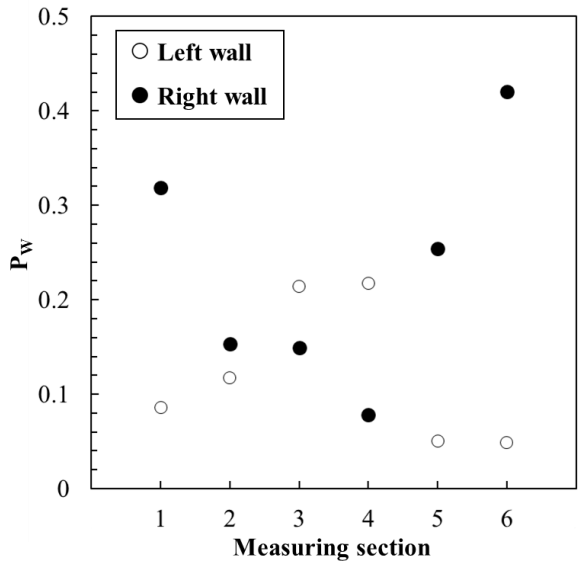

b) EXP-A317

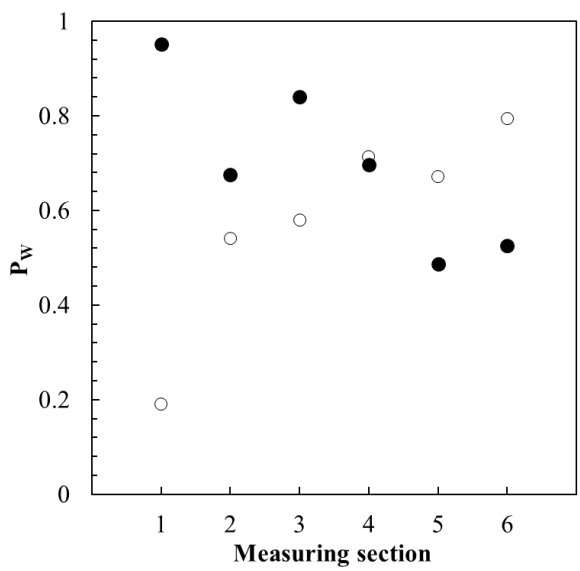

Figure 7.4 The values of P_W for each section in the remotely sensed data

7.2 Calculation of 2D dispersion coefficients

The dispersion coefficients were calculated using the 2D STRP-*i*, and the existing 2D STRP. The remotely measured tracer tests provided highly resolved concentration fields, so the continuous transverse concentration profiles can be obtained from left to right bank without interpolations. The transverse concentration profiles were extracted from approximately 100 points per section. This resolution corresponded to the transverse interval of 0.05 m. In order to calculate dispersion coefficients, the transverse concentration profiles were temporally extracted from the selected measuring sections. In this study, the measuring sections for calculation of dispersion coefficients were the same as those for the measurement of hydraulic data, shown in Fig. 6.3.

The temporal data for transverse concentration profiles (C-t-q distribution) at upstream sections for each longitudinal interval were used as the input distributions. In order to determine the optimal dispersion coefficients, the values which yield the best-fitted prediction distribution should be found based on the proper evaluation index. Piasecki and Katopodes (1999) attempted to optimize the 2D dispersion coefficients in the numerical model to the results of tracer test data using the conventional gradient-based technique. They reported that the objective function (sum of squared residuals) lost its monotonic convexity, and a unique solution was challenging to find due to various errors caused by measuring concentration values. In other words, the gradient-based optimization algorithm may fail to find a unique global minimum. Thus, in this study, the *Latin Hypercube Simulation* (McKay et al.,

1979; Eglajs and Audze, 1977; Iman and Helton, 1981) was employed to find the optimal values of 2D dispersion coefficients. The *Latin Hypercube Simulation* is a type of random search based on the stratified Monte Carlo sampling. In *Latin Hypercube Simulation*, the range of each input parameter is divided into *n* disjoint intervals with an equal marginal probability of 1/*n*. the samples are randomly selected once in each interval. Thus, *n* number of random samples are uniformly distributed across the range of each input parameter. The advantage of this method is that randomly selected samples are non-collapsing and more space-filling, compared to the results of the standard *Monte Carlo Simulation.*

The ranges of 2D dispersion coefficients for The *Latin Hypercube Simulation* were set, referring to the ranges of dimensionless dispersion coefficients reported by previous studies (Rutherford, 1994; Seo et al., 2016; Shin et al., 2019). The values of D_L/HU^* and D_T/HU^* were evaluated in the range from 1 to 25, and from 0.1 to 3.0, respectively. For calculation of dimensionless values, the shear velocity, U^*, was obtained using $\sqrt{gR_hS}$. The energy slope, *S*, was assumed as the values of 0.00125 that is the bottom slope of the experimental channels. Within these ranges, 5,000 samples for the pair of D_L and D_T were randomly generated.

a) RMSE of 2D STRP (From Sec.2 to Sec.3)

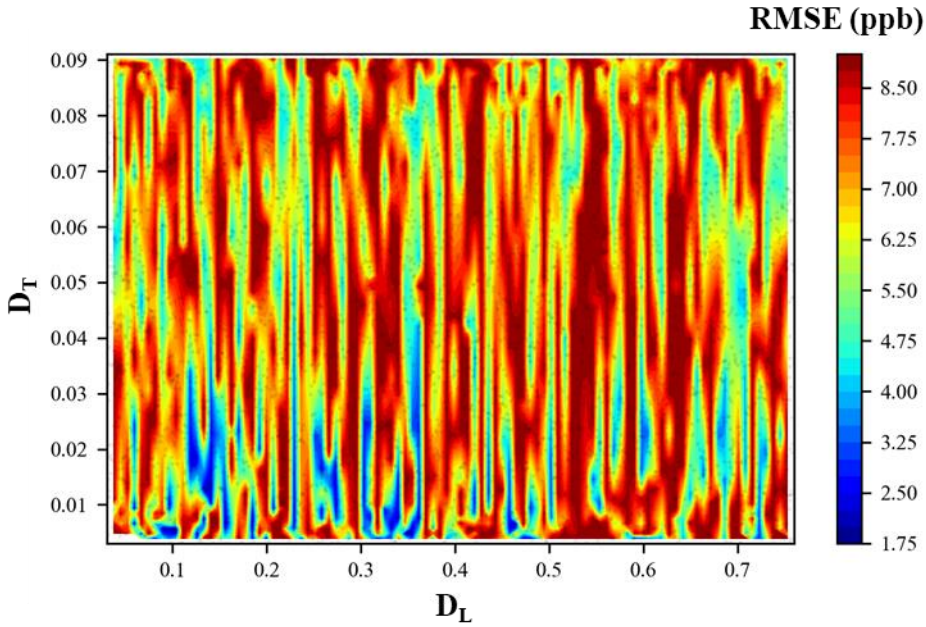

b) RMSE of 2D STRP-*i* (From Sec.2 to Sec.3)

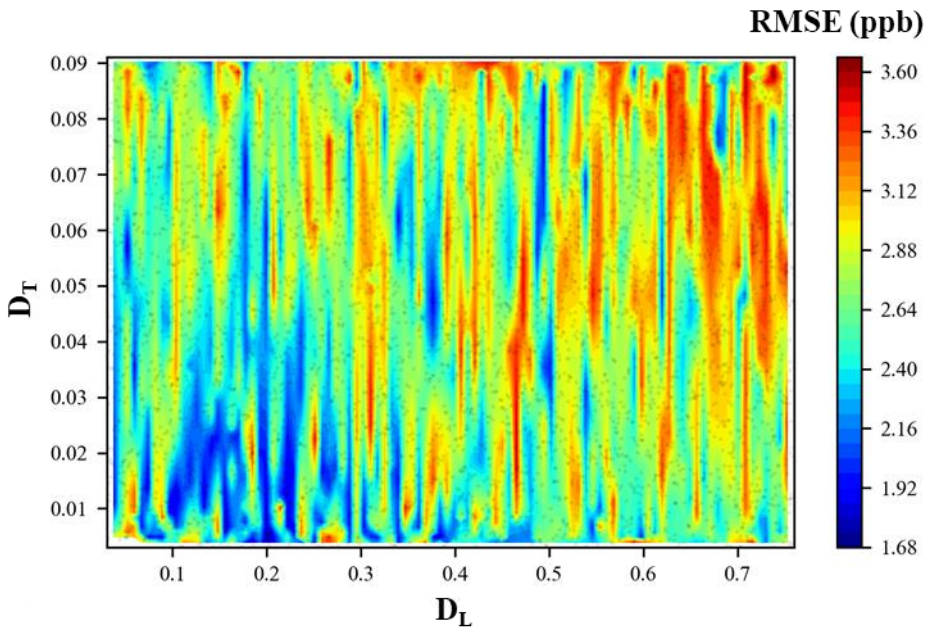

Figure 7.5 RMSE distributions by 2D STRP and 2D STRP-*i* on the randomly sampled dispersion coefficients (EXP-A315)

Fig. 7.5 shows the RMSE distributions of results predicted by 2D STRP and 2D STRP-*i* on the case of EXP-A315. As mentioned by Piasecki and Katopodes (1999), the RMSE distributions by randomly sampled dispersion coefficients were indeed non-convex with many local minima, so it is challenging to find the global minimum using the traditional gradient-based optimization techniques.

In addition, the best-fitted distribution could be differently determined from various statistical perspectives. Even if a certain dispersion coefficient yields the inaccurate concentration distribution with significant value of RMSE, these results could be evaluated as the best-fitted results on the other criteria such as maximum value, variance, and so on. In order to evaluate the results from the different types of objective functions, additional statistical indices were introduced as follows.

$$MaxE = \left| C_{\max}^{p} - C_{\max}^{m} \right| \tag{7.1}$$

$$V_t E = \left| \sigma_t^{p} - \sigma_t^{m} \right| \tag{7.2}$$

$$V_q E = \left| \sigma_q^{p} - \sigma_q^{m} \right| \tag{7.3}$$

$$\mathrm{R}^2 = 1 - \frac{\sum_{i=1}^{n} \left(C_i^{p} - C_i^{m} \right)^2}{\sum_{i=1}^{n} \left(C_i^{p} - \overline{C_i} \right)^2} \tag{6.9a}$$

where *MaxE* is the absolute error of peak concentration; V_tE and V_qE are the absolute error of temporal and transverse variance in the C-t-q distribution; R^2 is the coefficient of determination; the upper script of *p* and *m* are predicted and measured values. Each evaluation index was intended to evaluate the predicted distribution in terms of the error of the peak concentration (*MaxE*), the error of temporal variance (V_tE), the error of transverse variance (V_qE), and overall trend (R^2).

Fig. 7.6 shows the results of additional indices for error evaluations. The evaluation results describe that optimum values of both D_L and D_T can vary according to the type of objective function. However, most previous studies, which used 2D STRP, determined the optimal values of both D_L and D_T using the gauss-newton method with a single objective function, i.e., RMSE. Thus, it is possible that the previously reported values of 2D dispersion coefficients by 2D STRP may not be the global minimum. If measured concentration data has ideally no measurement error, and the tracer transport is well described by 2D ADE, optimum values should not depend on the evaluation indices. It is inferred that the measurement errors may cause trade-off in between evaluation indices. For example, when the *MaxE* is used as the optimum criterion, either V_tE or V_qE can increase to match the peak values of concentration if the peak concentration of the measured distributions at downstream section has a certain amount of error. Thus, it is hard to determine the optimum value of D_L and D_T using a single objective function.

a) *MaxE* of 2D STRP-*i* (From Sec.2 to Sec.3)

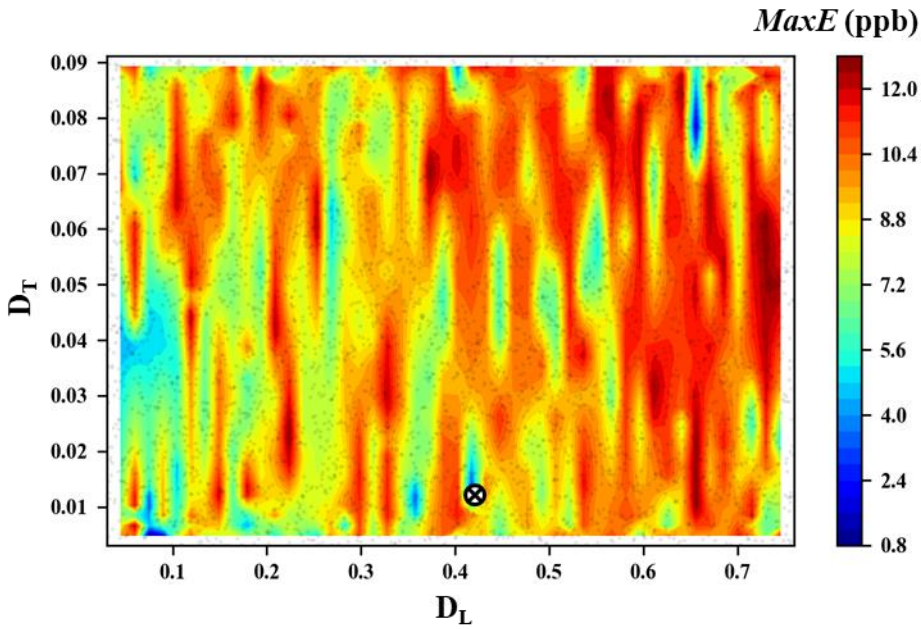

b) V_tE of 2D STRP-*i* (From Sec.2 to Sec.3)

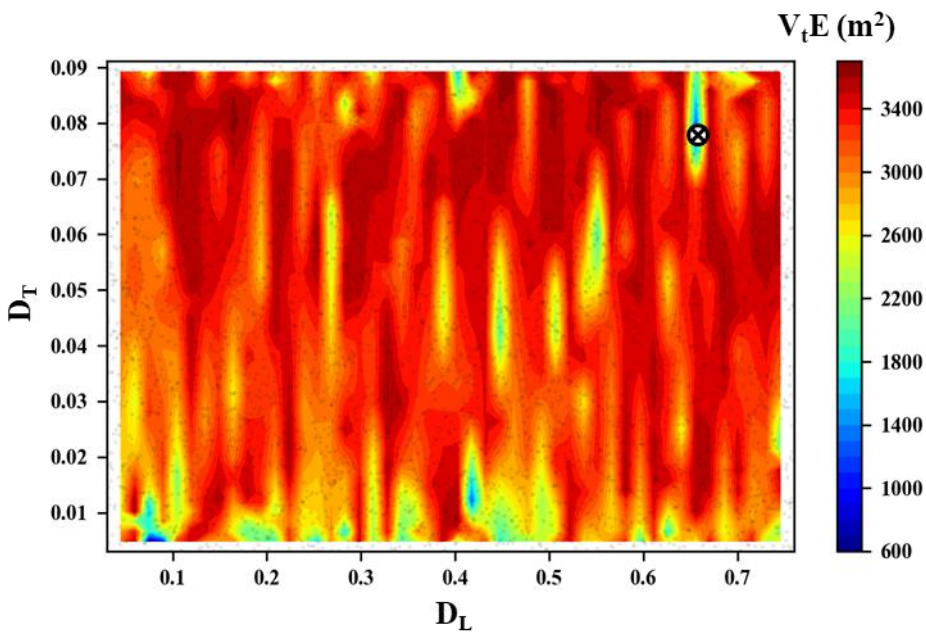

c) V_qE of 2D STRP-*i* (From Sec.2 to Sec.3)

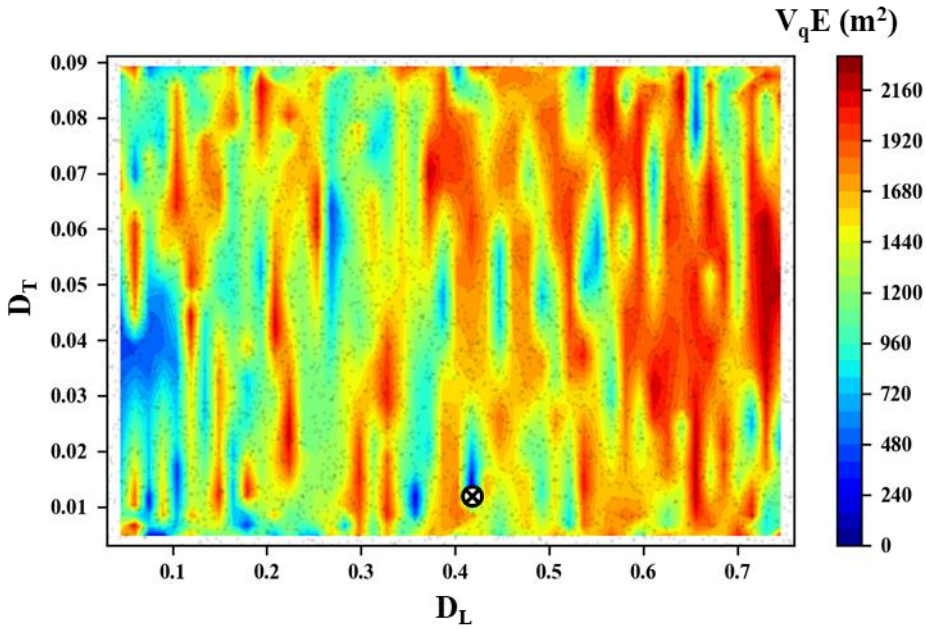

d) R^2 of 2D STRP-*i* (From Sec.2 to Sec.3)

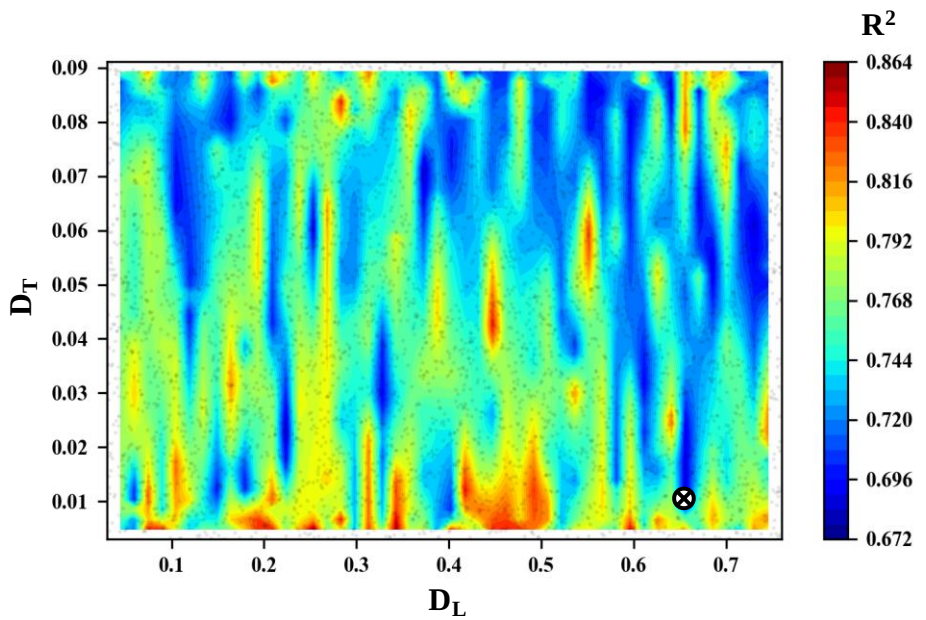

Figure 7.6 Evaluation results of 2D STRP-*i* on the randomly sampled dispersion coefficients (EXP-A315; the marks indicate the minimum values)

In this study, the index score was introduced to determine the optimum D_L and D_T to consider multiple objective indices. Each evaluation index used in this study was standardized by min-max scaling to transform in the range from 0 to 1 so that scaled values express the worst values as 0 and the best values as 1.

$$IS_{RMSE} = \frac{\left(RMSE\right)_{\max} - RMSE}{\left(RMSE\right)_{\max} - \left(RMSE\right)_{\min}} \tag{7.4}$$

$$IS_{MaxE} = \frac{\left(MaxE\right)_{\max} - \left(MaxE\right)}{\left(MaxE\right)_{\max} - \left(MaxE\right)_{\min}} \tag{7.5}$$

$$IS_{V_tE} = \frac{\left(V_tE\right)_{\max} - V_tE}{\left(V_tE\right)_{\max} - \left(V_tE\right)_{\min}} \tag{7.6}$$

$$IS_{V_qE} = \frac{\left(V_qE\right)_{\max} - V_qE}{\left(V_qE\right)_{\max} - \left(V_qE\right)_{\min}} \tag{7.7}$$

$$IS_{R^2} = \frac{R^2 - \left(R^2\right)_{\min}}{\left(R^2\right)_{\max} - \left(R^2\right)_{\min}} \tag{7.8}$$

where the subscript max and min indicates the maximum and minimum value of each index on the evaluated values for the pair of D_L and D_T. The determined dispersion coefficients and its index scores were summarized in Table 7.1, and the

Table 7.1 Summary of dispersion coefficients determined by 2D STRP and 2D STRP-*i*

Case	Upstream section	Downstream section	Method	D_L	D_T	D_L/HU*	D_T/HU*	Index score					
								IS_{RMSE}	IS_{ME}	IS_{VES}	IS_{VEq}	IS_{R^2}	Total Scour
EXP-A315	sec.1	sec.2	2D STRP-i	0.575	0.026	17.38	0.79	0.61	0.47	0.99	0.67	0.98	3.73
			2D STRP	0.662	0.006	20.00	0.18	0.64	0.98	0.94	0.72	0.69	3.96
	sec.2	sec.3	2D STRP-i	0.130	0.009	4.30	0.30	0.98	0.86	0.88	1.00	0.96	4.68
			2D STRP	0.239	0.004	7.86	0.12	0.97	0.99	0.90	0.98	0.97	4.81
	sec.3	sec.4	2D STRP-i	0.286	0.034	8.14	0.97	1.00	0.80	0.71	0.63	0.74	3.88
			2D STRP	0.410	0.005	11.66	0.15	0.81	0.90	0.89	0.94	0.58	4.12
	sec.4	sec.5	2D STRP-i	0.296	0.008	8.81	0.23	0.99	0.98	0.99	0.96	0.99	4.91
			2D STRP	0.175	0.004	5.21	0.11	0.99	0.97	0.99	0.96	1.00	4.92
	sec.5	sec.6	2D STRP-i	0.212	0.029	7.60	1.03	0.99	0.96	0.84	0.95	0.98	4.71
			2D STRP	0.117	0.004	4.19	0.13	0.98	0.97	1.00	0.99	0.98	4.92
EXP-A317	sec.1	sec.2	2D STRP-i	0.667	0.017	15.11	0.39	0.90	0.94	0.99	0.95	0.99	4.76
			2D STRP	0.625	0.026	14.15	0.79	0.88	0.87	0.98	1.00	0.97	4.69
	sec.2	sec.3	2D STRP-i	0.496	0.030	10.05	0.61	0.99	0.61	0.99	0.92	0.96	4.47
			2D STRP	0.588	0.009	11.91	0.30	0.85	0.98	0.69	0.81	0.82	4.15
	sec.3	sec.4	2D STRP-i	0.189	0.014	3.63	0.26	0.99	0.89	0.94	0.86	1.00	4.67
			2D STRP	0.249	0.011	4.78	0.32	1.00	0.98	1.00	0.89	0.99	4.85
	sec.4	sec.5	2D STRP-i	0.710	0.012	12.77	0.22	0.96	0.65	0.75	0.99	0.99	4.33
			2D STRP	0.781	0.004	14.04	0.11	0.99	0.94	0.81	0.97	0.98	4.69
	sec.5	sec.6	2D STRP-i	0.418	0.033	7.43	0.59	0.99	0.99	0.80	0.97	0.97	4.73
			2D STRP	0.161	0.003	2.86	0.11	0.98	0.88	1.00	0.94	0.99	4.78

results of best-fitted predictions were shown in figures from Fig. 7.7 to Fig. 7.10.

The observed C-t-q distributions at each section showed the skewed distribution with the long tail along the either left or right side of the riverbank. The elongation of tails of tracer clouds near the side banks resulted from the combination of the dispersion and the horizontally varied advection effect, which is caused by the meanders and irregularities of channels. As shown in the figures from Fig. 7.7 to Fig. 7.10, both results of the existing 2D STRP and 2D STRP-*i* well reproduced the highly distorted tracer clouds with long tails and time to peak concentrations for each section. However, the prediction results near the wall boundaries have discrepancies between 2D STRP and 2D STRP-*i*. For the results of 2D STRP-*i*, which is developed in this study, the gradient of concentration near the wall boundaries was close to zero-gradient, while the results from 2D STRP, which could not consider the effect of wall boundaries, showed the steep transverse concentration gradient near the wall.

a) Input C-t-q distribution at upstream section (sec. 2)

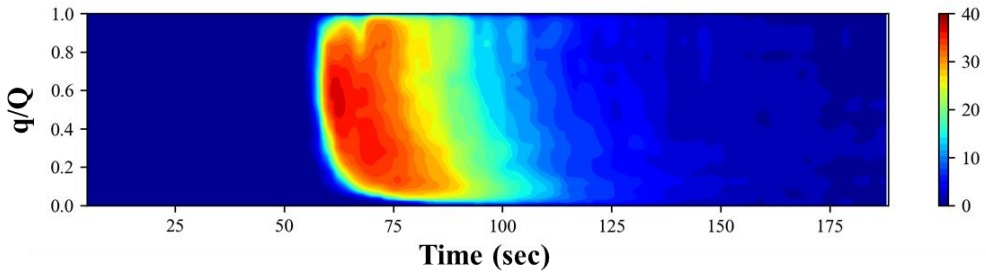

b) Predicted C-t-q distribution at downstream section by 2D STRP (sec. 3)

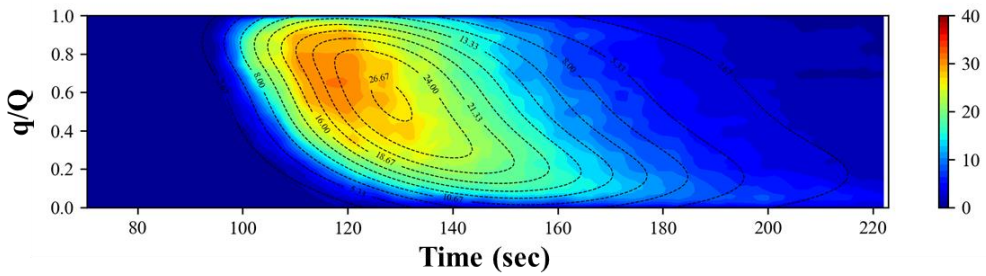

c) Predicted C-t-q distribution at downstream section by 2D STRP-*i* (sec. 3)

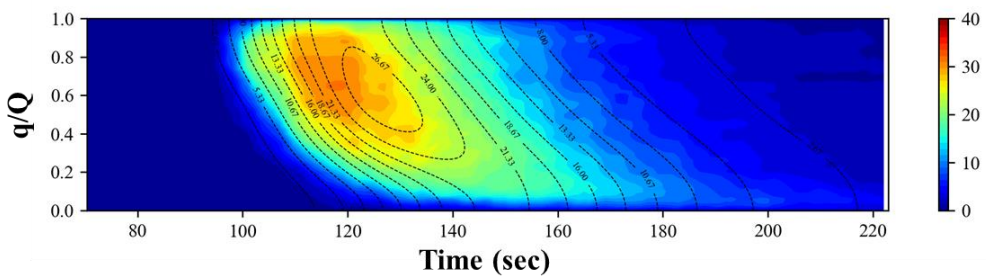

Figure 7.7 Predicted C-t-q distribution by 2D STRP and 2D STRP-*i* (From Sec. 2 to Sec. 3; EXP-A315; Filled color: measured value; Dotted line: predicted value)

a) Input C-t-q distribution at upstream section (sec. 4)

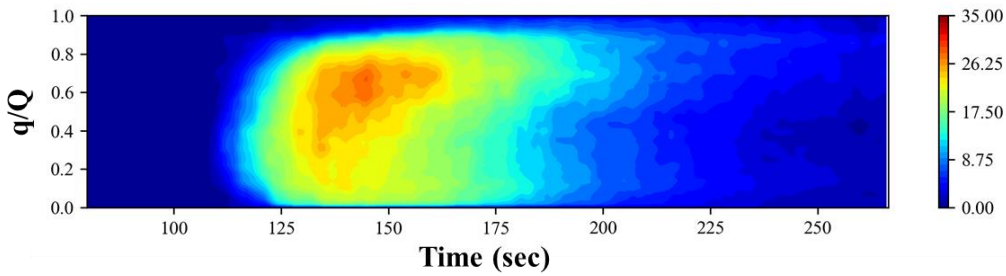

b) Predicted C-t-q distribution at downstream section by 2D STRP (sec. 5)

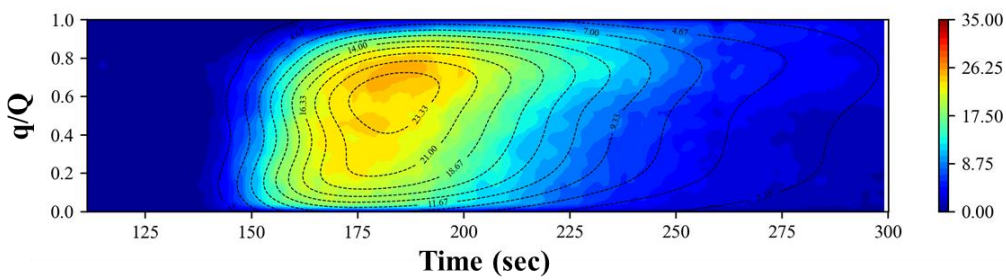

c) Predicted C-t-q distribution at downstream section by 2D STRP-*i* (sec. 5)

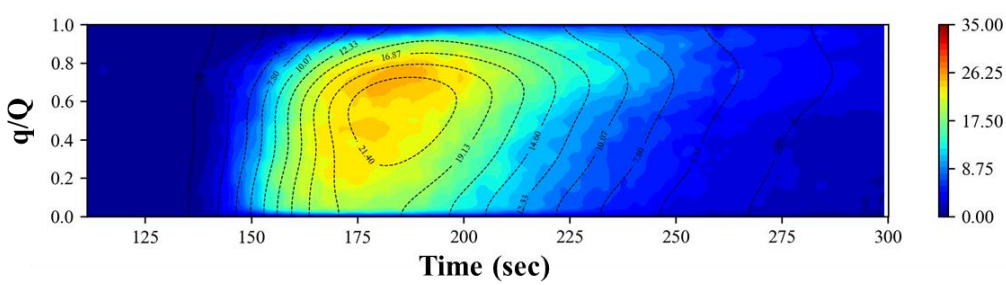

Figure 7.8 Predicted C-t-q distribution by 2D STRP and 2D STRP-*i* (From Sec. 4 to Sec. 5; EXP-A315; Filled color: measured value; Dotted line: predicted value)

a) Input C-t-q distribution at upstream section (sec. 2)

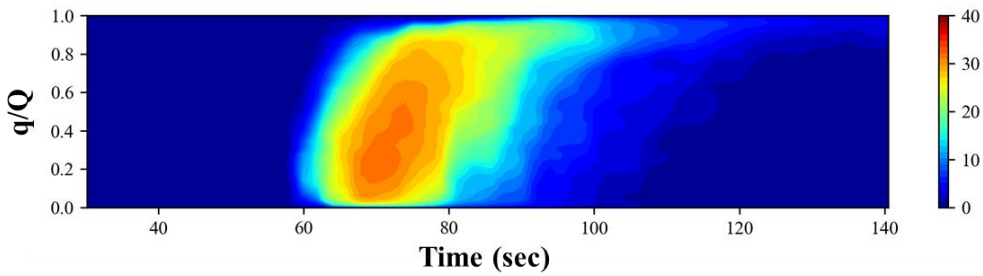

b) Predicted C-t-q distribution at downstream section by 2D STRP (sec. 3)

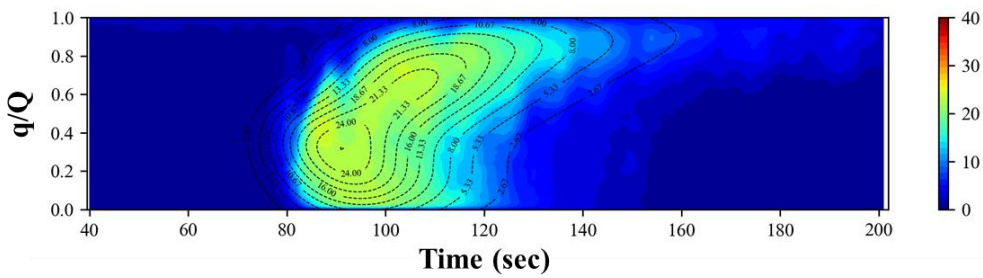

c) Predicted C-t-q distribution at downstream section by 2D STRP-*i* (sec. 3)

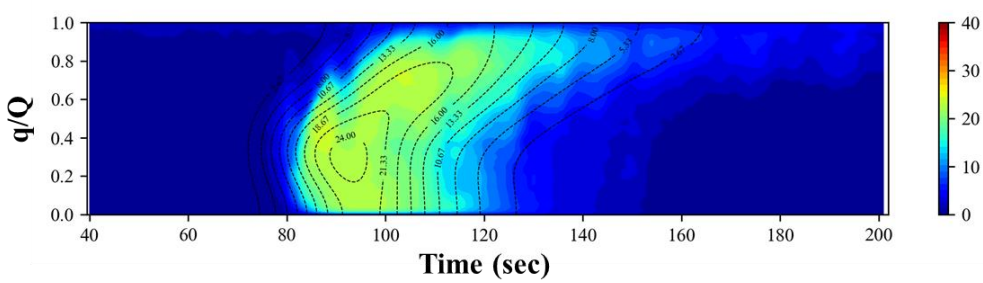

Figure 7.9 Predicted C-t-q distribution by 2D STRP and 2D STRP-*i* (From Sec. 2 to Sec. 3; EXP-A317; Filled color: measured value; Dotted line: predicted value)

a) Input C-t-q distribution at upstream section (sec. 4)

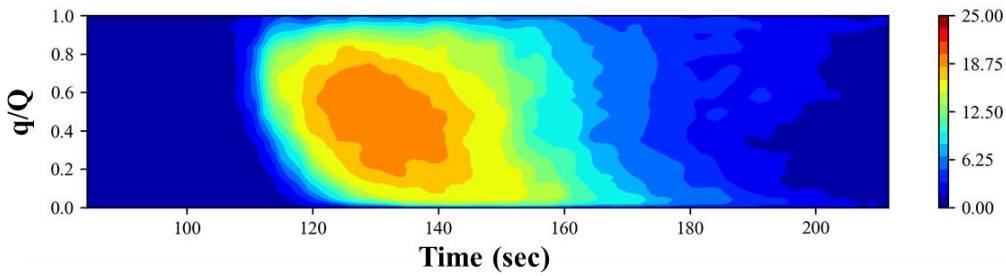

b) Predicted C-t-q distribution at downstream section by 2D STRP (sec. 5)

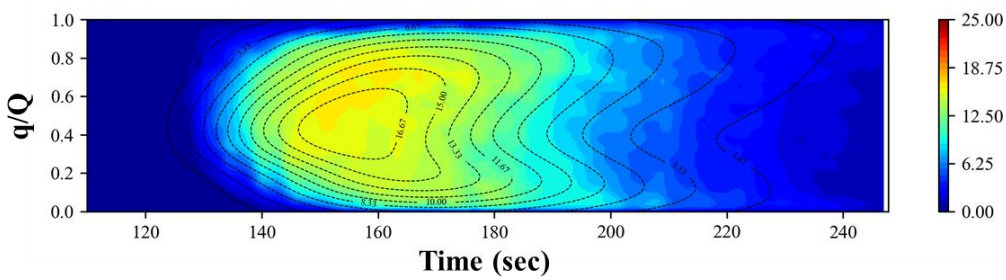

c) Predicted C-t-q distribution at downstream section by 2D STRP-*i* (sec. 5)

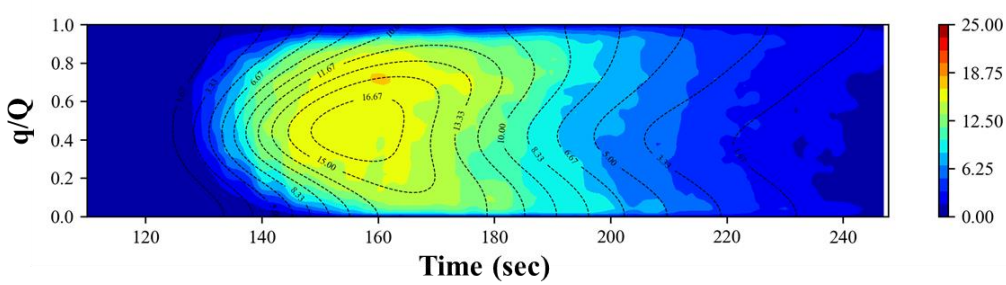

Figure 7.10 Predicted C-t-q distribution by 2D STRP and 2D STRP-*i* (From Sec. 4 to Sec. 5; EXP-A317; Filled color: measured value; Dotted line: predicted value)

Fig. 7.11 and Fig. 6.12 show the nondimensional dispersion coefficients determined at each interval for the experimental cases of EXP-A315 and EXP-A317. These figures represent that the nondimensional transverse dispersion coefficients by 2D STRP were generally underestimated compared to the results of 2D STRP-*i* developed in this study, while and longitudinal dispersion coefficients were predicted as a similar tendency. In Fig. 7.11 representing the determined longitudinal dispersion coefficients, the nondimensional longitudinal dispersion coefficients, which have been previously obtained by theoretical methods (Eq. 2.7), were plotted as gray-colored lines (Elder, 1959; Shin et al., 2019). Notably, the results from Shin et al. (2019) in Fig. 7.11 were the maximum values calculated by using ADCP measured-velocity profiles in REC channel that is used in this study. The results of 2D STRP-*i* in this study were typically higher than the Elder's value (5.93) but lower than Shin et al. (2019) except for the first section. In the case of transverse dispersion coefficients, Fischer et al. (1979) and Rutherford (1994) have summarized the range of transverse dispersion coefficients, collecting the previous experimental data, shown as gray-colored lines in Fig. 7.12. the transverse dispersion coefficients by 2D STRP-*i* were widely varied over the sections but mainly classified into *'gently meandering'* for both cases. However, the results of 2D STRP tended to be underestimated compared to the results of 2D STRP-*i*. As shown in Fig. 7.4, the remotely sensed tracer data showed that the tracer clouds were transported in contact with the wall boundaries even in the first section for both EXP-A315 and EXP-A317. Because of the limitation of 2D STRP, the transverse dispersive fluxes near the wall boundaries caused the loss of the total mass due to the lack of treatment of boundaries.

a) EXP-A315

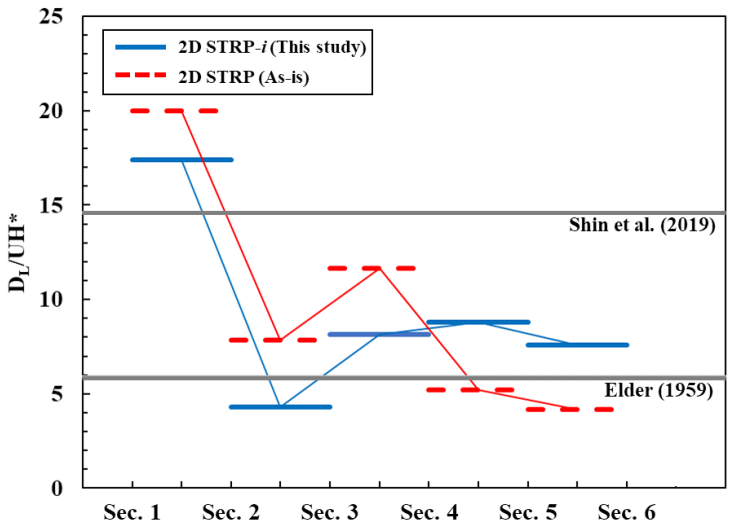

b) EXP-A317

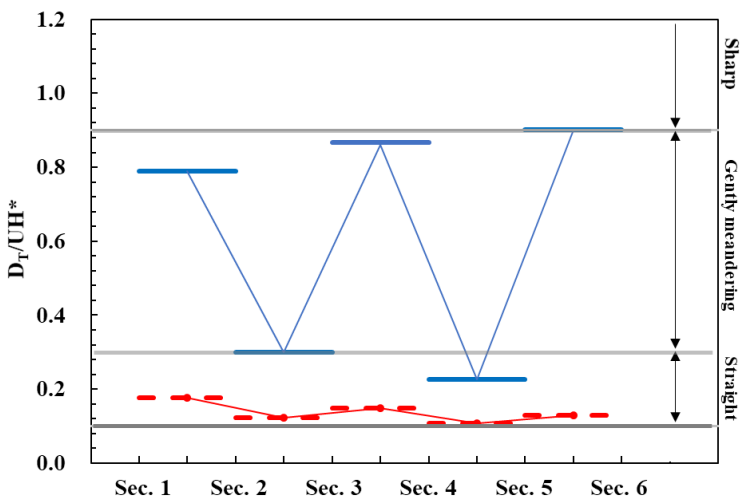

Figure 7.11 Comparison of longitudinal dispersion coefficients by routing methods

a) EXP-A315

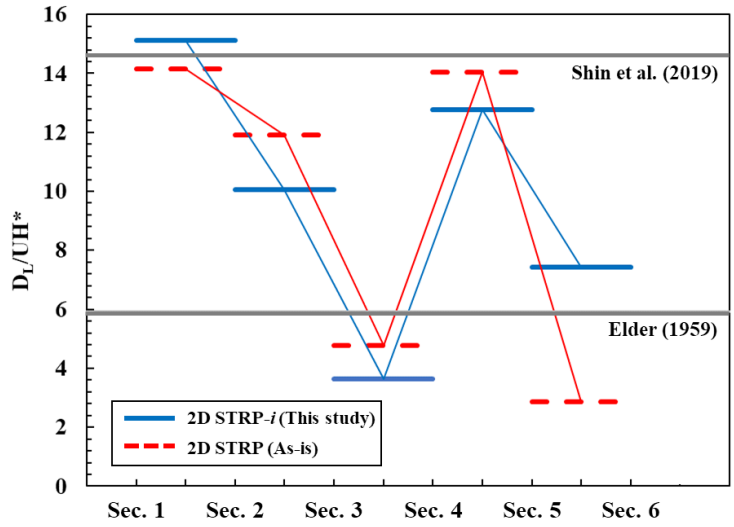

b) EXP-A317

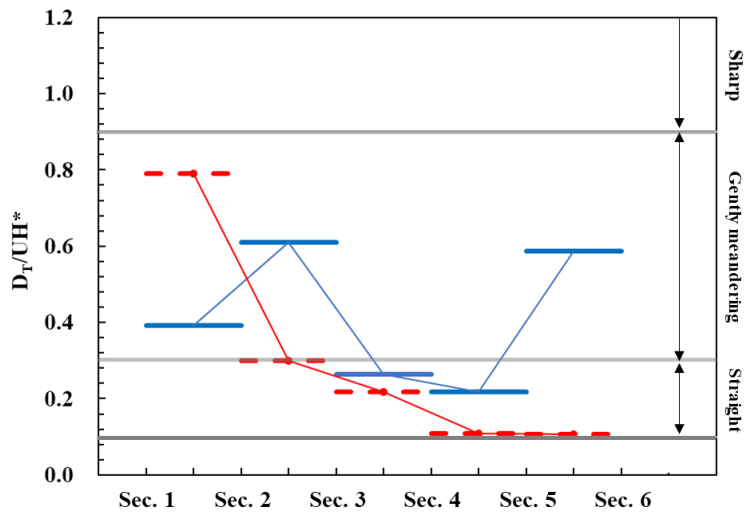

Figure 7.12 Comparison of transverse dispersion coefficients by routing methods

Thus, the transverse dispersion coefficients could be selected less than the proper values in the optimization procedures in order to conserve the tracer mass in the optimization procedure. In spite of that, the longitudinal dispersion coefficients of both methods showed similar tendencies for each section. The longitudinal dispersion coefficients are the proportional factor of the longitudinal gradient of concentration fields, so the magnitude of the longitudinal dispersion coefficient cannot affect the loss of mass in 2D STRP. Therefore, the best-fitted distribution by the existing 2D STRP tended to be determined as weighted in the longitudinal dispersion coefficients rather than the transverse dispersion coefficients.

In summary, the use of routing-based methods can unreliably determine the dispersion coefficients in the optimization phase due to the uncertainties of measurement errors. Moreover, the existing 2D STRP tends to underestimate the transverse dispersion coefficients due to its functional limitations in the cases where the tracer clouds reach the wall boundaries. Thus, previously reported dispersion coefficients by routing-based methods must be reexamined and verified in terms of the optimization methods and the effect of wall boundaries.

8. Conclusions

8.1 Conclusions of this study

In this study, the limitations of 2D STRP were quantitatively analyzed using the synthetic concentration data. Then, in order to overcome the limitations of the existing 2D STRP, the new routing-based observation method (2D STRP-*i*) and the remote sensing-based experimental framework for tracer tests were developed. The followings are the conclusions of the present study.

i) Limitations of the existing 2D STRP:

The performance of existing 2D STRP was evaluated in terms of the variation of Peclet number and the spatially varied velocity distributions. The quantitative evaluations were performed using the synthetic data generated by the analytical solution and FVM-based numerical model, which was also implemented in this study. The existing 2D STRP performs reasonably in the condition of the high Peclet numbers because the existing 2D STRP was derived based on the frozen cloud approximation. It was found that the frozen cloud approximation was applicable for the cases of which the values of Peclet number over 2,250 in order to estimate the accurate spatial concentration fields. However, when the tracer clouds reached the side boundaries, the existing 2D STRP reproduced the unreliable temporal concentration distributions. When subject to the spatially varied flow, the 2D STRP well provided the distorted concentration fields caused

by spatially varied advection, but the predicted results were also affected by the effect of wall boundaries.

ii) Development of a new routing-based method for dispersion coefficients:

The new routing-based observation method (2D STRP-*i*) was developed in order to overcome the limitations of the existing 2D STRP. The 2D STRP-*i* derived from the 2D ADE in the orthogonal curvilinear coordinate system, assuming the steady-state flow condition. 2D STRP-*i* could adequately consider the spatially varied advection as well as the effect of wall boundaries. The verification of 2D STRP-*i* showed that the temporal distributions of tracer clouds were correctly predicted even if the significant impingement of tracer clouds on the wall boundaries occurred. However, 2D STRP-*i* was applicable in the high Peclet numbers because it was also derived following the frozen cloud approximation.

iii) Development of a remote sensing-based experimental framework for tracer tests

A new experimental framework for tracer tests using RGB images was developed in order to acquire the spatio-temporal concentration distribution of tracer clouds in open channel flows. Tracer tests using Rhodamine WT were conducted in the large-scale experimental channels to collect the RGB images using a commercial digital camera mounted on a UAV, and the concentration of Rhodamine WT using in-situ fluorometric probes. The correlation analysis showed that the in-situ measured concentrations of Rhodamine WT were strongly correlated with the digital number (DN) of the RGB images. The empirical relationship between the

DN values and the Rhodamine WT concentration data was obtained using an artificial neural network (ANN) model. The trained ANN models accurately retrieved the detailed spatio-temporal concentration distributions of all study areas that had an R^2 higher than 0.9. The acquired spatio-temporal concentration distributions by the proposed method based on the UAV images gave general as well as detailed views of the tracer cloud moving dynamically in open channel flows that cannot be easily observed using conventional in-situ measurements.

iv) Application of 2D STRP-*i* to experimental data

The 2D STRP-*i* was applied to the concentration data from tracer tests to calculate the values of D_L and D_T. In order to determine the optimum values of dispersion coefficients, the Latin Hypercube Simulation approach was adapted. The results of simulations showed that the RMSE distributions were non-convex with many local minima. In addition, the optimal dispersion coefficients varied according to the evaluation functions. In this study, the multiple evaluation indices were introduced to determine the dispersion coefficients more robustly. The results showed that the values of D_L were similarly found from both 2D STRP and 2D STRP-*i*, while the values of D_T by 2D STRP were significantly underestimated compared to the values by 2D STRP-*i* due to the lack of the consideration of the wall boundaries.

In previous studies, the 2D STRP has been the only available method to calculate the longitudinal and transverse dispersion coefficients simultaneously for 2D depth-

averaged pollutant transport models, especially for the condition of the transient concentration fields. Most of the published longitudinal dispersion coefficients for 2D ADE have been produced using 2D STRP. From the results of this study, it has been demonstrated that the existing 2D STRP has the possibility to provide the imprecise dispersion coefficients in the condition where the tracer clouds reach wall boundaries due to its functional limitation. Moreover, the use of routing-based methods can poorly determine the dispersion coefficients in the optimization phase due to the uncertainties of measurement errors. Thus, previously reported dispersion coefficients by routing-based methods have to be reexamined and verified in terms of the data qualities and the optimization methods.

8.2 Future study

This study mainly focused on the improvement of the routing-based observation method for the dispersion coefficients in the depth-averaged pollutant transport models. The 2D STRP-*i*, which is developed in this study, was validated using the synthetic data and the artificially constructed meandering channels. More evaluation is required to ensure the feasibility of 2D STRP-*i* in the natural river.

In order to determine the best-fitted distribution by 2D STRP-*i,* this study employed the Latin Hypercube Simulation. This approach is more reliable than the gradient-based optimization techniques in the aspect of the local minima problems. However, this approach required massive computational efforts. A more efficient method to find the optimum values of dispersion coefficients is desirable. The heuristic optimization methods, such as the kind of genetic algorithm, may be candidates.

The numerical model for 2D ADE in the orthogonal curvilinear coordinates was developed for the evaluation of 2D STRP and 2D STRP-*i*. In this study, the numerical model was used in simple geometries rather than irregularly-shaped channels in order to obtain the numerical solution of 2D ADE. In order to employ this numerical model for general purposes, the developed model has to be improved in terms of the numerical scheme. The temporal integration of this numerical model was treated as the first order explicit method. It may cause serious numerical diffusion in the simulation with the large time-step. Thus, the high order time derivative method, such as the 4^{th} order Runge-Kutta, could be improved the accuracy of this model.

Also, the implicit method may be desirable for the stable numerical solution for a large time-step.

In terms of remote sensing based-tracer tests, this study applies the ANN model to find the empirical relationship between the concentration of fluorescent dye and the digital number of RGB imagery. The various machine learning techniques have recently been adopted in the study of remote sensing for the monitoring of water qualities. More evaluation and comparison studies are needed to generalize the remote-sensing based-tracer tests. Moreover, this study used typical RGB imageries to detect the fluorescent dye. The acquisition of multi- or hyperspectral image data could facilitate the analysis of the optical characteristics of fluorescent dye in the natural river where the various optical signal is mixed.

References

Aguirre-Gomez, R. (2000). Detection of total suspended sediments in the North Sea using AVHRR and ship data. *International Journal of Remote Sensing*, 21(8), 1583-1596.

Baek, K. O., & Seo, I. W. (2010). Routing procedures for observed dispersion coefficients in two-dimensional river mixing. *Advances in Water Resources*, 33(12), 1551-1559.

Baek, K. O., & Seo, I. W. (2016). On the methods for determining the transverse dispersion coefficient in river mixing. *Advances in water resources*, 90, 1-9.

Baek, K. O., Seo, I. W., & Jeong, S. J. (2006). Evaluation of dispersion coefficients in meandering channels from transient tracer tests. *Journal of Hydraulic Engineering*, 132(10), 1021-1032.

Beltaos, S. (1980). Transverse mixing tests in natural streams. *Journal of the Hydraulics Division*, 106(10), 1607-1625.

Bencala, K. E., & Walters, R. A. (1983). Simulation of solute transport in a mountain pool-and-riffle stream: A transient storage model. *Water Resources Research*, 19(3), 718-724.

Brando, V. E., & Dekker, A. G. (2003). Satellite hyperspectral remote sensing for estimating estuarine and coastal water quality. *IEEE transactions on geoscience and remote sensing*, 41(6), 1378-1387.

Bukata, R. P., Jerome, J. H., Kondratyev, A. S., & Pozdnyakov, D. V. (2018). Optical properties and remote sensing of inland and coastal waters. CRC press.

Cannizzaro, J. P., and Carder, K. L. (2006). Estimating chlorophyll-a concentrations from remote-sensing reflectance in optically shallow waters. *Remote Sensing of*

Environment, 101(1), 13-24.

Carbonneau, P. E., Lane, S. N. and Bergeron, N. (2006). Feature based image processing methods applied to bathymetric measurements from airborne remote sensing in fluvial environments. *Earth Surface Processes and Landforms*, 31(11), 1413-1423.

Catts, G. P., Khorram, S., Cloern, J. E., Knight, A. W. and Degloria, S. D. (1985). Remote sensing of tidal chlorophyll-a variations in estuaries. *International Journal of Remote Sensing*, 6(11), 1685-1706.

Chacon-Torres, A., Ross, L. G., Beveridge, M. C. M. and Watson, A. I. (1992). The application of SPOT multispectral imagery for the assessment of water quality in Lake Patzcuaro, Mexico. *International Journal of Remote Sensing*, 13(4), 587-603.

Chang, Y. C. (1971). Lateral Mixing in Meandering channels. Ph.D. dissertation, University of Iowa, Iowa City.

Chen, J., Quan, W., Cui, T. and Song, Q. (2015). Estimation of total suspended matter concentration from MODIS data using a neural network model in the China eastern coastal zone. Estuarine, *Coastal and Shelf Science*, 155, 104-113.

Choi, H. J. (2017). Determination of Dispersion Coefficients of 2D Advection-Dispersion Model Based on Transient Tracer Tests. Ph.D. dissertation, Seoul National University.

Dekker, A. and Peters, S. (1993). The use of the Thematic Mapper for the analysis of eutrophic lakes: a case study in the Netherlands. *International Journal of Remote Sensing*, 14(5), 799-821.

Dekker, A., Zamurović-Nenad, Ž., Hoogenboom, H. and Peters, S. (1996). Remote sensing, ecological water quality modelling and in situ measurements: a case study in shallow lakes. *Hydrological Sciences Journal*, 41(4), 531-547.

Detert, M., & Weitbrecht, V. (2015). A low-cost airborne velocimetry system: proof

of concept. *Journal of Hydraulic Research*, 53(4), 532-539.

Dierberg, F. E. and Carriker, N. E. (1994). Field testing two instruments for remotely sensing water quality in the Tennessee Valley. *Environmental science & technology*, 28(1), 16-25.

Duchi, J., Hazan, E. and Singer, Y. (2011). Adaptive subgradient methods for online learning and stochastic optimization. *Journal of Machine Learning Research*, 12(Jul), 2121-2159.

Eglajs, V., & Audze, P. (1977). New approach to the design of multifactor experiments. *Problems of Dynamics and Strengths*, 35(1), 104-107.

Estep, L. (1994). Bottom influence on the estimation of chlorophyll concentration in water from remotely sensed data. *Remote Sensing*, 15(1), 205-214.

Ferziger, J. H., & Perić, M. (2002). Computational methods for fluid dynamics. Vol. 3. Berlin: springer.

Fischer, H. B. (1966). Longitudinal dispersion in laboratory and natural streams. Report No. KH-R-12, California Institute of Technology.

Fisher, H. B. (1968). Dispersion predictions in natural streams. *Journal of the Sanitary Engineering Division*, 94(5), 927-944.

Fischer, H. B, List, E., Koh, R., Imberger, J. and Brooks, N. (1979). Mixing in inland and coastal waters. Academic Press, New York.

Flener, C., Lotsari, E., Alho, P. and Käyhkö, J. (2012). Comparison of empirical and theoretical remote sensing based bathymetry models in river environments. *River Research and Applications*, 28(1), 118-133.

Flynn, K. F. and Chapra, S. C. (2014). Remote sensing of submerged aquatic vegetation in a shallow non-turbid river using an unmanned aerial vehicle. *Remote Sensing*, 6(12), 12815-12836.

Fonstad, M. A. and Marcus, W. A. (2005). Remote sensing of stream depths with

hydraulically assisted bathymetry (HAB) models. *Geomorphology*, 72(1-4), 320-339.

Fraser, R. (1998). Multispectral remote sensing of turbidity among Nebraska Sand Hills lakes. *International Journal of Remote Sensing*, 19(15), 3011-3016.

Fujita, I., Muste, M. and Kruger, A. (1998). Large-scale particle image velocimetry for flow analysis in hydraulic engineering applications. *Journal of hydraulic Research*, 36(3), 397-414.

Fukuoka, S., & Sayre, W. W. (1973). Longitudinal dispersion in sinuous channels. *Journal of the Hydraulics Division*, 99(1), 195-217.

Gholizadeh, M., Melesse, A., & Reddi, L. (2016). A comprehensive review on water quality parameters estimation using remote sensing techniques. *Sensors*, 16(8), 1298.

Glorot, X. and Bengio, Y. (2010). Understanding the difficulty of training deep feedforward neural networks. *PMLR*, 9, 249–256. https://doi.org/10.1.1.207.2059

Godfrey, R. G. and Frederick, B. J. (1970). Stream dispersion at selected sites. Professional Paper, No. 433-K, U.S. Geological Survey.

Gooseff, M. N., Wondzell, S. M., Haggerty, R., & Anderson, J. (2003). Comparing transient storage modeling and residence time distribution (RTD) analysis in geomorphically varied reaches in the Lookout Creek basin, Oregon, USA. *Advances in Water Resources*, 26(9), 925-937.

Harden, T. O., & Shen, H. T. (1979). Numerical simulation of mixing in natural rivers. *Journal of the Hydraulics Division*, 105(4), 393-408.

Harten, A. (1983). High resolution schemes for hyperbolic conservation laws. *Journal of computational physics*, 49(3), 357-393.

Harrington Jr, J. A., Schiebe, F. R. and Nix, J. F. (1992). Remote sensing of Lake Chicot, Arkansas: Monitoring suspended sediments, turbidity, and Secchi depth with Landsat MSS data. *Remote Sensing of environment*, 39(1), 15-27.

Holley, E. R., Siemons, J., & Abraham, G. (1972). Some aspects of analyzing

transverse diffusion in rivers. *Journal of Hydraulic Research*, 10(1), 27-57.

Hwang, H. and Haddad, R. A. (1995). Adaptive median filters: new algorithms and results. *IEEE Transactions on image processing*, 4(4), 499-502.

Iman, R. L., Davenport, J. M., & Zeigler, D. K. (1980). Latin hypercube sampling (program user's guide). [LHC, in FORTRAN] (No. SAND-79-1473). Sandia Labs., Albuquerque, NM (USA).

Jordan, D. C. and Fonstad, M. A. (2005). Two dimensional mapping of river bathymetry and power using aerial photography and GIS on the Brazos River, Texas. *Geocarto International*, 20(3), 13-20.

Jung, S. H., Seo, I. W., Kim, Y. D., & Park, I. (2019). Feasibility of Velocity-Based Method for Transverse Mixing Coefficients in River Mixing Analysis. *Journal of Hydraulic Engineering*, 145(11), 04019040.

Keiner, L. E. and Yan, X.-H. (1998). A neural network model for estimating sea surface chlorophyll and sediments from thematic mapper imagery. *Remote Sensing of environment*, 66(2), 153-165.

Kilpatrick, F. A. (1970). Dosage requirements for slug injections of rhodamine BA and WT dyes. U.S. Government Printing Office, Washington, DC.

Kilpatrick, F. A. and Wilson, J. F. (1989). Measurement of time of travel in streams by dye tracing. Tecniques of Water-Resources Investigation 3-A9, U.S. Geological Survey.

Krishnappan, B. G., & Lau, Y. L. (1977). Transverse mixing in meandering channels with varying bottom topography. *Journal of Hydraulic Research*, 15(4), 351-370.

Laanen, M.L. (2007). Yellow matters improving the remote sensing of coloured dissolved organic matter in inland freshwaters. Ph.D. dissertation, VU University, Amsterdam.

Lathrop, R. G. (1992). Landsat Thematic Mapper monitoring of turbid inland water

quality. *Photogrammetric Engineering and Remote Sensing*, 58, 465-470

Lathrop, R. G., Lillesand, T. M. and Yandell, B. S. (1991). Testing the utility of simple multi-date Thematic Mapper calibration algorithms for monitoring turbid inland waters. *Remote Sensing*, 12(10), 2045-2063.

Lau, Y. L., & Krishnappan, B. G. (1981). Modeling transverse mixing in natural streams. *Journal of the Hydraulics Division*, 107(2), 209-226.

Lien, F. S., & Leschziner, M. A. (1994). Upstream monotonic interpolation for scalar transport with application to complex turbulent flows. *International Journal for Numerical Methods in Fluids*, 19(6), 527-548.

Legleiter, C. J., Roberts, D. A., Marcus, W. A., & Fonstad, M. A. (2004). Passive optical remote sensing of river channel morphology and in-stream habitat: Physical basis and feasibility. *Remote Sensing of Environment*, 93(4), 493-510.

Legleiter, C. J. and Fonstad, M. A. (2012). An introduction to the physical basis for deriving river information by optical remote sensing. In: Carbonneau, P., Piégay, H. (eds.) Fluvial Remote Sensing for Science and Management, pp. 43–69. Wiley-Blackwell, Chichester, UK.

Lee, Z., Carder, K. L., Mobley, C. D., Steward, R. G., and Patch, J. S. (1999). Hyperspectral remote sensing for shallow waters: 2. Deriving bottom depths and water properties by optimization. *Applied optics*, 38(18), 3831-3843.

Lien, F. S., & Leschziner, M. A. (1994). Upstream monotonic interpolation for scalar transport with application to complex turbulent flows. *International Journal for Numerical Methods in Fluids*, 19(6), 527-548.

Liu, Y., Islam, M. A. and Gao, J. (2003). Quantification of shallow water quality parameters by means of remote sensing. *Progress in physical geography*, 27(1), 24-43.

Louchard, E. M., Reid, R. P., Stephens, F. C., Davis, C. O., Leathers, R. A., and T.

Valerie, D. (2003). Optical remote sensing of benthic habitats and bathymetry in coastal environments at Lee Stocking Island, Bahamas: A comparative spectral classification approach. *Limnology and Oceanography*, 48, 511-521.

Lyzenga, D. R. (1981). Remote sensing of bottom reflectance and water attenuation parameters in shallow water using aircraft and Landsat data. *International Journal of Remote Sensing*, 2(1), 71-82.

Maritorena, S., Morel, A. and Gentili, B. (1994). Diffuse reflectance of oceanic shallow waters: Influence of water depth and bottom albedo. *Limnology and oceanography*, 39(7), 1689-1703.

Matthews, M. W. (2011). A current review of empirical procedures of remote sensing in inland and near-coastal transitional waters. *International Journal of Remote Sensing*, 32(21), 6855-6899.

McKay, M. D., Beckman, R. J., & Conover, W. J. (1979). Comparison of three methods for selecting values of input variables in the analysis of output from a computer code. *Technometrics*, 21(2), 239-245.

Mobley, C. D. (1994). Light and Water: Radiative Transfer in Natural Waters. Academic Press, New York.

Mobley, C. D., Sundman, L. K., Davis, C. O., Bowles, J. H., Downes, T. V., Leathers, R. A., Montes M.J., Bissett W.P., Kohler D.D.R., Reid R.P., Louchard E.M. and Gleason A. (2005). Interpretation of hyperspectral remote-sensing imagery by spectrum matching and look-up tables. *Applied Optics*, 44(17), 3576-3592.

Mukherjee, A., Fryar, A. E., & LaSage, D. M. (2005). Using tracer tests to assess natural attenuation of contaminants along a channelized Coastal Plain stream. *Environmental & Engineering Geoscience*, 11(4), 371-382.

Nazeer, M., Wong, M. S. and Nichol, J. E. (2017). A new approach for the estimation of phytoplankton cell counts associated with algal blooms. *Science of the total environment*, 590, 125-138.

Nordin, C. F. and Sabol, G. V. (1974). Empirical data on longitudinal dispersion in rivers. Water-Resources Investigations Report 74-20, U.S. Geological Survey.

Olmanson, L. G., Brezonik, P. L., & Bauer, M. E. (2013). Airborne hyperspectral remote sensing to assess spatial distribution of water quality characteristics in large rivers: The Mississippi River and its tributaries in Minnesota. *Remote Sensing of Environment*, 130, 254-265.

Palmer, S. C., Kutser, T., & Hunter, P. D. (2015). Remote sensing of inland waters: Challenges, progress and future directions. *Remote Sensing of Environment*, 157, 1–8.

Park, I. (2017). A Two-dimensional Particle Dispersion Model for Prediction of Pollutant Mixing in Open Channels. Ph.D. dissertation, Seoul National University.

Pattiaratchi, C., Lavery, P., Wyllie, A. and Hick, P. (1994). Estimates of water quality in coastal waters using multi-date Landsat Thematic Mapper data. *International Journal of Remote Sensing*, 15(8), 1571-1584.

Peddle, D. R., White, H. P., Soffer, R. J., Miller, J. R. and LeDrew, E. F. (2001). Reflectance processing of remote sensing spectroradiometer data. *Computers & Geosciences*, 27(2), 203-213.

Philpot, W. D. (1987). Radiative transfer in stratified waters: a single-scattering approximation for irradiance. *Applied optics*, 26(19), 4123-4132.

Piasecki, M., & Katopodes, N. D. (1999). Identification of stream dispersion coefficients by adjoint sensitivity method. *Journal of Hydraulic Engineering*, 125(7), 714-724.

Pozdnyakov, D., Grassl, H. and Graßl, H. (2003). Color of Inland and Coastal Waters: A Methodology for its Interpretation, Springer Science & Business Media.

Rimmer, J., Collins, M. and Pattiaratchi, C. (1987). Mapping of water quality in coastal waters using Airborne Thematic Mapper data. *International Journal of*

Remote Sensing, 8(1), 85-102.

Ritchie, J. C., Cooper, C. M. and Schiebe, F. R. (1990). The relationship of MSS and TM digital data with suspended sediments, chlorophyll, and temperature in Moon Lake, Mississippi. *Remote Sensing of environment*, 33(2), 137-148.

Ritchie, J. C., McHenry, J. R., Schiebe, F. R. and Wilson, R. B. (1975). relationship of reflected solar radiation and the concentration of sediment in the surface water of reservoirs. *Remote sensing of earth resources*.

Roe, P. L. (1985). Modelling of Discontinuous Flows. *Lectures in Applied Mathematics*, 22.

Rowiński, P. M., & Chrzanowski, M. M. (2011). Influence of selected fluorescent dyes on small aquatic organisms. *Acta Geophysica*, 59(1), 91-109.

Rowiński, P. M., Guymer, I. A. N., & Kwiatkowski, K. (2008). Response to the slug injection of a tracer—a large-scale experiment in a natural river. *Hydrological sciences journal*, 53(6), 1300-1309.

Rumelhart, D. E., Hinton, G. E. and Williams, R. J. (1986). Learning representations by back-propagating errors. *nature*, 323(6088), 533.

Rutherford, J. C. (1994). River mixing, Chichester, England, John Wiley and Sons, 48-51.

Sayre, W. W. (1968). A laboratory investigation of open-channel dispersion processes for dissolved, suspended, and floating dispersants. US Government Printing Office.

Schiebe, F., Harrington Jr, J. and Ritchie, J. (1992). Remote sensing of suspended sediments: the Lake Chicot, Arkansas project. *International Journal of Remote Sensing*, 13(8), 1487-1509.

Seo, I. W., & Baek, K. O. (2004). Estimation of the longitudinal dispersion coefficient using the velocity profile in natural streams. *Journal of hydraulic*

engineering, 130(3), 227-236.

Seo, I., Baek, K. O. and Jeon, T. M. (2006). Analysis of transverse mixing in natural streams under slug tests. *Journal of Hydraulic Research*, 44(3), 350-362.

Seo, I. W., Choi, H. J., Kim, Y. D. and Han, E. J. (2016). Analysis of two-dimensional mixing in natural streams based on transient tracer tests. *Journal of Hydraulic Engineering*, 142(8), 04016020.

Seo, I. W., Lee, M. E., & Baek, K. O. (2008). 2D modeling of heterogeneous dispersion in meandering channels. *Journal of Hydraulic Engineering*, 134(2), 196-204.

Shen, H. T. (1978). Transient mixing in river channels. *Journal of the Environmental Engineering Division*, 104(3), 445-459.

Shin, J., Seo, I. W., & Baek, D. (2019). Longitudinal and transverse dispersion coefficients of 2D contaminant transport model for mixing analysis in open channels. *Journal of Hydrology*, 124302.

Singh, S. K., & Beck, M. B. (2003). Dispersion coefficient of streams from tracer experiment data. *Journal of environmental engineering*, 129(6), 539-546.

Sun, Y., Wells, M., Bailey, S., Anderson, E. J., & Schwab, D. J. (2011). Study on the physical mixing patterns in the St. Clair River by dye release. In Proc., 15th Workshop on Physical Processes in Natural Waters (pp. 180-182).

Sweby, P. K. (1984). High resolution schemes using flux limiters for hyperbolic conservation laws. *SIAM journal on numerical analysis*, 21(5), 995-1011.

Tamminga, A., Hugenholtz, C., Eaton, B. and Lapointe, M. (2015). Hyperspatial remote sensing of channel reach morphology and hydraulic fish habitat using an unmanned aerial vehicle (UAV): a first assessment in the context of river research and management. *River Research and Applications*, 31(3), 379-391.

Transon, J., d'Andrimont, R., Maugnard, A., & Defourny, P. (2018). Survey of

hyperspectral earth observation applications from space in the sentinel-2 context. *Remote Sensing*, 10(2), 157.

Van Albada, G.D., Van Leer, B., & Roberts, W.W. (1982). A comparative study of computational methods in cosmic gas dynamics. *Astronomy and Astrophysics*, 108: 76–84

Van Leer, B. (1974). Towards the ultimate conservative difference scheme. II. Monotonicity and conservation combined in a second-order scheme. *Journal of computational physics*, 14(4), 361-370.

Versteeg, H. K., & Malalasekera, W. (2007). An introduction to computational fluid dynamics: the finite volume method. Pearson education.

Whitlock, C. H., Kuo, C. Y., & LeCroy, S. R. (1982). Criteria for the use of regression analysis for remote sensing of sediment and pollutants. *Remote Sensing of Environment*, 12(2), 151-168.

Wigmore, O., & Mark, B. G. (2017). Monitoring tropical debris-covered glacier dynamics from high-resolution unmanned aerial vehicle photogrammetry, Cordillera Blanca, Peru. *The Cryosphere*, (11), 2463.

Wilson, J. F., Cobb, E. D., & Kilpatrick, F. A. (1986). Fluorometric procedures for dye tracing (p. 31). Department of the Interior, US Geological Survey.

Winterbottom, S. J. and Gilvear, D. J. (1997). Quantification of channel bed morphology in gravel-bed rivers using airborne multispectral imagery and aerial photography. *River Research and Applications*, 13(6), 489-499.

Woodget, A. S., Austrums, R., Maddock, I. P. and Habit, E. (2017). Drones and digital photogrammetry: From classifications to continuums for monitoring river habitat and hydromorphology. *Wiley Interdisciplinary Reviews: Water*, 4(4).

Yotsukura, N. (1977). Derivation of solute-transport equations for a turbulent natural-channel flow. Jour. Research U.S. Geol. Survey., 5(3), 277-284.

Yotsukura, N., & Cobb, E. D. (1972). Transverse diffusion of solutions in natural streams. US Geo. Survey Paper, (582).

Yotsukura, N., & Sayre, W. W. (1976). Transverse mixing in natural channels. *Water Resources Research*, 12(4), 695-704.

Zhang, D., Jiang, C., Liang, D., & Cheng, L. (2015). A review on TVD schemes and a refined flux-limiter for steady-state calculations. *Journal of Computational Physics*, 302, 114-154.

Zhang, Y., Pulliainen, J., Koponen, S. and Hallikainen, M. (2002). Application of an empirical neural network to surface water quality estimation in the Gulf of Finland using combined optical data and microwave data. *Remote Sensing of Environment*, 81(2-3), 327-336.

Appendix

Appendix A. Program code of numerical model for 2D ADE

```
# Code Writer : D. Baek
# Code Description : FVM model for 2D ADE in natural coordinates
# Programming Language : Python 3.7
# Required library : numpy, matplotlib, numba (optional)

import numpy as np
from matplotlib import pyplot as plt
from copy import deepcopy

#input value by user
mass = 1    # mass injected
w = 12    # channel width
h_value = 1    # mean water dpeth
u_value = 0.5    # mean longitudinal velocity
v_value = 0      # mean transverse velocity

DL_value = 0.1    # longitudinal dispersion coeff.
DT_value = 0.01    # transverse dispersion coeff.

src_value = 0    # source value
LCT  =     u_value*(w/2)**2/DT_value*1.5*0.3     # distance for complete of transverse mixing
LCV = 0    # distance for complete of vertical mixing (optional)

# simulation condition
t_end = LCT/(u_value*1.5)    # end time for simulation
D_size = [w, LCT-LCV]    # domain size
n_num = 501    # number of calculation cell in transverse direction
dn = D_size[0]/n_num    # cell size in transverse direction
s_num = 501    # number of calculation cell in longitudinal direction
ds = D_size[1]/s_num    # cell size in longitudinal direction

# generation of Computational grid
grid_s_itv = np.arange((LCV-ds*10)-(ds/2),LCT+ds, ds/2)
grid_n_itv = np.arange(0,D_size[0]+dn, dn/2)
[grid_s, grid_n] = np.meshgrid(grid_s_itv, grid_n_itv)
```

```
node_s_itv = np.arange(grid_s_itv[1], LCT, ds)
node_n_itv = np.arange(grid_n_itv[1], D_size[0], dn)
[node_s, node_n] = np.meshgrid(node_s_itv, node_n_itv)

# defining variables at surface of cell
ms = np.ones([np.shape(grid_s)[0], np.shape(grid_s)[1]])
mn = np.ones([np.shape(grid_n)[0], np.shape(grid_n)[1]])
h = np.ones([np.shape(grid_n)[0], np.shape(grid_n)[1]])*h_value
u = stats.beta.pdf(grid_n/w, 1.2, 1.2)*u_value
v = np.ones([np.shape(grid_n)[0], np.shape(grid_n)[1]])*v_value
DL = np.ones([np.shape(grid_n)[0], np.shape(grid_n)[1]])*DL_value
DT = np.ones([np.shape(grid_n)[0], np.shape(grid_n)[1]])*DT_value

Fh = mn*h*u
Fv = ms*h*v
Eh = (mn/ms)*h*DL/ds
Ev = (ms/mn)*h*DT/dn

# defining variables at the center of cell
hP = np.ones([np.shape(node_n)[0], np.shape(node_n)[1]])*h_value
lamdaP = np.ones([np.shape(node_n)[0], np.shape(node_n)[1]])*src_value

# estimate the time step for numerical stability
dt=1 / (    (np.max(u)/ds)+(2*DL_value/ds**2)+(2*DT_value/dn**2)       )
dt = dt*0.9
write_step = 15 # write interval of numerical solutions

# setting the boundary conditions
Fh_mx, Fv_mx, Eh_mx, Ev_mx, mn_mx, ms_mx= param(np.shape(node_s)[0],
np.shape(node_s)[1], Fh, Fv, Eh, Ev, mn, ms)
Fh_e = Fh_mx[:,:,0]
Fh_w = Fh_mx[:,:,1]
Fv_n = Fv_mx[:,:,0]
Fv_n[0,:] = 0
Fv_s = Fv_mx[:,:,1]
Fv_s[-1,:] =
Eh_e = Eh_mx[:,:,0]
Eh_e[:,-1] = 0
Eh_w = Eh_mx[:,:,1]
Eh_w[:,0] = Eh_w[:,0]*2
Ev_n = Ev_mx[:,:,0]
```

```
Ev_n[0,:] = 0
Ev_s = Ev_mx[:,:,1]
Ev_s[-1,:] = 0
mn_e = mn_mx[:,:,0]
mn_w = mn_mx[:,:,1]
ms_n = ms_mx[:,:,0]
ms_s = ms_mx[:,:,1]

# setting the initial concentration field
C0 = np.zeros([np.shape(node_n)[0], np.shape(node_n)[1]])
inj_loc = np.int(C0.shape[0]/2)
C0[inj_loc, 10] = mass / (ds*dn*h_value)
C_pre = deepcopy(C0)

# computation start
ttt=0
for t in range(0, int(t_end/dt)) :

    C_inlet = np.zeros(np.shape(C0)[0])
    C = C_pre[:,:]

    TERM1 = np.zeros([np.shape(C0)[0], np.shape(C0)[1]])
    TERM2 = np.zeros([np.shape(C0)[0], np.shape(C0)[1]])
    TERM3 = np.zeros([np.shape(C0)[0], np.shape(C0)[1]])
    TERM4 = np.zeros([np.shape(C0)[0], np.shape(C0)[1]])
    TERM5 = np.zeros([np.shape(C0)[0], np.shape(C0)[1]])

    C_P = C[:,:]
    C_E = shift_nan(C_P, -1, 1)
    C_E[:,-1] = C_P[:,-1]
    C_W = shift_nan(C_P, 1, 1)
    C_W[:,0] = C_inlet[:]
    C_WW = shift_nan(C_P, 2, 1)
    C_WW[:,0] = C_inlet[:]
    C_WW[:,1] = C_inlet[:]

    C_N = shift_nan(C_P, 1, 0)
    C_N[0,:] = C_P[0,:] #dummy
    C_S = shift_nan(C_P, -1, 0)
    C_S[-1,:] = C_P[-1,:]

    C_SS = shift_nan(C_P, -2, 0)
```

```
        C_SS[-1,:] = C_P[-1,:]
        C_SS[-2,:] = C_P[-2,:]

# Conc. Slope for TVD scheme
        r_e = (C_P-C_W) / (C_E-C_P+0.0000000000000001)
        r_w = (C_W-C_WW) / (C_P-C_W+0.0000000000000001)
        r_n = (C_P-C_S) / (C_N-C_P+0.0000000000000001)
        r_s = (C_S-C_SS) / (C_P-C_S+0.0000000000000001)

        limiter_e = (r_e+r_e**2) / (1+r_e**2)
        limiter_w = (r_w+r_w**2) / (1+r_w**2)
        limiter_n = (r_n+r_n**2) / (1+r_n**2)
        limiter_s = (r_s+r_s**2) / (1+r_s**2)

        C_e = C_P + 0.5 * limiter_e * (C_E-C_P)
        C_w = C_W + 0.5 * limiter_w * (C_P-C_W)
        C_n = C_P + 0.5 * limiter_n * (C_N-C_P)
        C_s = C_S + 0.5 * limiter_s * (C_P-C_S)

        TERM1 = -(Fh_e*C_e - Fh_w*C_w) * dn
        TERM2 = -(Fv_n*C_n - Fv_s*C_s) * ds
        TERM3 = (Eh_e*(C_E-C_P) - Eh_w*(C_P-C_W) )*dn
        TERM4 = (Ev_n*(C_N-C_P) - Ev_s*(C_P-C_S) )*ds
        TERM5 = lamdaP*ds*dn

        C_pre = C + dt/(hP*ds*dn) * (TERM1 + TERM2 + TERM3 + TERM4 + TERM5)

        if t==ttt*write_step:
                filename = "P9000_U1_"+str(s_num)+"_step"+str(t)+".csv"
                np.save(filename, C_pre)
                ttt=ttt+1

np.save("node_s", node_s)
np.save("node_n", node_n)

def shift_nan(A, n, axis):
        shift_tmp = np.empty((np.shape(A)[0], np.shape(A)[1]))
        shift_tmp[:] = float('nan')
        if axis==0:
                if n>=0:
                        shift_tmp[n:, :] = A[:-n,:]
                else:
```

```
                shift_tmp[:n, :] = A[-n:,:]

        else:
                if n>=0:
                        shift_tmp[:, n:] = A[:,:-n]
                else:
                        shift_tmp[:, :n] = A[:, -n:]

        return shift_tmp

# limiter functions for TVD
def limfunc(r, f):
        if f == 1:
                limout = 0 # UD
        elif f == 2:
                limout = 1 # CDS
        elif f == 3:
                limout = (3+r)/4 # QUICK
        elif f == 4:
                limout = (r+r**2) / (1+r**2) # Van Albada
        elif f == 5:
                D1 = np.zeros([np.shape(r)[0], np.shape(r)[1]])
                D2 = np.min(np.dstack([r*2, np.ones([np.shape(r)[0],
np.shape(r)[1]])]),2)
                D3 = np.min(np.dstack([r, np.ones([np.shape(r)[0],
np.shape(r)[1]])*2]),2)
                limout = np.max(np.dstack([D1, D2, D3]),2) # SUPERBEE
        elif f == 6:
                D1 = np.zeros([np.shape(r)[0], np.shape(r)[1]])
                D2 = np.min(np.dstack([r*2, (1+3*r)/4, (3+r)/4,
np.ones([np.shape(r)[0], np.shape(r)[1]])*2]),2)
                limout = np.max(np.dstack([D1, D2]),2) # UMIST

        elif f == 7:
                limout = (r+np.abs(r)) / (1+r) # Van Leer

        elif f == 8:
                        D1 = np.min(np.dstack([r, np.ones([np.shape(r)[0],
np.shape(r)[1]]) ]),2)
                        D2 = r
                        D3 = np.min(np.dstack([D1, D2]),2)
                        D3[D3<0] = 0
```

```
                limout = D3 # min-mod

        elif f == 9:
                D1 = np.zeros([np.shape(r)[0], np.shape(r)[1]])
                D2 = np.min(np.dstack([r*1.5, np.ones([np.shape(r)[0],
np.shape(r)[1]])]),2)
                D3 = np.min(np.dstack([r, np.ones([np.shape(r)[0],
np.shape(r)[1]])*1.5]),2)
                limout = np.max(np.dstack([D1, D2, D3]),2) # sweby beta 1.5

        return limout

def param(i_size, j_size, Fh, Fv, Eh, Ev, mn, ms):
        ms_mx = np.zeros([i_size, j_size, 2])
        mn_mx = np.zeros([i_size, j_size, 2])
        Fh_mx = np.zeros([i_size, j_size, 2])
        Fv_mx = np.zeros([i_size, j_size, 2])
        Eh_mx = np.zeros([i_size, j_size, 2])
        Ev_mx = np.zeros([i_size, j_size, 2])
        for i in range(0, i_size): #np.shape(C0)[0]
                for j in range (0, j_size): #np.shape(C0)[1]
                        Fh_mx[i,j,0] = Fh[2*i+1, 2*j+2]              #0 east
                        Fh_mx[i,j,1] = Fh[2*i+1, 2*j]   #1 west
                        Fv_mx[i,j,0] = Fv[2*i, 2*j+1]   #0 north
                        Fv_mx[i,j,1] = Fv[2*i+2, 2*j+1]#1 south

                        Eh_mx[i,j,0] = Eh[2*i+1, 2*j+2]            #0 east
                        Eh_mx[i,j,1] = Eh[2*i+1, 2*j]   #1 west
                        Ev_mx[i,j,0] = Ev[2*i, 2*j+1]   #0 north
                        Ev_mx[i,j,1] = Ev[2*i+2, 2*j+1]#1 south

                        mn_mx[i,j,0] = mn[2*i+1, 2*j+2]
                        mn_mx[i,j,1] = mn[2*i+1, 2*j]
                        ms_mx[i,j,0] = ms[2*i, 2*j+1]
                        ms_mx[i,j,1] = ms[2*i+2, 2*j+1]
        return Fh_mx, Fv_mx, Eh_mx, Ev_mx, mn_mx, ms_mx
```

Appendix B. Tracer test results in EXP-A315

Table B1. Velocity and water depth measurement using ADCP
a) Sec. 1

UTM Easting (m)	UTM Northing (m)	Water depth (m)	Distance from left bank (m)	Streamwise Velocity (cm/s)	Transverse Velocity (cm/s)	Vertical Velocity (cm/s)
460,876.8	4,046,210.5	0.1	0.4	58.5	8.7	-2.1
460,876.9	4,046,210.6	0.1	0.5	62.8	8.4	-1.8
460,877.0	4,046,210.6	0.1	0.6	77.1	10.9	-1.5
460,877.1	4,046,210.6	0.1	0.7	90.2	9.6	-1.5
460,877.1	4,046,210.6	0.2	0.7	92.8	8.4	-1.7
460,877.2	4,046,210.6	0.1	0.8	97.8	9.4	-1.5
460,877.2	4,046,210.6	0.2	0.8	99.9	7.5	-1.5
460,877.2	4,046,210.6	0.3	0.8	102.4	7.0	-2.0
460,877.3	4,046,210.6	0.1	0.9	103.3	5.8	-1.2
460,877.3	4,046,210.6	0.2	0.9	104.1	4.2	-1.2
460,877.3	4,046,210.6	0.3	0.9	105.0	1.8	-1.5
460,877.3	4,046,210.6	0.4	0.9	105.3	-1.4	-1.6
460,877.4	4,046,210.7	0.1	1.0	102.3	2.7	-1.3
460,877.4	4,046,210.7	0.2	1.0	102.5	1.2	-1.1
460,877.4	4,046,210.7	0.3	1.0	102.8	-0.9	-1.1
460,877.4	4,046,210.7	0.4	1.0	102.6	-1.9	-0.7
460,877.5	4,046,210.7	0.1	1.1	100.0	0.0	-1.3
460,877.5	4,046,210.7	0.2	1.1	100.4	-1.2	-1.5
460,877.5	4,046,210.7	0.3	1.1	101.1	-3.1	-1.3
460,877.5	4,046,210.7	0.4	1.1	99.2	-4.7	-1.6
460,877.6	4,046,210.7	0.1	1.2	97.8	0.4	-1.6
460,877.6	4,046,210.7	0.2	1.2	97.9	-0.9	-2.0
460,877.6	4,046,210.7	0.3	1.2	98.5	-2.3	-1.7
460,877.6	4,046,210.7	0.4	1.2	96.8	-4.4	-1.7
460,877.6	4,046,210.7	0.5	1.2	95.7	-5.0	-0.9
460,877.7	4,046,210.7	0.1	1.3	96.9	2.3	-0.9
460,877.7	4,046,210.7	0.2	1.3	97.2	0.9	-1.4
460,877.7	4,046,210.7	0.3	1.3	97.6	-2.3	-1.4
460,877.7	4,046,210.7	0.4	1.3	93.8	-6.1	-2.1
460,877.8	4,046,210.7	0.1	1.4	95.0	4.2	-0.6
460,877.8	4,046,210.7	0.2	1.4	95.3	2.3	-0.9
460,877.8	4,046,210.7	0.3	1.4	95.9	-1.8	-1.0
460,877.8	4,046,210.7	0.4	1.4	92.6	-5.3	-1.5
460,877.8	4,046,210.7	0.5	1.4	90.7	-7.6	-1.4
460,877.9	4,046,210.8	0.1	1.5	93.2	4.8	-0.3
460,877.9	4,046,210.8	0.2	1.5	94.2	2.4	-0.4
460,877.9	4,046,210.8	0.3	1.5	95.1	-1.5	-0.8
460,877.9	4,046,210.8	0.4	1.5	91.7	-4.1	-1.5
460,877.9	4,046,210.8	0.5	1.5	89.4	-5.0	-1.9
460,878.0	4,046,210.8	0.1	1.6	91.0	4.2	-0.7
460,878.0	4,046,210.8	0.2	1.6	91.9	2.0	-0.7
460,878.0	4,046,210.8	0.3	1.6	93.4	-1.4	-1.3
460,878.0	4,046,210.8	0.4	1.6	90.7	-2.3	-1.5
460,878.0	4,046,210.8	0.5	1.6	89.1	-2.3	-1.7
460,878.0	4,046,210.8	0.1	1.7	88.9	2.9	-0.2
460,878.0	4,046,210.8	0.2	1.7	90.4	1.2	-0.6
460,878.0	4,046,210.8	0.3	1.7	92.4	-1.6	-1.3
460,878.0	4,046,210.8	0.4	1.7	89.7	-1.8	-1.3

460,878.0	4,046,210.8	0.5	1.7	87.8	-1.6	-1.3
460,878.1	4,046,210.8	0.1	1.8	88.1	2.2	-0.5
460,878.1	4,046,210.8	0.2	1.8	90.0	1.0	-1.0
460,878.1	4,046,210.8	0.3	1.8	91.6	-0.5	-1.6
460,878.1	4,046,210.8	0.4	1.8	88.9	-0.7	-1.3
460,878.1	4,046,210.8	0.5	1.8	86.5	-0.4	-0.9
460,878.2	4,046,210.8	0.1	1.9	87.1	3.5	-0.4
460,878.2	4,046,210.8	0.2	1.9	89.7	2.6	-1.1
460,878.2	4,046,210.8	0.3	1.9	91.1	2.3	-1.6
460,878.2	4,046,210.8	0.4	1.9	89.5	1.1	-1.4
460,878.2	4,046,210.8	0.5	1.9	86.8	1.2	-0.9
460,878.3	4,046,210.9	0.1	2.0	86.5	4.1	-0.5
460,878.3	4,046,210.9	0.2	2.0	87.9	3.5	-0.8
460,878.3	4,046,210.9	0.3	2.0	87.3	4.2	-1.3
460,878.3	4,046,210.9	0.4	2.0	85.7	2.0	-0.9
460,878.3	4,046,210.9	0.5	2.0	83.2	1.7	-0.7
460,878.4	4,046,210.9	0.1	2.1	82.9	3.4	0.1
460,878.4	4,046,210.9	0.2	2.1	83.1	3.1	0.1
460,878.4	4,046,210.9	0.3	2.1	80.8	3.3	-0.2
460,878.4	4,046,210.9	0.4	2.1	79.3	0.8	-0.2
460,878.4	4,046,210.9	0.5	2.1	77.1	0.0	-0.3
460,878.5	4,046,210.9	0.1	2.2	81.5	3.0	0.1
460,878.5	4,046,210.9	0.2	2.2	79.5	2.2	0.1
460,878.5	4,046,210.9	0.3	2.2	75.9	1.6	0.3
460,878.5	4,046,210.9	0.4	2.2	73.1	-0.7	0.5
460,878.5	4,046,210.9	0.5	2.2	71.8	-1.4	0.7
460,878.6	4,046,210.9	0.1	2.3	80.8	3.3	0.2
460,878.6	4,046,210.9	0.2	2.3	77.6	2.2	-0.1
460,878.6	4,046,210.9	0.3	2.3	74.0	1.0	0.3
460,878.6	4,046,210.9	0.4	2.3	70.5	-0.7	0.6
460,878.6	4,046,210.9	0.5	2.3	70.1	-1.0	1.3
460,878.7	4,046,210.9	0.1	2.4	79.0	3.2	0.5
460,878.7	4,046,210.9	0.2	2.4	75.5	1.8	0.1
460,878.7	4,046,210.9	0.3	2.4	72.6	-0.2	0.2
460,878.7	4,046,210.9	0.4	2.4	69.2	-1.9	0.6
460,878.8	4,046,211.0	0.1	2.5	75.1	1.4	1.1
460,878.8	4,046,211.0	0.2	2.5	72.9	0.1	0.7
460,878.8	4,046,211.0	0.3	2.5	70.1	-2.4	0.4
460,878.8	4,046,211.0	0.4	2.5	67.0	-3.8	0.5
460,878.9	4,046,211.0	0.1	2.6	72.4	-0.1	1.2
460,878.9	4,046,211.0	0.2	2.6	70.4	-1.4	0.9
460,878.9	4,046,211.0	0.3	2.6	66.0	-3.5	0.5
460,878.9	4,046,211.0	0.4	2.6	62.7	-4.6	0.4
460,879.0	4,046,211.0	0.1	2.7	72.4	-0.4	0.6
460,879.0	4,046,211.0	0.2	2.7	70.2	-1.6	0.2
460,879.0	4,046,211.0	0.3	2.7	64.9	-3.4	-0.2
460,879.0	4,046,211.0	0.4	2.7	61.1	-3.9	-0.4
460,879.1	4,046,211.0	0.1	2.8	71.8	0.6	0.1
460,879.1	4,046,211.0	0.2	2.8	69.2	-0.7	-0.2
460,879.1	4,046,211.0	0.3	2.8	63.0	-2.4	-0.4
460,879.1	4,046,211.0	0.4	2.8	59.0	-2.7	-0.6
460,879.2	4,046,211.0	0.1	2.9	70.4	1.3	-0.3
460,879.2	4,046,211.0	0.2	2.9	67.5	0.1	-0.5
460,879.2	4,046,211.0	0.3	2.9	60.6	-1.8	-0.5
460,879.2	4,046,211.0	0.4	2.9	56.2	-2.3	-0.6
460,879.3	4,046,211.1	0.1	3.0	67.9	1.3	-0.1
460,879.3	4,046,211.1	0.2	3.0	64.4	0.1	-0.2
460,879.3	4,046,211.1	0.3	3.0	56.3	-0.9	-0.1
460,879.3	4,046,211.1	0.4	3.0	50.7	-1.4	0.0

460,879.4	4,046,211.1	0.1	3.1	65.6	0.8	0.2
460,879.4	4,046,211.1	0.2	3.1	61.3	0.0	0.2
460,879.4	4,046,211.1	0.3	3.1	52.8	-0.4	0.4
460,879.4	4,046,211.1	0.4	3.1	46.4	-0.8	0.7
460,879.5	4,046,211.1	0.1	3.2	62.9	1.0	0.5
460,879.5	4,046,211.1	0.2	3.2	58.5	0.7	0.4
460,879.5	4,046,211.1	0.3	3.2	50.5	0.0	0.7
460,879.5	4,046,211.1	0.4	3.2	44.4	-0.2	0.9
460,879.6	4,046,211.1	0.1	3.3	60.1	2.3	0.4
460,879.6	4,046,211.1	0.2	3.3	56.2	1.4	0.2
460,879.6	4,046,211.1	0.3	3.3	48.2	0.0	0.3
460,879.6	4,046,211.1	0.4	3.3	43.1	-1.0	0.3
460,879.7	4,046,211.1	0.1	3.4	57.2	2.7	0.1
460,879.7	4,046,211.1	0.2	3.4	54.2	1.2	-0.2
460,879.7	4,046,211.1	0.3	3.4	47.3	-0.6	-0.8
460,879.7	4,046,211.1	0.4	3.4	43.9	-2.1	-1.2
460,879.8	4,046,211.2	0.1	3.5	54.7	0.8	0.3
460,879.8	4,046,211.2	0.2	3.5	52.1	-0.7	-0.1
460,879.8	4,046,211.2	0.3	3.5	46.7	-1.7	-1.1
460,879.8	4,046,211.2	0.4	3.5	44.1	-3.6	-1.8
460,879.9	4,046,211.2	0.1	3.6	52.1	-0.3	0.3
460,879.9	4,046,211.2	0.2	3.6	49.9	-1.2	-0.1
460,879.9	4,046,211.2	0.3	3.6	47.2	-1.9	-0.9
460,880.0	4,046,211.2	0.1	3.7	48.3	-0.3	0.5
460,880.0	4,046,211.2	0.2	3.7	46.2	-0.6	0.0
460,880.0	4,046,211.2	0.3	3.7	44.5	-0.8	-0.3
460,880.1	4,046,211.2	0.1	3.8	43.0	0.5	0.6
460,880.1	4,046,211.2	0.2	3.8	41.0	0.4	0.1
460,880.1	4,046,211.2	0.3	3.8	40.2	-0.1	-0.5
460,880.2	4,046,211.2	0.1	3.9	37.4	0.6	0.8
460,880.2	4,046,211.2	0.2	3.9	35.6	-0.3	0.1
460,880.2	4,046,211.2	0.3	3.9	35.2	-1.3	-0.5
460,880.3	4,046,211.3	0.1	4.0	35.1	0.3	0.4
460,880.3	4,046,211.3	0.2	4.0	33.1	-1.2	-0.1
460,880.3	4,046,211.3	0.3	4.0	31.8	-2.5	-0.6
460,880.4	4,046,211.3	0.1	4.1	33.8	-0.4	-0.1
460,880.4	4,046,211.3	0.2	4.1	31.8	-1.6	-0.3
460,880.4	4,046,211.3	0.3	4.1	30.1	-2.2	-0.5
460,880.5	4,046,211.3	0.1	4.2	32.4	-1.2	-0.5
460,880.5	4,046,211.3	0.2	4.2	30.9	-1.5	-0.5
460,880.5	4,046,211.3	0.3	4.2	28.9	-1.6	-0.3
460,880.6	4,046,211.3	0.1	4.3	29.5	-2.8	-0.6
460,880.6	4,046,211.3	0.2	4.3	27.8	-2.1	-0.5
460,880.7	4,046,211.3	0.1	4.4	27.8	-3.7	-0.4
460,880.7	4,046,211.3	0.2	4.4	26.8	-3.4	-0.5
460,880.7	4,046,211.3	0.3	4.4	25.9	-3.6	-0.7
460,880.8	4,046,211.4	0.1	4.5	27.0	-3.8	-0.2
460,880.8	4,046,211.4	0.2	4.5	26.1	-3.4	-0.3
460,880.9	4,046,211.4	0.1	4.6	25.3	-4.0	0.4
460,880.9	4,046,211.4	0.2	4.6	25.3	-4.0	0.4
460,881.0	4,046,211.4	0.1	4.7	15.9	-2.3	3.0
460,881.0	4,046,211.4	0.2	4.7	15.9	-2.3	3.0
460,881.1	4,046,211.4	0.1	4.8	12.1	-5.6	4.6
460,881.1	4,046,211.4	0.2	4.8	12.1	-5.6	4.6
460,881.2	4,046,211.4	0.1	4.9	8.8	-2.6	4.0
460,881.3	4,046,211.5	0.1	5.0	17.7	-5.5	0.2

b) Sec. 2

UTM Easting (m)	UTM Northing (m)	Water depth (m)	Distance from left bank (m)	Streamwise Velocity (cm/s)	Transverse Velocity (cm/s)	Vertical Velocity (cm/s)
460,869.0	4,046,220.3	0.1	0.6	22.4	-1.7	-1.0
460,869.0	4,046,220.4	0.1	0.7	23.7	-2.0	0.0
460,869.0	4,046,220.5	0.1	0.8	24.2	-2.6	0.7
460,869.0	4,046,220.6	0.1	0.9	25.2	-2.3	0.8
460,869.0	4,046,220.6	0.2	0.9	25.2	-2.3	0.8
460,869.0	4,046,220.7	0.1	1.0	24.3	-1.4	0.6
460,869.0	4,046,220.7	0.2	1.0	24.3	-1.4	0.6
460,869.0	4,046,220.8	0.1	1.1	26.3	-0.6	0.4
460,869.0	4,046,220.8	0.2	1.1	26.3	-0.6	0.4
460,869.0	4,046,220.9	0.1	1.2	28.1	-0.8	0.2
460,869.0	4,046,220.9	0.2	1.2	28.1	-0.8	0.2
460,869.0	4,046,221.0	0.1	1.3	30.4	-1.1	-0.2
460,869.0	4,046,221.0	0.2	1.3	30.4	-1.1	-0.2
460,869.1	4,046,221.1	0.1	1.4	29.9	-1.5	-0.1
460,869.1	4,046,221.1	0.2	1.4	29.9	-1.5	-0.1
460,869.1	4,046,221.2	0.1	1.5	29.3	-2.3	-0.2
460,869.1	4,046,221.2	0.2	1.5	29.3	-2.3	-0.2
460,869.1	4,046,221.3	0.1	1.6	31.1	-3.2	0.5
460,869.1	4,046,221.3	0.2	1.6	33.6	-0.4	1.0
460,869.1	4,046,221.4	0.1	1.7	34.7	-3.8	0.8
460,869.1	4,046,221.4	0.2	1.7	37.1	-0.2	1.3
460,869.1	4,046,221.4	0.3	1.7	37.7	2.4	1.5
460,869.1	4,046,221.5	0.1	1.8	37.4	-5.0	1.3
460,869.1	4,046,221.5	0.2	1.8	39.2	-1.2	1.6
460,869.1	4,046,221.5	0.3	1.8	40.0	0.4	1.3
460,869.1	4,046,221.6	0.1	1.9	39.6	-6.2	1.1
460,869.1	4,046,221.6	0.2	1.9	40.0	-4.4	1.1
460,869.1	4,046,221.6	0.3	1.9	38.2	-3.8	0.9
460,869.1	4,046,221.7	0.1	2.0	42.6	-5.6	1.0
460,869.1	4,046,221.7	0.2	2.0	42.9	-4.2	1.0
460,869.1	4,046,221.7	0.3	2.0	39.4	-4.0	1.7
460,869.1	4,046,221.7	0.4	2.0	37.9	-2.8	2.6
460,869.1	4,046,221.8	0.1	2.1	44.6	-4.8	1.4
460,869.1	4,046,221.8	0.2	2.1	45.1	-3.3	1.5
460,869.1	4,046,221.8	0.3	2.1	40.9	-3.8	2.4
460,869.1	4,046,221.8	0.4	2.1	39.5	-3.2	3.2
460,869.1	4,046,221.9	0.1	2.2	45.6	-6.1	1.7
460,869.1	4,046,221.9	0.2	2.2	46.3	-5.0	1.7
460,869.1	4,046,221.9	0.3	2.2	44.1	-6.2	2.7
460,869.1	4,046,221.9	0.4	2.2	43.3	-5.9	3.5
460,869.1	4,046,222.0	0.1	2.3	44.8	-9.9	1.8
460,869.1	4,046,222.0	0.2	2.3	45.3	-9.0	2.1
460,869.1	4,046,222.0	0.3	2.3	45.4	-9.3	2.8
460,869.1	4,046,222.0	0.4	2.3	45.1	-8.5	3.5
460,869.1	4,046,222.1	0.1	2.4	45.9	-13.1	1.6
460,869.1	4,046,222.1	0.2	2.4	46.0	-11.9	1.9
460,869.1	4,046,222.1	0.3	2.4	47.0	-11.4	2.7
460,869.1	4,046,222.1	0.4	2.4	46.5	-10.3	3.3
460,869.1	4,046,222.2	0.1	2.5	47.1	-14.7	1.0
460,869.1	4,046,222.2	0.2	2.5	47.6	-12.8	1.5
460,869.1	4,046,222.2	0.3	2.5	49.9	-11.7	2.1
460,869.1	4,046,222.2	0.4	2.5	51.3	-9.3	2.2
460,869.1	4,046,222.3	0.1	2.6	48.4	-15.3	0.5
460,869.1	4,046,222.3	0.2	2.6	49.3	-13.2	0.7

460,869.1	4,046,222.3	0.3	2.6	52.3	-12.2	0.8
460,869.1	4,046,222.3	0.4	2.6	54.9	-10.9	0.5
460,869.1	4,046,222.3	0.5	2.6	57.1	-11.9	0.2
460,869.1	4,046,222.4	0.1	2.7	50.9	-16.7	-0.4
460,869.1	4,046,222.4	0.2	2.7	52.1	-14.3	-0.6
460,869.1	4,046,222.4	0.3	2.7	55.1	-12.9	-0.7
460,869.1	4,046,222.4	0.4	2.7	56.6	-10.2	-0.7
460,869.1	4,046,222.4	0.5	2.7	57.7	-10.5	-0.6
460,869.1	4,046,222.5	0.1	2.8	56.0	-19.1	-0.4
460,869.1	4,046,222.5	0.2	2.8	56.9	-15.8	-0.7
460,869.1	4,046,222.5	0.3	2.8	58.1	-11.8	-1.1
460,869.1	4,046,222.5	0.4	2.8	58.8	-7.7	-0.9
460,869.1	4,046,222.5	0.5	2.8	58.8	-6.9	-0.6
460,869.1	4,046,222.6	0.1	2.9	60.0	-21.8	-0.7
460,869.1	4,046,222.6	0.2	2.9	60.8	-18.1	-1.0
460,869.1	4,046,222.6	0.3	2.9	61.0	-11.8	-1.3
460,869.1	4,046,222.6	0.4	2.9	59.9	-5.4	-1.1
460,869.1	4,046,222.6	0.5	2.9	58.6	-2.6	-0.8
460,869.1	4,046,222.7	0.1	3.0	60.0	-21.7	-0.6
460,869.1	4,046,222.7	0.2	3.0	61.1	-19.0	-0.9
460,869.1	4,046,222.7	0.3	3.0	62.4	-12.4	-1.3
460,869.1	4,046,222.7	0.4	3.0	61.9	-5.1	-1.3
460,869.1	4,046,222.7	0.5	3.0	61.2	-1.0	-1.3
460,869.1	4,046,222.8	0.1	3.1	58.6	-19.6	-0.8
460,869.1	4,046,222.8	0.2	3.1	59.6	-17.8	-1.2
460,869.1	4,046,222.8	0.3	3.1	62.4	-12.7	-1.5
460,869.1	4,046,222.8	0.4	3.1	62.0	-6.5	-1.8
460,869.1	4,046,222.8	0.5	3.1	62.2	-2.6	-1.6
460,869.1	4,046,222.9	0.1	3.2	59.0	-20.2	-0.6
460,869.1	4,046,222.9	0.2	3.2	60.4	-18.5	-1.0
460,869.1	4,046,222.9	0.3	3.2	64.2	-14.3	-1.4
460,869.1	4,046,222.9	0.4	3.2	64.2	-8.2	-1.4
460,869.1	4,046,222.9	0.5	3.2	64.8	-4.6	-1.2
460,869.1	4,046,223.0	0.1	3.3	61.9	-21.6	-0.5
460,869.1	4,046,223.0	0.2	3.3	63.1	-19.5	-1.1
460,869.1	4,046,223.0	0.3	3.3	65.4	-15.3	-1.3
460,869.1	4,046,223.0	0.4	3.3	65.1	-9.5	-1.3
460,869.1	4,046,223.0	0.5	3.3	64.9	-6.6	-0.9
460,869.1	4,046,223.1	0.1	3.4	65.2	-22.9	-0.3
460,869.1	4,046,223.1	0.2	3.4	66.5	-20.2	-0.5
460,869.1	4,046,223.1	0.3	3.4	67.1	-16.2	-0.8
460,869.1	4,046,223.1	0.4	3.4	66.1	-9.9	-0.9
460,869.1	4,046,223.1	0.5	3.4	64.5	-7.4	-0.9
460,869.1	4,046,223.2	0.1	3.5	66.3	-22.6	0.3
460,869.1	4,046,223.2	0.2	3.5	67.8	-19.7	0.2
460,869.1	4,046,223.2	0.3	3.5	67.2	-15.8	-0.1
460,869.1	4,046,223.2	0.4	3.5	65.9	-9.6	-0.6
460,869.1	4,046,223.2	0.5	3.5	63.5	-7.4	-0.9
460,869.1	4,046,223.3	0.1	3.6	67.8	-24.0	0.5
460,869.1	4,046,223.3	0.2	3.6	69.1	-21.6	0.6
460,869.1	4,046,223.3	0.3	3.6	67.8	-16.4	0.2
460,869.1	4,046,223.3	0.4	3.6	66.0	-10.0	-0.3
460,869.1	4,046,223.3	0.5	3.6	63.2	-6.6	-0.8
460,869.1	4,046,223.4	0.1	3.7	68.3	-25.6	1.1
460,869.1	4,046,223.4	0.2	3.7	68.4	-23.6	0.9
460,869.1	4,046,223.4	0.3	3.7	66.6	-17.2	0.2
460,869.1	4,046,223.4	0.4	3.7	64.5	-9.7	-0.4
460,869.1	4,046,223.4	0.5	3.7	62.4	-4.9	-0.9
460,869.2	4,046,223.5	0.1	3.8	68.9	-26.2	1.1

460,869.2	4,046,223.5	0.2	3.8	68.3	-24.3	0.9
460,869.2	4,046,223.5	0.3	3.8	65.8	-18.2	0.1
460,869.2	4,046,223.5	0.4	3.8	62.9	-10.2	-0.6
460,869.2	4,046,223.5	0.5	3.8	60.8	-5.1	-1.1
460,869.2	4,046,223.6	0.1	3.9	68.8	-25.1	0.8
460,869.2	4,046,223.6	0.2	3.9	67.8	-22.7	0.5
460,869.2	4,046,223.6	0.3	3.9	65.7	-17.2	-0.3
460,869.2	4,046,223.6	0.4	3.9	63.2	-8.2	-1.3
460,869.2	4,046,223.6	0.5	3.9	61.8	-3.3	-2.0
460,869.2	4,046,223.7	0.1	4.0	68.3	-22.2	-0.2
460,869.2	4,046,223.7	0.2	4.0	68.2	-20.3	-0.5
460,869.2	4,046,223.7	0.3	4.0	65.4	-16.1	-1.3
460,869.2	4,046,223.7	0.4	4.0	64.0	-7.9	-2.3
460,869.2	4,046,223.7	0.5	4.0	61.8	-3.5	-2.9
460,869.2	4,046,223.8	0.1	4.1	68.7	-18.9	-1.0
460,869.2	4,046,223.8	0.2	4.1	68.5	-17.5	-1.6
460,869.2	4,046,223.8	0.3	4.1	66.3	-12.8	-2.8
460,869.2	4,046,223.8	0.4	4.1	64.3	-5.9	-3.9
460,869.2	4,046,223.8	0.5	4.1	62.3	-1.4	-4.4
460,869.2	4,046,223.9	0.1	4.2	67.6	-15.9	-1.2
460,869.2	4,046,223.9	0.2	4.2	67.3	-15.3	-1.6
460,869.2	4,046,223.9	0.3	4.2	65.4	-11.7	-2.8
460,869.2	4,046,223.9	0.4	4.2	63.4	-7.0	-3.7
460,869.2	4,046,223.9	0.5	4.2	61.4	-2.8	-4.4
460,869.2	4,046,224.0	0.1	4.3	65.5	-13.0	-2.1
460,869.2	4,046,224.0	0.2	4.3	65.4	-12.4	-2.1
460,869.2	4,046,224.0	0.3	4.3	63.9	-10.6	-2.7
460,869.2	4,046,224.0	0.4	4.3	61.6	-8.6	-3.2
460,869.2	4,046,224.1	0.1	4.4	64.7	-6.3	-2.6
460,869.2	4,046,224.1	0.2	4.4	65.0	-7.0	-2.6
460,869.2	4,046,224.1	0.3	4.4	63.1	-7.5	-2.8
460,869.2	4,046,224.1	0.4	4.4	62.4	-9.5	-2.5
460,869.2	4,046,224.2	0.1	4.5	65.1	-3.2	-3.2
460,869.2	4,046,224.2	0.2	4.5	65.1	-3.6	-3.3
460,869.2	4,046,224.2	0.3	4.5	63.1	-3.5	-3.4
460,869.2	4,046,224.3	0.1	4.6	65.5	0.2	-3.0
460,869.2	4,046,224.3	0.2	4.6	64.3	0.8	-3.1
460,869.2	4,046,224.3	0.3	4.6	63.3	4.7	-3.2
460,869.2	4,046,224.4	0.1	4.7	61.1	2.2	-3.3
460,869.2	4,046,224.4	0.2	4.7	59.5	3.7	-2.8
460,869.2	4,046,224.4	0.3	4.7	58.3	8.0	-2.5
460,869.2	4,046,224.5	0.1	4.8	53.7	9.0	-3.5
460,869.2	4,046,224.5	0.2	4.8	53.7	9.7	-2.8
460,869.2	4,046,224.5	0.3	4.8	53.7	14.4	-2.5
460,869.2	4,046,224.6	0.1	4.9	45.5	11.2	-3.1
460,869.2	4,046,224.6	0.2	4.9	46.3	11.0	-2.8
460,869.2	4,046,224.7	0.1	5.0	42.0	12.4	-2.9
460,869.2	4,046,224.7	0.2	5.0	42.0	12.4	-2.9

c) Sec. 3

UTM Easting (m)	UTM Northing (m)	Water depth (m)	Distance from left bank (m)	Streamwise Velocity (cm/s)	Transverse Velocity (cm/s)	Vertical Velocity (cm/s)
460853.3	4046208.6	0.1	0.4	51.3	3.8	-0.5
460853.2	4046208.6	0.1	0.5	54.1	3.4	-0.2
460853.1	4046208.7	0.1	0.6	55.3	1.6	-0.8
460853.1	4046208.7	0.2	0.6	55.3	1.6	-0.8
460853.0	4046208.8	0.1	0.7	55.7	-1.1	-1.8
460853.0	4046208.8	0.2	0.7	54.7	-1.0	-1.7
460853.0	4046208.8	0.1	0.8	54.6	-2.4	-2.0
460853.0	4046208.8	0.2	0.8	53.8	-2.3	-1.8
460853.0	4046208.8	0.3	0.8	53.4	-2.0	-2.0
460852.9	4046208.9	0.1	0.9	56.1	-0.7	-1.3
460852.9	4046208.9	0.2	0.9	54.7	-0.7	-1.2
460852.9	4046208.9	0.3	0.9	53.7	-0.3	-1.3
460852.8	4046209.0	0.1	1.0	58.3	2.8	-0.2
460852.8	4046209.0	0.2	1.0	56.9	2.4	-0.4
460852.8	4046209.0	0.3	1.0	55.9	2.3	-0.5
460852.7	4046209.0	0.1	1.1	61.0	3.8	0.0
460852.7	4046209.0	0.2	1.1	58.9	3.7	-0.1
460852.7	4046209.0	0.3	1.1	55.9	1.6	-0.1
460852.6	4046209.1	0.1	1.2	62.1	3.4	-0.1
460852.6	4046209.1	0.2	1.2	60.1	3.5	-0.2
460852.6	4046209.1	0.3	1.2	57.5	0.9	-0.3
460852.6	4046209.1	0.4	1.2	55.0	-0.9	-0.5
460852.6	4046209.1	0.1	1.3	62.5	2.4	0.1
460852.6	4046209.1	0.2	1.3	60.8	2.4	-0.1
460852.6	4046209.1	0.3	1.3	57.8	-0.2	-0.4
460852.6	4046209.1	0.4	1.3	55.7	-1.6	-0.6
460852.5	4046209.2	0.1	1.4	64.1	3.1	0.3
460852.5	4046209.2	0.2	1.4	62.6	2.8	0.1
460852.5	4046209.2	0.3	1.4	59.6	1.2	-0.3
460852.5	4046209.2	0.4	1.4	57.7	0.1	-0.5
460852.4	4046209.3	0.1	1.5	66.4	3.0	0.7
460852.4	4046209.3	0.2	1.5	64.8	2.6	0.6
460852.4	4046209.3	0.3	1.5	59.9	1.6	-0.1
460852.4	4046209.3	0.4	1.5	56.9	0.5	-0.4
460852.3	4046209.3	0.1	1.6	68.6	2.7	0.9
460852.3	4046209.3	0.2	1.6	67.5	2.3	0.8
460852.3	4046209.3	0.3	1.6	62.7	1.7	0.2
460852.3	4046209.3	0.4	1.6	59.8	0.8	-0.2
460852.2	4046209.4	0.1	1.7	70.0	1.7	0.7
460852.2	4046209.4	0.2	1.7	69.6	2.0	0.6
460852.2	4046209.4	0.3	1.7	65.7	2.5	0.1
460852.2	4046209.4	0.4	1.7	63.3	2.5	-0.4
460852.2	4046209.4	0.1	1.8	70.7	0.9	0.7
460852.2	4046209.4	0.2	1.8	70.8	1.9	0.5
460852.2	4046209.4	0.3	1.8	68.2	2.9	0.0
460852.2	4046209.4	0.4	1.8	66.5	3.6	-0.4
460852.1	4046209.5	0.1	1.9	71.9	1.0	0.7
460852.1	4046209.5	0.2	1.9	71.7	2.2	0.6
460852.1	4046209.5	0.3	1.9	69.1	2.8	0.1
460852.1	4046209.5	0.4	1.9	67.2	3.3	-0.3
460852.0	4046209.6	0.1	2.0	73.1	2.1	1.0
460852.0	4046209.6	0.2	2.0	72.4	2.8	0.9
460852.0	4046209.6	0.3	2.0	69.4	2.1	0.3
460852.0	4046209.6	0.4	2.0	67.1	1.8	0.0

460851.9	4046209.6	0.1	2.1	74.5	3.1	0.9
460851.9	4046209.6	0.2	2.1	73.6	3.2	0.8
460851.9	4046209.6	0.3	2.1	70.5	2.3	0.3
460851.9	4046209.6	0.4	2.1	68.1	1.4	0.0
460851.9	4046209.7	0.1	2.2	75.4	2.3	0.6
460851.9	4046209.7	0.2	2.2	74.4	2.4	0.5
460851.9	4046209.7	0.3	2.2	71.5	2.4	0.0
460851.9	4046209.7	0.4	2.2	69.3	1.8	-0.2
460851.8	4046209.7	0.1	2.3	76.6	0.6	0.3
460851.8	4046209.7	0.2	2.3	75.7	0.9	0.3
460851.8	4046209.7	0.3	2.3	73.0	2.0	-0.1
460851.8	4046209.7	0.4	2.3	70.8	1.9	-0.3
460851.7	4046209.8	0.1	2.4	77.8	-0.4	0.2
460851.7	4046209.8	0.2	2.4	77.3	0.3	0.3
460851.7	4046209.8	0.3	2.4	75.2	1.7	-0.1
460851.7	4046209.8	0.4	2.4	73.4	2.0	-0.3
460851.6	4046209.9	0.1	2.5	79.5	0.2	0.0
460851.6	4046209.9	0.2	2.5	79.5	0.7	0.1
460851.6	4046209.9	0.3	2.5	77.1	1.4	-0.1
460851.6	4046209.9	0.4	2.5	75.5	1.4	-0.3
460851.5	4046209.9	0.1	2.6	81.4	1.2	-0.2
460851.5	4046209.9	0.2	2.6	81.5	1.5	-0.2
460851.5	4046209.9	0.3	2.6	79.6	1.7	-0.2
460851.5	4046209.9	0.4	2.6	78.2	1.5	-0.5
460851.5	4046210.0	0.1	2.7	83.9	2.0	-0.2
460851.5	4046210.0	0.2	2.7	83.5	2.0	-0.2
460851.5	4046210.0	0.3	2.7	79.1	2.1	0.1
460851.4	4046210.1	0.1	2.8	86.1	2.5	-0.1
460851.4	4046210.1	0.2	2.8	85.3	2.6	-0.1
460851.4	4046210.1	0.3	2.8	81.5	3.0	0.1
460851.4	4046210.1	0.4	2.8	78.4	3.3	0.0
460851.3	4046210.1	0.1	2.9	87.8	2.4	0.1
460851.3	4046210.1	0.2	2.9	86.8	2.6	0.1
460851.3	4046210.1	0.3	2.9	83.0	3.1	0.3
460851.2	4046210.2	0.1	3.0	89.1	1.5	0.4
460851.2	4046210.2	0.2	3.0	87.7	1.7	0.4
460851.2	4046210.2	0.3	3.0	87.0	1.9	0.6
460851.1	4046210.2	0.1	3.1	89.9	1.1	0.7
460851.1	4046210.2	0.2	3.1	88.0	1.2	0.8
460851.1	4046210.2	0.3	3.1	86.4	1.8	1.1
460851.1	4046210.3	0.1	3.2	90.4	0.4	0.7
460851.1	4046210.3	0.2	3.2	88.1	0.5	0.9
460851.1	4046210.3	0.3	3.2	83.2	1.3	1.3
460851.1	4046210.3	0.4	3.2	79.2	1.9	1.5
460851.0	4046210.4	0.1	3.3	91.0	-0.6	0.4
460851.0	4046210.4	0.2	3.3	88.8	-0.4	0.6
460851.0	4046210.4	0.3	3.3	83.7	0.4	1.0
460851.0	4046210.4	0.4	3.3	79.7	1.4	1.2
460850.9	4046210.4	0.1	3.4	91.8	-0.5	0.2
460850.9	4046210.4	0.2	3.4	89.9	0.1	0.4
460850.9	4046210.4	0.3	3.4	85.0	0.9	0.8
460850.8	4046210.5	0.1	3.5	91.8	0.0	0.1
460850.8	4046210.5	0.2	3.5	89.7	0.7	0.2
460850.8	4046210.5	0.3	3.5	88.9	1.5	0.5
460850.7	4046210.5	0.1	3.6	90.2	0.7	0.6
460850.7	4046210.5	0.2	3.6	88.3	1.6	0.7
460850.7	4046210.5	0.3	3.6	87.7	3.5	1.1
460850.7	4046210.6	0.1	3.7	88.8	2.2	1.1
460850.7	4046210.6	0.2	3.7	87.3	2.6	1.2

460850.7	4046210.6	0.3	3.7	86.6	3.8	1.6
460850.6	4046210.7	0.1	3.8	85.5	3.3	1.9
460850.6	4046210.7	0.2	3.8	85.1	1.9	1.6
460850.6	4046210.7	0.3	3.8	83.7	2.0	1.7
460850.5	4046210.7	0.1	3.9	84.2	3.7	1.6
460850.5	4046210.7	0.2	3.9	84.3	2.1	1.3
460850.5	4046210.7	0.3	3.9	82.5	1.1	1.5
460850.4	4046210.8	0.1	4.0	81.8	3.4	1.2
460850.4	4046210.8	0.2	4.0	81.7	1.4	0.8
460850.4	4046210.9	0.1	4.1	80.0	3.6	0.7
460850.4	4046210.9	0.2	4.1	80.0	3.6	0.7
460850.3	4046210.9	0.1	4.2	77.7	5.6	0.7

d) Sec. 4

UTM Easting (m)	UTM Northing (m)	Water depth (m)	Distance from left bank (m)	Streamwise Velocity (cm/s)	Transverse Velocity (cm/s)	Vertical Velocity (cm/s)
460840.7	4046202.2	0.1	0.4	49.5	17.2	-4.1
460840.7	4046202.3	0.1	0.5	50.5	17.1	-3.6
460840.7	4046202.3	0.2	0.5	52.6	12.9	-4.6
460840.8	4046202.4	0.1	0.6	54.9	17.0	-3.1
460840.8	4046202.4	0.2	0.6	55.4	14.2	-4.0
460840.8	4046202.4	0.3	0.6	54.1	13.1	-5.7
460840.8	4046202.5	0.1	0.7	56.2	16.4	-1.5
460840.8	4046202.5	0.2	0.7	56.1	13.8	-2.6
460840.8	4046202.5	0.3	0.7	55.0	12.9	-3.9
460840.8	4046202.6	0.1	0.8	58.4	14.0	-0.8
460840.8	4046202.6	0.2	0.8	56.6	13.5	-1.2
460840.8	4046202.6	0.3	0.8	55.4	13.1	-1.8
460840.8	4046202.7	0.1	0.9	59.8	13.6	-1.2
460840.8	4046202.7	0.2	0.9	59.1	12.1	-1.5
460840.8	4046202.7	0.3	0.9	59.4	10.6	-1.7
460840.8	4046202.8	0.1	1.0	63.5	14.4	-2.1
460840.8	4046202.8	0.2	1.0	63.2	12.0	-2.4
460840.8	4046202.8	0.3	1.0	62.3	8.2	-2.9
460840.9	4046202.9	0.1	1.1	66.2	18.6	-3.1
460840.9	4046202.9	0.2	1.1	66.3	16.2	-3.5
460840.9	4046202.9	0.3	1.1	64.8	11.0	-4.3
460840.9	4046202.9	0.4	1.1	63.8	7.5	-5.0
460840.9	4046203.0	0.1	1.2	67.3	22.1	-3.4
460840.9	4046203.0	0.2	1.2	66.7	19.6	-4.0
460840.9	4046203.0	0.3	1.2	63.4	12.7	-5.1
460840.9	4046203.0	0.4	1.2	62.0	8.8	-5.7
460840.9	4046203.1	0.1	1.3	65.2	23.9	-3.1
460840.9	4046203.1	0.2	1.3	64.6	22.0	-3.7
460840.9	4046203.1	0.3	1.3	62.6	16.2	-5.1
460840.9	4046203.1	0.4	1.3	61.2	12.8	-5.8
460840.9	4046203.2	0.1	1.4	63.6	26.0	-2.5
460840.9	4046203.2	0.2	1.4	62.7	24.0	-3.1
460840.9	4046203.2	0.3	1.4	60.8	18.9	-4.4
460840.9	4046203.2	0.4	1.4	61.2	15.0	-5.3
460840.9	4046203.3	0.1	1.5	64.0	28.5	-2.0
460840.9	4046203.3	0.2	1.5	62.4	26.4	-2.6
460840.9	4046203.3	0.3	1.5	61.0	21.6	-3.9
460840.9	4046203.3	0.4	1.5	61.3	17.6	-4.7
460840.9	4046203.3	0.5	1.5	62.8	14.1	-5.6
460840.9	4046203.4	0.1	1.6	65.0	31.1	-1.7
460840.9	4046203.4	0.2	1.6	62.5	28.4	-2.2
460840.9	4046203.4	0.3	1.6	60.5	22.2	-3.2
460840.9	4046203.4	0.4	1.6	61.0	18.7	-4.1
460841.0	4046203.5	0.1	1.7	66.3	31.4	-0.9
460841.0	4046203.5	0.2	1.7	62.7	27.7	-1.5
460841.0	4046203.5	0.3	1.7	59.7	19.4	-2.3
460841.0	4046203.5	0.4	1.7	56.9	16.5	-2.8
460841.0	4046203.6	0.1	1.8	67.1	29.3	0.3
460841.0	4046203.6	0.2	1.8	63.0	24.5	-0.3
460841.0	4046203.6	0.3	1.8	59.5	15.9	-0.8
460841.0	4046203.6	0.4	1.8	56.0	12.4	-1.1
460841.0	4046203.7	0.1	1.9	69.0	27.2	1.6
460841.0	4046203.7	0.2	1.9	64.3	22.4	1.0
460841.0	4046203.7	0.3	1.9	60.5	14.5	0.5

460841.0	4046203.7	0.4	1.9	55.8	10.0	0.2
460841.0	4046203.8	0.1	2.0	71.0	25.3	1.9
460841.0	4046203.8	0.2	2.0	66.2	20.9	1.4
460841.0	4046203.8	0.3	2.0	61.8	14.7	0.6
460841.0	4046203.8	0.4	2.0	57.1	11.0	0.1
460841.0	4046203.9	0.1	2.1	71.4	27.4	1.6
460841.0	4046203.9	0.2	2.1	67.0	23.2	0.8
460841.0	4046203.9	0.3	2.1	62.7	17.2	-0.2
460841.0	4046203.9	0.4	2.1	58.0	13.6	-1.2
460841.1	4046204.0	0.1	2.2	72.0	29.7	0.4
460841.1	4046204.0	0.2	2.2	68.0	25.3	-0.3
460841.1	4046204.0	0.3	2.2	64.5	18.2	-1.2
460841.1	4046204.0	0.4	2.2	60.1	14.4	-2.1
460841.1	4046204.1	0.1	2.3	71.3	31.0	-0.1
460841.1	4046204.1	0.2	2.3	68.4	27.1	-0.8
460841.1	4046204.1	0.3	2.3	65.7	19.7	-1.7
460841.1	4046204.1	0.4	2.3	62.1	15.5	-2.6
460841.1	4046204.2	0.1	2.4	69.2	30.7	-0.1
460841.1	4046204.2	0.2	2.4	66.7	27.4	-0.7
460841.1	4046204.2	0.3	2.4	65.5	21.1	-1.6
460841.1	4046204.2	0.4	2.4	62.9	17.6	-2.1
460841.1	4046204.3	0.1	2.5	65.5	31.1	0.0
460841.1	4046204.3	0.2	2.5	64.5	28.2	-0.4
460841.1	4046204.3	0.3	2.5	64.0	22.9	-1.7
460841.1	4046204.3	0.4	2.5	62.4	20.1	-2.3
460841.1	4046204.4	0.1	2.6	62.6	30.4	0.0
460841.1	4046204.4	0.2	2.6	62.2	28.4	-0.4
460841.1	4046204.4	0.3	2.6	62.4	23.6	-1.5
460841.1	4046204.4	0.4	2.6	61.3	21.7	-2.0
460841.1	4046204.5	0.1	2.7	60.4	27.7	-0.4
460841.1	4046204.5	0.2	2.7	61.1	26.9	-0.7
460841.1	4046204.5	0.3	2.7	62.0	23.0	-1.7
460841.1	4046204.5	0.4	2.7	61.4	22.0	-2.2
460841.2	4046204.6	0.1	2.8	58.0	24.8	-0.5
460841.2	4046204.6	0.2	2.8	59.0	25.0	-0.7
460841.2	4046204.6	0.3	2.8	61.2	22.1	-1.5
460841.2	4046204.6	0.4	2.8	60.7	21.1	-2.0
460841.2	4046204.7	0.1	2.9	53.8	24.0	-0.7
460841.2	4046204.7	0.2	2.9	55.5	24.3	-0.7
460841.2	4046204.7	0.3	2.9	59.6	22.9	-1.2
460841.2	4046204.7	0.4	2.9	60.1	20.4	-1.2
460841.2	4046204.7	0.5	2.9	60.7	17.7	-1.5
460841.2	4046204.8	0.1	3.0	49.8	22.6	-0.2
460841.2	4046204.8	0.2	3.0	51.8	22.8	-0.2
460841.2	4046204.8	0.3	3.0	56.5	22.2	-0.3
460841.2	4046204.8	0.4	3.0	57.9	18.6	-0.3
460841.2	4046204.8	0.5	3.0	59.0	16.4	-0.4
460841.2	4046204.9	0.1	3.1	45.6	21.6	0.5
460841.2	4046204.9	0.2	3.1	48.4	21.4	0.5
460841.2	4046204.9	0.3	3.1	53.7	21.7	0.3
460841.2	4046204.9	0.4	3.1	55.2	17.1	0.3
460841.2	4046204.9	0.5	3.1	55.9	15.2	0.3
460841.2	4046204.9	0.1	3.2	42.9	19.9	1.5
460841.2	4046204.9	0.2	3.2	45.7	19.7	1.1
460841.2	4046204.9	0.3	3.2	51.3	20.1	0.8
460841.2	4046204.9	0.4	3.2	52.5	16.9	0.2
460841.2	4046204.9	0.5	3.2	53.2	15.7	0.0
460841.2	4046205.0	0.1	3.3	38.6	20.3	1.8
460841.2	4046205.0	0.2	3.3	41.8	19.8	1.3

460841.2	4046205.0	0.3	3.3	47.7	18.9	0.8
460841.2	4046205.0	0.4	3.3	49.3	16.0	0.0
460841.2	4046205.0	0.5	3.3	49.9	14.5	-0.2
460841.3	4046205.1	0.1	3.4	34.3	18.9	1.8
460841.3	4046205.1	0.2	3.4	36.8	18.4	1.4
460841.3	4046205.1	0.3	3.4	42.6	16.6	0.9
460841.3	4046205.1	0.4	3.4	45.6	15.3	0.2
460841.3	4046205.1	0.5	3.4	47.9	14.0	0.0
460841.3	4046205.2	0.1	3.5	31.2	17.1	1.2
460841.3	4046205.2	0.2	3.5	33.6	16.5	1.2
460841.3	4046205.2	0.3	3.5	38.5	14.9	1.1
460841.3	4046205.2	0.4	3.5	42.3	13.3	1.1
460841.3	4046205.3	0.1	3.6	26.1	13.5	1.2
460841.3	4046205.3	0.2	3.6	29.0	13.2	1.4
460841.3	4046205.3	0.3	3.6	34.1	12.3	1.6
460841.3	4046205.3	0.4	3.6	38.5	11.5	2.1
460841.3	4046205.4	0.1	3.7	22.9	11.5	0.9
460841.3	4046205.4	0.2	3.7	26.1	10.9	1.3
460841.3	4046205.4	0.3	3.7	30.4	10.2	2.0
460841.3	4046205.4	0.4	3.7	34.6	9.3	2.6
460841.3	4046205.5	0.1	3.8	18.3	7.6	1.1
460841.3	4046205.5	0.2	3.8	20.6	6.7	1.4
460841.3	4046205.5	0.3	3.8	24.8	6.7	2.1
460841.3	4046205.5	0.4	3.8	28.3	6.0	2.5
460841.4	4046205.6	0.1	3.9	16.6	4.8	0.9
460841.4	4046205.6	0.2	3.9	17.9	4.2	1.1
460841.4	4046205.6	0.3	3.9	20.5	4.6	1.8
460841.4	4046205.7	0.1	4.0	16.1	0.6	-1.3
460841.4	4046205.7	0.2	4.0	16.1	0.3	-0.9
460841.4	4046205.8	0.1	4.1	15.6	0.1	-2.6
460841.4	4046205.8	0.2	4.1	15.6	0.1	-2.6

e) Sec. 5

UTM Easting (m)	UTM Northing (m)	Water depth (m)	Distance from left bank (m)	Streamwise Velocity (cm/s)	Transverse Velocity (cm/s)	Vertical Velocity (cm/s)
460828.4	4046217.8	0.1	0.8	66.5	-29.3	-1.1
460828.4	4046217.8	0.2	0.8	70.8	-27.3	-1.1
460828.4	4046217.8	0.3	0.8	76.2	-29.4	-1.5
460828.5	4046217.8	0.1	0.9	61.9	-22.8	-1.2
460828.5	4046217.8	0.2	0.9	67.2	-23.6	-1.1
460828.5	4046217.8	0.3	0.9	72.5	-26.3	-0.8
460828.6	4046217.8	0.1	1.0	60.0	-20.5	-2.9
460828.6	4046217.8	0.2	1.0	66.2	-23.6	-2.4
460828.6	4046217.8	0.3	1.0	68.5	-26.7	-2.0
460828.7	4046217.9	0.1	1.1	61.2	-20.9	-2.0
460828.7	4046217.9	0.2	1.1	62.9	-24.2	-2.0
460828.7	4046217.9	0.3	1.1	63.1	-27.8	-1.9
460828.7	4046217.9	0.4	1.1	65.4	-31.4	-2.3
460828.8	4046217.9	0.1	1.2	66.9	-25.9	-0.9
460828.8	4046217.9	0.2	1.2	66.0	-27.4	-1.5
460828.8	4046217.9	0.3	1.2	63.5	-29.6	-2.0
460828.8	4046217.9	0.4	1.2	63.1	-32.2	-2.6
460828.9	4046217.9	0.1	1.3	71.0	-31.6	-0.4
460828.9	4046217.9	0.2	1.3	67.9	-31.2	-1.1
460828.9	4046217.9	0.3	1.3	64.8	-33.0	-1.7
460828.9	4046217.9	0.4	1.3	62.7	-34.1	-2.2
460829.0	4046217.9	0.1	1.4	73.4	-33.6	-0.6
460829.0	4046217.9	0.2	1.4	71.4	-33.1	-1.4
460829.0	4046217.9	0.3	1.4	69.0	-35.3	-1.8
460829.0	4046217.9	0.4	1.4	67.5	-36.2	-2.2
460829.1	4046218.0	0.1	1.5	73.6	-33.2	-0.7
460829.1	4046218.0	0.2	1.5	72.0	-32.9	-1.5
460829.1	4046218.0	0.3	1.5	71.2	-34.1	-1.8
460829.1	4046218.0	0.4	1.5	70.5	-34.5	-2.1
460829.2	4046218.0	0.1	1.6	73.7	-31.2	-0.5
460829.2	4046218.0	0.2	1.6	72.2	-31.7	-1.0
460829.2	4046218.0	0.3	1.6	71.3	-31.9	-1.6
460829.2	4046218.0	0.4	1.6	70.5	-32.0	-1.9
460829.3	4046218.0	0.1	1.7	72.8	-31.2	-0.3
460829.3	4046218.0	0.2	1.7	71.5	-32.3	-0.5
460829.3	4046218.0	0.3	1.7	68.9	-31.4	-1.3
460829.3	4046218.0	0.4	1.7	67.2	-31.2	-1.7
460829.4	4046218.0	0.1	1.8	71.9	-32.0	-0.3
460829.4	4046218.0	0.2	1.8	70.8	-33.0	-0.5
460829.4	4046218.0	0.3	1.8	66.6	-32.8	-1.1
460829.4	4046218.0	0.4	1.8	64.1	-32.9	-1.4
460829.5	4046218.1	0.1	1.9	71.1	-31.8	-0.4
460829.5	4046218.1	0.2	1.9	70.0	-32.5	-0.6
460829.5	4046218.1	0.3	1.9	65.4	-33.0	-0.9
460829.5	4046218.1	0.4	1.9	62.8	-33.3	-1.1
460829.6	4046218.1	0.1	2.0	70.5	-30.6	-0.4
460829.6	4046218.1	0.2	2.0	69.1	-31.0	-0.6
460829.6	4046218.1	0.3	2.0	64.1	-31.8	-0.8
460829.6	4046218.1	0.4	2.0	61.1	-32.2	-0.9
460829.7	4046218.1	0.1	2.1	69.8	-28.1	-0.2
460829.7	4046218.1	0.2	2.1	68.2	-28.9	-0.4
460829.7	4046218.1	0.3	2.1	63.1	-30.1	-0.7
460829.7	4046218.1	0.4	2.1	59.9	-30.7	-0.9
460829.8	4046218.1	0.1	2.2	67.7	-26.3	0.5

460829.8	4046218.1	0.2	2.2	66.2	-27.3	0.2
460829.8	4046218.1	0.3	2.2	60.5	-28.6	-0.3
460829.8	4046218.1	0.4	2.2	57.1	-29.3	-0.6
460829.9	4046218.2	0.1	2.3	65.7	-26.1	0.8
460829.9	4046218.2	0.2	2.3	64.3	-27.0	0.6
460829.9	4046218.2	0.3	2.3	59.2	-27.4	-0.2
460829.9	4046218.2	0.4	2.3	56.2	-27.7	-0.6
460830.0	4046218.2	0.1	2.4	64.7	-26.2	0.8
460830.0	4046218.2	0.2	2.4	63.4	-27.0	0.6
460830.0	4046218.2	0.3	2.4	58.6	-26.6	-0.1
460830.0	4046218.2	0.4	2.4	55.7	-26.3	-0.5
460830.1	4046218.2	0.1	2.5	65.9	-26.5	0.3
460830.1	4046218.2	0.2	2.5	64.4	-27.3	0.1
460830.1	4046218.2	0.3	2.5	59.1	-26.6	-0.5
460830.1	4046218.2	0.4	2.5	55.8	-26.0	-0.9
460830.2	4046218.2	0.1	2.6	66.6	-26.7	0.1
460830.2	4046218.2	0.2	2.6	64.7	-27.7	0.0
460830.2	4046218.2	0.3	2.6	59.0	-27.8	-0.6
460830.2	4046218.2	0.4	2.6	55.3	-27.5	-0.9
460830.3	4046218.2	0.1	2.7	66.6	-27.1	0.0
460830.3	4046218.2	0.2	2.7	64.2	-28.1	0.0
460830.3	4046218.2	0.3	2.7	58.0	-28.7	-0.7
460830.3	4046218.2	0.4	2.7	53.6	-28.5	-1.1
460830.4	4046218.3	0.1	2.8	66.1	-27.3	-0.1
460830.4	4046218.3	0.2	2.8	63.6	-28.3	-0.1
460830.4	4046218.3	0.3	2.8	54.8	-29.0	-0.5
460830.4	4046218.3	0.4	2.8	48.9	-28.8	-0.6
460830.5	4046218.3	0.1	2.9	65.1	-26.0	0.1
460830.5	4046218.3	0.2	2.9	62.6	-26.5	0.1
460830.5	4046218.3	0.3	2.9	52.7	-26.2	-0.1
460830.5	4046218.3	0.4	2.9	46.3	-25.4	-0.1
460830.6	4046218.3	0.1	3.0	63.4	-25.5	0.3
460830.6	4046218.3	0.2	3.0	61.0	-25.6	0.2
460830.6	4046218.3	0.3	3.0	52.4	-25.6	0.2
460830.6	4046218.3	0.4	3.0	45.7	-24.5	0.3
460830.7	4046218.3	0.1	3.1	60.3	-25.1	0.8
460830.7	4046218.3	0.2	3.1	57.5	-25.1	0.6
460830.7	4046218.3	0.3	3.1	53.1	-24.8	0.5
460830.8	4046218.4	0.1	3.2	55.6	-25.1	0.8
460830.8	4046218.4	0.2	3.2	53.2	-25.7	0.7
460830.8	4046218.4	0.3	3.2	51.4	-26.7	0.5
460830.9	4046218.4	0.1	3.3	53.0	-24.7	0.6
460830.9	4046218.4	0.2	3.3	50.4	-24.6	0.7
460830.9	4046218.4	0.3	3.3	48.3	-25.3	0.6
460831.0	4046218.4	0.1	3.4	50.6	-25.0	0.6
460831.0	4046218.4	0.2	3.4	47.9	-24.2	0.6
460831.0	4046218.4	0.3	3.4	45.8	-24.0	0.5
460831.1	4046218.4	0.1	3.5	49.2	-25.8	0.7
460831.1	4046218.4	0.2	3.5	45.3	-24.2	0.6
460831.1	4046218.4	0.3	3.5	41.8	-22.9	0.4
460831.2	4046218.5	0.1	3.6	46.3	-25.4	0.9
460831.2	4046218.5	0.2	3.6	42.2	-23.4	0.6
460831.2	4046218.5	0.3	3.6	38.6	-21.3	0.3
460831.2	4046218.5	0.1	3.7	44.2	-23.8	0.9
460831.2	4046218.5	0.2	3.7	39.0	-20.9	0.5
460831.2	4046218.5	0.3	3.7	35.1	-18.4	-0.1
460831.3	4046218.5	0.1	3.8	42.4	-21.6	0.8
460831.3	4046218.5	0.2	3.8	36.6	-17.8	0.3
460831.3	4046218.5	0.3	3.8	32.7	-15.2	-0.2

460831.4	4046218.5	0.1	3.9	39.8	-20.1	0.6
460831.4	4046218.5	0.2	3.9	32.6	-15.9	0.2
460831.4	4046218.5	0.3	3.9	27.7	-13.1	-0.3
460831.5	4046218.6	0.1	4.0	36.9	-18.3	0.4
460831.5	4046218.6	0.2	4.0	31.6	-15.5	0.2
460831.5	4046218.6	0.3	4.0	26.2	-12.8	-0.2
460831.6	4046218.6	0.1	4.1	33.2	-17.8	0.2
460831.6	4046218.6	0.2	4.1	30.3	-16.3	0.1
460831.7	4046218.6	0.1	4.2	28.3	-17.0	-0.4
460831.7	4046218.6	0.2	4.2	28.3	-17.0	-0.4
460831.8	4046218.6	0.1	4.3	26.5	-17.7	-0.4
460831.8	4046218.6	0.2	4.3	26.5	-17.7	-0.4
460831.9	4046218.6	0.1	4.4	25.0	-16.9	-0.9
460832.0	4046218.7	0.1	4.5	28.6	-17.7	-0.6

f) Sec. 6

UTM Easting (m)	UTM Northing (m)	Water depth (m)	Distance from left bank (m)	Streamwise Velocity (cm/s)	Transverse Velocity (cm/s)	Vertical Velocity (cm/s)
460821.7	4046229.8	0.1	0.4	22.4	-6.4	-0.6
460821.7	4046229.9	0.1	0.5	25.9	-5.2	-0.5
460821.8	4046230.0	0.1	0.6	26.3	-4.4	-0.9
460821.8	4046230.0	0.2	0.6	26.3	-4.4	-0.9
460821.8	4046230.1	0.1	0.7	27.7	-5.5	-0.8
460821.8	4046230.1	0.2	0.7	27.7	-5.5	-0.8
460821.8	4046230.2	0.1	0.8	30.8	-5.5	-0.7
460821.8	4046230.2	0.2	0.8	30.8	-5.5	-0.7
460821.9	4046230.3	0.1	0.9	37.3	-6.8	-0.5
460821.9	4046230.3	0.2	0.9	37.0	-5.8	-0.4
460821.9	4046230.4	0.1	1.0	41.6	-7.3	-0.5
460821.9	4046230.4	0.2	1.0	39.8	-5.6	-0.3
460821.9	4046230.4	0.3	1.0	38.2	-3.2	0.0
460822.0	4046230.5	0.1	1.1	43.2	-9.4	-0.7
460822.0	4046230.5	0.2	1.1	40.6	-6.6	-0.4
460822.0	4046230.5	0.3	1.1	38.7	-3.7	0.0
460822.0	4046230.6	0.1	1.2	44.3	-10.1	-0.4
460822.0	4046230.6	0.2	1.2	41.5	-7.5	-0.1
460822.0	4046230.6	0.3	1.2	39.2	-4.9	0.4
460822.0	4046230.7	0.1	1.3	47.4	-11.8	-0.1
460822.0	4046230.7	0.2	1.3	43.8	-9.9	0.3
460822.0	4046230.7	0.3	1.3	40.8	-8.0	0.8
460822.1	4046230.8	0.1	1.4	49.8	-13.6	0.3
460822.1	4046230.8	0.2	1.4	46.2	-11.6	0.7
460822.1	4046230.8	0.3	1.4	43.2	-9.6	1.1
460822.1	4046230.9	0.1	1.5	51.6	-15.9	0.5
460822.1	4046230.9	0.2	1.5	48.5	-13.8	0.8
460822.1	4046230.9	0.3	1.5	46.1	-9.1	0.2
460822.1	4046231.0	0.1	1.6	53.6	-16.2	0.7
460822.1	4046231.0	0.2	1.6	51.6	-13.5	0.9
460822.1	4046231.0	0.3	1.6	49.4	-6.5	0.5
460822.1	4046231.0	0.4	1.6	47.4	-2.2	0.6
460822.2	4046231.0	0.1	1.7	55.6	-16.2	0.9
460822.2	4046231.0	0.2	1.7	54.2	-13.9	0.9
460822.2	4046231.0	0.3	1.7	52.1	-5.1	0.6
460822.2	4046231.0	0.4	1.7	49.9	-1.2	0.7
460822.2	4046231.1	0.1	1.8	59.6	-15.8	0.8
460822.2	4046231.1	0.2	1.8	58.0	-13.5	0.7
460822.2	4046231.1	0.3	1.8	55.6	-5.8	0.8
460822.2	4046231.1	0.4	1.8	52.9	-2.9	1.0
460822.3	4046231.2	0.1	1.9	63.2	-15.2	1.1
460822.3	4046231.2	0.2	1.9	61.2	-13.1	0.8
460822.3	4046231.2	0.3	1.9	58.2	-6.6	0.4
460822.3	4046231.2	0.4	1.9	54.9	-4.4	0.2
460822.3	4046231.3	0.1	2.0	68.3	-17.0	0.5
460822.3	4046231.3	0.2	2.0	65.7	-14.4	0.2
460822.3	4046231.3	0.3	2.0	61.8	-8.8	-0.1
460822.3	4046231.3	0.4	2.0	58.1	-6.4	-0.2
460822.3	4046231.4	0.1	2.1	69.3	-16.3	0.2
460822.3	4046231.4	0.2	2.1	66.6	-13.9	-0.2
460822.3	4046231.4	0.3	2.1	61.0	-7.3	0.0
460822.3	4046231.4	0.4	2.1	56.5	-4.4	0.1
460822.4	4046231.5	0.1	2.2	69.2	-17.2	0.1
460822.4	4046231.5	0.2	2.2	66.6	-13.9	-0.2

460822.4	4046231.5	0.3	2.2	61.2	-6.5	0.0
460822.4	4046231.5	0.4	2.2	57.5	-2.4	0.1
460822.4	4046231.6	0.1	2.3	70.0	-16.2	0.9
460822.4	4046231.6	0.2	2.3	66.2	-12.5	0.5
460822.4	4046231.6	0.3	2.3	59.7	-5.3	0.0
460822.4	4046231.6	0.4	2.3	55.9	-1.0	-0.2
460822.5	4046231.7	0.1	2.4	74.0	-18.5	0.8
460822.5	4046231.7	0.2	2.4	69.5	-13.6	0.4
460822.5	4046231.7	0.3	2.4	62.8	-6.7	-0.4
460822.5	4046231.7	0.4	2.4	58.9	-1.5	-0.7
460822.5	4046231.8	0.1	2.5	74.5	-19.0	-0.2
460822.5	4046231.8	0.2	2.5	70.2	-13.4	-0.2
460822.5	4046231.8	0.3	2.5	62.6	-6.7	-0.6
460822.5	4046231.8	0.4	2.5	58.2	-2.0	-0.8
460822.5	4046231.9	0.1	2.6	72.4	-18.6	-0.4
460822.5	4046231.9	0.2	2.6	69.7	-12.2	-0.3
460822.5	4046231.9	0.3	2.6	62.3	-4.2	-0.8
460822.5	4046231.9	0.4	2.6	58.0	1.1	-0.7
460822.6	4046232.0	0.1	2.7	69.3	-17.8	-0.3
460822.6	4046232.0	0.2	2.7	67.2	-10.9	-0.2
460822.6	4046232.0	0.3	2.7	61.3	-1.8	-0.8
460822.6	4046232.0	0.4	2.7	57.7	3.6	-0.6
460822.6	4046232.1	0.1	2.8	68.9	-16.6	0.1
460822.6	4046232.1	0.2	2.8	67.0	-9.9	-0.2
460822.6	4046232.1	0.3	2.8	61.5	-0.8	-1.0
460822.6	4046232.1	0.4	2.8	58.0	4.9	-1.2
460822.7	4046232.1	0.1	2.9	68.3	-13.9	0.2
460822.7	4046232.1	0.2	2.9	66.4	-8.5	-0.2
460822.7	4046232.1	0.3	2.9	62.0	-0.4	-0.7
460822.7	4046232.1	0.4	2.9	59.7	4.2	-1.1
460822.7	4046232.2	0.1	3.0	68.1	-12.0	0.3
460822.7	4046232.2	0.2	3.0	66.3	-7.9	-0.1
460822.7	4046232.2	0.3	3.0	61.5	-1.1	-0.6
460822.7	4046232.2	0.4	3.0	59.2	2.9	-1.0
460822.7	4046232.3	0.1	3.1	67.6	-12.1	0.4
460822.7	4046232.3	0.2	3.1	65.9	-9.0	-0.2
460822.7	4046232.3	0.3	3.1	60.9	-2.3	-0.9
460822.7	4046232.3	0.4	3.1	58.9	1.9	-1.3
460822.8	4046232.4	0.1	3.2	68.0	-14.6	-0.2
460822.8	4046232.4	0.2	3.2	65.9	-11.1	-0.7
460822.8	4046232.4	0.3	3.2	60.5	-3.3	-1.8
460822.8	4046232.4	0.4	3.2	57.8	1.9	-2.2
460822.8	4046232.5	0.1	3.3	68.0	-14.2	-0.6
460822.8	4046232.5	0.2	3.3	65.9	-10.1	-1.2
460822.8	4046232.5	0.3	3.3	61.7	-3.1	-2.3
460822.8	4046232.5	0.4	3.3	58.6	2.1	-2.8
460822.9	4046232.6	0.1	3.4	68.0	-12.6	-1.1
460822.9	4046232.6	0.2	3.4	66.1	-8.7	-1.7
460822.9	4046232.6	0.3	3.4	63.6	-2.4	-2.6
460822.9	4046232.7	0.1	3.5	66.8	-10.3	-1.4
460822.9	4046232.7	0.2	3.5	65.7	-7.3	-2.1
460822.9	4046232.7	0.3	3.5	64.5	-4.0	-2.7
460822.9	4046232.8	0.1	3.6	64.8	-9.8	-1.7
460822.9	4046232.8	0.2	3.6	64.4	-7.4	-2.3
460822.9	4046232.8	0.3	3.6	63.7	-4.5	-2.9
460823.0	4046232.9	0.1	3.7	63.4	-8.3	-2.0
460823.0	4046232.9	0.2	3.7	62.0	-6.8	-2.3
460823.0	4046232.9	0.3	3.7	60.9	-5.0	-2.8
460823.0	4046233.0	0.1	3.8	63.0	-5.8	-2.1

460823.0	4046233.0	0.2	3.8	61.4	-5.2	-2.3
460823.0	4046233.0	0.3	3.8	60.2	-3.5	-2.6
460823.0	4046233.1	0.1	3.9	62.6	-6.8	-1.7
460823.0	4046233.1	0.2	3.9	60.9	-6.6	-1.7
460823.1	4046233.2	0.1	4.0	61.3	-4.7	-1.5
460823.1	4046233.2	0.2	4.0	61.3	-4.7	-1.5
460823.1	4046233.3	0.1	4.1	60.5	-6.3	-1.2

Table B2. Concentration measurements using fluorometer

a) Sec. 2

y/W / Time (sec)	Concentration (ppb)				
	0.167	**0.333**	**0.500**	**0.667**	**0.833**
42	0.0	0.0	0.0	0.0	0.0
43	0.0	0.1	0.0	0.0	0.0
44	0.0	0.2	0.0	0.0	0.0
45	0.0	0.3	0.0	0.0	0.0
46	0.0	0.3	0.0	0.0	0.0
47	0.0	0.3	0.0	0.0	0.0
48	0.0	0.3	0.0	0.0	0.0
49	0.0	0.4	0.0	0.0	0.0
50	0.0	0.6	0.0	0.2	0.0
51	0.0	1.2	0.0	1.0	0.2
52	0.0	1.5	0.0	2.6	0.6
53	0.0	1.9	0.5	4.0	1.0
54	0.0	2.3	1.0	5.8	1.9
55	0.0	2.9	3.0	9.9	3.6
56	0.0	4.0	5.4	13.8	6.4
57	0.0	6.2	8.8	17.1	10.6
58	0.0	8.4	12.3	20.1	13.2
59	0.1	10.4	14.8	23.2	15.7
60	0.1	11.9	18.9	26.0	17.7
61	0.1	13.6	20.7	28.4	19.4
62	0.1	15.0	24.6	30.4	21.4
63	0.2	16.8	26.8	32.7	22.2
64	0.3	18.7	27.7	34.9	23.2
65	1.3	20.0	28.9	36.5	24.2
66	2.6	21.2	30.5	37.7	25.2
67	4.5	22.3	32.2	38.8	26.1
68	6.9	23.0	33.5	39.6	26.9
69	9.7	24.9	34.8	39.9	27.8
70	12.0	26.0	36.2	40.3	28.8
71	14.2	26.7	37.1	40.7	29.6
72	16.4	27.6	37.4	40.6	30.1
73	18.2	28.5	37.5	40.4	30.3
74	19.8	29.0	37.9	40.1	30.3
75	21.3	29.7	37.5	39.7	30.4
76	23.0	30.0	36.9	39.3	30.1
77	24.5	30.4	36.8	39.1	29.9
78	25.6	30.7	36.5	39.0	30.0
79	26.9	30.9	36.2	38.7	29.5
80	27.6	30.5	35.3	37.3	29.2
81	28.3	30.2	33.8	36.5	28.7
82	28.9	30.0	32.9	35.3	28.3
83	29.3	29.9	31.7	34.1	27.9
84	29.7	29.6	31.0	33.2	27.2
85	30.0	29.4	30.5	32.2	26.6
86	30.1	29.4	30.1	31.4	26.2
87	30.2	29.1	29.3	30.3	25.4
88	30.1	28.9	28.7	29.3	24.6
89	30.1	28.2	28.3	28.3	23.8
90	30.0	27.8	27.4	27.3	23.1
91	30.0	27.4	25.8	26.2	22.5
92	29.8	26.9	24.7	25.2	21.8

93	29.6	26.5	24.1	24.3	21.2
94	29.4	25.9	23.0	23.7	20.6
95	28.8	25.5	21.8	22.7	20.1
96	28.1	24.8	20.6	21.9	19.3
97	27.6	24.1	19.9	21.1	18.7
98	27.1	23.3	19.2	20.1	18.1
99	26.7	22.8	18.0	19.5	17.5
100	26.2	22.3	17.6	18.9	17.0
101	25.7	22.0	17.4	18.1	16.3
102	25.2	21.7	17.1	17.4	15.7
103	24.5	21.5	16.6	16.8	15.1
104	24.3	21.1	15.7	16.1	14.4
105	23.4	20.4	15.0	15.5	13.9
106	23.0	19.7	14.2	14.8	13.2
107	22.5	19.3	13.4	14.4	12.6
108	22.0	19.0	12.8	13.7	12.2
109	21.3	18.6	12.3	13.1	11.9
110	20.6	18.3	12.1	12.6	11.6
111	19.9	17.8	11.6	12.1	10.8
112	19.5	17.2	11.3	11.7	10.4
113	19.0	16.5	10.9	11.3	10.0
114	18.5	15.9	10.4	10.7	9.6
115	17.9	15.3	9.8	10.4	9.2
116	17.3	15.0	9.2	10.0	8.8
117	17.1	14.4	8.7	9.4	8.4
118	16.6	13.9	8.4	8.9	8.0
119	16.1	13.3	8.0	8.7	7.6
120	15.5	12.8	7.7	8.3	7.3
121	15.0	12.5	7.3	8.0	7.0
122	14.4	12.2	7.3	7.7	6.9
123	14.0	12.0	7.1	7.3	6.7
124	13.5	11.7	7.2	7.0	6.5
125	12.9	11.3	6.8	6.9	6.3
126	12.4	11.1	6.6	6.8	6.1
127	12.2	10.6	6.3	6.6	5.8
128	11.8	10.3	6.0	6.6	5.5
129	11.4	10.0	5.9	6.4	5.2
130	11.0	9.8	5.7	6.1	5.2
131	10.7	9.6	5.2	5.9	5.1
132	10.4	9.4	5.1	5.6	4.9
133	10.0	9.2	5.0	5.5	4.7
134	9.7	9.0	5.1	5.3	4.4
135	9.3	8.7	4.8	5.1	4.2
136	8.7	8.2	4.7	4.9	4.1
137	8.6	8.0	4.5	4.7	4.0
138	8.3	7.9	4.5	4.6	3.8
139	8.0	7.6	4.5	4.5	3.7
140	7.8	7.5	4.3	4.4	3.5
141	7.6	7.3	4.0	4.3	3.4
142	7.4	7.2	3.9	4.2	3.5
143	7.0	6.8	3.8	3.9	3.5
144	6.7	6.6	3.6	3.7	3.4
145	6.6	6.4	3.5	3.7	3.4
146	6.4	6.2	3.2	3.6	3.3
147	6.1	6.0	3.1	3.5	3.2
148	5.9	6.0	2.9	3.4	3.2
149	5.8	5.8	2.6	3.3	3.0
150	5.8	5.7	2.6	3.2	2.8
151	5.6	5.6	2.7	3.1	2.7

152	5.6	5.4	2.8	3.0	2.6
153	5.4	5.2	2.7	2.9	2.6
154	5.2	5.0	2.5	2.8	2.6
155	5.2	4.9	2.4	2.6	2.7
156	5.0	4.6	2.7	2.6	2.5
157	5.0	4.5	2.7	2.5	2.4
158	4.9	4.5	2.5	2.5	2.4
159	4.8	4.4	2.5	2.4	2.5
160	4.6	4.3	2.5	2.4	2.4
161	4.4	4.4	2.4	2.2	2.2
162	4.3	4.4	2.2	2.1	2.0
163	4.2	4.4	2.2	1.9	2.0
164	4.2	4.3	2.2	1.8	2.0
165	4.1	4.3	2.3	1.6	1.8
166	4.0	4.2	2.0	1.6	1.7
167	3.9	4.1	2.0	1.4	1.8
168	3.6	3.8	2.0	1.4	1.6
169	3.6	3.5	2.0	1.3	1.5
170	3.6	3.3	2.0	1.4	1.5
171	3.6	3.3	1.7	1.4	1.5
172	3.6	3.2	1.7	1.3	1.4
173	3.6	3.1	1.7	1.2	1.4
174	3.5	3.0	1.5	1.1	1.4
175	3.5	3.1	1.5	1.0	1.3
176	3.4	3.1	1.6	0.9	1.2
177	3.2	2.8	1.5	1.0	1.1
178	3.2	2.9	1.6	0.9	1.0
179	3.2	2.8	1.7	0.8	1.1
180	3.2	2.9	1.5	0.8	1.1
181	3.2	2.7	1.4	1.0	1.1
182	3.1	2.7	1.4	1.0	1.0
183	2.8	2.7	1.4	1.0	1.0
184	2.6	2.7	1.1	1.2	1.0
185	2.4	2.8	1.0	1.2	1.0
186	2.2	2.7	1.0	1.1	1.1
187	2.2	2.7	0.8	1.3	1.1
188	2.2	2.8	0.8	1.2	1.0
189	2.2	2.7	1.0	1.0	1.1
190	2.1	2.6	0.8	0.9	1.1
191	2.1	2.5	0.6	0.8	1.0
192	2.0	2.4	0.5	0.7	1.0
193	2.0	2.4	0.5	0.7	1.0
194	2.0	2.2	0.5	0.6	1.0
195	2.0	2.1	0.5	0.6	1.0
196	1.8	2.1	0.4	0.6	0.9
197	1.8	2.0	0.5	0.6	0.8
198	1.8	1.7	0.5	0.5	0.8
199	1.8	1.8	0.5	0.4	0.8
200	1.7	1.6	0.4	0.4	0.7
201	1.7	1.6	0.3	0.4	0.7
202	1.7	1.6	0.3	0.4	0.7
203	1.6	1.6	0.5	0.5	0.6
204	1.7	1.6	0.2	0.6	0.6
205	1.6	1.6	0.1	0.5	0.6
206	1.7	1.6	0.1	0.5	0.6
207	1.8	1.5	0.0	0.4	0.5
208	1.7	1.6	0.0	0.4	0.4
209	1.6	1.5	-0.2	0.4	0.4
210	1.6	1.4	0.0	0.3	0.4

211	1.5	1.3	0.0	0.3	0.3
212	1.5	1.2	0.1	0.2	0.3
213	1.6	1.3	0.4	0.3	0.4
214	1.6	1.3	0.4	0.1	0.4
215	1.6	1.3	0.3	0.1	0.4
216	1.6	1.3	0.3	0.2	0.5
217	1.6	1.3	0.2	0.2	0.5
218	1.5	1.3	0.3	0.2	0.4
219	1.6	1.5	0.3	0.1	0.4
220	1.4	1.5	0.5	0.1	0.3
221	1.4	1.4	0.4	0.1	0.4
222	1.3	1.2	0.4	0.2	0.2
223	1.3	1.0	0.3	0.1	0.2
224	1.2	0.9	0.3	0.1	0.3
225	1.3	0.9	0.2	0.0	0.2
226	1.3	0.9	0.2	0.0	0.3
227	1.3	0.9	0.1	0.1	0.3
228	1.2	1.0	0.2	0.1	0.2
229	1.2	0.9	0.2	0.1	0.3
230	1.1	0.9	0.2	0.2	0.2
231	1.0	1.0	0.4	0.2	0.0
232	0.9	0.9	0.4	0.2	0.1
233	0.9	0.9	0.2	0.2	0.1
234	1.0	0.9	0.2	0.3	0.2
235	1.0	0.9	0.2	0.4	0.3
236	1.0	0.8	0.1	0.3	0.3
237	1.0	0.7	0.0	0.4	0.3
238	1.0	0.7	0.0	0.5	0.3
239	1.0	0.7	0.1	0.6	0.3
240	0.9	0.7	0.2	0.5	0.2
241	0.8	0.6	0.2	0.6	0.3
242	0.7	0.6	0.3	0.6	0.4
243	0.7	0.7	0.5	0.6	0.4
244	0.6	0.7	0.4	0.6	0.4
245	0.6	0.5	0.3	0.6	0.4
246	0.7	0.6	0.5	0.5	0.6
247	0.7	0.5	0.5	0.4	0.6
248	0.6	0.6	0.5	0.5	0.7
249	0.5	0.6	0.4	0.5	0.7
250	0.5	0.5	0.3	0.3	0.6
251	0.7	0.4	0.3	0.3	0.5
252	0.7	0.4	0.3	0.2	0.6
253	0.8	0.3	0.1	0.4	0.6
254	0.7	0.2	0.1	0.3	0.4
255	0.7	0.2	0.0	0.2	0.3
256	0.7	0.2	0.0	0.3	0.3
257	0.7	0.2	-0.1	0.4	0.2
258	0.6	0.3	-0.3	0.5	0.3
259	0.6	0.2	-0.3	0.4	0.4
260	0.4	0.3	-0.1	0.4	0.4
261	0.5	0.2	0.0	0.4	0.6
262	0.6	0.4	0.0	0.4	0.6
263	0.6	0.5	0.1	0.4	0.7
264	0.6	0.6	0.2	0.3	0.7
265	0.5	0.7	0.2	0.3	0.6
266	0.5	0.7	0.0	0.4	0.5
267	0.6	0.5	0.0	0.4	0.4
268	0.6	0.5	0.3	0.3	0.5
269	0.6	0.6	0.3	0.3	0.5

270	0.6	0.7	0.3	0.2	0.4
271	0.6	0.9	0.3	0.2	0.5
272	0.5	0.7	0.2	0.2	0.5
273	0.6	0.8	0.1	0.1	0.5
274	0.6	0.7	0.1	0.1	0.5
275	0.6	0.5	-0.1	0.0	0.4
276	0.6	0.5	-0.3	0.0	0.6
277	0.6	0.6	-0.2	-0.1	0.6
278	0.7	0.6	-0.3	0.1	0.5
279	0.7	0.5	0.0	0.1	0.5
280	0.7	0.4	-0.1	0.1	0.5
281	0.8	0.4	-0.1	0.1	0.5
282	0.9	0.4	-0.1	0.2	0.4
283	0.9	0.3	0.0	0.2	0.5
284	0.8	0.3	0.2	0.0	0.4
285	0.8	0.4	0.2	0.0	0.4
286	0.7	0.3	0.1	0.0	0.3
287	0.7	0.2	0.0	0.1	0.4
288	0.8	0.1	0.0	0.1	0.4
289	0.9	0.1	0.0	0.1	0.3
290	0.8	0.0	0.0	0.1	0.3
291	0.8	0.0	-0.1	0.0	0.1
292	0.7	0.0	-0.1	0.1	0.1
293	0.7	0.0	0.1	-0.1	0.2
294	0.6	0.0	0.2	0.0	0.0
295	0.6	0.0	0.0	0.0	0.0
296	0.5	0.0	0.1	0.0	0.1
297	0.5	0.0	0.0	0.0	0.0
298	0.6	0.0	0.1	0.0	0.0
299	0.5	0.0	0.0	0.0	0.1

b) Sec. 4

y/W / Time (sec)	Concentration (ppb)				
	0.167	**0.333**	**0.500**	**0.667**	**0.833**
98	0.0	0.0	0.0	0.0	0.0
99	0.0	0.2	0.0	0.0	0.0
100	0.0	0.3	0.2	0.0	0.0
101	0.0	0.3	0.2	0.1	0.0
102	0.1	0.5	0.3	0.1	0.0
103	0.2	0.6	0.3	0.1	0.0
104	0.3	0.8	0.6	0.1	0.0
105	0.3	1.0	1.0	0.1	0.0
106	0.3	1.3	1.1	0.3	0.0
107	0.4	1.6	1.6	0.6	0.2
108	0.7	2.1	2.3	1.0	0.2
109	0.8	2.5	3.0	1.3	0.3
110	0.9	2.8	3.6	1.5	0.3
111	1.0	3.5	4.5	2.1	0.3
112	1.2	4.3	5.1	2.6	0.3
113	1.6	5.0	5.9	3.3	0.4
114	2.2	5.8	6.8	4.6	0.6
115	2.3	6.3	7.8	5.8	0.6
116	2.8	7.3	9.1	7.3	0.7
117	3.0	8.3	10.1	8.7	0.7
118	3.3	9.2	11.3	10.2	0.7
119	3.9	10.2	12.8	11.7	0.9
120	4.6	11.4	14.4	13.2	1.0
121	5.3	12.5	15.5	14.4	1.1
122	5.8	13.5	16.6	15.7	1.6
123	6.8	14.4	17.7	17.3	2.3
124	8.0	15.5	19.1	18.7	3.1
125	9.2	16.7	20.3	20.0	3.4
126	10.1	17.8	21.3	21.4	3.9
127	10.8	18.8	21.9	22.4	3.7
128	11.4	20.0	22.7	23.4	3.8
129	11.9	20.6	23.5	24.2	4.1
130	12.6	21.3	23.8	25.1	5.5
131	13.5	22.0	24.6	26.0	6.5
132	14.7	22.6	25.1	27.1	7.3
133	15.6	23.1	25.5	27.9	8.6
134	16.4	23.5	25.7	28.8	9.2
135	17.1	23.9	26.2	29.5	9.6
136	17.5	24.0	26.6	29.9	9.7
137	18.0	24.3	26.6	30.3	10.3
138	18.1	24.6	26.8	30.7	10.4
139	18.3	24.8	26.7	30.9	11.0
140	18.6	24.9	26.4	31.3	11.9
141	19.0	24.9	26.3	31.9	13.3
142	19.4	25.0	26.3	32.2	14.5
143	19.6	25.0	26.3	32.7	15.4
144	19.9	24.9	26.2	32.9	15.9
145	20.2	24.9	26.1	33.0	16.5
146	20.5	24.8	25.9	33.1	17.2
147	20.7	24.6	25.8	33.1	17.8
148	21.1	24.5	25.5	33.0	18.0
149	21.3	24.4	25.0	33.0	18.6
150	21.5	24.2	24.7	33.0	19.2

151	21.5	24.1	24.4	33.0	19.8
152	21.5	24.0	23.9	33.1	19.9
153	21.4	23.6	23.4	33.0	19.9
154	21.3	23.3	22.9	32.7	20.1
155	21.1	23.1	22.5	32.3	20.2
156	20.9	22.7	21.9	31.9	19.9
157	20.8	22.5	21.5	31.6	19.7
158	20.7	22.2	21.1	31.1	19.8
159	20.6	21.8	20.6	30.6	19.6
160	20.4	21.4	20.2	30.2	19.8
161	20.1	21.1	19.7	29.8	19.8
162	19.8	20.8	19.3	29.2	19.8
163	19.4	20.4	18.7	28.6	19.8
164	18.9	20.0	18.5	28.1	19.8
165	18.7	19.6	18.1	27.7	19.9
166	18.4	19.3	17.8	27.2	19.8
167	18.1	19.0	17.4	26.5	19.8
168	17.7	18.7	17.0	26.0	19.6
169	17.4	18.3	16.5	25.5	19.5
170	17.2	18.0	16.1	24.8	19.5
171	17.0	17.8	15.9	24.1	19.3
172	16.7	17.3	15.5	23.5	19.2
173	16.5	16.9	15.0	22.9	19.1
174	16.3	16.6	14.7	22.8	19.0
175	15.9	16.1	14.2	22.2	18.8
176	15.6	15.8	13.6	21.8	18.7
177	15.3	15.4	13.3	21.5	18.5
178	15.1	15.0	12.9	21.1	18.4
179	15.0	14.6	12.5	20.8	18.2
180	14.7	14.2	12.2	20.1	17.9
181	14.3	13.8	11.8	19.6	17.6
182	14.1	13.6	11.5	19.1	17.6
183	14.0	13.1	11.1	18.6	17.4
184	13.8	12.8	10.8	18.0	17.3
185	13.5	12.3	10.6	17.4	16.9
186	13.2	12.1	10.4	17.0	16.7
187	12.9	11.7	10.1	16.5	16.5
188	12.6	11.5	9.8	15.9	16.4
189	12.3	11.2	9.7	15.5	16.1
190	12.0	10.9	9.6	15.0	15.9
191	11.8	10.6	9.5	14.6	15.5
192	11.8	10.5	9.2	14.2	15.4
193	11.5	10.2	8.8	13.8	15.2
194	11.4	10.0	8.6	13.4	15.0
195	11.0	9.8	8.4	13.1	14.8
196	10.9	9.5	8.2	12.8	14.6
197	10.8	9.1	8.0	12.4	14.3
198	10.5	8.9	7.8	12.0	13.9
199	10.2	8.9	7.6	11.7	13.7
200	10.0	8.7	7.2	11.3	13.5
201	9.8	8.6	7.0	11.0	13.3
202	9.5	8.4	6.8	10.8	12.9
203	9.3	8.1	6.7	10.4	12.6
204	9.0	7.9	6.4	10.2	12.2
205	8.7	7.8	6.2	9.7	12.2
206	8.5	7.7	6.0	9.3	12.3
207	8.4	7.5	5.7	9.1	12.2
208	8.3	7.5	5.6	8.5	12.0
209	8.1	7.3	5.4	8.3	11.7

210	8.0	7.1	5.5	8.0	11.4
211	7.8	6.9	5.2	7.6	11.1
212	7.6	6.7	4.9	7.4	11.0
213	7.4	6.6	4.9	7.3	10.7
214	7.3	6.6	4.8	7.1	10.4
215	7.1	6.6	4.6	6.9	10.2
216	6.8	6.5	4.6	6.6	9.9
217	6.6	6.4	4.7	6.4	9.8
218	6.5	6.2	4.5	6.1	9.6
219	6.2	6.0	4.4	6.1	9.3
220	5.9	5.8	4.2	5.9	9.1
221	5.9	5.7	4.1	5.8	8.9
222	5.6	5.6	4.0	5.6	8.6
223	5.5	5.4	3.8	5.4	8.5
224	5.5	5.2	3.8	5.2	8.4
225	5.5	5.2	3.6	5.0	8.3
226	5.4	4.9	3.6	4.8	7.9
227	5.3	4.7	3.5	4.7	7.6
228	5.3	4.6	3.4	4.5	7.5
229	5.2	4.4	3.3	4.4	7.3
230	5.0	4.2	3.3	4.3	7.0
231	4.9	4.2	3.2	4.2	6.8
232	4.6	4.0	3.2	4.2	6.8
233	4.4	4.0	3.3	4.2	6.6
234	4.2	3.9	3.2	3.9	6.5
235	4.3	3.8	3.0	3.9	6.4
236	4.2	3.6	2.9	3.8	6.3
237	4.1	3.6	2.9	3.7	6.3
238	4.1	3.5	2.8	3.7	6.1
239	4.0	3.5	2.7	3.5	6.0
240	3.9	3.4	2.7	3.4	5.7
241	3.9	3.3	2.6	3.3	5.8
242	4.1	3.4	2.5	3.1	5.6
243	4.0	3.4	2.4	3.0	5.5
244	4.0	3.3	2.4	3.0	5.3
245	3.8	3.2	2.4	2.8	5.1
246	3.7	3.1	2.3	2.8	4.9
247	3.5	3.0	2.2	2.7	5.1
248	3.4	3.0	2.2	2.6	5.2
249	3.5	2.9	2.1	2.6	5.3
250	3.4	2.8	2.1	2.4	5.2
251	3.3	2.6	2.0	2.5	5.1
252	3.2	2.5	2.0	2.3	5.1
253	3.3	2.5	2.0	2.2	5.1
254	3.2	2.3	1.8	2.3	4.8
255	3.0	2.2	1.9	2.3	4.7
256	2.7	2.1	1.8	2.2	4.5
257	2.6	2.0	1.8	1.9	4.2
258	2.6	1.9	1.9	2.0	4.2
259	2.7	1.9	1.9	2.1	4.2
260	2.6	2.0	1.8	2.0	4.1
261	2.6	1.9	1.9	1.9	4.1
262	2.6	1.9	1.9	2.0	4.1
263	2.4	1.9	1.8	1.9	4.2
264	2.3	1.8	1.7	1.9	4.2
265	2.4	1.8	1.7	2.1	4.3
266	2.3	1.9	1.6	2.0	4.3
267	2.3	1.9	1.6	1.9	4.0
268	2.1	1.9	1.5	2.0	3.8

269	2.1	1.9	1.5	1.8	3.9
270	2.1	2.0	1.5	1.7	3.8
271	2.1	2.1	1.4	1.6	3.8
272	2.1	2.1	1.5	1.6	4.0
273	2.0	2.0	1.3	1.6	3.9
274	2.1	2.1	1.3	1.6	3.9
275	2.1	2.0	1.3	1.6	3.9
276	2.1	1.9	1.3	1.6	3.9
277	2.1	1.8	1.3	1.6	4.0
278	2.0	1.7	1.2	1.6	3.8
279	1.9	1.6	1.0	1.5	3.6
280	2.0	1.6	1.0	1.4	3.5
281	1.8	1.5	1.0	1.5	3.4
282	1.8	1.5	1.1	1.4	3.5
283	1.6	1.6	1.1	1.4	3.6
284	1.8	1.4	1.2	1.4	3.5
285	1.9	1.3	1.2	1.4	3.3
286	1.8	1.3	1.2	1.4	3.3
287	1.9	1.3	1.1	1.5	3.3
288	1.8	1.3	1.0	1.4	3.2
289	1.8	1.4	1.0	1.4	3.1
290	1.8	1.3	1.0	1.4	3.0
291	1.8	1.2	1.0	1.4	2.9
292	1.7	1.3	1.1	1.4	2.9
293	1.6	1.2	1.0	1.4	2.9
294	1.6	1.2	1.1	1.3	2.7
295	1.5	1.2	1.0	1.3	2.7
296	1.5	1.3	1.0	1.3	2.6
297	1.5	1.3	1.0	1.2	2.6
298	1.5	1.1	1.0	1.2	2.4
299	1.5	0.9	1.0	1.0	2.4
300	1.4	0.7	0.9	0.9	2.3
301	1.3	0.7	0.8	0.8	2.3
302	1.3	0.6	0.7	0.8	2.2
303	1.4	0.6	0.7	0.8	2.3
304	1.3	0.6	0.7	0.8	2.3
305	1.2	0.7	0.6	0.7	2.1
306	1.2	0.8	0.6	0.7	2.1
307	1.2	0.7	0.6	0.8	2.1
308	1.2	0.8	0.6	0.8	2.0
309	1.1	0.7	0.7	0.7	2.0
310	1.1	0.6	0.6	0.6	2.0
311	1.2	0.7	0.5	0.7	1.9
312	1.1	0.8	0.6	0.9	1.8
313	1.1	0.7	0.6	0.8	1.7
314	1.1	0.8	0.5	0.8	1.8
315	1.1	0.8	0.5	0.9	1.8
316	1.2	0.9	0.5	0.9	1.9
317	1.1	0.9	0.6	0.9	2.0
318	1.1	1.0	0.5	0.8	1.8
319	1.2	1.0	0.5	0.8	1.9
320	1.4	0.9	0.6	0.8	1.8
321	1.3	1.0	0.6	0.9	2.0
322	1.3	1.1	0.6	0.8	1.9
323	1.2	1.1	0.6	0.7	1.8
324	1.2	1.2	0.6	0.6	1.8
325	1.1	1.3	0.6	0.7	1.9
326	1.2	1.2	0.6	0.7	1.8
327	1.2	1.3	0.5	0.7	1.8

328	1.1	1.4	0.6	0.6	1.8
329	1.2	1.4	0.7	0.6	1.6
330	1.0	1.5	0.6	0.6	1.5
331	0.9	1.4	0.6	0.6	1.5
332	0.8	1.3	0.6	0.7	1.4
333	0.7	1.1	0.6	0.6	1.3
334	0.7	1.1	0.6	0.6	1.0
335	0.6	1.1	0.6	0.5	1.0
336	0.6	1.0	0.6	0.5	1.0
337	0.5	1.1	0.5	0.5	1.1
338	0.6	1.2	0.6	0.5	1.1
339	0.6	1.1	0.5	0.4	1.1
340	0.5	1.1	0.4	0.3	1.1
341	0.5	1.1	0.4	0.3	1.2
342	0.6	1.0	0.4	0.3	1.4
343	0.7	1.0	0.4	0.3	1.2
344	0.8	1.0	0.4	0.3	1.2
345	0.6	1.2	0.4	0.3	1.2
346	0.6	1.1	0.4	0.3	1.2
347	0.5	1.2	0.3	0.3	1.3
348	0.6	1.2	0.4	0.3	1.2
349	0.5	1.1	0.3	0.2	1.2
350	0.5	1.0	0.3	0.2	1.4
351	0.6	0.9	0.4	0.3	1.6
352	0.7	0.9	0.3	0.2	1.6
353	0.6	1.0	0.4	0.1	1.7
354	0.6	1.0	0.5	0.2	1.6
355	0.6	1.1	0.2	0.2	1.5
356	0.6	1.1	0.3	0.2	1.6
357	0.6	1.0	0.3	0.3	1.6
358	0.7	0.9	0.3	0.3	1.6
359	0.8	0.9	0.2	0.2	1.6
360	0.9	0.8	0.2	0.1	1.4
361	0.9	0.8	0.2	0.1	1.5
362	0.8	0.7	0.1	0.1	1.4
363	0.8	0.8	0.2	0.2	1.4
364	0.6	0.7	0.3	0.3	1.3
365	0.6	0.8	0.3	0.3	1.2
366	0.7	0.8	0.5	0.3	1.2
367	0.7	0.9	0.5	0.3	1.2
368	0.7	0.9	0.4	0.3	1.2
369	0.8	0.8	0.5	0.4	1.2
370	0.7	0.8	0.4	0.3	1.2
371	0.7	0.7	0.4	0.3	1.0
372	0.7	0.6	0.3	0.2	0.9
373	0.6	0.5	0.4	0.2	0.8
374	0.5	0.6	0.3	0.3	0.8
375	0.3	0.8	0.3	0.4	0.9
376	0.2	0.8	0.3	0.5	0.9
377	0.2	0.6	0.3	0.5	1.0
378	0.2	0.7	0.3	0.5	0.8
379	0.2	0.7	0.2	0.5	1.0
380	0.2	0.6	0.3	0.4	1.0
381	0.2	0.6	0.3	0.5	1.1
382	0.3	0.6	0.1	0.4	1.1
383	0.4	0.7	0.2	0.4	1.0
384	0.4	0.7	0.2	0.5	1.0
385	0.4	0.7	0.1	0.5	1.0
386	0.4	0.7	0.2	0.5	1.0

387	0.5	0.8	0.1	0.5	1.0
388	0.4	0.7	0.1	0.4	0.9
389	0.6	0.6	0.1	0.4	1.1
390	0.5	0.6	0.2	0.4	1.0
391	0.4	0.6	0.3	0.3	0.9
392	0.4	0.6	0.3	0.3	0.7
393	0.5	0.6	0.3	0.2	0.8
394	0.5	0.5	0.3	0.2	0.9
395	0.5	0.4	0.3	0.1	0.9
396	0.4	0.5	0.3	0.1	0.9
397	0.4	0.6	0.1	0.1	0.9
398	0.4	0.6	0.1	0.1	1.2
399	0.5	0.7	0.1	0.1	1.1
400	0.6	0.5	-0.1	0.2	1.0
401	0.5	0.5	0.0	0.2	1.0
402	0.5	0.4	0.1	0.3	1.0
403	0.4	0.4	0.1	0.4	1.0
404	0.4	0.3	0.2	0.3	0.9
405	0.5	0.3	0.1	0.2	1.0
406	0.4	0.4	0.1	0.2	0.9
407	0.3	0.3	0.2	0.2	0.9
408	0.2	0.1	0.2	0.2	0.9
409	0.2	0.2	0.3	0.1	0.9
410	0.1	0.2	0.3	0.1	0.8
411	0.0	0.3	0.2	0.0	0.7
412	0.2	0.2	0.2	0.0	0.6
413	0.5	0.2	0.2	0.1	0.7
414	0.4	0.3	0.2	0.1	0.5
415	0.5	0.3	0.2	0.0	0.4
416	0.5	0.4	0.1	0.1	0.4
417	0.6	0.5	0.0	0.0	0.5
418	0.6	0.7	-0.1	0.0	0.5
419	0.6	0.5	0.0	-0.1	0.4
420	0.6	0.5	0.0	0.0	0.3
421	0.6	0.6	-0.1	0.0	0.4
422	0.6	0.6	-0.1	0.1	0.5
423	0.5	0.6	0.0	0.0	0.6
424	0.4	0.4	0.1	0.1	0.6
425	0.3	0.4	0.3	0.1	0.6
426	0.4	0.6	0.2	0.2	0.6
427	0.5	0.6	0.3	0.3	0.5
428	0.6	0.9	0.4	0.3	0.6
429	0.4	1.0	0.4	0.3	0.6
430	0.6	1.1	0.3	0.3	0.7
431	0.5	1.2	0.4	0.4	0.5
432	0.5	1.1	0.3	0.4	0.5
433	0.5	1.2	0.4	0.6	0.5
434	0.6	1.2	0.3	0.5	0.4
435	0.5	1.0	0.4	0.5	0.5
436	0.4	1.0	0.3	0.4	0.5
437	0.4	1.0	0.4	0.3	0.6
438	0.4	1.0	0.4	0.2	0.7
439	0.5	1.0	0.4	0.3	0.5
440	0.6	0.9	0.0	0.2	0.6
441	0.6	1.0	0.1	0.2	0.6
442	0.5	0.9	0.0	0.2	0.6
443	0.6	0.9	0.0	0.1	0.7

c) Sec. 6

y/W / Time (sec)	Concentration (ppb)				
	0.167	**0.333**	**0.500**	**0.667**	**0.833**
140	0.0	0.0	0.0	0.0	-
141	0.0	0.1	0.0	0.0	-
142	0.0	0.1	0.0	0.0	-
143	0.0	0.1	0.0	0.0	-
144	0.0	0.1	0.0	0.0	-
145	0.0	0.2	0.0	0.0	-
146	0.0	0.2	0.2	0.0	-
147	0.0	0.2	0.3	0.0	-
148	0.0	0.2	0.5	0.0	-
149	0.0	0.3	0.5	0.0	-
150	0.0	0.2	0.7	0.0	-
151	0.0	0.3	0.5	0.0	-
152	0.0	0.4	0.6	0.0	-
153	0.0	0.3	0.8	0.0	-
154	0.0	0.5	0.7	0.0	-
155	0.0	0.5	0.7	0.0	-
156	0.0	0.7	1.1	0.1	-
157	0.0	1.0	1.1	0.2	-
158	0.0	1.4	1.2	0.3	-
159	0.0	1.6	1.4	0.2	-
160	0.0	1.8	1.5	0.3	-
161	0.0	2.0	1.7	0.4	-
162	0.0	2.1	2.1	0.6	-
163	0.0	2.3	2.3	0.8	-
164	0.0	2.7	2.7	1.0	-
165	0.0	2.9	3.1	1.3	-
166	0.0	3.1	3.3	1.4	-
167	0.0	3.6	4.0	1.7	-
168	0.0	4.3	4.2	2.1	-
169	0.0	4.8	4.4	2.5	-
170	0.0	5.3	4.7	3.0	-
171	0.0	5.9	5.1	3.3	-
172	0.0	6.5	5.9	3.5	-
173	0.0	7.0	6.4	3.9	-
174	0.0	7.4	7.2	4.4	-
175	0.0	7.9	7.6	4.8	-
176	0.0	8.5	8.2	5.3	-
177	0.0	9.0	9.1	5.6	-
178	0.0	9.4	9.6	5.9	-
179	0.0	10.0	10.2	6.4	-
180	0.0	10.5	10.7	6.8	-
181	0.0	11.0	11.4	7.5	-
182	0.0	11.4	11.8	8.0	-
183	0.0	11.8	12.4	8.4	-
184	0.0	12.3	12.9	9.3	-
185	0.0	12.8	13.3	10.1	-
186	0.0	13.4	13.5	10.5	-
187	0.1	13.8	13.8	10.7	-
188	0.3	14.2	14.3	10.9	-
189	0.5	14.5	14.7	11.4	-
190	0.8	15.0	15.1	11.8	-
191	1.0	15.4	15.4	12.2	-
192	1.3	15.8	15.8	12.5	-

193	1.6	16.2	16.1	12.8	-
194	1.8	16.5	16.4	13.3	-
195	2.1	16.8	16.8	13.6	-
196	2.4	17.2	17.2	14.2	-
197	2.6	17.5	17.4	14.9	-
198	2.8	17.6	17.4	15.1	-
199	2.9	17.8	17.6	15.3	-
200	3.1	17.9	17.7	15.4	-
201	3.4	18.1	18.0	15.7	-
202	3.5	18.2	18.2	15.8	-
203	3.6	18.3	18.1	16.0	-
204	3.7	18.4	18.1	16.2	-
205	3.7	18.7	17.9	16.4	-
206	3.8	18.7	17.9	16.5	-
207	3.6	18.7	17.9	16.6	-
208	3.7	18.8	17.9	16.7	-
209	3.7	18.7	17.8	16.8	-
210	3.8	18.6	17.7	16.7	-
211	3.8	18.7	17.5	16.8	-
212	3.8	18.5	17.3	16.9	-
213	3.9	18.6	17.2	17.0	-
214	4.0	18.5	17.0	17.0	-
215	4.0	18.5	17.0	17.1	-
216	4.1	18.3	16.9	17.3	-
217	4.1	18.2	16.8	17.3	-
218	4.2	18.1	16.6	17.4	-
219	4.2	18.0	16.4	17.4	-
220	4.3	17.8	16.2	17.4	-
221	4.3	17.6	16.3	17.3	-
222	4.4	17.4	16.3	17.4	-
223	4.3	17.4	16.1	17.3	-
224	4.1	17.3	16.1	17.2	-
225	4.2	17.0	15.8	17.0	-
226	4.0	16.9	15.5	17.0	-
227	4.1	16.6	15.2	16.8	-
228	4.2	16.5	15.1	16.5	-
229	4.3	16.4	14.8	16.3	-
230	4.3	16.3	14.8	16.2	-
231	4.2	16.1	14.5	16.1	-
232	4.3	15.9	14.2	15.8	-
233	4.1	15.8	13.8	15.6	-
234	4.0	15.5	13.4	15.4	-
235	4.0	15.4	13.2	15.3	-
236	4.0	15.1	13.0	15.3	-
237	4.0	14.9	12.9	15.1	-
238	3.8	14.6	12.6	14.7	-
239	3.8	14.4	12.3	14.4	-
240	3.8	14.2	12.2	14.2	-
241	3.9	13.9	12.0	13.9	-
242	3.9	13.7	11.7	13.7	-
243	3.8	13.5	11.5	13.5	-
244	3.7	13.3	11.2	13.4	-
245	3.8	13.1	10.9	13.2	-
246	3.7	12.9	10.8	12.9	-
247	3.7	12.8	10.7	12.8	-
248	3.8	12.6	10.5	12.6	-
249	3.6	12.4	10.1	12.2	-
250	3.5	12.2	9.8	12.1	-
251	3.4	11.9	9.7	11.9	-

252	3.3	11.7	9.5	11.7	-
253	3.2	11.6	9.5	11.4	-
254	3.3	11.3	9.3	11.3	-
255	3.4	11.0	9.0	11.1	-
256	3.4	10.7	8.8	10.9	-
257	3.4	10.5	8.7	10.8	-
258	3.4	10.2	8.5	10.6	-
259	3.2	10.1	8.1	10.3	-
260	3.2	9.9	7.9	10.2	-
261	3.2	9.7	7.9	9.9	-
262	3.1	9.4	7.5	9.6	-
263	3.0	9.3	7.5	9.4	-
264	3.0	9.1	7.4	9.2	-
265	2.9	8.9	7.1	8.9	-
266	2.9	8.8	6.9	8.7	-
267	3.0	8.7	6.8	8.7	-
268	2.9	8.5	6.8	8.6	-
269	2.8	8.4	6.7	8.5	-
270	2.7	8.3	6.6	8.4	-
271	2.6	8.1	6.5	8.3	-
272	2.6	7.9	6.3	8.1	-
273	2.6	7.8	5.9	8.0	-
274	2.3	7.5	5.7	7.8	-
275	2.4	7.4	5.8	7.8	-
276	2.3	7.3	5.7	7.5	-
277	2.1	7.3	5.6	7.4	-
278	2.1	7.2	5.4	7.2	-
279	2.1	7.1	5.3	6.9	-
280	1.9	7.0	5.1	6.8	-
281	1.8	6.8	5.1	6.7	-
282	2.0	6.7	5.0	6.7	-
283	2.0	6.6	4.9	6.6	-
284	1.9	6.5	4.9	6.6	-
285	1.8	6.4	4.9	6.6	-
286	2.0	6.2	4.9	6.4	-
287	1.9	6.1	4.8	6.3	-
288	2.0	6.0	4.7	6.2	-
289	1.9	5.8	4.7	6.1	-
290	2.0	5.6	4.7	6.1	-
291	1.9	5.4	4.6	6.0	-
292	2.0	5.3	4.5	5.9	-
293	2.0	5.1	4.5	5.8	-
294	2.0	5.1	4.5	5.6	-
295	1.9	5.0	4.3	5.5	-
296	1.9	4.9	4.4	5.4	-
297	1.8	4.7	4.2	5.3	-
298	1.7	4.7	4.3	5.1	-
299	1.9	4.5	4.0	5.0	-
300	2.0	4.3	4.0	4.8	-
301	1.9	4.3	4.1	4.7	-
302	1.8	4.4	4.0	4.6	-
303	1.9	4.3	3.8	4.5	-
304	1.8	4.3	3.6	4.5	-
305	1.8	4.2	3.6	4.4	-
306	1.8	4.1	3.5	4.3	-
307	1.6	4.0	3.3	4.3	-
308	1.7	4.1	3.2	4.3	-
309	1.6	4.0	3.2	4.2	-
310	1.6	3.9	3.0	4.0	-

311	1.6	3.9	2.9	4.0	-
312	1.5	3.8	2.9	4.0	-
313	1.6	3.6	2.8	3.8	-
314	1.5	3.6	2.8	3.7	-
315	1.2	3.5	2.8	3.6	-
316	1.1	3.5	2.8	3.6	-
317	1.2	3.5	2.6	3.6	-
318	1.1	3.4	2.6	3.6	-
319	1.1	3.4	2.5	3.4	-
320	1.2	3.3	2.4	3.3	-
321	1.1	3.3	2.3	3.3	-
322	1.1	3.4	2.2	3.3	-
323	1.0	3.3	2.1	3.2	-
324	1.2	3.2	2.1	3.1	-
325	1.1	3.2	2.0	3.1	-
326	1.1	3.1	1.9	3.1	-
327	1.1	2.9	2.0	3.0	-
328	1.0	2.9	2.1	2.9	-
329	1.1	2.9	2.1	2.8	-
330	0.9	2.9	2.1	2.7	-
331	1.0	2.8	1.9	2.7	-
332	0.9	2.7	2.0	2.6	-
333	1.0	2.7	1.9	2.7	-
334	0.8	2.6	2.0	2.7	-
335	0.9	2.4	1.9	2.7	-
336	0.9	2.5	1.8	2.7	-
337	1.0	2.4	1.8	2.7	-
338	0.9	2.4	1.9	2.7	-
339	0.9	2.5	1.8	2.7	-
340	0.8	2.4	1.8	2.6	-
341	0.7	2.4	1.9	2.6	-
342	0.8	2.4	1.8	2.5	-
343	0.8	2.4	1.8	2.5	-
344	0.8	2.2	1.7	2.4	-
345	1.0	2.1	1.5	2.3	-
346	0.9	2.1	1.4	2.2	-
347	1.0	2.1	1.4	2.2	-
348	1.0	2.2	1.5	2.1	-
349	0.9	2.0	1.6	2.2	-
350	1.0	1.9	1.5	2.1	-
351	1.0	1.9	1.5	2.0	-
352	0.9	1.9	1.3	1.8	-
353	0.9	1.8	1.2	1.8	-
354	1.0	1.6	1.0	1.7	-
355	0.8	1.6	1.0	1.7	-
356	0.8	1.6	1.2	1.7	-
357	0.8	1.6	1.3	1.7	-
358	0.8	1.7	1.3	1.7	-
359	0.9	1.7	1.3	1.7	-
360	1.0	1.6	1.3	1.7	-
361	0.9	1.6	1.5	1.7	-
362	1.0	1.6	1.5	1.6	-
363	0.9	1.7	1.5	1.7	-
364	0.9	1.6	1.5	1.6	-
365	0.8	1.5	1.4	1.6	-
366	0.6	1.4	1.3	1.7	-
367	0.6	1.4	1.3	1.7	-
368	0.5	1.4	1.2	1.7	-
369	0.4	1.4	1.2	1.6	-

370	0.5	1.4	1.2	1.5	-
371	0.4	1.3	1.4	1.6	-
372	0.3	1.2	1.1	1.5	-
373	0.1	1.2	1.3	1.6	-
374	0.1	1.0	1.4	1.5	-
375	0.2	1.0	1.5	1.5	-
376	0.1	1.0	1.3	1.4	-
377	0.1	1.1	1.2	1.4	-
378	0.1	1.1	1.1	1.3	-
379	0.2	1.0	1.0	1.4	-
380	0.1	1.0	0.8	1.4	-
381	0.3	1.0	0.8	1.4	-
382	0.4	1.0	0.8	1.4	-
383	0.4	1.1	0.8	1.4	-
384	0.4	1.0	0.9	1.4	-
385	0.3	1.0	0.9	1.4	-
386	0.5	1.0	0.9	1.3	-
387	0.5	1.0	0.9	1.3	-
388	0.5	1.0	0.9	1.3	-
389	0.6	0.8	0.8	1.3	-
390	0.6	0.9	0.7	1.2	-
391	0.5	0.9	0.6	1.2	-
392	0.6	1.0	0.5	1.2	-
393	0.6	1.0	0.5	1.1	-
394	0.6	1.0	0.6	1.1	-
395	0.6	1.0	0.4	1.1	-
396	0.4	0.9	0.4	1.1	-
397	0.4	0.9	0.4	1.0	-
398	0.4	0.9	0.3	1.0	-
399	0.4	0.9	0.2	1.0	-
400	0.4	1.0	0.4	0.9	-
401	0.4	0.9	0.7	0.9	-
402	0.2	1.0	0.8	0.9	-
403	0.3	1.0	0.7	0.8	-
404	0.2	0.9	0.8	0.9	-
405	0.3	0.9	0.8	0.9	-
406	0.3	0.8	1.0	1.0	-
407	0.5	0.9	1.2	0.9	-
408	0.5	0.8	1.3	0.8	-
409	0.5	0.7	1.2	0.9	-
410	0.5	0.7	1.1	0.9	-
411	0.6	0.7	1.2	0.9	-
412	0.5	0.7	1.0	0.9	-
413	0.5	0.7	0.9	0.8	-
414	0.5	0.6	0.8	0.9	-
415	0.5	0.6	0.8	0.9	-
416	0.5	0.6	0.8	1.0	-
417	0.6	0.7	0.8	1.0	-
418	0.6	0.7	0.7	1.0	-
419	0.7	0.7	0.8	0.9	-
420	0.5	0.7	0.9	0.9	-
421	0.5	0.6	0.9	1.0	-
422	0.5	0.6	0.9	0.9	-
423	0.5	0.5	0.9	0.9	-
424	0.6	0.4	0.9	0.8	-
425	0.6	0.4	0.9	0.8	-
426	0.5	0.5	0.7	0.9	-
427	0.6	0.6	0.8	0.8	-
428	0.6	0.5	0.6	0.8	-

429	0.6	0.5	0.6	0.8	-
430	0.5	0.6	0.6	0.8	-
431	0.4	0.7	0.5	0.8	-
432	0.5	0.6	0.7	0.8	-
433	0.6	0.6	0.6	0.8	-
434	0.6	0.7	0.6	0.8	-
435	0.5	0.7	0.6	0.9	-
436	0.5	0.6	0.6	0.9	-
437	0.5	0.5	0.6	0.9	-
438	0.6	0.5	0.8	0.8	-
439	0.6	0.5	0.8	0.7	-
440	0.7	0.5	0.7	0.6	-
441	0.7	0.5	0.7	0.6	-
442	0.7	0.5	0.7	0.6	-
443	0.7	0.6	0.8	0.6	-

Appendix C. Tracer test results in EXP-A317

Table C1. Velocity and water depth measurement using ADCP
a) Sec. 1

UTM Easting (m)	UTM Northing (m)	Water depth (m)	Distance from left bank (m)	Streamwise Velocity (cm/s)	Transverse Velocity (cm/s)	Vertical Velocity (cm/s)
460755.1	4046217.1	0.1	0.5	57.1	-2.1	3.7
460755.2	4046217.2	0.1	0.6	56.4	-7.2	2.9
460755.2	4046217.2	0.2	0.6	56.4	-7.2	2.9
460755.2	4046217.3	0.1	0.7	60.5	-7.6	3.2
460755.2	4046217.3	0.2	0.7	59.5	-7.3	2.9
460755.3	4046217.3	0.1	0.8	60.9	-11.9	3.5
460755.3	4046217.3	0.2	0.8	61.2	-10.0	3.5
460755.3	4046217.3	0.3	0.8	63.0	-10.6	3.1
460755.3	4046217.4	0.1	0.9	65.6	-10.0	3.7
460755.3	4046217.4	0.2	0.9	66.4	-7.3	3.9
460755.3	4046217.4	0.3	0.9	71.4	-5.1	3.5
460755.4	4046217.5	0.1	1.0	66.8	-10.8	3.1
460755.4	4046217.5	0.2	1.0	68.2	-7.6	3.7
460755.4	4046217.5	0.3	1.0	71.6	-5.9	3.0
460755.4	4046217.5	0.4	1.0	72.0	-0.9	3.0
460755.4	4046217.6	0.1	1.1	68.8	-12.6	2.0
460755.4	4046217.6	0.2	1.1	69.6	-9.5	2.3
460755.4	4046217.6	0.3	1.1	70.6	-5.9	2.0
460755.4	4046217.6	0.4	1.1	70.4	-2.4	2.0
460755.5	4046217.7	0.1	1.2	69.3	-13.1	1.8
460755.5	4046217.7	0.2	1.2	69.2	-11.5	1.8
460755.5	4046217.7	0.3	1.2	67.2	-10.3	1.4
460755.5	4046217.7	0.4	1.2	65.5	-8.9	1.4
460755.5	4046217.8	0.1	1.3	71.5	-12.6	1.9
460755.5	4046217.8	0.2	1.3	73.2	-11.1	1.8
460755.5	4046217.8	0.3	1.3	72.6	-9.8	1.4
460755.5	4046217.8	0.4	1.3	72.7	-9.3	1.5
460755.6	4046217.9	0.1	1.4	74.8	-9.2	2.7
460755.6	4046217.9	0.2	1.4	77.5	-8.5	2.3
460755.6	4046217.9	0.3	1.4	77.6	-8.9	1.0
460755.6	4046217.9	0.4	1.4	77.6	-11.6	0.0
460755.6	4046218.0	0.1	1.5	78.8	-10.7	2.4
460755.6	4046218.0	0.2	1.5	81.3	-9.6	1.6
460755.6	4046218.0	0.3	1.5	81.2	-7.9	-0.2
460755.6	4046218.0	0.4	1.5	79.5	-9.0	-1.0
460755.6	4046218.0	0.5	1.5	75.4	-10.0	-1.7
460755.7	4046218.0	0.1	1.6	85.2	-13.0	1.7
460755.7	4046218.0	0.2	1.6	86.1	-12.6	0.9
460755.7	4046218.0	0.3	1.6	84.3	-10.2	-0.7
460755.7	4046218.0	0.4	1.6	78.4	-11.7	-1.6
460755.7	4046218.0	0.5	1.6	73.6	-11.7	-2.0
460755.7	4046218.1	0.1	1.7	88.2	-15.8	0.7
460755.7	4046218.1	0.2	1.7	88.5	-15.5	-0.2
460755.7	4046218.1	0.3	1.7	87.1	-13.1	-1.6
460755.7	4046218.1	0.4	1.7	81.3	-12.3	-2.0
460755.7	4046218.1	0.5	1.7	77.5	-11.1	-2.1
460755.7	4046218.2	0.1	1.8	88.0	-14.1	0.8
460755.7	4046218.2	0.2	1.8	88.7	-14.6	-0.1

460755.7	4046218.2	0.3	1.8	88.7	-15.2	-1.4
460755.7	4046218.2	0.4	1.8	84.6	-16.4	-2.4
460755.7	4046218.2	0.5	1.8	80.9	-18.3	-3.0
460755.8	4046218.3	0.1	1.9	84.8	-14.6	-0.1
460755.8	4046218.3	0.2	1.9	86.5	-15.6	-1.4
460755.8	4046218.3	0.3	1.9	88.5	-18.2	-3.4
460755.8	4046218.3	0.4	1.9	86.7	-19.6	-4.5
460755.8	4046218.3	0.5	1.9	81.5	-22.9	-4.9
460755.8	4046218.3	0.6	1.9	77.2	-24.1	-4.9
460755.8	4046218.4	0.1	2.0	85.7	-14.3	-1.8
460755.8	4046218.4	0.2	2.0	87.4	-15.9	-3.2
460755.8	4046218.4	0.3	2.0	88.1	-19.8	-5.0
460755.8	4046218.4	0.4	2.0	86.0	-22.9	-6.1
460755.8	4046218.4	0.5	2.0	79.5	-25.5	-6.2
460755.8	4046218.4	0.6	2.0	76.1	-26.0	-6.5
460755.9	4046218.5	0.1	2.1	88.3	-14.5	-3.3
460755.9	4046218.5	0.2	2.1	89.3	-16.0	-4.5
460755.9	4046218.5	0.3	2.1	89.1	-19.2	-6.5
460755.9	4046218.5	0.4	2.1	86.3	-22.5	-7.1
460755.9	4046218.5	0.5	2.1	80.6	-23.3	-7.0
460755.9	4046218.5	0.6	2.1	77.9	-23.7	-7.2
460755.9	4046218.6	0.1	2.2	92.1	-11.2	-3.2
460755.9	4046218.6	0.2	2.2	93.0	-12.7	-4.1
460755.9	4046218.6	0.3	2.2	93.5	-14.7	-6.0
460755.9	4046218.6	0.4	2.2	90.4	-18.9	-6.3
460755.9	4046218.6	0.5	2.2	83.5	-19.5	-5.1
460755.9	4046218.6	0.6	2.2	80.1	-20.2	-4.5
460756.0	4046218.7	0.1	2.3	93.9	-10.7	-2.0
460756.0	4046218.7	0.2	2.3	94.2	-11.0	-2.9
460756.0	4046218.7	0.3	2.3	95.9	-12.3	-4.3
460756.0	4046218.7	0.4	2.3	89.6	-16.7	-4.2
460756.0	4046218.7	0.5	2.3	84.0	-18.2	-2.9
460756.0	4046218.7	0.6	2.3	78.4	-20.5	-2.1
460756.0	4046218.8	0.1	2.4	94.8	-10.6	-1.3
460756.0	4046218.8	0.2	2.4	96.1	-10.4	-2.0
460756.0	4046218.8	0.3	2.4	97.9	-11.2	-3.0
460756.0	4046218.8	0.4	2.4	89.5	-16.2	-2.9
460756.0	4046218.8	0.5	2.4	82.2	-19.4	-1.3
460756.1	4046218.8	0.1	2.5	94.5	-12.0	-0.9
460756.1	4046218.8	0.2	2.5	95.1	-11.2	-1.6
460756.1	4046218.8	0.3	2.5	95.4	-13.0	-2.5
460756.1	4046218.8	0.4	2.5	86.4	-18.2	-2.6
460756.1	4046218.8	0.5	2.5	81.4	-22.5	-2.4
460756.1	4046218.9	0.1	2.6	93.1	-11.9	-0.9
460756.1	4046218.9	0.2	2.6	94.7	-11.4	-1.4
460756.1	4046218.9	0.3	2.6	94.3	-13.9	-2.5
460756.1	4046218.9	0.4	2.6	88.0	-19.2	-2.5
460756.1	4046218.9	0.5	2.6	83.0	-23.6	-2.5
460756.2	4046219.0	0.1	2.7	92.0	-13.0	-1.0
460756.2	4046219.0	0.2	2.7	93.6	-12.4	-1.2
460756.2	4046219.0	0.3	2.7	93.4	-14.4	-2.0
460756.2	4046219.0	0.4	2.7	87.6	-18.8	-2.3
460756.2	4046219.0	0.5	2.7	74.6	-23.6	-2.5
460756.2	4046219.1	0.1	2.8	92.2	-13.2	-0.8
460756.2	4046219.1	0.2	2.8	94.9	-13.5	-0.7
460756.2	4046219.1	0.3	2.8	96.3	-15.5	-0.7
460756.2	4046219.1	0.4	2.8	90.7	-20.3	-0.7
460756.2	4046219.1	0.5	2.8	74.4	-27.4	-1.3
460756.2	4046219.1	0.6	2.8	64.8	-31.7	-1.8

460756.3	4046219.2	0.1	2.9	90.8	-13.6	-1.0
460756.3	4046219.2	0.2	2.9	94.8	-14.0	-1.1
460756.3	4046219.2	0.3	2.9	97.0	-15.5	-1.0
460756.3	4046219.2	0.4	2.9	93.3	-19.6	-1.2
460756.3	4046219.2	0.5	2.9	74.0	-28.2	-1.6
460756.3	4046219.2	0.6	2.9	64.5	-33.0	-2.1
460756.3	4046219.3	0.1	3.0	92.2	-12.5	-0.5
460756.3	4046219.3	0.2	3.0	95.5	-14.3	-0.9
460756.3	4046219.3	0.3	3.0	97.0	-15.7	-1.0
460756.3	4046219.3	0.4	3.0	93.3	-20.3	-1.5
460756.3	4046219.3	0.5	3.0	78.1	-28.9	-1.5
460756.3	4046219.3	0.6	3.0	71.8	-34.5	-1.6
460756.4	4046219.4	0.1	3.1	90.9	-11.6	-0.9
460756.4	4046219.4	0.2	3.1	93.8	-13.1	-1.2
460756.4	4046219.4	0.3	3.1	94.3	-13.6	-1.7
460756.4	4046219.4	0.4	3.1	90.4	-17.3	-2.2
460756.4	4046219.4	0.5	3.1	77.4	-24.8	-1.8
460756.4	4046219.4	0.6	3.1	72.7	-29.5	-1.5
460756.4	4046219.5	0.1	3.2	91.6	-11.8	-1.0
460756.4	4046219.5	0.2	3.2	92.7	-13.9	-1.1
460756.4	4046219.5	0.3	3.2	93.1	-14.4	-1.3
460756.4	4046219.5	0.4	3.2	87.8	-18.5	-1.7
460756.4	4046219.5	0.5	3.2	77.7	-23.9	-1.4
460756.4	4046219.5	0.6	3.2	73.5	-28.0	-1.3
460756.4	4046219.5	0.1	3.3	87.6	-12.8	-1.6
460756.4	4046219.5	0.2	3.3	89.3	-14.6	-1.3
460756.4	4046219.5	0.3	3.3	91.2	-14.3	-1.0
460756.4	4046219.5	0.4	3.3	87.1	-18.9	-1.1
460756.4	4046219.5	0.5	3.3	80.0	-22.8	-0.9
460756.4	4046219.5	0.6	3.3	75.8	-27.0	-1.0
460756.5	4046219.6	0.1	3.4	84.7	-14.5	-1.4
460756.5	4046219.6	0.2	3.4	85.4	-16.2	-1.6
460756.5	4046219.6	0.3	3.4	86.3	-17.1	-0.8
460756.5	4046219.6	0.4	3.4	82.7	-22.3	-0.9
460756.5	4046219.6	0.5	3.4	77.7	-25.7	-0.1
460756.5	4046219.6	0.6	3.4	74.4	-29.2	-0.1
460756.5	4046219.7	0.1	3.5	83.7	-13.4	-1.2
460756.5	4046219.7	0.2	3.5	84.4	-15.3	-1.2
460756.5	4046219.7	0.3	3.5	86.8	-17.2	-0.2
460756.5	4046219.7	0.4	3.5	84.3	-23.9	-0.2
460756.5	4046219.7	0.5	3.5	81.8	-26.5	0.4
460756.5	4046219.7	0.6	3.5	79.2	-29.1	0.3
460756.6	4046219.8	0.1	3.6	82.7	-13.8	-1.3
460756.6	4046219.8	0.2	3.6	83.6	-15.4	-1.5
460756.6	4046219.8	0.3	3.6	85.9	-19.5	-0.3
460756.6	4046219.8	0.4	3.6	84.0	-26.9	0.0
460756.6	4046219.8	0.5	3.6	81.3	-30.2	0.7
460756.6	4046219.8	0.6	3.6	78.8	-30.9	0.4
460756.6	4046219.9	0.1	3.7	82.6	-13.2	-1.2
460756.6	4046219.9	0.2	3.7	84.5	-14.9	-0.9
460756.6	4046219.9	0.3	3.7	87.1	-18.6	0.0
460756.6	4046219.9	0.4	3.7	86.4	-24.5	0.4
460756.6	4046219.9	0.5	3.7	84.2	-28.6	0.7
460756.6	4046219.9	0.6	3.7	82.6	-28.9	0.7
460756.7	4046220.0	0.1	3.8	81.5	-12.3	-0.6
460756.7	4046220.0	0.2	3.8	83.3	-15.0	-0.6
460756.7	4046220.0	0.3	3.8	85.3	-19.6	0.0
460756.7	4046220.0	0.4	3.8	84.6	-22.9	0.2
460756.7	4046220.0	0.5	3.8	82.4	-26.9	0.7

460756.7	4046220.0	0.6	3.8	80.8	-25.5	0.7
460756.7	4046220.1	0.1	3.9	79.4	-12.8	0.4
460756.7	4046220.1	0.2	3.9	81.5	-15.5	0.3
460756.7	4046220.1	0.3	3.9	83.9	-19.3	0.4
460756.7	4046220.1	0.4	3.9	84.0	-21.0	0.5
460756.7	4046220.1	0.5	3.9	82.8	-23.5	1.0
460756.8	4046220.2	0.1	4.0	75.4	-14.2	0.8
460756.8	4046220.2	0.2	4.0	78.1	-16.1	0.7
460756.8	4046220.2	0.3	4.0	82.7	-20.4	1.0
460756.8	4046220.2	0.4	4.0	82.2	-22.0	1.3
460756.8	4046220.2	0.5	4.0	81.6	-23.0	1.8
460756.8	4046220.3	0.1	4.1	69.1	-16.2	0.7
460756.8	4046220.3	0.2	4.1	72.6	-17.5	1.2
460756.8	4046220.3	0.3	4.1	77.1	-21.1	2.1
460756.8	4046220.3	0.4	4.1	77.4	-21.8	3.2
460756.8	4046220.3	0.5	4.1	76.3	-22.6	3.8
460756.9	4046220.3	0.1	4.2	68.3	-15.6	1.1
460756.9	4046220.3	0.2	4.2	72.1	-16.7	1.4
460756.9	4046220.3	0.3	4.2	76.1	-21.0	2.3
460756.9	4046220.3	0.4	4.2	75.5	-21.3	3.3
460756.9	4046220.3	0.5	4.2	73.4	-22.5	3.9
460756.9	4046220.4	0.1	4.3	68.5	-15.2	1.6
460756.9	4046220.4	0.2	4.3	71.5	-17.0	1.7
460756.9	4046220.4	0.3	4.3	73.3	-21.0	2.4
460756.9	4046220.4	0.4	4.3	73.4	-20.9	3.1
460756.9	4046220.4	0.5	4.3	71.1	-21.2	3.7
460757.0	4046220.5	0.1	4.4	68.6	-16.9	2.5
460757.0	4046220.5	0.2	4.4	71.3	-17.6	2.1
460757.0	4046220.5	0.3	4.4	72.6	-20.0	1.7
460757.0	4046220.5	0.4	4.4	72.6	-19.9	1.2
460757.0	4046220.6	0.1	4.5	66.8	-17.9	3.4
460757.0	4046220.6	0.2	4.5	69.4	-18.4	3.4
460757.0	4046220.6	0.3	4.5	70.6	-21.9	2.9
460757.0	4046220.6	0.4	4.5	70.5	-22.1	2.4
460757.1	4046220.7	0.1	4.6	64.9	-18.0	3.8
460757.1	4046220.7	0.2	4.6	67.1	-19.9	4.1
460757.1	4046220.7	0.3	4.6	69.4	-22.8	3.6
460757.1	4046220.7	0.4	4.6	69.4	-24.1	3.2
460757.1	4046220.8	0.1	4.7	62.3	-16.4	3.3
460757.1	4046220.8	0.2	4.7	63.0	-19.3	4.1
460757.1	4046220.8	0.3	4.7	65.2	-23.3	4.5
460757.1	4046220.9	0.1	4.8	58.7	-19.9	3.1
460757.1	4046220.9	0.2	4.8	57.0	-22.4	3.6
460757.1	4046220.9	0.3	4.8	56.9	-23.6	4.0
460757.2	4046221.0	0.1	4.9	52.3	-23.3	3.5
460757.2	4046221.0	0.2	4.9	51.2	-23.9	3.7
460757.2	4046221.0	0.3	4.9	48.6	-24.8	4.3
460757.2	4046221.1	0.1	5.0	49.1	-23.7	3.1
460757.2	4046221.1	0.2	5.0	48.4	-24.0	3.2
460757.3	4046221.1	0.1	5.1	48.0	-19.2	1.4
460757.3	4046221.1	0.2	5.1	48.0	-19.2	1.4
460757.3	4046221.2	0.1	5.2	48.8	-15.4	-0.4
460757.3	4046221.2	0.2	5.2	48.8	-15.4	-0.4

b) Sec. 2

UTM Easting (m)	UTM Northing (m)	Water depth (m)	Distance from left bank (m)	Streamwise Velocity (cm/s)	Transverse Velocity (cm/s)	Vertical Velocity (cm/s)
460749.0	4046234.8	0.1	0.3	69.7	-2.1	1.3
460749.0	4046234.8	0.2	0.3	69.7	-2.1	1.3
460749.1	4046234.8	0.1	0.4	75.0	-1.2	0.0
460749.1	4046234.8	0.2	0.4	75.0	-1.2	0.0
460749.2	4046234.9	0.1	0.5	84.0	-1.0	-0.5
460749.2	4046234.9	0.2	0.5	83.5	-1.9	-0.2
460749.3	4046234.9	0.1	0.6	86.2	2.6	0.6
460749.3	4046234.9	0.2	0.6	84.7	1.8	1.0
460749.3	4046234.9	0.3	0.6	84.6	2.6	0.8
460749.4	4046234.9	0.1	0.7	87.5	0.1	1.3
460749.4	4046234.9	0.2	0.7	84.7	-0.9	1.7
460749.4	4046234.9	0.3	0.7	81.0	0.3	0.7
460749.5	4046234.9	0.1	0.8	91.9	-2.1	0.7
460749.5	4046234.9	0.2	0.8	89.7	-2.1	0.6
460749.5	4046234.9	0.3	0.8	85.9	-2.0	-0.4
460749.5	4046234.9	0.4	0.8	80.8	-1.8	-0.8
460749.6	4046234.9	0.1	0.9	92.8	-5.5	-0.1
460749.6	4046234.9	0.2	0.9	91.2	-4.5	-0.1
460749.6	4046234.9	0.3	0.9	87.1	-3.7	-0.6
460749.6	4046234.9	0.4	0.9	82.9	-2.9	-1.1
460749.7	4046234.9	0.1	1.0	94.7	-3.4	-0.1
460749.7	4046234.9	0.2	1.0	94.4	-2.1	-0.1
460749.7	4046234.9	0.3	1.0	92.7	-3.0	0.0
460749.7	4046234.9	0.4	1.0	89.3	-2.9	-0.3
460749.7	4046234.9	0.5	1.0	86.0	-5.3	-0.5
460749.8	4046234.9	0.1	1.1	94.6	-1.1	0.5
460749.8	4046234.9	0.2	1.1	93.4	0.0	0.7
460749.8	4046234.9	0.3	1.1	91.9	-0.7	0.7
460749.8	4046234.9	0.4	1.1	88.3	-1.7	0.0
460749.9	4046234.9	0.1	1.2	95.3	0.8	0.5
460749.9	4046234.9	0.2	1.2	94.6	0.6	0.5
460749.9	4046234.9	0.3	1.2	93.4	-1.4	0.9
460749.9	4046234.9	0.4	1.2	91.0	-2.8	0.8
460750.0	4046234.9	0.1	1.3	95.8	2.7	0.8
460750.0	4046234.9	0.2	1.3	94.0	2.3	0.4
460750.0	4046234.9	0.3	1.3	91.8	0.7	0.5
460750.0	4046234.9	0.4	1.3	87.7	-1.3	0.0
460750.1	4046234.9	0.1	1.4	94.2	4.6	0.3
460750.1	4046234.9	0.2	1.4	93.4	4.3	-0.3
460750.1	4046234.9	0.3	1.4	92.5	4.2	-0.3
460750.1	4046234.9	0.4	1.4	90.2	2.3	-0.6
460750.2	4046234.9	0.1	1.5	95.9	5.6	-0.2
460750.2	4046234.9	0.2	1.5	94.4	5.6	-0.7
460750.2	4046234.9	0.3	1.5	94.1	5.9	-1.4
460750.2	4046234.9	0.4	1.5	90.6	2.3	-1.3
460750.3	4046234.9	0.1	1.6	95.6	5.2	-0.2
460750.3	4046234.9	0.2	1.6	95.5	6.6	-0.9
460750.3	4046234.9	0.3	1.6	96.9	6.3	-1.9
460750.3	4046234.9	0.4	1.6	92.7	3.0	-1.8
460750.3	4046234.9	0.5	1.6	91.1	-0.7	-1.6
460750.4	4046234.9	0.1	1.7	97.2	3.8	0.0
460750.4	4046234.9	0.2	1.7	96.7	4.5	-0.6
460750.4	4046234.9	0.3	1.7	98.0	3.2	-1.9
460750.4	4046234.9	0.4	1.7	91.1	0.9	-1.7

460750.4	4046234.9	0.5	1.7	88.9	-0.3	-1.8
460750.5	4046234.9	0.1	1.8	94.0	3.6	0.5
460750.5	4046234.9	0.2	1.8	93.9	4.3	-0.3
460750.5	4046234.9	0.3	1.8	94.3	3.5	-1.8
460750.5	4046234.9	0.4	1.8	88.2	2.5	-2.4
460750.5	4046234.9	0.5	1.8	84.8	2.2	-2.4
460750.5	4046234.9	0.6	1.8	81.8	3.9	-1.6
460750.6	4046234.9	0.1	1.9	91.5	2.8	0.1
460750.6	4046234.9	0.2	1.9	91.7	2.0	-0.6
460750.6	4046234.9	0.3	1.9	92.8	1.4	-2.1
460750.6	4046234.9	0.4	1.9	87.7	2.2	-2.5
460750.6	4046234.9	0.5	1.9	85.5	4.6	-2.7
460750.6	4046234.9	0.6	1.9	83.2	6.7	-2.0
460750.7	4046234.9	0.1	2.0	88.8	2.5	-0.4
460750.7	4046234.9	0.2	2.0	89.4	2.7	-0.6
460750.7	4046234.9	0.3	2.0	90.2	2.5	-1.8
460750.7	4046234.9	0.4	2.0	86.5	3.6	-2.2
460750.7	4046234.9	0.5	2.0	84.0	4.3	-2.7
460750.7	4046234.9	0.6	2.0	82.2	5.0	-2.5
460750.8	4046234.9	0.1	2.1	86.3	2.6	-0.1
460750.8	4046234.9	0.2	2.1	86.8	3.2	-0.3
460750.8	4046234.9	0.3	2.1	88.1	3.4	-1.5
460750.8	4046234.9	0.4	2.1	85.8	4.1	-1.6
460750.8	4046234.9	0.5	2.1	85.3	4.1	-2.1
460750.8	4046234.9	0.6	2.1	84.4	3.7	-1.8
460750.9	4046234.9	0.1	2.2	84.0	3.1	0.8
460750.9	4046234.9	0.2	2.2	85.1	2.7	0.5
460750.9	4046234.9	0.3	2.2	85.7	2.6	-0.1
460750.9	4046234.9	0.4	2.2	85.0	1.5	-0.4
460750.9	4046234.9	0.5	2.2	82.7	0.6	-1.1
460750.9	4046234.9	0.6	2.2	81.9	-1.0	-1.1
460751.0	4046235.0	0.1	2.3	81.2	3.2	0.9
460751.0	4046235.0	0.2	2.3	82.2	2.3	0.6
460751.0	4046235.0	0.3	2.3	83.4	2.1	0.3
460751.0	4046235.0	0.4	2.3	83.6	0.1	0.3
460751.0	4046235.0	0.5	2.3	81.4	-1.0	-0.5
460751.0	4046235.0	0.6	2.3	80.2	-2.9	-0.6
460751.1	4046235.0	0.1	2.4	80.4	3.3	0.7
460751.1	4046235.0	0.2	2.4	82.5	2.1	0.5
460751.1	4046235.0	0.3	2.4	84.3	2.8	0.5
460751.1	4046235.0	0.4	2.4	83.6	1.1	0.2
460751.1	4046235.0	0.5	2.4	79.1	0.2	-0.2
460751.1	4046235.0	0.6	2.4	76.4	-2.3	-0.7
460751.2	4046235.0	0.1	2.5	78.2	3.0	0.3
460751.2	4046235.0	0.2	2.5	79.4	3.2	0.2
460751.2	4046235.0	0.3	2.5	81.2	3.9	-0.2
460751.2	4046235.0	0.4	2.5	80.6	2.4	-0.3
460751.2	4046235.0	0.5	2.5	77.3	1.0	-0.6
460751.2	4046235.0	0.6	2.5	74.5	-1.2	-0.8
460751.3	4046235.0	0.1	2.6	77.6	5.1	0.6
460751.3	4046235.0	0.2	2.6	78.7	4.9	0.3
460751.3	4046235.0	0.3	2.6	80.0	5.1	-0.1
460751.3	4046235.0	0.4	2.6	79.4	3.6	-0.5
460751.3	4046235.0	0.5	2.6	76.2	2.2	-0.6
460751.3	4046235.0	0.6	2.6	73.9	0.8	-0.8
460751.4	4046235.0	0.1	2.7	75.6	4.6	0.6
460751.4	4046235.0	0.2	2.7	76.3	4.3	0.5
460751.4	4046235.0	0.3	2.7	77.8	3.0	0.1
460751.4	4046235.0	0.4	2.7	78.0	0.9	-0.2

460751.4	4046235.0	0.5	2.7	75.4	-0.9	-0.3
460751.4	4046235.0	0.6	2.7	73.1	-1.8	-0.4
460751.5	4046235.0	0.1	2.8	75.2	5.7	0.7
460751.5	4046235.0	0.2	2.8	76.6	4.9	0.6
460751.5	4046235.0	0.3	2.8	78.3	3.4	0.3
460751.5	4046235.0	0.4	2.8	78.5	0.8	0.1
460751.5	4046235.0	0.5	2.8	75.0	-1.7	-0.1
460751.5	4046235.0	0.6	2.8	72.6	-3.3	-0.1
460751.6	4046235.0	0.1	2.9	72.7	5.3	0.6
460751.6	4046235.0	0.2	2.9	74.3	4.5	0.5
460751.6	4046235.0	0.3	2.9	76.6	2.3	0.2
460751.6	4046235.0	0.4	2.9	77.1	-0.4	0.0
460751.6	4046235.0	0.5	2.9	73.9	-3.2	-0.3
460751.6	4046235.0	0.6	2.9	71.4	-4.6	-0.4
460751.7	4046235.0	0.1	3.0	69.1	6.3	0.5
460751.7	4046235.0	0.2	3.0	71.1	5.2	0.4
460751.7	4046235.0	0.3	3.0	73.6	2.9	0.2
460751.7	4046235.0	0.4	3.0	74.8	0.8	-0.2
460751.7	4046235.0	0.5	3.0	71.7	-1.9	-0.6
460751.7	4046235.0	0.6	3.0	69.3	-3.2	-1.0
460751.8	4046235.0	0.1	3.1	66.8	5.7	0.3
460751.8	4046235.0	0.2	3.1	68.8	4.5	0.2
460751.8	4046235.0	0.3	3.1	71.8	2.2	0.0
460751.8	4046235.0	0.4	3.1	72.9	0.5	-0.1
460751.8	4046235.0	0.5	3.1	69.9	-1.7	-0.6
460751.8	4046235.0	0.6	3.1	67.5	-2.8	-0.9
460751.9	4046235.0	0.1	3.2	63.9	6.1	0.4
460751.9	4046235.0	0.2	3.2	66.1	4.8	0.2
460751.9	4046235.0	0.3	3.2	69.7	2.5	0.0
460751.9	4046235.0	0.4	3.2	71.6	0.5	-0.1
460751.9	4046235.0	0.5	3.2	68.8	-1.6	-0.4
460751.9	4046235.0	0.6	3.2	66.4	-2.8	-0.6
460752.0	4046235.0	0.1	3.3	62.7	7.0	0.3
460752.0	4046235.0	0.2	3.3	65.0	5.6	0.3
460752.0	4046235.0	0.3	3.3	68.9	3.0	0.1
460752.0	4046235.0	0.4	3.3	70.5	0.3	0.0
460752.0	4046235.0	0.5	3.3	67.8	-1.9	-0.3
460752.0	4046235.0	0.6	3.3	65.3	-3.0	-0.5
460752.1	4046235.0	0.1	3.4	59.6	7.0	0.4
460752.1	4046235.0	0.2	3.4	62.2	5.8	0.4
460752.1	4046235.0	0.3	3.4	66.6	3.3	0.3
460752.1	4046235.0	0.4	3.4	68.7	0.7	0.1
460752.1	4046235.0	0.5	3.4	66.4	-1.4	-0.4
460752.1	4046235.0	0.6	3.4	64.0	-2.4	-0.6
460752.2	4046235.0	0.1	3.5	58.9	6.2	0.7
460752.2	4046235.0	0.2	3.5	61.6	5.1	0.7
460752.2	4046235.0	0.3	3.5	65.8	2.6	0.6
460752.2	4046235.0	0.4	3.5	67.0	0.5	0.5
460752.2	4046235.0	0.5	3.5	64.4	-1.4	-0.2
460752.2	4046235.0	0.6	3.5	61.7	-2.1	-0.5
460752.3	4046235.0	0.1	3.6	57.9	4.5	0.8
460752.3	4046235.0	0.2	3.6	60.8	3.3	0.9
460752.3	4046235.0	0.3	3.6	65.1	0.8	0.8
460752.3	4046235.0	0.4	3.6	66.7	-0.4	0.8
460752.3	4046235.0	0.5	3.6	63.9	-1.6	0.1
460752.3	4046235.0	0.6	3.6	61.5	-1.8	-0.1
460752.4	4046235.0	0.1	3.7	56.4	6.0	0.9
460752.4	4046235.0	0.2	3.7	59.6	4.5	1.0
460752.4	4046235.0	0.3	3.7	63.9	1.6	0.9

460752.4	4046235.0	0.4	3.7	65.9	-0.2	0.8
460752.4	4046235.0	0.5	3.7	62.8	-1.0	0.4
460752.4	4046235.0	0.6	3.7	60.6	-0.8	0.2
460752.5	4046235.0	0.1	3.8	54.4	4.7	0.6
460752.5	4046235.0	0.2	3.8	57.4	3.7	0.6
460752.5	4046235.0	0.3	3.8	61.7	0.9	0.8
460752.5	4046235.0	0.4	3.8	64.0	0.3	0.8
460752.5	4046235.0	0.5	3.8	61.0	0.1	0.8
460752.5	4046235.0	0.6	3.8	59.0	1.0	0.7
460752.6	4046235.0	0.1	3.9	53.3	4.9	0.7
460752.6	4046235.0	0.2	3.9	55.8	4.0	0.7
460752.6	4046235.0	0.3	3.9	59.8	2.0	0.8
460752.6	4046235.0	0.4	3.9	61.5	1.5	0.7
460752.6	4046235.0	0.5	3.9	57.6	1.8	0.7
460752.6	4046235.0	0.6	3.9	54.9	2.4	0.6
460752.7	4046235.0	0.1	4.0	52.2	4.4	0.9
460752.7	4046235.0	0.2	4.0	53.9	3.3	0.8
460752.7	4046235.0	0.3	4.0	57.7	1.3	0.8
460752.7	4046235.0	0.4	4.0	58.7	0.7	0.7
460752.7	4046235.0	0.5	4.0	56.3	0.5	0.5
460752.7	4046235.0	0.6	4.0	53.6	0.7	0.4
460752.8	4046235.1	0.1	4.1	49.1	5.1	0.6
460752.8	4046235.1	0.2	4.1	51.0	3.7	0.6
460752.8	4046235.1	0.3	4.1	54.9	1.9	0.6
460752.8	4046235.1	0.4	4.1	56.0	0.2	0.3
460752.8	4046235.1	0.5	4.1	54.7	-0.2	0.1
460752.8	4046235.1	0.6	4.1	52.2	-1.0	-0.1
460752.9	4046235.1	0.1	4.2	45.6	5.1	0.6
460752.9	4046235.1	0.2	4.2	47.7	3.6	0.6
460752.9	4046235.1	0.3	4.2	51.5	1.3	0.6
460752.9	4046235.1	0.4	4.2	52.9	-0.9	0.5
460752.9	4046235.1	0.5	4.2	53.8	-1.8	0.2
460753.0	4046235.1	0.1	4.3	42.7	5.2	0.9
460753.0	4046235.1	0.2	4.3	45.1	3.9	0.9
460753.0	4046235.1	0.3	4.3	48.2	2.1	1.0
460753.0	4046235.1	0.4	4.3	49.6	-0.3	1.0
460753.0	4046235.1	0.5	4.3	49.5	-1.0	0.9
460753.1	4046235.1	0.1	4.4	41.4	4.5	1.4
460753.1	4046235.1	0.2	4.4	43.2	3.4	1.5
460753.1	4046235.1	0.3	4.4	45.0	2.3	1.6
460753.1	4046235.1	0.4	4.4	46.1	0.3	1.5
460753.1	4046235.1	0.5	4.4	45.8	-0.2	1.3
460753.2	4046235.1	0.1	4.5	39.0	2.0	1.5
460753.2	4046235.1	0.2	4.5	40.2	1.4	1.5
460753.2	4046235.1	0.3	4.5	40.9	0.7	1.5
460753.2	4046235.1	0.4	4.5	41.7	-0.8	1.4
460753.3	4046235.1	0.1	4.6	36.3	-0.5	1.3
460753.3	4046235.1	0.2	4.6	36.6	-0.6	1.2
460753.3	4046235.1	0.3	4.6	36.4	-0.3	1.1
460753.3	4046235.1	0.4	4.6	35.7	-1.2	1.0
460753.4	4046235.1	0.1	4.7	33.9	-0.6	1.5
460753.4	4046235.1	0.2	4.7	33.3	-0.5	1.3
460753.4	4046235.1	0.3	4.7	33.1	-0.6	1.0
460753.4	4046235.1	0.4	4.7	32.2	-1.4	0.8
460753.5	4046235.1	0.1	4.8	31.9	-0.9	1.4
460753.5	4046235.1	0.2	4.8	31.5	-0.6	1.2
460753.5	4046235.1	0.3	4.8	31.1	0.2	1.0
460753.6	4046235.1	0.1	4.9	29.5	-0.1	1.1
460753.6	4046235.1	0.2	4.9	29.6	-0.2	1.1

460753.6	4046235.1	0.3	4.9	29.5	-0.1	1.0
460753.7	4046235.1	0.1	5.0	26.0	0.6	0.2
460753.7	4046235.1	0.2	5.0	26.9	0.1	0.3
460753.8	4046235.1	0.1	5.1	22.1	2.0	0.0
460753.8	4046235.1	0.2	5.1	22.1	2.0	0.0
460753.9	4046235.1	0.1	5.2	20.1	2.1	-0.1
460753.9	4046235.1	0.2	5.2	20.1	2.1	-0.1

c) Sec. 3

UTM Easting (m)	UTM Northing (m)	Water depth (m)	Distance from left bank (m)	Streamwise Velocity (cm/s)	Transverse Velocity (cm/s)	Vertical Velocity (cm/s)
460,742.4	4,046,247.6	0.1	0.5	36.9	-7.2	-0.6
460,742.4	4,046,247.6	0.2	0.5	36.9	-7.2	-0.6
460,742.5	4,046,247.7	0.1	0.6	37.8	-7.3	-0.3
460,742.5	4,046,247.7	0.2	0.6	38.0	-5.5	0.2
460,742.5	4,046,247.8	0.1	0.7	38.8	-8.7	0.2
460,742.5	4,046,247.8	0.2	0.7	38.7	-5.5	1.0
460,742.5	4,046,247.8	0.3	0.7	37.7	-2.1	1.6
460,742.5	4,046,247.9	0.1	0.8	41.1	-7.1	0.7
460,742.5	4,046,247.9	0.2	0.8	41.5	-3.5	1.4
460,742.5	4,046,247.9	0.3	0.8	41.3	-1.5	1.5
460,742.5	4,046,248.0	0.1	0.9	44.1	-7.0	1.1
460,742.5	4,046,248.0	0.2	0.9	44.8	-4.9	1.6
460,742.5	4,046,248.0	0.3	0.9	46.8	-3.5	1.7
460,742.5	4,046,248.0	0.4	0.9	48.5	-2.9	1.8
460,742.5	4,046,248.1	0.1	1.0	48.3	-7.9	1.2
460,742.5	4,046,248.1	0.2	1.0	49.7	-6.4	1.6
460,742.5	4,046,248.1	0.3	1.0	51.4	-5.1	2.1
460,742.5	4,046,248.1	0.4	1.0	52.9	-4.3	2.4
460,742.6	4,046,248.2	0.1	1.1	50.4	-9.4	1.2
460,742.6	4,046,248.2	0.2	1.1	51.3	-8.5	1.5
460,742.6	4,046,248.2	0.3	1.1	54.0	-7.1	2.3
460,742.6	4,046,248.2	0.4	1.1	55.3	-6.2	2.6
460,742.6	4,046,248.3	0.1	1.2	52.7	-11.6	0.5
460,742.6	4,046,248.3	0.2	1.2	53.5	-11.1	1.1
460,742.6	4,046,248.3	0.3	1.2	54.8	-9.8	1.7
460,742.6	4,046,248.3	0.4	1.2	56.7	-10.0	2.5
460,742.6	4,046,248.4	0.1	1.3	53.9	-10.8	0.8
460,742.6	4,046,248.4	0.2	1.3	55.1	-11.0	1.1
460,742.6	4,046,248.4	0.3	1.3	55.9	-10.1	1.0
460,742.6	4,046,248.4	0.4	1.3	58.9	-8.8	1.4
460,742.6	4,046,248.4	0.5	1.3	59.7	-7.3	1.3
460,742.6	4,046,248.5	0.1	1.4	57.6	-12.3	0.5
460,742.6	4,046,248.5	0.2	1.4	58.2	-12.9	0.8
460,742.6	4,046,248.5	0.3	1.4	59.1	-11.7	0.6
460,742.6	4,046,248.5	0.4	1.4	60.0	-9.5	1.2
460,742.6	4,046,248.5	0.5	1.4	60.7	-6.4	0.5
460,742.6	4,046,248.6	0.1	1.5	60.5	-13.3	0.6
460,742.6	4,046,248.6	0.2	1.5	61.8	-13.0	0.5
460,742.6	4,046,248.6	0.3	1.5	63.6	-11.8	0.4
460,742.6	4,046,248.6	0.4	1.5	63.5	-7.4	1.2
460,742.6	4,046,248.6	0.5	1.5	61.9	-2.7	1.5
460,742.6	4,046,248.6	0.6	1.5	60.2	1.7	1.7
460,742.7	4,046,248.7	0.1	1.6	63.2	-15.9	0.1
460,742.7	4,046,248.7	0.2	1.6	64.0	-15.2	-0.2
460,742.7	4,046,248.7	0.3	1.6	66.7	-14.5	0.0
460,742.7	4,046,248.7	0.4	1.6	65.7	-10.3	1.2
460,742.7	4,046,248.7	0.5	1.6	63.6	-4.7	2.3
460,742.7	4,046,248.7	0.6	1.6	60.3	-0.4	2.3
460,742.7	4,046,248.8	0.1	1.7	62.0	-15.4	-0.4
460,742.7	4,046,248.8	0.2	1.7	64.0	-14.0	-0.8
460,742.7	4,046,248.8	0.3	1.7	68.1	-13.8	-0.3
460,742.7	4,046,248.8	0.4	1.7	69.7	-10.7	0.7
460,742.7	4,046,248.8	0.5	1.7	66.8	-6.5	2.5
460,742.7	4,046,248.8	0.6	1.7	63.2	-2.7	2.7

460,742.7	4,046,248.9	0.1	1.8	63.2	-15.1	0.4
460,742.7	4,046,248.9	0.2	1.8	63.8	-13.7	-0.1
460,742.7	4,046,248.9	0.3	1.8	67.8	-13.6	0.2
460,742.7	4,046,248.9	0.4	1.8	69.0	-10.7	0.3
460,742.7	4,046,248.9	0.5	1.8	68.2	-7.3	1.3
460,742.7	4,046,248.9	0.6	1.8	65.0	-3.5	1.1
460,742.7	4,046,249.0	0.1	1.9	64.3	-15.8	0.7
460,742.7	4,046,249.0	0.2	1.9	64.3	-14.6	0.3
460,742.7	4,046,249.0	0.3	1.9	67.9	-13.7	0.3
460,742.7	4,046,249.0	0.4	1.9	69.4	-9.7	0.5
460,742.7	4,046,249.0	0.5	1.9	68.0	-6.2	0.6
460,742.7	4,046,249.0	0.6	1.9	63.6	-1.6	-0.4
460,742.7	4,046,249.1	0.1	2.0	67.4	-17.4	0.9
460,742.7	4,046,249.1	0.2	2.0	66.9	-16.2	0.5
460,742.7	4,046,249.1	0.3	2.0	69.0	-14.3	0.0
460,742.7	4,046,249.1	0.4	2.0	70.0	-7.7	0.5
460,742.7	4,046,249.1	0.5	2.0	69.5	-2.8	0.1
460,742.7	4,046,249.1	0.6	2.0	67.2	2.1	-0.7
460,742.7	4,046,249.1	0.7	2.0	64.4	2.9	-2.1
460,742.8	4,046,249.2	0.1	2.1	70.4	-18.3	0.8
460,742.8	4,046,249.2	0.2	2.1	69.8	-16.9	0.4
460,742.8	4,046,249.2	0.3	2.1	72.8	-14.9	0.3
460,742.8	4,046,249.2	0.4	2.1	74.9	-8.3	1.0
460,742.8	4,046,249.2	0.5	2.1	74.2	-3.3	0.9
460,742.8	4,046,249.2	0.6	2.1	70.8	1.6	0.1
460,742.8	4,046,249.2	0.7	2.1	67.2	2.7	-0.9
460,742.8	4,046,249.2	0.1	2.2	72.8	-17.2	1.2
460,742.8	4,046,249.2	0.2	2.2	72.6	-15.3	0.8
460,742.8	4,046,249.2	0.3	2.2	75.8	-13.0	0.9
460,742.8	4,046,249.2	0.4	2.2	77.0	-8.8	0.8
460,742.8	4,046,249.2	0.5	2.2	76.4	-3.8	1.2
460,742.8	4,046,249.2	0.6	2.2	72.3	-0.4	1.2
460,742.8	4,046,249.2	0.7	2.2	69.5	2.2	1.3
460,742.8	4,046,249.3	0.1	2.3	75.6	-18.0	1.5
460,742.8	4,046,249.3	0.2	2.3	76.2	-16.2	1.2
460,742.8	4,046,249.3	0.3	2.3	79.9	-14.0	1.3
460,742.8	4,046,249.3	0.4	2.3	80.4	-11.2	1.5
460,742.8	4,046,249.3	0.5	2.3	77.2	-6.0	1.8
460,742.8	4,046,249.3	0.6	2.3	71.0	-2.5	2.2
460,742.8	4,046,249.3	0.7	2.3	66.3	1.1	2.6
460,742.8	4,046,249.4	0.1	2.4	74.4	-20.0	0.7
460,742.8	4,046,249.4	0.2	2.4	76.6	-18.9	0.7
460,742.8	4,046,249.4	0.3	2.4	80.1	-15.5	0.4
460,742.8	4,046,249.4	0.4	2.4	80.8	-12.1	1.0
460,742.8	4,046,249.4	0.5	2.4	75.4	-5.6	1.1
460,742.8	4,046,249.4	0.6	2.4	69.5	-2.4	1.8
460,742.8	4,046,249.4	0.7	2.4	65.1	1.3	1.9
460,742.8	4,046,249.5	0.1	2.5	76.8	-20.6	0.5
460,742.8	4,046,249.5	0.2	2.5	79.8	-20.9	0.3
460,742.8	4,046,249.5	0.3	2.5	84.0	-18.2	0.1
460,742.8	4,046,249.5	0.4	2.5	84.5	-13.7	0.4
460,742.8	4,046,249.5	0.5	2.5	77.3	-6.4	0.3
460,742.8	4,046,249.5	0.6	2.5	70.7	-0.1	1.1
460,742.8	4,046,249.5	0.7	2.5	65.2	3.7	1.0
460,742.9	4,046,249.6	0.1	2.6	78.7	-21.0	0.5
460,742.9	4,046,249.6	0.2	2.6	80.7	-21.6	0.0
460,742.9	4,046,249.6	0.3	2.6	84.4	-18.9	-0.6
460,742.9	4,046,249.6	0.4	2.6	85.5	-14.7	-0.7
460,742.9	4,046,249.6	0.5	2.6	79.0	-6.7	-0.7

460,742.9	4,046,249.6	0.6	2.6	72.6	-0.2	-0.1
460,742.9	4,046,249.6	0.7	2.6	66.9	4.4	-0.2
460,742.9	4,046,249.7	0.1	2.7	83.3	-20.3	1.1
460,742.9	4,046,249.7	0.2	2.7	84.3	-20.1	0.1
460,742.9	4,046,249.7	0.3	2.7	87.7	-18.4	-0.3
460,742.9	4,046,249.7	0.4	2.7	87.8	-15.3	-0.9
460,742.9	4,046,249.7	0.5	2.7	81.7	-8.7	-0.4
460,742.9	4,046,249.7	0.6	2.7	74.4	-0.6	0.2
460,742.9	4,046,249.7	0.7	2.7	67.6	5.0	0.3
460,742.9	4,046,249.8	0.1	2.8	85.9	-19.9	0.7
460,742.9	4,046,249.8	0.2	2.8	85.7	-19.0	-0.1
460,742.9	4,046,249.8	0.3	2.8	85.7	-17.4	-0.5
460,742.9	4,046,249.8	0.4	2.8	82.8	-14.5	-0.9
460,742.9	4,046,249.8	0.5	2.8	78.1	-8.6	0.2
460,742.9	4,046,249.8	0.6	2.8	73.7	-2.5	0.7
460,742.9	4,046,249.8	0.7	2.8	70.1	1.8	1.2
460,742.9	4,046,249.9	0.1	2.9	87.2	-21.2	0.7
460,742.9	4,046,249.9	0.2	2.9	86.9	-19.8	0.4
460,742.9	4,046,249.9	0.3	2.9	86.4	-17.4	0.6
460,742.9	4,046,249.9	0.4	2.9	82.2	-13.1	0.0
460,742.9	4,046,249.9	0.5	2.9	77.1	-7.4	1.0
460,742.9	4,046,249.9	0.6	2.9	72.3	-3.4	1.4
460,742.9	4,046,249.9	0.7	2.9	69.6	-0.3	2.1
460,742.9	4,046,250.0	0.1	3.0	87.9	-20.7	0.1
460,742.9	4,046,250.0	0.2	3.0	87.4	-19.1	0.2
460,742.9	4,046,250.0	0.3	3.0	84.9	-16.9	0.5
460,742.9	4,046,250.0	0.4	3.0	79.6	-11.7	0.1
460,742.9	4,046,250.0	0.5	3.0	73.6	-7.5	0.2
460,742.9	4,046,250.0	0.6	3.0	70.5	-6.6	0.7
460,742.9	4,046,250.0	0.7	3.0	68.6	-6.0	1.5
460,743.0	4,046,250.1	0.1	3.1	88.2	-20.7	0.2
460,743.0	4,046,250.1	0.2	3.1	88.3	-20.4	0.9
460,743.0	4,046,250.1	0.3	3.1	87.4	-20.2	1.9
460,743.0	4,046,250.1	0.4	3.1	82.7	-16.0	1.5
460,743.0	4,046,250.1	0.5	3.1	72.7	-10.9	0.6
460,743.0	4,046,250.1	0.6	3.1	67.7	-7.9	0.1
460,743.0	4,046,250.1	0.7	3.1	63.0	-5.8	0.1
460,743.0	4,046,250.2	0.1	3.2	88.4	-20.7	0.2
460,743.0	4,046,250.2	0.2	3.2	89.1	-21.7	0.7
460,743.0	4,046,250.2	0.3	3.2	88.6	-24.4	2.1
460,743.0	4,046,250.2	0.4	3.2	83.1	-19.4	1.7
460,743.0	4,046,250.2	0.5	3.2	72.6	-14.4	0.9
460,743.0	4,046,250.2	0.6	3.2	66.8	-8.1	0.0
460,743.0	4,046,250.2	0.7	3.2	59.5	-6.0	-0.3
460,743.0	4,046,250.3	0.1	3.3	86.5	-20.6	0.0
460,743.0	4,046,250.3	0.2	3.3	86.6	-22.6	0.4
460,743.0	4,046,250.3	0.3	3.3	86.8	-25.1	1.4
460,743.0	4,046,250.3	0.4	3.3	80.8	-20.3	1.0
460,743.0	4,046,250.3	0.5	3.3	73.0	-15.1	0.8
460,743.0	4,046,250.4	0.1	3.4	84.8	-20.5	-0.5
460,743.0	4,046,250.4	0.2	3.4	85.2	-22.1	-1.0
460,743.0	4,046,250.4	0.3	3.4	85.4	-24.2	-0.7
460,743.0	4,046,250.4	0.4	3.4	80.7	-18.1	-1.5
460,743.0	4,046,250.4	0.5	3.4	73.9	-14.8	-0.7
460,743.1	4,046,250.5	0.1	3.5	83.6	-17.2	-1.7
460,743.1	4,046,250.5	0.2	3.5	84.7	-19.0	-2.2
460,743.1	4,046,250.5	0.3	3.5	84.6	-19.8	-2.9
460,743.1	4,046,250.5	0.4	3.5	80.1	-16.1	-3.6
460,743.1	4,046,250.5	0.5	3.5	71.2	-12.1	-2.6

460,743.1	4,046,250.5	0.6	3.5	62.5	-6.1	-2.1
460,743.1	4,046,250.5	0.7	3.5	53.7	-3.2	-1.2
460,743.1	4,046,250.6	0.1	3.6	82.2	-15.7	-2.1
460,743.1	4,046,250.6	0.2	3.6	83.6	-17.6	-2.8
460,743.1	4,046,250.6	0.3	3.6	84.0	-19.1	-3.7
460,743.1	4,046,250.6	0.4	3.6	79.7	-14.4	-4.3
460,743.1	4,046,250.6	0.5	3.6	69.2	-9.7	-2.9
460,743.1	4,046,250.6	0.6	3.6	61.6	-2.2	-2.5
460,743.1	4,046,250.6	0.7	3.6	55.2	-0.4	-2.0
460,743.1	4,046,250.7	0.1	3.7	80.6	-15.4	-2.4
460,743.1	4,046,250.7	0.2	3.7	81.7	-17.6	-2.9
460,743.1	4,046,250.7	0.3	3.7	83.4	-18.4	-4.3
460,743.1	4,046,250.7	0.4	3.7	80.1	-13.5	-4.6
460,743.1	4,046,250.7	0.5	3.7	71.1	-6.7	-3.7
460,743.1	4,046,250.7	0.6	3.7	62.4	-2.3	-3.0
460,743.1	4,046,250.7	0.7	3.7	55.6	-0.5	-2.8
460,743.1	4,046,250.8	0.1	3.8	77.0	-11.5	-2.7
460,743.1	4,046,250.8	0.2	3.8	77.3	-13.0	-3.3
460,743.1	4,046,250.8	0.3	3.8	79.8	-13.9	-4.4
460,743.1	4,046,250.8	0.4	3.8	77.4	-9.8	-4.4
460,743.1	4,046,250.8	0.5	3.8	68.5	-4.2	-3.5
460,743.1	4,046,250.8	0.6	3.8	58.4	-0.6	-2.6
460,743.1	4,046,250.8	0.7	3.8	50.6	0.8	-2.5
460,743.1	4,046,250.9	0.1	3.9	73.5	-8.1	-2.3
460,743.1	4,046,250.9	0.2	3.9	74.7	-8.9	-2.5
460,743.1	4,046,250.9	0.3	3.9	77.3	-10.3	-3.2
460,743.1	4,046,250.9	0.4	3.9	76.9	-8.5	-3.4
460,743.1	4,046,250.9	0.5	3.9	68.0	-5.2	-3.4
460,743.1	4,046,250.9	0.6	3.9	56.1	-3.0	-2.1
460,743.1	4,046,250.9	0.7	3.9	46.9	-2.1	-1.6
460,743.2	4,046,251.0	0.1	4.0	69.9	-5.0	-2.1
460,743.2	4,046,251.0	0.2	4.0	70.7	-6.1	-2.3
460,743.2	4,046,251.0	0.3	4.0	73.1	-7.5	-2.6
460,743.2	4,046,251.0	0.4	4.0	73.6	-5.3	-3.0
460,743.2	4,046,251.0	0.5	4.0	68.4	-2.8	-3.2
460,743.2	4,046,251.0	0.6	4.0	58.4	-0.8	-2.4
460,743.2	4,046,251.0	0.7	4.0	49.9	-1.0	-1.7
460,743.2	4,046,251.1	0.1	4.1	66.3	-4.7	-1.2
460,743.2	4,046,251.1	0.2	4.1	67.8	-7.0	-1.2
460,743.2	4,046,251.1	0.3	4.1	70.6	-9.0	-1.1
460,743.2	4,046,251.1	0.4	4.1	71.4	-5.9	-1.9
460,743.2	4,046,251.1	0.5	4.1	68.7	-2.4	-2.7
460,743.2	4,046,251.1	0.6	4.1	63.2	0.0	-2.6
460,743.2	4,046,251.2	0.1	4.2	64.1	-3.8	-1.3
460,743.2	4,046,251.2	0.2	4.2	65.8	-7.0	-1.3
460,743.2	4,046,251.2	0.3	4.2	69.9	-7.9	-0.8
460,743.2	4,046,251.2	0.4	4.2	69.2	-6.0	-0.8
460,743.2	4,046,251.2	0.5	4.2	67.4	-1.0	-1.2
460,743.2	4,046,251.2	0.6	4.2	65.1	0.7	-1.7
460,743.2	4,046,251.3	0.1	4.3	62.6	-0.2	-0.9
460,743.2	4,046,251.3	0.2	4.3	64.4	-2.7	-0.8
460,743.2	4,046,251.3	0.3	4.3	68.0	-3.4	-0.2
460,743.2	4,046,251.3	0.4	4.3	65.4	-4.5	0.4
460,743.2	4,046,251.3	0.5	4.3	62.1	-1.7	0.1
460,743.2	4,046,251.3	0.6	4.3	59.1	-1.4	-0.1
460,743.2	4,046,251.4	0.1	4.4	61.0	-0.5	-0.3
460,743.2	4,046,251.4	0.2	4.4	61.8	-1.4	-0.3
460,743.2	4,046,251.4	0.3	4.4	65.8	-1.2	0.1
460,743.2	4,046,251.4	0.4	4.4	63.7	-3.5	0.6

460,743.2	4,046,251.4	0.5	4.4	62.2	-2.9	0.2
460,743.2	4,046,251.4	0.6	4.4	59.4	-4.2	0.0
460,743.3	4,046,251.5	0.1	4.5	59.3	-1.9	0.2
460,743.3	4,046,251.5	0.2	4.5	60.4	-3.1	0.0
460,743.3	4,046,251.5	0.3	4.5	63.0	-3.6	-0.4
460,743.3	4,046,251.5	0.4	4.5	61.1	-4.6	-0.5
460,743.3	4,046,251.5	0.5	4.5	60.3	-3.9	-1.1
460,743.3	4,046,251.5	0.6	4.5	58.4	-4.6	-1.3
460,743.3	4,046,251.6	0.1	4.6	56.1	-3.8	-0.1
460,743.3	4,046,251.6	0.2	4.6	57.5	-5.5	0.0
460,743.3	4,046,251.6	0.3	4.6	59.5	-6.0	-0.4
460,743.3	4,046,251.6	0.4	4.6	57.6	-5.4	-0.6
460,743.3	4,046,251.6	0.5	4.6	57.4	-3.6	-1.7
460,743.3	4,046,251.7	0.1	4.7	55.6	-4.5	0.2
460,743.3	4,046,251.7	0.2	4.7	57.2	-7.1	0.4
460,743.3	4,046,251.7	0.3	4.7	58.8	-7.5	0.2
460,743.3	4,046,251.7	0.4	4.7	55.9	-6.2	0.0
460,743.3	4,046,251.7	0.5	4.7	53.7	-3.3	-0.3
460,743.3	4,046,251.8	0.1	4.8	51.4	-2.4	1.0
460,743.3	4,046,251.8	0.2	4.8	52.6	-4.1	0.9
460,743.3	4,046,251.8	0.3	4.8	53.9	-3.7	0.6
460,743.3	4,046,251.8	0.4	4.8	53.1	-3.7	0.5
460,743.3	4,046,251.8	0.5	4.8	52.0	-1.2	0.3
460,743.3	4,046,251.9	0.1	4.9	50.4	-3.6	1.8
460,743.3	4,046,251.9	0.2	4.9	51.2	-4.4	1.6
460,743.3	4,046,251.9	0.3	4.9	52.9	-3.9	1.1
460,743.3	4,046,251.9	0.4	4.9	53.9	-3.9	0.9
460,743.4	4,046,252.0	0.1	5.0	48.2	-2.0	1.7
460,743.4	4,046,252.0	0.2	5.0	48.2	-2.4	1.5
460,743.4	4,046,252.0	0.3	5.0	48.9	-2.8	1.0
460,743.4	4,046,252.0	0.4	5.0	49.6	-2.6	0.6
460,743.4	4,046,252.1	0.1	5.1	49.5	-5.2	1.7
460,743.4	4,046,252.1	0.2	5.1	49.0	-5.1	1.5
460,743.4	4,046,252.1	0.3	5.1	49.6	-6.3	1.4
460,743.4	4,046,252.2	0.1	5.2	47.9	-5.0	1.9
460,743.4	4,046,252.2	0.2	5.2	47.0	-5.4	1.8
460,743.4	4,046,252.2	0.3	5.2	46.8	-6.8	1.9
460,743.4	4,046,252.3	0.1	5.3	46.3	-7.0	1.7
460,743.4	4,046,252.3	0.2	5.3	46.0	-7.2	1.8
460,743.4	4,046,252.3	0.3	5.3	46.0	-7.9	1.8
460,743.4	4,046,252.4	0.1	5.4	45.2	-6.8	1.3
460,743.4	4,046,252.4	0.2	5.4	43.3	-5.8	1.0
460,743.5	4,046,252.5	0.1	5.5	43.9	-8.4	-0.3
460,743.5	4,046,252.5	0.2	5.5	42.4	-6.9	-0.6
460,743.5	4,046,252.5	0.3	5.5	41.6	-3.8	-1.3
460,743.5	4,046,252.6	0.1	5.6	43.3	-10.1	-0.8
460,743.5	4,046,252.6	0.2	5.6	41.4	-7.6	-1.1

d) Sec. 4

UTM Easting (m)	UTM Northing (m)	Water depth (m)	Distance from left bank (m)	Streamwise Velocity (cm/s)	Transverse Velocity (cm/s)	Vertical Velocity (cm/s)
460,730.4	4,046,239.9	0.1	0.0	34.9	-2.9	0.5
460,730.4	4,046,239.9	0.2	0.0	34.9	-2.9	0.5
460,730.3	4,046,240.0	0.1	0.1	34.9	-3.2	0.7
460,730.3	4,046,240.0	0.2	0.1	34.9	-3.2	0.7
460,730.2	4,046,240.0	0.1	0.2	35.4	-2.9	1.1
460,730.2	4,046,240.0	0.2	0.2	35.6	-3.2	1.1
460,730.1	4,046,240.0	0.1	0.3	36.4	-4.2	1.1
460,730.1	4,046,240.0	0.2	0.3	36.3	-3.9	1.2
460,730.1	4,046,240.0	0.3	0.3	34.9	-2.8	1.4
460,730.1	4,046,240.1	0.1	0.4	38.0	-5.0	1.0
460,730.1	4,046,240.1	0.2	0.4	37.6	-4.2	1.1
460,730.1	4,046,240.1	0.3	0.4	36.8	-3.0	1.3
460,730.0	4,046,240.1	0.1	0.5	40.2	-5.7	1.1
460,730.0	4,046,240.1	0.2	0.5	39.3	-4.7	1.2
460,730.0	4,046,240.1	0.3	0.5	39.0	-3.4	1.2
460,729.9	4,046,240.1	0.1	0.6	42.2	-6.3	0.9
460,729.9	4,046,240.1	0.2	0.6	41.5	-5.2	1.1
460,729.9	4,046,240.1	0.3	0.6	41.8	-3.4	1.2
460,729.9	4,046,240.1	0.4	0.6	41.7	-2.1	1.3
460,729.8	4,046,240.2	0.1	0.7	45.4	-6.7	1.0
460,729.8	4,046,240.2	0.2	0.7	44.7	-5.2	1.1
460,729.8	4,046,240.2	0.3	0.7	44.3	-2.6	1.3
460,729.8	4,046,240.2	0.4	0.7	43.8	-0.8	1.4
460,729.7	4,046,240.2	0.1	0.8	48.4	-7.7	0.7
460,729.7	4,046,240.2	0.2	0.8	48.1	-6.1	0.8
460,729.7	4,046,240.2	0.3	0.8	47.6	-3.2	1.1
460,729.7	4,046,240.2	0.4	0.8	47.1	-1.3	1.3
460,729.6	4,046,240.2	0.1	0.9	50.0	-9.0	0.7
460,729.6	4,046,240.2	0.2	0.9	50.1	-7.5	0.7
460,729.6	4,046,240.2	0.3	0.9	49.6	-4.7	0.7
460,729.6	4,046,240.2	0.4	0.9	49.4	-2.9	0.7
460,729.5	4,046,240.3	0.1	1.0	51.5	-10.1	0.5
460,729.5	4,046,240.3	0.2	1.0	52.2	-9.1	0.6
460,729.5	4,046,240.3	0.3	1.0	52.8	-7.0	0.6
460,729.5	4,046,240.3	0.4	1.0	53.3	-5.2	0.5
460,729.5	4,046,240.3	0.5	1.0	53.2	-3.9	0.4
460,729.4	4,046,240.3	0.1	1.1	52.3	-10.3	0.5
460,729.4	4,046,240.3	0.2	1.1	53.5	-9.5	0.5
460,729.4	4,046,240.3	0.3	1.1	54.7	-7.5	0.5
460,729.4	4,046,240.3	0.4	1.1	54.8	-5.8	0.4
460,729.4	4,046,240.3	0.5	1.1	54.3	-4.8	0.4
460,729.3	4,046,240.3	0.1	1.2	53.7	-10.2	0.8
460,729.3	4,046,240.3	0.2	1.2	55.3	-9.6	0.8
460,729.3	4,046,240.3	0.3	1.2	57.3	-8.0	0.7
460,729.3	4,046,240.3	0.4	1.2	57.4	-6.2	0.8
460,729.3	4,046,240.3	0.5	1.2	57.0	-4.1	0.9
460,729.2	4,046,240.3	0.1	1.3	54.3	-10.5	0.8
460,729.2	4,046,240.3	0.2	1.3	55.8	-9.8	0.7
460,729.2	4,046,240.3	0.3	1.3	57.9	-8.4	0.6
460,729.2	4,046,240.3	0.4	1.3	57.8	-6.3	0.8
460,729.2	4,046,240.3	0.5	1.3	55.4	-4.8	1.0
460,729.2	4,046,240.3	0.6	1.3	53.1	-3.6	1.3
460,729.1	4,046,240.4	0.1	1.4	56.1	-10.1	0.8
460,729.1	4,046,240.4	0.2	1.4	57.4	-9.5	0.7

460,729.1	4,046,240.4	0.3	1.4	59.6	-8.2	0.7
460,729.1	4,046,240.4	0.4	1.4	59.1	-6.1	0.8
460,729.1	4,046,240.4	0.5	1.4	56.2	-4.3	0.9
460,729.1	4,046,240.4	0.6	1.4	53.6	-3.0	1.1
460,729.0	4,046,240.4	0.1	1.5	57.1	-11.1	0.5
460,729.0	4,046,240.4	0.2	1.5	58.4	-10.1	0.5
460,729.0	4,046,240.4	0.3	1.5	60.4	-8.5	0.5
460,729.0	4,046,240.4	0.4	1.5	59.7	-6.9	0.5
460,729.0	4,046,240.4	0.5	1.5	56.6	-6.5	0.3
460,729.0	4,046,240.4	0.6	1.5	54.0	-6.2	0.3
460,728.9	4,046,240.4	0.1	1.6	58.5	-11.4	0.5
460,728.9	4,046,240.4	0.2	1.6	59.8	-10.4	0.4
460,728.9	4,046,240.4	0.3	1.6	61.5	-8.7	0.3
460,728.9	4,046,240.4	0.4	1.6	61.2	-7.3	0.1
460,728.9	4,046,240.4	0.5	1.6	59.4	-5.4	-0.2
460,728.9	4,046,240.4	0.6	1.6	57.9	-4.7	-0.5
460,728.8	4,046,240.5	0.1	1.7	58.8	-11.8	0.7
460,728.8	4,046,240.5	0.2	1.7	59.9	-10.8	0.4
460,728.8	4,046,240.5	0.3	1.7	61.3	-9.0	0.1
460,728.8	4,046,240.5	0.4	1.7	61.6	-7.2	-0.1
460,728.8	4,046,240.5	0.5	1.7	60.2	-5.0	-0.4
460,728.8	4,046,240.5	0.6	1.7	59.3	-4.2	-0.6
460,728.7	4,046,240.5	0.1	1.8	60.2	-11.3	0.8
460,728.7	4,046,240.5	0.2	1.8	61.2	-10.5	0.5
460,728.7	4,046,240.5	0.3	1.8	62.5	-8.8	0.2
460,728.7	4,046,240.5	0.4	1.8	62.9	-6.6	-0.3
460,728.7	4,046,240.5	0.5	1.8	60.9	-3.1	-0.3
460,728.7	4,046,240.5	0.6	1.8	59.8	-1.5	-0.5
460,728.6	4,046,240.5	0.1	1.9	61.7	-11.2	0.9
460,728.6	4,046,240.5	0.2	1.9	62.4	-10.5	0.7
460,728.6	4,046,240.5	0.3	1.9	63.7	-9.1	0.4
460,728.6	4,046,240.5	0.4	1.9	63.7	-7.1	0.1
460,728.6	4,046,240.5	0.5	1.9	61.7	-3.7	0.1
460,728.6	4,046,240.5	0.6	1.9	60.4	-1.8	0.0
460,728.5	4,046,240.6	0.1	2.0	63.3	-12.1	1.0
460,728.5	4,046,240.6	0.2	2.0	63.9	-11.4	0.8
460,728.5	4,046,240.6	0.3	2.0	65.2	-10.3	0.6
460,728.5	4,046,240.6	0.4	2.0	65.3	-8.3	0.3
460,728.5	4,046,240.6	0.5	2.0	63.3	-4.6	0.3
460,728.5	4,046,240.6	0.6	2.0	61.9	-2.5	0.2
460,728.4	4,046,240.6	0.1	2.1	63.9	-12.3	1.1
460,728.4	4,046,240.6	0.2	2.1	64.5	-12.0	0.7
460,728.4	4,046,240.6	0.3	2.1	65.7	-11.1	0.4
460,728.4	4,046,240.6	0.4	2.1	66.5	-9.0	0.2
460,728.4	4,046,240.6	0.5	2.1	65.8	-5.9	0.0
460,728.4	4,046,240.6	0.6	2.1	65.3	-3.9	-0.2
460,728.4	4,046,240.6	0.1	2.2	64.0	-13.0	0.9
460,728.4	4,046,240.6	0.2	2.2	65.2	-12.9	0.5
460,728.4	4,046,240.6	0.3	2.2	66.9	-11.5	-0.1
460,728.4	4,046,240.6	0.4	2.2	68.4	-9.3	-0.2
460,728.4	4,046,240.6	0.5	2.2	67.9	-6.2	-0.4
460,728.4	4,046,240.6	0.6	2.2	67.3	-4.8	-0.4
460,728.3	4,046,240.7	0.1	2.3	65.3	-13.1	0.4
460,728.3	4,046,240.7	0.2	2.3	66.5	-12.5	0.1
460,728.3	4,046,240.7	0.3	2.3	67.8	-11.0	-0.5
460,728.3	4,046,240.7	0.4	2.3	69.5	-8.9	-0.5
460,728.3	4,046,240.7	0.5	2.3	68.8	-5.8	-0.8
460,728.3	4,046,240.7	0.6	2.3	68.4	-4.3	-0.9
460,728.2	4,046,240.7	0.1	2.4	67.4	-13.7	0.3

460,728.2	4,046,240.7	0.2	2.4	68.6	-12.5	-0.1
460,728.2	4,046,240.7	0.3	2.4	69.7	-11.1	-0.6
460,728.2	4,046,240.7	0.4	2.4	71.3	-9.2	-0.5
460,728.2	4,046,240.7	0.5	2.4	70.2	-6.1	-0.7
460,728.2	4,046,240.7	0.6	2.4	69.8	-4.6	-0.8
460,728.1	4,046,240.7	0.1	2.5	70.9	-12.8	0.4
460,728.1	4,046,240.7	0.2	2.5	71.4	-11.9	0.2
460,728.1	4,046,240.7	0.3	2.5	72.3	-10.3	-0.2
460,728.1	4,046,240.7	0.4	2.5	73.5	-8.9	-0.4
460,728.1	4,046,240.7	0.5	2.5	72.7	-5.9	-0.8
460,728.1	4,046,240.7	0.6	2.5	72.7	-4.4	-1.2
460,728.0	4,046,240.8	0.1	2.6	72.7	-12.5	0.5
460,728.0	4,046,240.8	0.2	2.6	73.2	-11.9	0.2
460,728.0	4,046,240.8	0.3	2.6	74.4	-10.6	-0.4
460,728.0	4,046,240.8	0.4	2.6	75.3	-9.6	-0.7
460,728.0	4,046,240.8	0.5	2.6	74.7	-7.2	-1.0
460,728.0	4,046,240.8	0.6	2.6	74.6	-6.0	-1.1
460,727.9	4,046,240.8	0.1	2.7	75.1	-13.2	0.1
460,727.9	4,046,240.8	0.2	2.7	75.4	-12.8	-0.2
460,727.9	4,046,240.8	0.3	2.7	76.7	-11.2	-0.5
460,727.9	4,046,240.8	0.4	2.7	76.5	-9.8	-0.8
460,727.9	4,046,240.8	0.5	2.7	75.2	-7.6	-1.0
460,727.9	4,046,240.8	0.6	2.7	74.5	-7.0	-1.4
460,727.8	4,046,240.8	0.1	2.8	75.2	-13.7	0.3
460,727.8	4,046,240.8	0.2	2.8	74.7	-13.2	-0.3
460,727.8	4,046,240.8	0.3	2.8	75.2	-12.3	-0.7
460,727.8	4,046,240.8	0.4	2.8	74.3	-11.0	-0.8
460,727.8	4,046,240.8	0.5	2.8	73.6	-9.2	-0.8
460,727.8	4,046,240.8	0.6	2.8	73.1	-8.3	-0.8
460,727.7	4,046,240.9	0.1	2.9	76.2	-14.4	0.4
460,727.7	4,046,240.9	0.2	2.9	74.9	-14.3	-0.3
460,727.7	4,046,240.9	0.3	2.9	75.0	-14.1	-0.7
460,727.7	4,046,240.9	0.4	2.9	73.3	-13.2	-1.0
460,727.7	4,046,240.9	0.5	2.9	73.7	-11.4	-0.9
460,727.7	4,046,240.9	0.6	2.9	73.4	-10.5	-1.0
460,727.6	4,046,240.9	0.1	3.0	76.5	-12.8	0.9
460,727.6	4,046,240.9	0.2	3.0	75.6	-12.2	0.2
460,727.6	4,046,240.9	0.3	3.0	76.4	-12.6	-0.5
460,727.6	4,046,240.9	0.4	3.0	75.0	-12.7	-0.9
460,727.6	4,046,240.9	0.5	3.0	74.8	-11.2	-1.4
460,727.6	4,046,240.9	0.6	3.0	73.7	-9.6	-1.4
460,727.5	4,046,240.9	0.1	3.1	78.0	-12.4	0.1
460,727.5	4,046,240.9	0.2	3.1	76.8	-12.0	-0.5
460,727.5	4,046,240.9	0.3	3.1	77.6	-12.6	-1.1
460,727.5	4,046,240.9	0.4	3.1	76.7	-13.4	-0.9
460,727.5	4,046,240.9	0.5	3.1	77.3	-11.9	-1.6
460,727.5	4,046,240.9	0.6	3.1	76.4	-10.4	-1.9
460,727.4	4,046,241.0	0.1	3.2	78.6	-12.2	-0.3
460,727.4	4,046,241.0	0.2	3.2	78.3	-11.3	-0.7
460,727.4	4,046,241.0	0.3	3.2	80.0	-11.2	-1.3
460,727.4	4,046,241.0	0.4	3.2	81.7	-10.9	-0.8
460,727.4	4,046,241.0	0.5	3.2	81.0	-9.7	-1.7
460,727.4	4,046,241.0	0.6	3.2	79.7	-8.3	-2.1
460,727.3	4,046,241.0	0.1	3.3	79.9	-11.6	-0.4
460,727.3	4,046,241.0	0.2	3.3	80.2	-11.2	-0.7
460,727.3	4,046,241.0	0.3	3.3	81.1	-10.9	-0.9
460,727.3	4,046,241.0	0.4	3.3	83.4	-10.4	0.0
460,727.3	4,046,241.0	0.5	3.3	83.0	-10.3	-0.9
460,727.3	4,046,241.0	0.6	3.3	83.3	-9.2	-1.6

460,727.2	4,046,241.0	0.1	3.4	80.3	-11.0	-0.7
460,727.2	4,046,241.0	0.2	3.4	82.7	-11.0	-1.0
460,727.2	4,046,241.0	0.3	3.4	84.7	-9.8	-1.1
460,727.2	4,046,241.0	0.4	3.4	87.9	-8.5	-0.1
460,727.2	4,046,241.0	0.5	3.4	86.3	-8.6	-0.9
460,727.2	4,046,241.0	0.6	3.4	85.9	-8.2	-1.6
460,727.1	4,046,241.1	0.1	3.5	82.4	-12.1	-0.9
460,727.1	4,046,241.1	0.2	3.5	84.4	-12.5	-1.3
460,727.1	4,046,241.1	0.3	3.5	86.1	-11.7	-1.2
460,727.1	4,046,241.1	0.4	3.5	87.9	-10.3	0.0
460,727.1	4,046,241.1	0.5	3.5	87.6	-9.7	-0.3
460,727.1	4,046,241.1	0.6	3.5	87.6	-9.3	-1.3
460,727.0	4,046,241.1	0.1	3.6	84.0	-12.9	-1.8
460,727.0	4,046,241.1	0.2	3.6	85.0	-13.0	-2.1
460,727.0	4,046,241.1	0.3	3.6	85.1	-11.7	-2.5
460,727.0	4,046,241.1	0.4	3.6	86.1	-8.8	-0.9
460,727.0	4,046,241.1	0.5	3.6	86.3	-7.2	-0.5
460,726.9	4,046,241.1	0.1	3.7	86.5	-13.7	-1.4
460,726.9	4,046,241.1	0.2	3.7	86.1	-13.4	-1.8
460,726.9	4,046,241.1	0.3	3.7	85.3	-11.8	-2.5
460,726.9	4,046,241.1	0.4	3.7	84.7	-8.8	-1.4
460,726.9	4,046,241.1	0.5	3.7	84.3	-6.5	-0.6
460,726.8	4,046,241.2	0.1	3.8	87.6	-15.2	-1.1
460,726.8	4,046,241.2	0.2	3.8	86.9	-13.2	-1.6
460,726.8	4,046,241.2	0.3	3.8	84.8	-11.5	-2.3
460,726.8	4,046,241.2	0.4	3.8	83.0	-6.7	-1.6
460,726.7	4,046,241.2	0.1	3.9	85.7	-15.7	-0.5
460,726.7	4,046,241.2	0.2	3.9	85.6	-14.2	-1.3
460,726.7	4,046,241.2	0.3	3.9	82.6	-12.0	-1.6
460,726.7	4,046,241.2	0.4	3.9	82.3	-8.6	-1.4
460,726.6	4,046,241.2	0.1	4.0	87.2	-15.7	-0.8
460,726.6	4,046,241.2	0.2	4.0	86.2	-13.9	-1.4
460,726.6	4,046,241.2	0.3	4.0	82.1	-12.5	-1.7
460,726.6	4,046,241.2	0.4	4.0	80.1	-8.6	-1.5
460,726.6	4,046,241.3	0.1	4.1	88.3	-13.5	-0.3
460,726.6	4,046,241.3	0.2	4.1	87.4	-13.1	-1.1
460,726.6	4,046,241.3	0.3	4.1	83.2	-10.9	-1.5
460,726.6	4,046,241.3	0.4	4.1	80.0	-6.1	-1.7
460,726.6	4,046,241.3	0.5	4.1	76.6	-2.4	-1.0
460,726.5	4,046,241.3	0.1	4.2	90.7	-15.3	-0.3
460,726.5	4,046,241.3	0.2	4.2	88.4	-13.9	-1.0
460,726.5	4,046,241.3	0.3	4.2	85.1	-11.5	-2.0
460,726.5	4,046,241.3	0.4	4.2	80.7	-5.8	-2.1
460,726.5	4,046,241.3	0.5	4.2	78.8	-2.8	-2.1
460,726.4	4,046,241.3	0.1	4.3	88.0	-14.5	-0.1
460,726.4	4,046,241.3	0.2	4.3	86.3	-12.4	-0.8
460,726.4	4,046,241.3	0.3	4.3	82.5	-8.0	-1.5
460,726.4	4,046,241.3	0.4	4.3	79.7	-1.8	-1.5
460,726.3	4,046,241.3	0.1	4.4	86.9	-14.0	0.1
460,726.3	4,046,241.3	0.2	4.4	83.8	-11.6	-0.4
460,726.3	4,046,241.3	0.3	4.4	78.6	-6.3	-1.4
460,726.3	4,046,241.3	0.4	4.4	75.5	-2.2	-1.3
460,726.2	4,046,241.4	0.1	4.5	85.1	-12.0	0.6
460,726.2	4,046,241.4	0.2	4.5	81.4	-10.1	-0.1
460,726.2	4,046,241.4	0.3	4.5	76.3	-5.5	-0.8
460,726.2	4,046,241.4	0.4	4.5	72.3	-1.8	-1.1
460,726.1	4,046,241.4	0.1	4.6	85.3	-11.7	0.9
460,726.1	4,046,241.4	0.2	4.6	81.0	-10.5	0.2
460,726.1	4,046,241.4	0.3	4.6	76.2	-8.1	-0.6

460,726.0	4,046,241.4	0.1	4.7	82.8	-11.1	0.5
460,726.0	4,046,241.4	0.2	4.7	80.1	-10.2	-0.1
460,726.0	4,046,241.4	0.3	4.7	77.8	-9.4	-0.7
460,725.9	4,046,241.5	0.1	4.8	82.2	-8.1	-0.2
460,725.9	4,046,241.5	0.2	4.8	80.6	-7.7	-1.0
460,725.9	4,046,241.5	0.3	4.8	78.9	-7.4	-1.8
460,725.8	4,046,241.5	0.1	4.9	78.1	-9.5	-1.4
460,725.8	4,046,241.5	0.2	4.9	78.3	-8.8	-1.9
460,725.8	4,046,241.5	0.3	4.9	77.4	-9.2	-3.0
460,725.7	4,046,241.5	0.1	5.0	77.2	-5.4	-1.7
460,725.7	4,046,241.5	0.2	5.0	77.3	-5.0	-2.4
460,725.6	4,046,241.6	0.1	5.1	74.3	-6.6	-2.2

e) Sec. 5

UTM Easting (m)	UTM Northing (m)	Water depth (m)	Distance from left bank (m)	Streamwise Velocity (cm/s)	Transverse Velocity (cm/s)	Vertical Velocity (cm/s)
460,714.0	4,046,225.3	0.1	0.0	39.3	4.9	-2.7
460,714.0	4,046,225.3	0.2	0.0	39.3	4.9	-2.7
460,714.0	4,046,225.4	0.1	0.1	40.1	6.8	-2.2
460,714.0	4,046,225.4	0.2	0.1	39.6	7.8	-1.5
460,714.0	4,046,225.5	0.1	0.2	41.8	7.7	-0.7
460,714.0	4,046,225.5	0.2	0.2	41.5	8.6	0.0
460,714.0	4,046,225.5	0.3	0.2	40.7	9.7	0.4
460,714.0	4,046,225.6	0.1	0.3	45.7	9.9	-0.1
460,714.0	4,046,225.6	0.2	0.3	44.8	10.3	0.4
460,714.0	4,046,225.6	0.3	0.3	43.3	10.1	0.3
460,714.1	4,046,225.7	0.1	0.4	46.9	9.8	0.0
460,714.1	4,046,225.7	0.2	0.4	46.5	9.6	-0.1
460,714.1	4,046,225.7	0.3	0.4	45.6	9.0	-0.7
460,714.1	4,046,225.7	0.4	0.4	43.6	7.7	-1.1
460,714.1	4,046,225.8	0.1	0.5	47.2	10.7	0.0
460,714.1	4,046,225.8	0.2	0.5	46.6	9.6	-0.4
460,714.1	4,046,225.8	0.3	0.5	45.2	7.7	-1.4
460,714.1	4,046,225.8	0.4	0.5	43.3	5.9	-1.9
460,714.1	4,046,225.9	0.1	0.6	48.8	9.7	0.6
460,714.1	4,046,225.9	0.2	0.6	48.0	9.1	0.4
460,714.1	4,046,225.9	0.3	0.6	47.0	7.9	-0.5
460,714.1	4,046,225.9	0.4	0.6	44.8	4.9	-0.8
460,714.1	4,046,226.0	0.1	0.7	53.0	10.4	1.6
460,714.1	4,046,226.0	0.2	0.7	51.6	10.6	1.5
460,714.1	4,046,226.0	0.3	0.7	50.4	9.5	0.8
460,714.1	4,046,226.0	0.4	0.7	46.7	6.5	0.7
460,714.1	4,046,226.0	0.5	0.7	45.4	3.7	0.3
460,714.1	4,046,226.1	0.1	0.8	55.7	10.0	1.9
460,714.1	4,046,226.1	0.2	0.8	54.7	11.1	1.6
460,714.1	4,046,226.1	0.3	0.8	54.5	11.3	1.2
460,714.1	4,046,226.1	0.4	0.8	51.0	8.5	0.6
460,714.1	4,046,226.1	0.5	0.8	50.1	6.2	0.3
460,714.1	4,046,226.2	0.1	0.9	56.9	10.7	1.6
460,714.1	4,046,226.2	0.2	0.9	56.3	11.6	1.2
460,714.1	4,046,226.2	0.3	0.9	57.8	11.4	0.2
460,714.1	4,046,226.2	0.4	0.9	54.9	9.7	-0.3
460,714.1	4,046,226.2	0.5	0.9	54.1	6.5	-1.0
460,714.1	4,046,226.3	0.1	1.0	58.2	10.8	1.5
460,714.1	4,046,226.3	0.2	1.0	58.7	11.5	0.8
460,714.1	4,046,226.3	0.3	1.0	62.2	11.6	-0.6
460,714.1	4,046,226.3	0.4	1.0	60.3	10.2	-1.5
460,714.1	4,046,226.3	0.5	1.0	59.3	6.2	-2.1
460,714.1	4,046,226.3	0.6	1.0	56.9	4.5	-2.5
460,714.1	4,046,226.4	0.1	1.1	58.7	12.1	1.0
460,714.1	4,046,226.4	0.2	1.1	60.6	12.7	0.3
460,714.1	4,046,226.4	0.3	1.1	64.7	12.9	-1.3
460,714.1	4,046,226.4	0.4	1.1	63.5	10.0	-2.1
460,714.1	4,046,226.4	0.5	1.1	61.5	5.4	-2.9
460,714.1	4,046,226.4	0.6	1.1	59.5	3.2	-2.9
460,714.1	4,046,226.5	0.1	1.2	60.2	12.1	-0.2
460,714.1	4,046,226.5	0.2	1.2	62.7	13.1	-0.9
460,714.1	4,046,226.5	0.3	1.2	67.7	13.7	-2.7
460,714.1	4,046,226.5	0.4	1.2	67.2	9.5	-3.5
460,714.1	4,046,226.5	0.5	1.2	65.2	4.5	-4.2

460,714.1	4,046,226.5	0.6	1.2	63.1	1.6	-4.2
460,714.1	4,046,226.6	0.1	1.3	59.2	13.1	-1.8
460,714.1	4,046,226.6	0.2	1.3	62.0	13.6	-2.4
460,714.1	4,046,226.6	0.3	1.3	67.1	13.8	-4.5
460,714.1	4,046,226.6	0.4	1.3	68.9	9.6	-4.8
460,714.1	4,046,226.6	0.5	1.3	67.8	5.1	-5.5
460,714.1	4,046,226.6	0.6	1.3	64.3	1.1	-5.6
460,714.2	4,046,226.7	0.1	1.4	61.6	14.6	-2.3
460,714.2	4,046,226.7	0.2	1.4	63.8	14.7	-3.1
460,714.2	4,046,226.7	0.3	1.4	68.8	15.4	-5.1
460,714.2	4,046,226.7	0.4	1.4	69.8	11.8	-5.2
460,714.2	4,046,226.7	0.5	1.4	69.0	7.5	-5.7
460,714.2	4,046,226.7	0.6	1.4	64.7	2.8	-5.8
460,714.2	4,046,226.7	0.7	1.4	62.3	1.0	-6.3
460,714.2	4,046,226.8	0.1	1.5	64.9	17.2	-2.1
460,714.2	4,046,226.8	0.2	1.5	66.7	17.3	-3.1
460,714.2	4,046,226.8	0.3	1.5	70.0	17.6	-4.8
460,714.2	4,046,226.8	0.4	1.5	69.8	15.6	-4.7
460,714.2	4,046,226.8	0.5	1.5	68.6	11.9	-5.1
460,714.2	4,046,226.8	0.6	1.5	66.0	7.0	-5.5
460,714.2	4,046,226.8	0.7	1.5	64.5	4.8	-6.2
460,714.2	4,046,226.9	0.1	1.6	69.2	19.3	-1.3
460,714.2	4,046,226.9	0.2	1.6	70.5	20.2	-2.4
460,714.2	4,046,226.9	0.3	1.6	72.7	20.4	-4.2
460,714.2	4,046,226.9	0.4	1.6	69.3	18.2	-4.5
460,714.2	4,046,226.9	0.5	1.6	66.4	13.4	-4.8
460,714.2	4,046,226.9	0.6	1.6	66.0	10.5	-5.1
460,714.2	4,046,226.9	0.7	1.6	65.6	9.0	-5.4
460,714.2	4,046,227.0	0.1	1.7	71.1	21.7	-1.0
460,714.2	4,046,227.0	0.2	1.7	73.0	23.8	-2.4
460,714.2	4,046,227.0	0.3	1.7	74.7	24.6	-4.4
460,714.2	4,046,227.0	0.4	1.7	70.8	23.1	-5.2
460,714.2	4,046,227.0	0.5	1.7	66.6	15.6	-5.4
460,714.2	4,046,227.0	0.6	1.7	66.1	13.5	-5.2
460,714.2	4,046,227.0	0.7	1.7	64.9	10.9	-4.8
460,714.2	4,046,227.1	0.1	1.8	72.1	22.2	-1.2
460,714.2	4,046,227.1	0.2	1.8	74.1	23.5	-2.3
460,714.2	4,046,227.1	0.3	1.8	77.4	24.5	-4.5
460,714.2	4,046,227.1	0.4	1.8	73.7	24.4	-5.6
460,714.2	4,046,227.1	0.5	1.8	70.9	19.7	-6.3
460,714.2	4,046,227.1	0.6	1.8	68.6	17.7	-6.0
460,714.2	4,046,227.1	0.7	1.8	67.0	14.8	-5.1
460,714.2	4,046,227.2	0.1	1.9	73.7	21.3	-2.5
460,714.2	4,046,227.2	0.2	1.9	76.7	23.7	-3.4
460,714.2	4,046,227.2	0.3	1.9	81.2	25.6	-5.5
460,714.2	4,046,227.2	0.4	1.9	78.3	26.6	-5.9
460,714.2	4,046,227.2	0.5	1.9	75.0	21.8	-6.6
460,714.2	4,046,227.2	0.6	1.9	72.3	19.7	-6.8
460,714.2	4,046,227.3	0.1	2.0	76.4	19.5	-3.0
460,714.2	4,046,227.3	0.2	2.0	79.0	21.3	-3.6
460,714.2	4,046,227.3	0.3	2.0	86.0	22.5	-5.6
460,714.2	4,046,227.3	0.4	2.0	82.5	24.4	-5.2
460,714.2	4,046,227.3	0.5	2.0	77.9	21.3	-5.9
460,714.2	4,046,227.3	0.6	2.0	75.2	19.6	-6.6
460,714.2	4,046,227.4	0.1	2.1	76.5	22.2	-2.8
460,714.2	4,046,227.4	0.2	2.1	79.4	24.9	-3.8
460,714.2	4,046,227.4	0.3	2.1	86.6	26.0	-5.5
460,714.2	4,046,227.4	0.4	2.1	84.2	24.9	-4.6
460,714.2	4,046,227.4	0.5	2.1	77.7	17.3	-4.3

460,714.2	4,046,227.4	0.6	2.1	74.9	13.8	-4.5
460,714.2	4,046,227.5	0.1	2.2	76.0	25.2	-1.5
460,714.2	4,046,227.5	0.2	2.2	78.4	27.5	-2.2
460,714.2	4,046,227.5	0.3	2.2	85.2	28.7	-3.5
460,714.2	4,046,227.5	0.4	2.2	82.1	24.6	-2.6
460,714.2	4,046,227.5	0.5	2.2	75.8	14.8	-2.2
460,714.2	4,046,227.5	0.6	2.2	72.8	10.1	-2.1
460,714.2	4,046,227.6	0.1	2.3	77.4	26.5	-0.6
460,714.2	4,046,227.6	0.2	2.3	79.3	29.4	-1.3
460,714.2	4,046,227.6	0.3	2.3	85.9	30.5	-2.1
460,714.2	4,046,227.6	0.4	2.3	80.6	24.7	-1.5
460,714.2	4,046,227.6	0.5	2.3	75.7	13.1	-1.1
460,714.2	4,046,227.6	0.6	2.3	73.1	8.0	-1.2
460,714.3	4,046,227.7	0.1	2.4	76.4	26.7	-0.4
460,714.3	4,046,227.7	0.2	2.4	79.0	30.0	-0.8
460,714.3	4,046,227.7	0.3	2.4	86.9	31.4	-1.2
460,714.3	4,046,227.7	0.4	2.4	81.1	24.7	-0.6
460,714.3	4,046,227.7	0.5	2.4	76.3	12.4	-0.5
460,714.3	4,046,227.7	0.6	2.4	72.1	6.4	-0.9
460,714.3	4,046,227.8	0.1	2.5	76.4	26.2	-1.0
460,714.3	4,046,227.8	0.2	2.5	80.5	27.9	-1.5
460,714.3	4,046,227.8	0.3	2.5	90.5	29.6	-1.9
460,714.3	4,046,227.8	0.4	2.5	86.5	24.0	-1.4
460,714.3	4,046,227.8	0.5	2.5	81.3	14.6	-1.1
460,714.3	4,046,227.8	0.6	2.5	76.7	9.7	-1.9
460,714.3	4,046,227.9	0.1	2.6	73.9	26.4	-2.0
460,714.3	4,046,227.9	0.2	2.6	79.2	28.8	-2.1
460,714.3	4,046,227.9	0.3	2.6	89.9	30.2	-3.0
460,714.3	4,046,227.9	0.4	2.6	89.0	24.3	-2.3
460,714.3	4,046,227.9	0.5	2.6	84.7	15.9	-2.5
460,714.3	4,046,227.9	0.6	2.6	80.0	10.6	-2.3
460,714.3	4,046,228.0	0.1	2.7	73.4	25.1	-1.7
460,714.3	4,046,228.0	0.2	2.7	79.1	26.9	-2.0
460,714.3	4,046,228.0	0.3	2.7	89.4	27.6	-3.2
460,714.3	4,046,228.0	0.4	2.7	89.0	24.0	-3.2
460,714.3	4,046,228.0	0.5	2.7	83.7	17.9	-4.0
460,714.3	4,046,228.0	0.6	2.7	77.3	13.9	-3.2
460,714.3	4,046,228.0	0.7	2.7	72.1	10.1	-2.4
460,714.3	4,046,228.1	0.1	2.8	70.3	24.4	-1.0
460,714.3	4,046,228.1	0.2	2.8	74.7	26.0	-1.3
460,714.3	4,046,228.1	0.3	2.8	83.9	25.6	-2.2
460,714.3	4,046,228.1	0.4	2.8	85.0	22.0	-2.2
460,714.3	4,046,228.1	0.5	2.8	80.7	15.5	-3.0
460,714.3	4,046,228.1	0.6	2.8	73.5	10.0	-2.0
460,714.3	4,046,228.1	0.7	2.8	67.9	6.0	-1.5
460,714.3	4,046,228.2	0.1	2.9	68.8	25.8	0.1
460,714.3	4,046,228.2	0.2	2.9	72.2	25.8	-0.4
460,714.3	4,046,228.2	0.3	2.9	79.3	25.5	-0.6
460,714.3	4,046,228.2	0.4	2.9	79.9	19.3	-0.9
460,714.3	4,046,228.2	0.5	2.9	74.1	12.7	-1.1
460,714.3	4,046,228.2	0.6	2.9	70.1	5.3	-0.8
460,714.3	4,046,228.2	0.7	2.9	64.9	1.4	-0.2
460,714.3	4,046,228.3	0.1	3.0	67.1	26.0	0.3
460,714.3	4,046,228.3	0.2	3.0	69.7	25.7	-0.3
460,714.3	4,046,228.3	0.3	3.0	75.1	25.1	-0.2
460,714.3	4,046,228.3	0.4	3.0	76.4	17.6	-0.4
460,714.3	4,046,228.3	0.5	3.0	72.9	10.4	0.5
460,714.3	4,046,228.3	0.6	3.0	71.6	2.4	0.5
460,714.3	4,046,228.3	0.7	3.0	66.9	-2.3	1.4

460,714.3	4,046,228.4	0.1	3.1	65.3	24.7	0.0
460,714.3	4,046,228.4	0.2	3.1	67.9	25.1	-0.5
460,714.3	4,046,228.4	0.3	3.1	73.1	24.2	-0.9
460,714.3	4,046,228.4	0.4	3.1	75.0	17.3	-0.8
460,714.3	4,046,228.4	0.5	3.1	73.3	11.3	0.1
460,714.3	4,046,228.4	0.6	3.1	73.4	2.9	1.1
460,714.3	4,046,228.5	0.1	3.2	60.7	22.5	-0.5
460,714.3	4,046,228.5	0.2	3.2	63.0	22.3	-0.8
460,714.3	4,046,228.5	0.3	3.2	68.6	21.1	-1.4
460,714.3	4,046,228.5	0.4	3.2	73.0	17.3	-0.7
460,714.3	4,046,228.5	0.5	3.2	74.5	13.2	-0.4
460,714.3	4,046,228.5	0.6	3.2	73.6	8.7	0.6
460,714.3	4,046,228.5	0.7	3.2	69.9	3.1	0.9
460,714.3	4,046,228.6	0.1	3.3	57.8	20.5	-0.4
460,714.3	4,046,228.6	0.2	3.3	61.3	20.8	-0.5
460,714.3	4,046,228.6	0.3	3.3	67.5	20.2	-1.2
460,714.3	4,046,228.6	0.4	3.3	73.0	17.6	-0.3
460,714.3	4,046,228.6	0.5	3.3	73.6	12.7	-0.5
460,714.3	4,046,228.6	0.6	3.3	71.9	7.1	0.4
460,714.3	4,046,228.7	0.1	3.4	56.4	19.9	0.1
460,714.3	4,046,228.7	0.2	3.4	59.9	19.7	0.0
460,714.3	4,046,228.7	0.3	3.4	65.6	19.9	-0.7
460,714.3	4,046,228.7	0.4	3.4	70.2	15.9	-0.7
460,714.3	4,046,228.7	0.5	3.4	69.7	10.7	-1.0
460,714.3	4,046,228.7	0.6	3.4	68.8	7.1	-1.0
460,714.4	4,046,228.8	0.1	3.5	56.8	20.4	0.4
460,714.4	4,046,228.8	0.2	3.5	60.6	20.7	0.3
460,714.4	4,046,228.8	0.3	3.5	66.5	20.4	-0.6
460,714.4	4,046,228.8	0.4	3.5	70.1	14.9	-0.6
460,714.4	4,046,228.8	0.5	3.5	68.5	9.5	0.1
460,714.4	4,046,228.8	0.6	3.5	67.5	5.8	0.7
460,714.4	4,046,228.9	0.1	3.6	56.8	21.4	0.2
460,714.4	4,046,228.9	0.2	3.6	60.2	21.5	0.3
460,714.4	4,046,228.9	0.3	3.6	64.9	21.4	-0.4
460,714.4	4,046,228.9	0.4	3.6	66.5	15.2	0.1
460,714.4	4,046,228.9	0.5	3.6	64.5	11.2	0.6
460,714.4	4,046,228.9	0.6	3.6	63.4	8.0	1.1
460,714.4	4,046,229.0	0.1	3.7	55.8	23.6	0.2
460,714.4	4,046,229.0	0.2	3.7	57.8	23.4	0.5
460,714.4	4,046,229.0	0.3	3.7	62.4	23.1	-0.1
460,714.4	4,046,229.0	0.4	3.7	63.5	17.4	0.9
460,714.4	4,046,229.0	0.5	3.7	63.1	14.0	1.3
460,714.4	4,046,229.0	0.6	3.7	61.9	11.4	2.1
460,714.4	4,046,229.1	0.1	3.8	51.6	23.7	0.5
460,714.4	4,046,229.1	0.2	3.8	53.8	23.4	0.8
460,714.4	4,046,229.1	0.3	3.8	58.0	22.4	0.3
460,714.4	4,046,229.1	0.4	3.8	60.3	17.6	1.0
460,714.4	4,046,229.1	0.5	3.8	60.7	14.5	0.5
460,714.4	4,046,229.2	0.1	3.9	45.8	23.3	1.4
460,714.4	4,046,229.2	0.2	3.9	48.1	22.4	1.6
460,714.4	4,046,229.2	0.3	3.9	52.3	21.3	1.1
460,714.4	4,046,229.2	0.4	3.9	56.7	16.6	1.6
460,714.4	4,046,229.2	0.5	3.9	58.6	14.6	1.4
460,714.4	4,046,229.3	0.1	4.0	46.2	18.6	3.0
460,714.4	4,046,229.3	0.2	4.0	48.7	18.0	2.9
460,714.4	4,046,229.3	0.3	4.0	51.0	16.5	2.4
460,714.4	4,046,229.3	0.4	4.0	53.8	11.6	2.7
460,714.4	4,046,229.3	0.5	4.0	53.9	8.9	2.7
460,714.4	4,046,229.4	0.1	4.1	47.0	14.6	2.9

460,714.4	4,046,229.4	0.2	4.1	48.4	13.5	3.0
460,714.4	4,046,229.4	0.3	4.1	50.0	11.9	2.8
460,714.4	4,046,229.4	0.4	4.1	51.2	7.9	3.4
460,714.4	4,046,229.4	0.5	4.1	51.3	6.1	3.5
460,714.4	4,046,229.5	0.1	4.2	49.3	11.7	2.7
460,714.4	4,046,229.5	0.2	4.2	49.6	10.5	2.7
460,714.4	4,046,229.5	0.3	4.2	50.0	8.0	2.6
460,714.4	4,046,229.5	0.4	4.2	49.9	4.1	3.2
460,714.4	4,046,229.5	0.5	4.2	49.8	1.8	3.5
460,714.4	4,046,229.6	0.1	4.3	45.2	12.4	1.0
460,714.4	4,046,229.6	0.2	4.3	46.1	10.7	1.1
460,714.4	4,046,229.6	0.3	4.3	46.9	5.8	1.6
460,714.4	4,046,229.6	0.4	4.3	48.2	2.9	2.2
460,714.4	4,046,229.7	0.1	4.4	42.4	12.8	0.5
460,714.4	4,046,229.7	0.2	4.4	43.9	11.2	0.6
460,714.4	4,046,229.7	0.3	4.4	45.4	6.0	1.0
460,714.4	4,046,229.7	0.4	4.4	46.1	2.8	1.4
460,714.5	4,046,229.8	0.1	4.5	37.3	11.7	-0.1
460,714.5	4,046,229.8	0.2	4.5	38.2	10.2	0.1
460,714.5	4,046,229.8	0.3	4.5	41.1	5.3	0.4
460,714.5	4,046,229.8	0.4	4.5	42.0	2.0	0.7
460,714.5	4,046,229.9	0.1	4.6	33.6	11.9	-0.5
460,714.5	4,046,229.9	0.2	4.6	34.0	9.7	0.1
460,714.5	4,046,229.9	0.3	4.6	36.7	7.2	0.5
460,714.5	4,046,230.0	0.1	4.7	31.1	10.7	-0.9
460,714.5	4,046,230.0	0.2	4.7	31.0	9.1	-0.3
460,714.5	4,046,230.0	0.3	4.7	30.9	7.4	0.3
460,714.5	4,046,230.1	0.1	4.8	28.3	10.0	-1.5
460,714.5	4,046,230.1	0.2	4.8	28.7	8.9	-1.0
460,714.5	4,046,230.2	0.1	4.9	26.2	5.0	-1.2
460,714.5	4,046,230.2	0.2	4.9	26.2	5.0	-1.2
460,714.5	4,046,230.3	0.1	5.0	23.5	3.3	-1.0
460,714.5	4,046,230.3	0.2	5.0	23.5	3.3	-1.0

f) Sec. 6

UTM Easting (m)	UTM Northing (m)	Water depth (m)	Distance from left bank (m)	Streamwise Velocity (cm/s)	Transverse Velocity (cm/s)	Vertical Velocity (cm/s)
460,700.2	4,046,244.7	0.1	0.1	80.3	4.4	-0.3
460,700.3	4,046,244.7	0.1	0.2	79.3	2.9	-1.4
460,700.3	4,046,244.7	0.2	0.2	79.3	2.9	-1.4
460,700.4	4,046,244.7	0.1	0.3	80.3	1.0	-2.0
460,700.4	4,046,244.7	0.2	0.3	78.4	0.8	-1.9
460,700.5	4,046,244.7	0.1	0.4	83.3	1.8	-2.4
460,700.5	4,046,244.7	0.2	0.4	78.1	-1.2	-1.9
460,700.5	4,046,244.7	0.3	0.4	73.7	-2.6	-1.8
460,700.6	4,046,244.7	0.1	0.5	82.7	6.5	-0.8
460,700.6	4,046,244.7	0.2	0.5	76.6	3.2	-0.2
460,700.6	4,046,244.7	0.3	0.5	72.2	1.3	-0.1
460,700.7	4,046,244.7	0.1	0.6	84.5	10.6	0.2
460,700.7	4,046,244.7	0.2	0.6	77.5	5.6	0.7
460,700.7	4,046,244.7	0.3	0.6	75.3	1.7	0.4
460,700.8	4,046,244.7	0.1	0.7	85.1	12.2	0.6
460,700.8	4,046,244.7	0.2	0.7	81.3	10.0	0.6
460,700.8	4,046,244.7	0.3	0.7	79.1	5.8	-0.2
460,700.8	4,046,244.7	0.4	0.7	76.7	1.2	-0.2
460,700.9	4,046,244.7	0.1	0.8	89.4	9.8	-0.7
460,700.9	4,046,244.7	0.2	0.8	86.0	7.5	-0.7
460,700.9	4,046,244.7	0.3	0.8	83.6	3.8	-1.7
460,700.9	4,046,244.7	0.4	0.8	80.8	-0.3	-1.5
460,701.0	4,046,244.7	0.1	0.9	89.2	10.7	-0.4
460,701.0	4,046,244.7	0.2	0.9	88.5	10.0	-1.0
460,701.0	4,046,244.7	0.3	0.9	84.0	8.1	-2.1
460,701.0	4,046,244.7	0.4	0.9	82.2	5.6	-2.3
460,701.1	4,046,244.7	0.1	1.0	89.3	10.0	-0.4
460,701.1	4,046,244.7	0.2	1.0	89.2	9.2	-0.8
460,701.1	4,046,244.7	0.3	1.0	85.4	8.9	-1.7
460,701.1	4,046,244.7	0.4	1.0	82.2	8.0	-1.8
460,701.2	4,046,244.7	0.1	1.1	90.2	10.4	0.6
460,701.2	4,046,244.7	0.2	1.1	90.4	9.8	0.0
460,701.2	4,046,244.7	0.3	1.1	86.4	9.5	-0.8
460,701.2	4,046,244.7	0.4	1.1	82.2	8.8	-1.5
460,701.2	4,046,244.7	0.5	1.1	77.2	9.0	-1.7
460,701.3	4,046,244.7	0.1	1.2	90.6	9.6	0.7
460,701.3	4,046,244.7	0.2	1.2	90.6	8.5	0.2
460,701.3	4,046,244.7	0.3	1.2	88.2	8.0	-0.6
460,701.3	4,046,244.7	0.4	1.2	83.4	7.0	-1.5
460,701.3	4,046,244.7	0.5	1.2	79.7	7.4	-1.9
460,701.4	4,046,244.7	0.1	1.3	88.9	9.7	0.3
460,701.4	4,046,244.7	0.2	1.3	88.5	8.3	-0.1
460,701.4	4,046,244.7	0.3	1.3	87.1	7.0	-0.8
460,701.4	4,046,244.7	0.4	1.3	84.2	5.3	-1.5
460,701.4	4,046,244.7	0.5	1.3	82.6	5.3	-2.1
460,701.5	4,046,244.7	0.1	1.4	86.8	11.4	-0.4
460,701.5	4,046,244.7	0.2	1.4	86.5	9.6	-0.6
460,701.5	4,046,244.7	0.3	1.4	85.2	7.6	-1.8
460,701.5	4,046,244.7	0.4	1.4	83.3	5.0	-2.1
460,701.5	4,046,244.7	0.5	1.4	81.7	4.7	-2.9
460,701.5	4,046,244.7	0.6	1.4	80.4	4.5	-2.9
460,701.6	4,046,244.7	0.1	1.5	83.4	12.4	-1.0
460,701.6	4,046,244.7	0.2	1.5	82.5	10.5	-1.2
460,701.6	4,046,244.7	0.3	1.5	80.5	8.7	-2.2

460,701.6	4,046,244.7	0.4	1.5	80.1	6.0	-2.3
460,701.6	4,046,244.7	0.5	1.5	79.5	4.7	-2.8
460,701.6	4,046,244.7	0.6	1.5	79.3	4.0	-3.1
460,701.7	4,046,244.7	0.1	1.6	82.2	13.1	-0.6
460,701.7	4,046,244.7	0.2	1.6	81.4	11.5	-0.9
460,701.7	4,046,244.7	0.3	1.6	79.8	9.8	-2.1
460,701.7	4,046,244.7	0.4	1.6	79.9	6.2	-2.2
460,701.7	4,046,244.7	0.5	1.6	78.7	4.4	-2.8
460,701.7	4,046,244.7	0.6	1.6	78.4	3.5	-2.9
460,701.8	4,046,244.7	0.1	1.7	80.0	12.8	-0.1
460,701.8	4,046,244.7	0.2	1.7	79.3	12.1	-0.3
460,701.8	4,046,244.7	0.3	1.7	78.9	11.1	-0.7
460,701.8	4,046,244.7	0.4	1.7	79.9	8.2	-0.7
460,701.8	4,046,244.7	0.5	1.7	79.4	5.0	-1.5
460,701.8	4,046,244.7	0.6	1.7	78.8	3.3	-2.2
460,701.9	4,046,244.6	0.1	1.8	80.4	14.1	0.4
460,701.9	4,046,244.6	0.2	1.8	80.3	13.4	0.3
460,701.9	4,046,244.6	0.3	1.8	81.3	11.8	-0.1
460,701.9	4,046,244.6	0.4	1.8	81.2	8.1	0.1
460,701.9	4,046,244.6	0.5	1.8	79.2	5.1	-0.9
460,701.9	4,046,244.6	0.6	1.8	77.6	4.1	-1.2
460,702.0	4,046,244.6	0.1	1.9	80.1	15.7	0.3
460,702.0	4,046,244.6	0.2	1.9	80.4	14.4	0.4
460,702.0	4,046,244.6	0.3	1.9	81.6	12.7	-0.3
460,702.0	4,046,244.6	0.4	1.9	80.1	8.2	-0.3
460,702.0	4,046,244.6	0.5	1.9	77.3	4.6	-1.2
460,702.0	4,046,244.6	0.6	1.9	75.1	3.1	-1.3
460,702.1	4,046,244.6	0.1	2.0	80.0	15.7	0.7
460,702.1	4,046,244.6	0.2	2.0	80.0	14.0	0.1
460,702.1	4,046,244.6	0.3	2.0	79.8	12.0	-1.0
460,702.1	4,046,244.6	0.4	2.0	77.3	7.1	-1.0
460,702.1	4,046,244.6	0.5	2.0	74.0	3.6	-1.4
460,702.1	4,046,244.6	0.6	2.0	72.8	2.2	-1.1
460,702.2	4,046,244.6	0.1	2.1	77.9	14.1	0.4
460,702.2	4,046,244.6	0.2	2.1	78.0	12.2	-0.3
460,702.2	4,046,244.6	0.3	2.1	77.4	10.5	-1.5
460,702.2	4,046,244.6	0.4	2.1	74.7	5.9	-1.4
460,702.2	4,046,244.6	0.5	2.1	72.0	2.5	-1.7
460,702.2	4,046,244.6	0.6	2.1	70.8	0.3	-1.3
460,702.3	4,046,244.6	0.1	2.2	75.0	11.9	0.6
460,702.3	4,046,244.6	0.2	2.2	74.9	10.1	-0.1
460,702.3	4,046,244.6	0.3	2.2	72.9	8.4	-1.0
460,702.3	4,046,244.6	0.4	2.2	71.0	5.0	-0.5
460,702.3	4,046,244.6	0.5	2.2	68.8	1.8	-0.6
460,702.3	4,046,244.6	0.6	2.2	68.8	-0.4	-0.1
460,702.4	4,046,244.6	0.1	2.3	73.5	10.4	0.7
460,702.4	4,046,244.6	0.2	2.3	73.3	9.0	0.1
460,702.4	4,046,244.6	0.3	2.3	71.6	7.6	-0.8
460,702.4	4,046,244.6	0.4	2.3	69.7	4.4	-0.8
460,702.4	4,046,244.6	0.5	2.3	67.3	1.5	-0.7
460,702.4	4,046,244.6	0.6	2.3	67.0	-0.5	-0.3
460,702.5	4,046,244.6	0.1	2.4	71.8	9.9	0.9
460,702.5	4,046,244.6	0.2	2.4	71.6	8.5	0.4
460,702.5	4,046,244.6	0.3	2.4	69.9	7.6	-0.5
460,702.5	4,046,244.6	0.4	2.4	69.4	5.0	-0.8
460,702.5	4,046,244.6	0.5	2.4	67.7	2.9	-0.8
460,702.5	4,046,244.6	0.6	2.4	68.1	1.0	-0.3
460,702.6	4,046,244.6	0.1	2.5	70.3	9.6	0.4
460,702.6	4,046,244.6	0.2	2.5	71.0	9.6	-0.3

460,702.6	4,046,244.6	0.3	2.5	71.9	9.1	-1.2
460,702.6	4,046,244.6	0.4	2.5	71.4	7.3	-1.1
460,702.6	4,046,244.6	0.5	2.5	69.0	4.6	-1.0
460,702.6	4,046,244.6	0.6	2.5	67.2	3.1	-0.4
460,702.7	4,046,244.6	0.1	2.6	67.1	11.6	0.2
460,702.7	4,046,244.6	0.2	2.6	68.0	11.4	-0.4
460,702.7	4,046,244.6	0.3	2.6	69.2	10.2	-1.3
460,702.7	4,046,244.6	0.4	2.6	70.9	7.5	-1.0
460,702.7	4,046,244.6	0.5	2.6	68.7	4.6	-1.0
460,702.7	4,046,244.6	0.6	2.6	67.3	3.9	-0.5
460,702.8	4,046,244.6	0.1	2.7	67.0	12.1	0.3
460,702.8	4,046,244.6	0.2	2.7	68.1	13.1	-0.5
460,702.8	4,046,244.6	0.3	2.7	69.6	12.0	-1.3
460,702.8	4,046,244.6	0.4	2.7	71.0	8.5	-0.7
460,702.8	4,046,244.6	0.5	2.7	67.4	3.2	-0.6
460,702.8	4,046,244.6	0.6	2.7	66.0	1.5	0.0
460,702.9	4,046,244.6	0.1	2.8	64.8	12.1	0.8
460,702.9	4,046,244.6	0.2	2.8	65.5	12.1	0.1
460,702.9	4,046,244.6	0.3	2.8	66.2	10.7	-0.7
460,702.9	4,046,244.6	0.4	2.8	68.8	6.8	-0.6
460,702.9	4,046,244.6	0.5	2.8	66.0	2.5	-0.7
460,702.9	4,046,244.6	0.6	2.8	65.8	0.6	-0.2
460,703.0	4,046,244.6	0.1	2.9	64.8	12.3	0.7
460,703.0	4,046,244.6	0.2	2.9	65.9	12.0	-0.2
460,703.0	4,046,244.6	0.3	2.9	68.5	11.4	-0.9
460,703.0	4,046,244.6	0.4	2.9	70.0	7.3	-0.8
460,703.0	4,046,244.6	0.5	2.9	66.7	3.0	-0.7
460,703.0	4,046,244.6	0.6	2.9	64.9	0.3	-0.2
460,703.1	4,046,244.6	0.1	3.0	62.5	12.1	0.5
460,703.1	4,046,244.6	0.2	3.0	63.6	11.0	0.0
460,703.1	4,046,244.6	0.3	3.0	66.5	10.1	-0.8
460,703.1	4,046,244.6	0.4	3.0	66.6	6.7	-0.9
460,703.1	4,046,244.6	0.5	3.0	63.4	4.5	-0.6
460,703.1	4,046,244.6	0.6	3.0	60.0	2.6	-0.1
460,703.2	4,046,244.6	0.1	3.1	60.9	12.1	0.3
460,703.2	4,046,244.6	0.2	3.1	62.2	11.1	-0.1
460,703.2	4,046,244.6	0.3	3.1	65.6	10.5	-0.8
460,703.2	4,046,244.6	0.4	3.1	65.6	7.1	-1.0
460,703.2	4,046,244.6	0.5	3.1	62.2	4.6	-0.8
460,703.2	4,046,244.6	0.6	3.1	58.6	2.4	-0.3
460,703.3	4,046,244.6	0.1	3.2	58.2	9.8	0.4
460,703.3	4,046,244.6	0.2	3.2	59.9	9.2	0.3
460,703.3	4,046,244.6	0.3	3.2	62.9	8.5	-0.1
460,703.3	4,046,244.6	0.4	3.2	63.4	6.0	0.0
460,703.3	4,046,244.6	0.5	3.2	61.0	2.8	0.0
460,703.3	4,046,244.6	0.6	3.2	58.6	0.1	0.4
460,703.4	4,046,244.6	0.1	3.3	55.5	9.8	0.3
460,703.4	4,046,244.6	0.2	3.3	57.5	9.3	0.3
460,703.4	4,046,244.6	0.3	3.3	61.2	8.0	0.0
460,703.4	4,046,244.6	0.4	3.3	63.5	5.2	0.1
460,703.4	4,046,244.6	0.5	3.3	61.9	1.4	-0.2
460,703.4	4,046,244.6	0.6	3.3	60.7	-0.9	-0.1
460,703.5	4,046,244.6	0.1	3.4	53.9	10.3	0.1
460,703.5	4,046,244.6	0.2	3.4	56.0	9.5	0.1
460,703.5	4,046,244.6	0.3	3.4	59.7	7.5	0.0
460,703.5	4,046,244.6	0.4	3.4	61.8	4.9	0.1
460,703.5	4,046,244.6	0.5	3.4	60.2	2.1	-0.1
460,703.5	4,046,244.6	0.6	3.4	58.8	0.8	0.0
460,703.6	4,046,244.6	0.1	3.5	52.2	10.9	-0.3

460,703.6	4,046,244.6	0.2	3.5	54.6	10.0	-0.4
460,703.6	4,046,244.6	0.3	3.5	59.0	8.0	-0.5
460,703.6	4,046,244.6	0.4	3.5	60.8	5.6	-0.3
460,703.6	4,046,244.6	0.5	3.5	58.5	3.6	-0.5
460,703.6	4,046,244.6	0.6	3.5	56.2	2.9	-0.5
460,703.7	4,046,244.6	0.1	3.6	51.2	10.1	-0.4
460,703.7	4,046,244.6	0.2	3.6	53.8	9.3	-0.5
460,703.7	4,046,244.6	0.3	3.6	58.6	7.1	-0.5
460,703.7	4,046,244.6	0.4	3.6	60.5	5.5	-0.3
460,703.7	4,046,244.6	0.5	3.6	58.8	3.4	-0.3
460,703.7	4,046,244.6	0.6	3.6	56.5	3.0	-0.4
460,703.8	4,046,244.6	0.1	3.7	50.4	8.3	-0.2
460,703.8	4,046,244.6	0.2	3.7	53.4	7.8	-0.3
460,703.8	4,046,244.6	0.3	3.7	58.7	6.0	-0.3
460,703.8	4,046,244.6	0.4	3.7	60.8	4.7	0.0
460,703.8	4,046,244.6	0.5	3.7	58.7	3.6	0.5
460,703.8	4,046,244.6	0.6	3.7	56.2	3.2	0.6
460,703.9	4,046,244.6	0.1	3.8	49.7	7.8	0.0
460,703.9	4,046,244.6	0.2	3.8	52.5	7.1	0.1
460,703.9	4,046,244.6	0.3	3.8	57.5	5.1	0.1
460,703.9	4,046,244.6	0.4	3.8	58.7	3.8	0.4
460,703.9	4,046,244.6	0.5	3.8	57.4	3.2	0.8
460,703.9	4,046,244.6	0.6	3.8	54.7	3.1	1.1
460,704.0	4,046,244.6	0.1	3.9	48.7	8.0	0.7
460,704.0	4,046,244.6	0.2	3.9	51.3	7.2	0.8
460,704.0	4,046,244.6	0.3	3.9	55.5	5.1	1.0
460,704.0	4,046,244.6	0.4	3.9	55.8	3.8	0.9
460,704.0	4,046,244.6	0.5	3.9	54.2	4.1	1.3
460,704.1	4,046,244.6	0.1	4.0	47.9	8.7	0.9
460,704.1	4,046,244.6	0.2	4.0	49.9	7.9	1.1
460,704.1	4,046,244.6	0.3	4.0	53.0	5.5	1.5
460,704.1	4,046,244.6	0.4	4.0	51.5	3.2	1.4
460,704.1	4,046,244.6	0.5	4.0	50.3	1.7	1.4
460,704.2	4,046,244.6	0.1	4.1	47.2	7.3	1.3
460,704.2	4,046,244.6	0.2	4.1	48.3	6.6	1.4
460,704.2	4,046,244.6	0.3	4.1	50.0	4.7	1.8
460,704.2	4,046,244.6	0.4	4.1	48.9	3.0	1.6
460,704.2	4,046,244.6	0.5	4.1	47.9	1.5	1.6
460,704.3	4,046,244.6	0.1	4.2	46.5	5.8	1.5
460,704.3	4,046,244.6	0.2	4.2	47.0	5.1	1.6
460,704.3	4,046,244.6	0.3	4.2	47.7	3.4	1.8
460,704.3	4,046,244.6	0.4	4.2	46.2	1.8	1.9
460,704.4	4,046,244.6	0.1	4.3	44.5	5.2	1.8
460,704.4	4,046,244.6	0.2	4.3	45.0	4.4	1.8
460,704.4	4,046,244.6	0.3	4.3	45.6	2.9	1.9
460,704.4	4,046,244.6	0.4	4.3	45.2	2.5	1.8
460,704.5	4,046,244.6	0.1	4.4	41.2	5.0	1.9
460,704.5	4,046,244.6	0.2	4.4	41.7	4.3	1.9
460,704.5	4,046,244.6	0.3	4.4	42.9	2.8	2.0
460,704.5	4,046,244.6	0.4	4.4	43.1	2.3	1.8
460,704.6	4,046,244.6	0.1	4.5	39.1	5.1	1.5
460,704.6	4,046,244.6	0.2	4.5	39.2	4.5	1.4
460,704.6	4,046,244.6	0.3	4.5	40.4	3.1	1.5
460,704.6	4,046,244.6	0.4	4.5	41.3	2.5	1.4
460,704.7	4,046,244.6	0.1	4.6	36.7	5.2	1.0
460,704.7	4,046,244.6	0.2	4.6	36.1	4.2	1.0
460,704.7	4,046,244.6	0.3	4.6	36.3	2.7	1.1
460,704.8	4,046,244.6	0.1	4.7	33.8	6.0	0.3
460,704.8	4,046,244.6	0.2	4.7	33.8	5.0	0.4

460,704.8	4,046,244.6	0.3	4.7	33.0	3.1	0.7
460,704.9	4,046,244.6	0.1	4.8	29.2	9.0	-1.2
460,704.9	4,046,244.6	0.2	4.8	29.6	7.7	-0.9
460,705.0	4,046,244.6	0.1	4.9	26.3	10.9	-2.3
460,705.0	4,046,244.6	0.2	4.9	26.3	10.9	-2.3
460,705.1	4,046,244.6	0.1	5.0	25.7	13.1	-3.1
460,705.1	4,046,244.6	0.2	5.0	25.7	13.1	-3.1

Table C2. Concentration measurements using fluorometer

a) Sec. 2

y/W / Time (sec)	Concentration (ppb)				
	0.167	**0.333**	**0.500**	**0.667**	**0.833**
48	0.0	0.0	0.0	0.0	0.0
49	0.0	0.1	0.0	0.0	0.0
50	0.0	0.2	0.1	0.0	0.0
51	0.1	0.7	0.4	0.0	0.0
52	0.1	1.7	0.9	0.0	0.0
53	0.6	4.6	1.8	0.0	0.0
54	0.7	7.6	3.0	0.0	0.0
55	1.1	12.3	4.7	0.0	0.0
56	3.1	15.4	7.3	0.0	0.0
57	5.8	19.6	9.8	0.2	0.0
58	8.5	24.8	12.2	1.0	0.0
59	11.1	31.5	15.2	2.8	0.1
60	15.6	37.5	20.1	4.7	0.8
61	21.4	43.2	26.3	6.7	2.1
62	27.0	49.3	31.2	7.9	3.5
63	30.3	55.0	37.3	11.0	4.1
64	32.9	61.3	43.5	15.2	4.9
65	34.6	66.2	49.2	20.1	6.2
66	36.5	69.2	54.0	24.8	7.3
67	38.3	71.5	57.8	32.0	8.9
68	39.5	73.6	60.9	40.3	10.3
69	40.5	74.7	63.7	47.0	12.4
70	41.1	74.5	66.1	51.5	13.8
71	40.9	72.8	67.7	56.2	15.8
72	40.6	71.5	68.7	60.9	19.1
73	39.6	69.9	69.1	63.6	22.3
74	38.0	68.4	68.7	64.1	24.4
75	36.8	66.5	68.6	64.3	27.0
76	35.5	64.2	66.9	64.5	29.1
77	34.4	62.8	65.4	64.9	30.7
78	33.1	60.4	63.6	63.7	32.7
79	31.4	58.0	60.9	61.8	34.1
80	29.6	55.4	58.6	58.1	35.5
81	28.0	52.5	56.0	54.6	36.6
82	26.6	49.8	53.6	51.5	37.6
83	25.8	47.1	51.0	48.8	38.5
84	24.6	44.5	48.5	46.4	38.7
85	23.8	42.0	46.3	43.7	39.0
86	22.6	39.2	44.2	41.8	39.4
87	21.2	37.0	42.0	39.5	39.1
88	19.9	34.9	39.9	37.3	38.5
89	19.1	33.0	37.6	35.1	38.0
90	18.2	31.2	35.4	33.2	37.2
91	17.2	29.4	33.3	30.9	36.5
92	16.2	27.9	31.5	29.1	35.9
93	15.2	26.4	29.4	27.2	35.8
94	14.2	25.2	28.0	25.5	35.0
95	13.2	24.0	26.2	24.2	34.5
96	12.1	22.6	24.6	22.5	33.8
97	11.3	21.2	23.3	20.9	32.8
98	10.6	19.7	21.8	19.5	32.2

99	9.7	18.3	20.5	18.2	31.3
100	9.1	17.1	19.3	17.0	30.3
101	8.7	15.9	17.9	15.9	29.3
102	8.1	15.3	17.0	14.8	28.1
103	7.5	14.2	15.9	13.9	26.8
104	7.0	13.5	15.2	12.8	25.4
105	6.5	12.8	14.2	12.0	24.4
106	6.0	11.9	13.4	11.1	22.7
107	5.7	11.2	12.7	10.3	21.8
108	5.3	10.6	11.8	9.6	20.9
109	5.1	10.0	11.0	9.1	19.9
110	4.5	9.5	10.5	8.3	18.8
111	4.5	8.7	9.7	7.8	17.7
112	4.1	8.2	9.0	7.2	16.9
113	3.9	7.6	8.5	6.8	16.1
114	3.9	7.1	7.8	6.4	15.4
115	3.6	6.7	7.4	5.9	14.7
116	3.5	6.3	7.1	5.6	14.1
117	3.4	5.8	6.6	5.3	13.4
118	3.2	5.5	6.2	5.0	12.7
119	2.9	5.2	6.0	4.6	12.3
120	2.7	5.0	5.6	4.3	12.0
121	2.7	4.6	5.2	3.9	11.5
122	2.5	4.0	4.7	3.6	10.9
123	2.5	4.0	4.3	3.3	10.3
124	2.4	3.7	4.2	3.2	9.6
125	2.2	3.5	4.0	3.1	8.7
126	2.0	3.3	3.7	2.9	8.1
127	1.9	3.2	3.4	2.6	7.5
128	1.7	3.1	3.1	2.7	7.2
129	1.7	2.7	2.8	2.5	6.9
130	1.4	2.3	2.5	2.6	6.4
131	1.3	2.0	2.5	2.5	6.0
132	1.4	2.1	2.4	2.7	5.8
133	1.3	1.8	2.2	2.4	5.6
134	1.0	1.6	2.3	2.2	5.6
135	1.2	1.6	2.3	2.0	5.3
136	1.1	1.3	2.2	2.0	5.2
137	1.2	1.3	1.8	1.9	5.0
138	1.1	1.1	2.1	1.8	5.1
139	0.9	1.1	2.1	1.6	5.2
140	0.7	1.1	2.2	1.4	4.9
141	0.6	1.0	2.1	1.3	4.8
142	0.4	1.0	1.9	1.1	4.5
143	0.3	1.0	2.1	1.0	4.4
144	0.3	0.8	1.9	1.1	4.1
145	0.3	1.1	1.8	1.0	4.1
146	0.3	1.1	1.3	0.8	3.9
147	0.3	1.1	1.2	0.7	3.7
148	0.3	0.9	1.1	0.7	3.5
149	0.3	0.9	1.0	0.7	3.4
150	0.3	0.8	1.0	0.5	3.1
151	0.2	1.0	1.0	0.4	2.8
152	0.0	1.0	0.9	0.4	2.6
153	0.0	1.2	0.8	0.5	2.6
154	0.0	0.8	0.9	0.4	2.5
155	0.0	0.7	0.9	0.2	2.5
156	0.0	0.9	1.0	0.3	2.5
157	0.0	1.0	1.1	0.1	2.5

158	0.0	1.1	1.3	0.1	2.2
159	0.0	1.1	1.4	0.1	1.9
160	0.0	1.3	1.3	0.3	1.8
161	0.0	1.1	1.1	0.2	1.6
162	0.0	0.6	0.9	0.1	1.8
163	0.0	0.8	0.8	0.0	1.8
164	0.0	0.9	0.9	0.0	1.9
165	0.0	0.9	1.0	0.0	1.8
166	0.0	0.9	0.8	0.0	1.7
167	0.0	0.9	0.7	0.0	1.6
168	0.0	0.7	0.6	0.0	1.4
169	0.0	0.7	0.6	0.0	1.2
170	0.0	0.7	0.6	0.0	1.1
171	0.0	0.6	0.6	0.0	1.1
172	0.0	0.7	0.7	0.0	1.3
173	0.0	0.9	0.4	0.0	1.3
174	0.0	0.9	0.5	0.0	1.3
175	0.0	1.0	0.4	0.0	1.2
176	0.0	0.9	0.3	0.0	1.0
177	0.0	1.0	0.3	0.0	0.9
178	0.0	1.0	0.3	0.0	0.8
179	0.0	1.2	0.3	0.0	0.7
180	0.0	1.4	0.2	0.0	0.7
181	0.0	1.3	0.4	0.0	0.8
182	0.0	1.3	0.6	0.0	0.9
183	0.0	1.3	0.6	0.0	0.8
184	0.0	1.2	0.4	0.0	0.8
185	0.0	1.1	0.3	0.0	0.9
186	0.0	1.0	0.5	0.0	1.0
187	0.0	0.9	0.5	0.0	1.1
188	0.0	1.0	0.4	0.0	1.1
189	0.0	0.9	0.2	0.0	0.9
190	0.0	0.8	0.3	0.0	1.0
191	0.0	0.7	0.2	0.0	0.8
192	0.0	0.8	0.0	0.0	0.7
193	0.0	0.9	0.0	0.0	0.6
194	0.0	0.8	0.0	0.0	0.8
195	0.0	0.7	0.0	0.0	0.9
196	0.0	0.9	0.0	0.0	0.7
197	0.0	0.7	0.0	0.0	0.4
198	0.0	0.6	0.0	0.0	0.3
199	0.0	0.4	0.0	0.0	0.3
200	0.0	0.3	0.0	0.0	0.4
201	0.0	0.2	0.0	0.0	0.4
202	0.0	0.2	0.0	0.0	0.4
203	0.0	0.2	0.0	0.0	0.4
204	0.0	0.2	0.0	0.0	0.1
205	0.0	0.2	0.0	0.0	0.1
206	0.0	0.0	0.0	0.0	0.2
207	0.0	0.0	0.0	0.0	0.3
208	0.0	0.0	0.0	0.0	0.3
209	0.0	0.0	0.0	0.0	0.0

b) Sec. 4

y/W / Time (sec)	Concentration (ppb)				
	0.167	**0.333**	**0.500**	**0.667**	**0.833**
95	-	-	0.0	0.0	0.0
96	-	-	0.2	0.0	0.0
97	-	-	0.2	0.2	0.0
98	-	-	0.3	0.4	0.0
99	-	-	0.3	0.7	0.2
100	-	-	0.5	1.2	0.6
101	-	-	0.9	1.5	0.6
102	-	-	1.7	2.0	1.1
103	-	-	2.5	3.0	2.0
104	-	-	3.8	5.1	2.5
105	-	-	5.3	7.0	4.2
106	-	-	7.2	9.1	6.4
107	-	-	9.7	10.9	8.1
108	-	-	12.2	12.9	9.2
109	-	-	14.9	15.0	10.5
110	-	-	17.3	16.7	12.2
111	-	-	19.7	18.4	13.4
112	-	-	22.1	20.3	15.1
113	-	-	23.9	21.7	16.3
114	-	-	26.1	23.3	17.5
115	-	-	27.9	24.8	18.6
116	-	-	29.9	26.7	19.5
117	-	-	32.1	28.4	20.7
118	-	-	34.3	30.1	21.8
119	-	-	36.4	31.5	22.5
120	-	-	37.9	32.7	23.4
121	-	-	39.8	34.0	24.6
122	-	-	41.1	34.8	25.2
123	-	-	42.7	35.2	25.5
124	-	-	44.0	36.7	25.8
125	-	-	45.1	37.4	26.0
126	-	-	46.0	37.7	26.1
127	-	-	46.3	37.8	26.1
128	-	-	46.7	37.8	26.9
129	-	-	47.2	37.7	26.8
130	-	-	47.6	37.5	26.7
131	-	-	47.9	37.3	27.2
132	-	-	47.8	37.0	27.4
133	-	-	47.6	36.4	27.6
134	-	-	46.9	35.9	27.4
135	-	-	46.5	35.4	27.0
136	-	-	46.1	35.3	26.4
137	-	-	45.6	35.1	25.8
138	-	-	44.8	34.7	25.2
139	-	-	44.1	34.2	25.3
140	-	-	43.2	33.3	24.7
141	-	-	42.4	32.6	24.2
142	-	-	41.6	31.9	23.5
143	-	-	40.5	30.9	23.4
144	-	-	39.3	29.9	22.9
145	-	-	38.5	29.2	22.7
146	-	-	37.2	28.3	22.3
147	-	-	36.5	27.5	22.4

148	-	-	35.6	26.6	21.8
149	-	-	34.7	25.8	21.5
150	-	-	33.8	25.1	20.7
151	-	-	32.9	24.3	20.2
152	-	-	31.8	23.3	19.4
153	-	-	30.5	22.8	18.9
154	-	-	29.2	22.0	18.1
155	-	-	28.1	21.3	16.8
156	-	-	27.1	20.4	16.2
157	-	-	26.5	19.6	15.5
158	-	-	25.6	19.1	14.8
159	-	-	24.7	18.4	15.0
160	-	-	23.8	17.7	14.1
161	-	-	23.0	16.9	13.7
162	-	-	22.1	16.3	13.3
163	-	-	21.4	15.6	13.0
164	-	-	20.4	15.0	12.8
165	-	-	19.6	14.4	12.2
166	-	-	19.1	13.9	11.5
167	-	-	18.3	13.3	11.2
168	-	-	17.4	12.9	11.2
169	-	-	16.7	12.1	10.7
170	-	-	15.8	11.6	10.5
171	-	-	14.9	11.1	9.9
172	-	-	14.5	10.5	10.3
173	-	-	13.9	9.8	10.1
174	-	-	13.3	9.4	9.5
175	-	-	12.8	8.9	8.8
176	-	-	12.5	8.4	8.6
177	-	-	12.1	7.9	8.6
178	-	-	11.6	7.5	8.4
179	-	-	11.3	7.3	8.2
180	-	-	11.0	7.3	8.0
181	-	-	10.3	6.9	8.3
182	-	-	9.9	6.9	7.9
183	-	-	9.5	7.0	7.5
184	-	-	9.0	7.2	7.3
185	-	-	8.7	7.2	6.8
186	-	-	8.6	7.1	6.6
187	-	-	8.2	7.1	6.0
188	-	-	7.9	7.0	5.8
189	-	-	7.5	6.4	5.2
190	-	-	7.4	6.1	4.8
191	-	-	6.8	5.9	4.5
192	-	-	6.4	5.4	4.2
193	-	-	6.1	5.0	4.0
194	-	-	5.9	4.7	3.6
195	-	-	5.6	4.4	3.7
196	-	-	5.1	4.3	4.2
197	-	-	4.7	4.3	4.3
198	-	-	4.6	3.9	3.9
199	-	-	4.5	3.5	4.4
200	-	-	4.5	3.2	4.0
201	-	-	4.4	3.0	4.4
202	-	-	4.2	3.0	4.0
203	-	-	3.9	3.1	3.8
204	-	-	3.7	3.1	3.6
205	-	-	3.3	3.0	3.1
206	-	-	3.3	2.9	3.2

207	-	-	3.1	2.8	3.1
208	-	-	3.0	2.8	2.6
209	-	-	2.7	2.6	2.4
210	-	-	2.6	2.5	1.8
211	-	-	2.4	2.4	1.6
212	-	-	2.7	2.5	1.2
213	-	-	2.5	2.4	0.9
214	-	-	2.1	2.2	0.7
215	-	-	2.1	2.4	0.4
216	-	-	2.0	2.3	0.0
217	-	-	1.8	2.4	0.0
218	-	-	1.7	2.3	0.0
219	-	-	1.6	2.3	0.0
220	-	-	1.7	2.1	0.0
221	-	-	1.8	2.2	0.0
222	-	-	1.7	2.2	0.0
223	-	-	1.5	2.1	0.0
224	-	-	1.6	2.1	0.0
225	-	-	1.6	1.9	0.0
226	-	-	1.6	1.8	0.0
227	-	-	1.4	1.7	0.0
228	-	-	1.3	1.8	0.0
229	-	-	1.2	1.7	0.0
230	-	-	1.2	1.5	0.0
231	-	-	1.3	1.5	0.0
232	-	-	1.3	1.6	0.0
233	-	-	1.1	1.5	0.0
234	-	-	0.9	1.6	0.0
235	-	-	0.7	1.4	0.0
236	-	-	0.8	1.4	0.0
237	-	-	0.9	1.2	0.0
238	-	-	1.0	1.1	0.0
239	-	-	0.9	0.9	0.0
240	-	-	1.1	1.2	0.0
241	-	-	1.2	1.5	0.0
242	-	-	1.1	1.5	0.0
243	-	-	1.2	1.5	0.0
244	-	-	1.0	1.4	0.0
245	-	-	0.9	1.2	0.0
246	-	-	1.0	1.0	0.0
247	-	-	0.6	0.9	0.0
248	-	-	0.4	0.7	0.0
249	-	-	0.5	0.8	0.0
250	-	-	0.3	0.8	0.0
251	-	-	0.7	1.1	0.0
252	-	-	0.6	1.2	0.0
253	-	-	0.9	1.3	0.0
254	-	-	0.8	1.3	0.0
255	-	-	0.5	1.3	0.0
256	-	-	0.8	1.1	0.0
257	-	-	0.8	0.9	0.0
258	-	-	0.7	0.8	0.0
259	-	-	0.9	0.8	0.0
260	-	-	0.7	0.7	0.0
261	-	-	0.7	0.6	0.0
262	-	-	0.6	0.7	0.0
263	-	-	0.6	0.7	0.0
264	-	-	0.5	0.5	0.0
265	-	-	0.6	0.5	0.0

266	-	-	0.5	0.6	0.0
267	-	-	0.7	0.9	0.0
268	-	-	0.9	0.6	0.0
269	-	-	0.4	0.8	0.0
270	-	-	0.4	0.5	0.0
271	-	-	0.3	0.7	0.0
272	-	-	0.3	0.7	0.0
273	-	-	0.3	0.9	0.0
274	-	-	0.1	0.9	0.0
275	-	-	0.2	0.9	0.0
276	-	-	0.5	0.8	0.0
277	-	-	0.3	0.9	0.0
278	-	-	0.3	0.9	0.0
279	-	-	0.5	0.9	0.0
280	-	-	0.4	0.9	0.0
281	-	-	0.2	1.1	0.0
282	-	-	0.3	1.2	0.0
283	-	-	0.4	1.1	0.0
284	-	-	0.4	1.2	0.0
285	-	-	0.0	1.0	0.0
286	-	-	0.0	1.0	0.0
287	-	-	0.0	0.8	0.0
288	-	-	0.0	0.9	0.0
289	-	-	0.0	0.9	0.0
290	-	-	0.0	0.8	0.0
291	-	-	0.0	0.6	0.0
292	-	-	0.0	0.7	0.0
293	-	-	0.0	0.6	0.0
294	-	-	0.0	0.8	0.0
295	-	-	0.0	0.8	0.0
296	-	-	0.0	0.9	0.0
297	-	-	0.0	0.9	0.0
298	-	-	0.0	0.8	0.0
299	-	-	0.0	0.8	0.0
300	-	-	0.0	0.9	0.0

c) Sec. 6

y/W / Time (sec)	Concentration (ppb)				
	0.167	**0.333**	**0.500**	**0.667**	**0.833**
142	0.0	0.0	0.0	0.0	0.0
143	0.0	0.0	0.2	0.0	0.0
144	0.0	0.0	0.4	0.0	0.0
145	0.0	0.0	0.6	0.0	0.0
146	0.0	0.2	0.7	0.0	0.0
147	0.0	0.3	0.9	0.0	0.0
148	0.0	0.3	0.9	0.0	0.0
149	0.2	0.5	0.8	0.0	0.0
150	0.4	0.6	0.7	0.0	0.0
151	0.5	0.7	0.8	0.0	0.0
152	0.4	0.9	0.8	0.1	0.0
153	0.7	1.1	1.0	0.1	0.0
154	1.2	1.8	1.1	0.2	0.0
155	1.8	2.0	1.1	0.3	0.0
156	2.5	2.2	1.1	0.5	0.0
157	3.1	2.8	1.2	0.6	0.0
158	4.1	3.4	1.4	0.7	0.4
159	4.5	4.0	1.6	0.8	0.5
160	5.3	4.6	1.9	1.1	0.5
161	5.8	5.1	2.4	1.3	0.7
162	6.4	5.9	2.8	1.4	0.7
163	7.3	6.4	3.4	1.6	1.0
164	8.3	6.7	4.0	1.8	1.2
165	9.1	8.3	4.7	2.1	1.6
166	10.1	9.2	5.2	2.6	2.0
167	10.5	10.0	5.8	3.1	2.6
168	11.3	10.5	6.4	3.7	3.0
169	12.2	11.1	7.2	4.4	3.4
170	13.0	11.8	8.1	5.0	3.8
171	14.0	12.1	8.9	5.5	3.9
172	14.7	12.4	9.7	6.2	4.2
173	15.4	14.0	10.6	7.0	4.9
174	16.1	15.0	11.5	7.9	5.3
175	16.9	16.0	11.9	8.4	5.5
176	17.4	16.5	13.0	9.3	6.0
177	18.1	17.3	14.0	10.2	6.7
178	18.8	17.7	14.9	11.0	7.2
179	19.4	18.0	15.8	11.4	7.9
180	19.8	18.2	16.7	12.3	8.7
181	20.2	19.2	17.5	13.0	9.5
182	20.5	19.9	18.2	13.9	10.3
183	21.2	20.3	19.3	14.6	10.8
184	21.7	20.7	20.1	15.5	11.5
185	22.2	21.0	20.7	16.2	12.2
186	22.8	21.5	21.3	16.9	12.6
187	23.4	21.9	21.9	17.5	13.2
188	23.7	22.4	22.3	18.2	13.8
189	24.2	22.8	22.9	19.0	14.3
190	24.6	23.2	23.3	19.7	14.9
191	24.8	23.4	23.9	20.1	15.6
192	25.2	23.7	24.4	20.7	16.1
193	25.4	24.1	24.8	21.2	16.8
194	25.7	24.6	25.3	21.6	17.2

195	25.7	24.8	25.8	21.9	17.5
196	25.5	24.9	26.1	22.3	18.0
197	25.5	24.8	26.1	22.5	18.5
198	25.5	24.9	26.4	22.6	18.7
199	25.5	24.9	26.6	22.9	18.9
200	25.5	25.0	26.7	23.3	19.3
201	25.3	25.0	26.8	23.5	19.8
202	25.2	25.0	26.9	23.7	20.2
203	25.3	24.7	26.8	23.6	20.4
204	25.3	24.5	26.4	23.6	20.9
205	25.3	24.3	26.2	23.7	21.3
206	25.0	24.2	26.0	23.8	21.6
207	24.9	23.8	25.9	24.0	21.7
208	24.9	23.7	25.9	24.1	22.0
209	24.5	23.4	25.9	24.0	22.1
210	24.2	23.3	25.7	24.0	22.3
211	23.8	23.0	25.3	23.9	22.7
212	23.5	22.6	24.9	23.7	22.9
213	23.2	22.3	24.5	23.6	23.0
214	22.8	21.9	24.2	23.4	23.1
215	22.5	21.3	23.9	23.1	22.9
216	22.3	21.0	23.6	22.9	22.9
217	22.0	20.6	23.3	22.8	22.8
218	21.8	20.4	22.8	22.4	22.8
219	21.4	19.9	22.4	22.2	22.8
220	20.9	19.5	22.1	21.9	22.6
221	20.3	19.1	21.8	21.7	22.4
222	19.9	18.7	21.4	21.5	22.3
223	19.5	18.3	21.3	21.2	22.3
224	19.4	18.0	20.9	20.9	22.1
225	19.0	17.8	20.6	20.5	21.9
226	18.7	17.3	20.3	20.4	21.6
227	18.0	17.0	20.1	20.0	21.6
228	17.5	16.6	19.6	19.7	21.4
229	16.9	16.3	19.1	19.4	21.1
230	16.5	16.0	18.7	19.1	21.1
231	16.1	15.6	18.3	18.7	20.9
232	15.7	15.3	18.1	18.3	20.6
233	15.2	14.8	17.6	18.0	20.4
234	15.2	14.3	17.4	17.8	20.2
235	15.3	14.2	17.0	17.4	20.0
236	15.0	13.8	16.8	17.0	19.9
237	14.6	13.4	16.4	16.6	19.6
238	14.2	13.2	16.0	16.3	19.3
239	13.7	12.9	15.7	15.9	19.1
240	13.5	12.6	15.3	15.5	18.8
241	13.0	12.3	15.1	15.2	18.4
242	12.7	12.1	14.5	14.8	18.2
243	12.5	11.7	14.2	14.5	18.0
244	12.1	11.2	13.7	14.1	17.8
245	11.6	10.7	13.3	13.5	17.5
246	11.5	10.5	13.0	13.2	17.2
247	11.1	10.1	12.7	12.8	17.0
248	10.8	10.0	12.3	12.5	16.5
249	10.6	9.7	12.1	12.2	16.2
250	10.5	9.3	11.7	11.9	15.8
251	10.3	9.0	11.3	11.6	15.5
252	10.2	8.9	11.0	11.6	15.2
253	9.9	8.4	10.6	11.2	14.8

254	9.8	8.3	10.1	10.9	14.5
255	9.6	8.1	9.6	10.6	14.2
256	9.4	8.0	9.4	10.2	13.8
257	9.1	7.8	9.3	10.0	13.4
258	8.8	7.7	9.2	9.7	13.1
259	8.5	7.4	9.0	9.4	12.9
260	8.4	7.1	8.7	9.1	12.4
261	8.3	7.1	8.3	8.9	12.2
262	8.1	6.9	8.1	8.6	11.8
263	7.9	6.6	7.9	8.5	11.6
264	7.7	6.5	7.5	8.3	11.2
265	7.5	6.3	7.2	8.0	11.2
266	7.3	6.0	6.9	7.9	11.0
267	7.0	6.0	6.7	7.6	10.8
268	7.2	6.0	6.5	7.4	10.5
269	7.1	5.9	6.3	7.2	10.5
270	6.6	5.8	6.0	6.9	10.2
271	6.6	5.5	5.9	6.8	9.9
272	6.3	5.4	5.8	6.5	9.6
273	6.2	5.3	5.7	6.1	9.2
274	5.9	5.1	5.5	5.9	9.0
275	5.4	4.9	5.3	5.8	8.8
276	5.4	4.9	5.1	5.6	8.6
277	5.2	4.9	5.0	5.4	8.5
278	5.0	4.8	4.9	5.2	8.3
279	5.0	4.7	4.8	5.1	8.0
280	5.0	4.6	4.6	5.0	7.7
281	5.3	4.6	4.4	4.9	7.5
282	5.2	4.4	4.3	4.6	7.5
283	5.0	4.1	4.2	4.5	7.3
284	4.9	3.8	4.2	4.4	7.1
285	4.9	3.8	4.1	4.5	6.9
286	4.8	3.6	4.0	4.3	7.0
287	4.5	3.6	4.0	4.1	6.7
288	4.4	3.7	4.0	4.0	6.5
289	4.3	3.6	4.1	4.0	6.5
290	4.2	3.7	4.3	3.9	6.3
291	4.1	3.7	4.2	4.0	6.2
292	4.0	3.8	4.1	3.7	5.9
293	3.7	3.5	3.9	3.6	5.7
294	3.6	3.2	4.0	3.6	5.5
295	3.5	3.2	3.8	3.5	5.4
296	3.5	2.9	3.8	3.4	5.3
297	3.3	2.8	3.7	3.2	5.1
298	3.2	2.7	3.5	3.3	4.9
299	3.0	2.5	3.3	3.2	4.9
300	3.4	2.5	2.9	3.1	4.8
301	3.3	2.6	2.9	3.0	4.7
302	3.2	2.6	2.8	2.9	4.6
303	3.2	2.5	2.8	2.8	4.5
304	3.0	2.3	2.7	2.8	4.4
305	2.9	2.3	2.7	2.8	4.2
306	3.0	2.3	2.8	2.7	4.2
307	2.9	2.2	3.1	2.6	4.0
308	2.8	2.3	3.0	2.6	3.9
309	2.8	2.2	2.9	2.5	3.7
310	2.6	2.2	2.8	2.3	3.6
311	2.5	2.2	2.6	2.5	3.4
312	2.5	2.0	2.6	2.4	3.1

313	2.5	2.1	2.6	2.2	3.0
314	2.3	1.9	2.5	2.1	3.0
315	2.2	1.8	2.3	2.2	2.8
316	2.1	1.8	2.3	2.0	2.8
317	1.8	1.6	2.2	2.0	2.7
318	1.9	1.4	2.1	1.9	2.6
319	1.8	1.4	2.0	1.8	2.4
320	1.6	1.4	1.9	1.7	2.5
321	1.7	1.4	1.7	1.6	2.4
322	1.8	1.4	1.8	1.4	2.4
323	1.8	1.5	1.6	1.4	2.5
324	1.8	1.5	1.7	1.3	2.6
325	1.9	1.6	1.8	1.3	2.5
326	1.7	1.4	1.8	1.3	2.3
327	1.7	1.4	1.7	1.2	2.3
328	1.7	1.3	1.6	1.2	2.3
329	1.7	1.2	1.6	1.1	2.3
330	2.0	1.3	1.5	1.1	2.4
331	2.0	1.3	1.6	1.1	2.4
332	2.1	1.5	1.5	1.1	2.3
333	1.9	1.3	1.6	1.0	2.2
334	1.6	1.2	1.4	1.0	2.2
335	1.6	1.0	1.6	1.2	2.3
336	2.1	0.9	1.6	1.1	2.1
337	2.0	0.9	1.6	1.1	2.2
338	1.8	0.8	1.4	0.9	2.1
339	1.8	0.9	1.4	0.9	2.0
340	2.0	0.9	1.4	0.8	2.0
341	1.9	0.9	1.2	0.8	2.0
342	2.0	0.8	0.9	0.8	1.7
343	1.9	0.8	0.8	0.8	1.6
344	1.8	0.8	1.0	0.7	1.7
345	1.8	0.7	0.9	0.7	1.7
346	1.9	0.7	1.1	0.8	1.5
347	2.1	0.7	0.8	0.7	1.6
348	1.8	0.7	0.8	0.7	1.5
349	1.6	0.8	0.8	0.6	1.5
350	1.7	0.7	0.8	0.6	1.5
351	1.5	0.5	0.7	0.6	1.6
352	1.6	0.6	0.6	0.6	1.6
353	1.5	0.5	0.6	0.7	1.5
354	1.5	0.6	0.4	0.6	1.5
355	1.6	0.7	0.4	0.4	1.3
356	1.5	0.7	0.4	0.4	1.4
357	1.6	0.8	0.4	0.3	1.3
358	1.6	0.7	0.5	0.5	1.2
359	1.6	0.8	0.4	0.4	1.2
360	1.3	0.8	0.2	0.4	1.0
361	1.3	0.8	0.2	0.4	0.9
362	1.7	0.8	0.3	0.4	0.9
363	1.4	0.7	0.2	0.4	0.8
364	1.1	0.7	0.5	0.4	1.0
365	1.2	0.7	0.4	0.4	1.1
366	1.1	0.8	0.4	0.6	1.1
367	1.1	0.8	0.3	0.6	1.1
368	1.0	0.5	0.4	0.4	1.1
369	1.0	0.5	0.3	0.5	1.3
370	1.2	0.5	0.2	0.5	1.2
371	1.2	0.5	0.4	0.5	1.0

372	1.1	0.6	0.7	0.5	1.0
373	1.0	0.6	0.8	0.6	0.9
374	1.0	0.4	0.8	0.5	0.8
375	1.0	0.3	0.8	0.6	0.6
376	1.1	0.4	0.7	0.5	0.6
377	0.9	0.3	0.7	0.4	0.7
378	1.1	0.1	0.7	0.4	0.7
379	1.0	0.2	0.8	0.4	0.7
380	1.1	0.2	0.9	0.3	0.5
381	1.1	0.0	1.2	0.2	0.7
382	1.5	0.2	1.2	0.1	0.7
383	1.4	0.4	1.0	0.0	0.6
384	1.3	0.5	1.0	0.0	0.6
385	1.5	0.6	1.0	0.0	0.6
386	1.5	0.7	0.9	0.0	0.5
387	1.4	0.5	0.7	0.0	0.6
388	1.6	0.4	0.7	0.0	0.6
389	1.6	0.4	0.8	0.0	0.6
390	1.7	0.2	0.8	0.0	0.6
391	1.9	0.0	0.7	0.0	0.5
392	1.8	0.0	0.8	0.0	0.4
393	1.5	0.0	0.7	0.0	0.3
394	1.7	0.1	0.7	0.0	0.4
395	1.2	0.1	0.6	0.0	0.3
396	1.2	0.0	0.5	0.0	0.5
397	1.0	-0.1	0.3	0.0	0.6
398	1.0	-0.1	0.4	0.0	0.7
399	1.0	0.0	0.4	0.0	0.8
400	0.9	0.2	0.5	0.0	0.9
401	1.3	0.2	0.4	0.0	0.9
402	1.1	0.2	0.5	0.0	0.7
403	1.0	0.2	0.4	0.0	0.7
404	1.2	0.4	0.4	0.0	0.6
405	1.0	0.2	0.4	0.0	0.6
406	1.0	0.1	0.2	0.0	0.4
407	0.9	0.2	0.2	0.0	0.4
408	0.8	0.3	0.1	0.0	0.5
409	0.7	0.2	0.0	0.0	0.4
410	0.6	0.3	0.2	0.0	0.3
411	0.6	0.4	0.3	0.0	0.4
412	0.6	0.3	0.2	0.0	0.5
413	0.4	0.3	-0.1	0.0	0.6
414	0.3	0.4	0.1	0.0	0.6
415	0.3	0.3	0.2	0.0	0.6
416	0.5	0.3	0.3	0.0	0.5
417	0.5	0.4	0.2	0.0	0.8
418	0.6	0.3	0.0	0.0	0.7
419	0.4	0.5	0.1	0.0	0.6
420	0.1	0.6	0.2	0.0	0.7
421	0.3	0.6	0.3	0.0	0.5
422	0.5	0.9	0.4	0.0	0.4
423	0.5	0.9	0.5	0.0	0.5
424	0.7	0.9	0.5	0.0	0.5
425	0.8	1.0	0.6	0.0	0.4
426	0.9	0.9	0.7	0.0	0.5
427	1.1	0.9	0.6	0.0	0.4
428	1.0	1.0	0.7	0.0	0.3
429	1.0	1.0	0.7	0.0	0.2
430	0.9	0.9	0.7	0.0	0.2

431	0.8	0.9	0.5	0.0	0.2
432	0.5	1.0	0.3	0.0	0.3
433	0.7	0.9	0.2	0.0	0.4
434	0.5	0.8	0.3	0.0	0.3
435	0.5	0.6	0.3	0.0	0.4
436	0.2	0.5	0.3	0.0	0.4
437	0.4	0.7	0.3	0.0	0.3
438	0.1	0.6	0.3	0.0	0.3
439	0.1	0.5	0.3	0.0	0.5
440	0.0	0.3	0.3	0.0	0.5
441	0.0	0.3	0.3	0.0	0.5
442	0.0	0.1	0.3	0.0	0.4
443	0.0	0.1	0.2	0.0	0.5
444	0.0	0.1	0.0	0.0	0.4
445	0.0	0.3	0.0	0.0	0.3
446	0.0	0.1	0.0	0.0	0.4
447	0.0	0.0	0.0	0.0	0.4
448	0.0	0.0	0.0	0.0	0.3
449	0.0	0.0	0.0	0.0	0.3
450	0.0	0.0	0.0	0.0	0.3
451	0.0	0.0	0.0	0.0	0.3
452	0.0	0.0	0.0	0.0	0.2
453	0.0	0.0	0.0	0.0	0.2
454	0.0	0.0	0.0	0.0	0.2
455	0.0	0.0	0.0	0.0	0.1
456	0.0	0.0	0.0	0.0	0.1
457	0.0	0.0	0.0	0.0	0.2
458	0.0	0.0	0.0	0.0	0.2
459	0.0	0.0	0.0	0.0	0.2
460	0.0	0.0	0.0	0.0	0.3
461	0.0	0.0	0.0	0.0	0.4
462	0.0	0.0	0.0	0.0	0.2
463	0.0	0.0	0.0	0.0	0.1
464	0.0	0.0	0.0	0.0	0.2
465	0.0	0.0	0.0	0.0	0.3
466	0.0	0.0	0.0	0.0	0.4
467	0.0	0.0	0.0	0.0	0.3
468	0.0	0.0	0.0	0.0	0.2
469	0.0	0.0	0.0	0.0	0.4
470	0.0	0.0	0.0	0.0	0.3
471	0.0	0.0	0.0	0.0	0.3
472	0.0	0.0	0.0	0.0	0.2
473	0.0	0.0	0.0	0.0	0.1
474	0.0	0.0	0.0	0.0	0.1
475	0.0	0.0	0.0	0.0	0.2
476	0.0	0.0	0.0	0.0	0.3
477	0.0	0.0	0.0	0.0	0.2
478	0.0	0.0	0.0	0.0	0.3
479	0.0	0.0	0.0	0.0	0.4

국문초록

개수로에서 2차원 분산계수 추적법 및 원격관측 추적자 실험에의 적용

서울대학교 대학원
건설환경공학부
백 동 해

2 차원 수심평균 된 이송-분산 방정식은 하천환경에서 다양한 용존성 오염물질의 혼합현상을 모의하기 위해 널리 활용되어 왔다. 수심평균 된 2 차원 이송-분산 방정식의 분산계수는 3 차원 이송-확산 방정식에 대해 수심 평균을 취하는 과정에서 연직방향상 질량이송의 편차를 Fick 의 법칙에 의해 모형화함에 따라 생성된다. 2 차원 혼합모형에서 분산계수는 하천의 전단흐름에 의해 야기되는 오염물질의 퍼짐 현상을 표현하는 중요한 인자로서 작용하므로 정교한 오염물질 혼합거동을 모의하기 위해서는 적절한 분산계수를 산정하는 것이 필수적이다. 분산계수를 실험적으로 산정하는 방법으로는 크게 모멘트법과 추적법으로 나뉘며, 비정상상태의 혼합거동에 대해 종방향 및 횡방향 분산계수를 모두 산정할 수 있는 방법은 추적법 계열의 2 차원 유관추적법(2D STRP)이 유일하다. 본 연구에서는 해석해 및 수치해 기반의 자료를 바탕으로 2D STRP 의 적용범위 및 정확도를 정량적으로 분석하였다. 분석된 정보를 바탕으로 2D STRP 및 기존의 접촉식 계측 기반 추적자실험법의 한계를 극복하기

위해 개선된 2 차원 유관추적법(2D STRP−*i*) 및 원격탐사 기반의 추적자 실험법을 개발하였다.

기존 2D STRP 의 성능은 다양한 Peclet 수의 범위 및 비균등 유속분포에 대해서 평가되었다. 평가 결과, 2D STRP 는 Peclet 수가 높은 조건일수록 농도분포의 예측 정확도가 상승하였으나, 추적자의 농도분포가 하안경계에 도달하는 경우에는 부정확한 결과를 초래하는 것으로 나타났다.

본 연구에서는 기존 2D STRP 의 한계를 보완하여 더욱 정확한 분산계수를 산정하고자, 하안 경계면 조건을 고려한 2 차원 유관추적법(2D STRP−*i*)을 개발하였다. 2D STRP−*i* 는 직교−곡선좌표계 기반의 2 차원 이송−분산 방정식을 바탕으로 횡방향 유속분포 및 하안 경계조건을 고려하여 유도되었다. 제안된 2D STRP−*i* 는 공간적으로 상이한 이송효과 및 하안경계 조건을 적절히 반영함으로써 기존의 2D STRP 에 비해 농도분포의 예측 정확도를 월등히 개선시키는 것으로 평가되었다.

또한, 본 연구에서는 시공간적으로 높은 해상도의 추적자 농도 자료를 취득하고자 원격탐사기반의 추적자실험법을 개발하였다. 원격탐사기반의 추적자실험법은 소형 무인항공기에 장착된 상용 디지털카메라의 각 밴드별 화소강도의 변화를 이용하여 하천에 주입된 형광색소(Rhodamine WT)의 농도를 측정하는 방법이다. 추적자실험을 통해 취득된 형광색소의 농도 및 디지털 영상자료를 이용하여 인공신경망 기반의 경험적 회귀모형을 구축하였으며, 학습된 회귀모형은 결정계수 0.9이상의 우수한 정확도를 보이는 것으로 나타났다.

원격탐사기반 추적자실험법에 의해 측정된 농도자료에 대해 기존의 2D STRP와 본 연구에서 제안된 2D STRP−*i*를 적용하여 분산계수를 산정 및 비교하였다. 최적 분산계수의 결정은 Latin Hypercube 모의법을 이용하였으며, 최적의 분산계수는 실측된 농도분포와 예측된 농도분포 간 오차를 평가하는 기준에 따라 상이한 값으로 산정되었다. 따라서, 본 연구에

서는 다양한 통계적 특성을 만족시키는 강건한 분산계수를 산정하기 위해 정규화된 다수의 평가지표를 고려하여 분산계수의 최적값을 결정하였다. 기존 2D STRP 및 제안된 2D STRP−*i*에 의해 산정된 분산계수값을 비교한 결과, 기존 2D STRP 및 2D STRP−*i*에 의해 산정된 종방향 분산계수는 유사한 경향을 보이는 것으로 나타났으나, 횡방향 분산계수는 하안 경계면의 효과에 의해 기존 2D STRP의 결과가 과소산정되는 것으로 나타냈다.

주요어: 수심평균 2차원 혼합모형, 전단류 분산, 추적법, 원격탐사기법, 시공간적 농도분포, 인공신경망, 2차원 추적자실험법

학번: 2015−30277